Parameterisation of Orographic Cloud

A Thesis Submitted in Partial Fulfilment
of the Requirements for the Degree
of
Doctor of Philosophy in Physics
at the
University of Canterbury

by

Samuel M. Dean

University of Canterbury
2002

Abstract

Orographic cloud is investigated in a global context using both observations and a global climate model. Climatological cloud amounts from the International Satellite Cloud Climatology Project (ISCCP) are used in conjunction with wind reanalyses to study orographic cirrus amounts over the globe. Significant increases in cirrus are seen over many land areas, with respect to any surrounding oceans. To aid in interpretation of this result special attention is given to the New Zealand region as a case study for orographic cloud formation. Cirrus is found be more prevalent over New Zealand when compared to the adjacent ocean to the west.

ISCCP cloud amounts are also compared with a ten year simulation of the UK Meteorological Office's Unified Model. The model is found to be considerably lacking in both cirrus and total high cloud over major mountain ranges. The model is also found to lack trailing cirrus clouds in the lee of orography despite the inclusion of a prognostic ice variable capable of being advected by the model winds.

To improve the simulations of orographic cirrus and high cloud in the Unified Model a linear hydrostatic gravity wave scheme that predicts both the amplitude and phase of subgrid orographic gravity waves is introduced. The temperature perturbation caused by these waves in the troposphere is used to modify the amount of both liquid and ice cloud. One important feature of the parameterisation is that the launch amplitude of the gravity waves is predicted by a directional variance function which accounts for anisotropy in the subgrid orography. The parameterisation is explored in the context of an off-line testbed before implementation in the Unified Model.

In a ten year simulation the parameterisation is found to increase the high cloud amounts over a number of the world's major mountain ranges. However, this extra cloud is optically thick and unable to remove the deficiency in optically thin cirrus amounts. Suggestions, as part of future work, for improvements to the model and orographic cloud parameterisation are also made.

Acknowledgements

First and foremost I wish to thank my supervisor Bryan Lawrence for his guidance through this thesis and the inspiration to study atmospheric science. Thanks Mate. Next must stand Scott Osprey who has been a good colleague, office mate, flatty, and friend throughout hours of debates on physics and the rest of life. Good stuff!

A number of people have also made important contributions to the early direction of this thesis. These include Darlene Heuff, Don Grainger, Stuart Webster and Dave Stainforth. Special mention must go to Jamie Kettleborough and my girlfriend Barbara who took the time to read this thesis and debate over points of grammar. Barbara's proofreading has also been floorless.

I also acknowledge the provision of the ERA-15 data by the ECMWF and the ISCCP data by the NASA Langley Research Center Atmospheric Sciences Data Center.

To my best mate Matt and all of the members of the Physics Department at the University of Canterbury who made my six years there so enjoyable, and leaving so difficult.

I also owe a large debt of gratitude to the British Atmospheric Data Centre as well as the department of Atmospheric, Oceanic and Planetary Physics, University of Oxford who both provided me with facilities and support during the last year of this thesis. A special mention must go to my room mates during this time Mark, Alison and Gewen for putting up with my incessant babble about sport and New Zealand.

Finally to my family without whom none of this would be possible: Katie, Hamish Beth, Dad and Mum. Thank you for your constant love and support. This is for you...

If Clouds were the mere result of the condensation of vapour in the masses of the atmosphere which they occupy, if their variations were produced by the movements of the atmosphere alone, then indeed might the study of them be deemed a useless pursuit of shadows, an attempt to describe forms which, being the sport of the winds, must be ever varying, and therefore not to be defined. But the case is not so with clouds...

Luke Howard, December 1802

Contents

Figures

Tables

Chapter 1

Introduction

Aotearoa, the Maori name for New Zealand, translates as 'land of the long white cloud'. This name illustrates that the importance of cloud on the region's weather and climate has long been recognised. The long white cloud referred to would not exist if it were not for the presence of New Zealand's mountains. These clouds, which are created by air being lifted over mountains, are referred to as orographic clouds. A photo of such orographic clouds over New Zealand is shown in figure 1.1.

Figure 1.1: A photo of orographic clouds taken from outside Christchurch, New Zealand. Photo courtesy of Juern Schmelzer.

Highlighted by the rising sun, low level orographic clouds can be identified near the mountains. Higher up a solid band of dark orographic cloud can also be seen. This cloud is created in an atmospheric wave over the mountain. When such clouds form in the upper atmosphere, where it is cold enough for water to freeze, it is considered orographic cirrus. In certain situations the ice formed can evaporate very slowly and so it can be blown hundreds of kilometres with the wind. Because these orographic cirrus clouds can cover large areas they can have a significant impact on the global cloud cover.

Clouds in general play a very important role in the radiation budget of the atmosphere through their ability to reflect and absorb radiation. As a result they have a strong influ-

ence on the temperatures that we experience at ground level. Additionally, clouds affect the water budget through their ability to store and release water from the atmosphere as rain. They also have a less dramatic, but nevertheless important, influence on the general circulation for periods of days to weeks, by altering temperature gradients and atmospheric stability.

These factors suggest that there could be large feedbacks from future changes in cloud amount, when compared to external changes such as 'greenhouse' gas concentrations. This has long been recognised by climate modellers, who use sophisticated numerical models to mimic the atmosphere. These models can be used to help understand the atmosphere as well as to assess the impact of anthropogenic activities such as global warming. The Intergovernmental Panel on Climate Change (IPCC) has stated that the phenomena of climate variability are sensitive to orographic effects and that numerical simulation of many key climatic elements such as rainfall and cloud cover strongly depend on orography. These issues may have potentially important consequences for the planetary-scale distribution of climate change (*IPCC*, 2001).

The aim of this thesis is to investigate orographic cloud over both New Zealand and globally by using observations as well as a global climate model. By then improving the simulation of orographic clouds in this climate model it becomes possible to address the importance of orographic clouds on the present and future climate of the Earth.

1.1 New Zealand

Throughout this thesis the region which encompasses New Zealand and its surrounding oceans is used as a case study for orographic cloud formation. New Zealand is not unique in generating large orographic cirrus clouds, but its narrow land mass and high mountains make it an ideal testbed for studying relatively simplified mountain flows and the resulting clouds that form. In particular the mountain ranges of the South Island of New Zealand present a high barrier to the mid-latitude westerly flow. Many of the mountain ranges are over 1000m high and Mt Cook, the highest peak, stands at 3754m. The combination of the steep land mass and surrounding ocean also results in little convective activity to confuse the interpretation of orographic wave clouds.

Anticyclones and depressions pass over New Zealand regularly from the west. Strong north-westerly winds occur over the South Island when an anticyclone is located to the north-east of New Zealand and a depression to the south-west. There is also often an associated cold front. These north-west winds can persist for a number of days and result in airflows which are perpendicular to the main orientation of the mountain ranges.

In such a situation a solid sheet of cloud often forms which streams away from the mountains for distances which can range from tens to hundreds of kilometres. The distinct

leading boundary of the cloud at low levels, which can first appear above or a small distance downwind of the ranges, has led to the cloud being known locally as a Northwest Arch. The photo shown as figure 1.1 illustrates this sharp edge and a satellite image of an Arch from space is presented as figure 1.2.

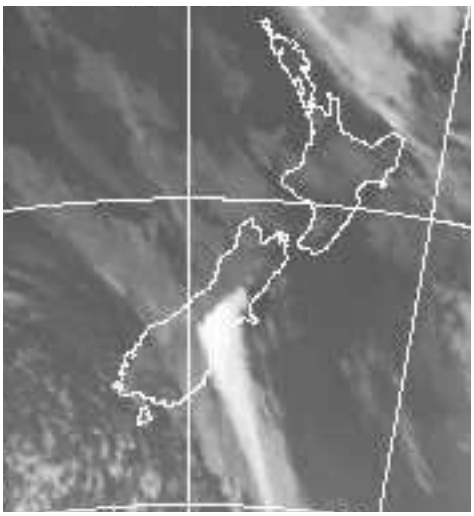

Figure 1.2: A satellite image of a Northwest Arch with cloud being blown away from the mountains.

The Arch can be preceded by cirrus upwind of the mountains but also often occurs when the flow was previously cloud free. Before progressing it will be necessary to more carefully introduce the concepts involved in orographic cloud formation.

1.2 Gravity Waves

It is readily believable that orographic clouds can form when air that is adjacent to a mountain is lifted sufficiently for the air to cool to the saturation point. This is the point where condensation of water from vapour in the air dominates over evaporation and a cloud will begin to form. This is the effect that often leads to the upwind side of mountains receiving considerably more precipitation than the downwind side.

But how can small mountains, which occupy only a small fraction of the atmosphere's total depth, create clouds with bases that can be ten times higher than the mountain top? The answer is that because the atmosphere is stratified it is exceedingly sensitive to any vertical motions. Consider a parcel of air which is displaced above its equilibrium height by flowing up a mountain. The parcel of air will now be more dense than the air around it and will feel a net downward force. This net downward force is known as a buoyancy force and results from an imbalance between the surrounding vertical pressure gradient force and the gravitational force acting on the parcel. If a parcel were instead

displaced below its equilibrium point then the buoyancy force would act upwards. It is now apparent that any parcel which is given a perturbation by a mountain can rapidly begin to oscillate about its equilibrium point, and this so-called buoyancy oscillation can be transmitted to the air above and below. In this way vertical motion generated at the bottom of the atmosphere can be transmitted (or propagate) high into the upper atmosphere. These propagating buoyancy oscillations are commonly known as *gravity waves*, because of the inherent role gravity plays in both the downward gravitational force and the vertical pressure gradient force.

In the troposphere these vertical motions have the same ability to form clouds as the air that was directly adjacent to the mountain. Figure 1.3 is an example of how a gravity wave propagating above an idealised bell shaped ridge appears in the streamlines of the flow. Where the streamlines are displaced above equilibrium the air will be cooled. If this cooling is sufficient for the air to reach the saturation point then naturally a cloud will form. A couple of the possible places where this could occur in figure 1.3 are shaded. Label A is where the Northwest Arch cloud in figure 1.2 would be located.

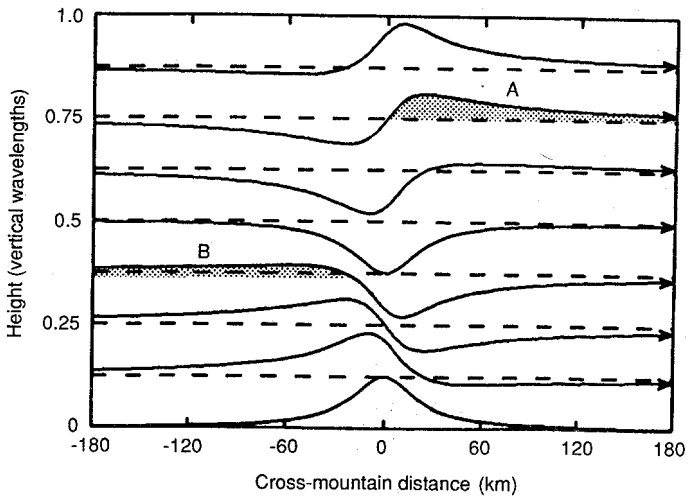

Figure 1.3: Streamlines of a flow moving from left to right over a broad isolated mountain ridge which illustrate a vertically propagating gravity wave. Orographic clouds may form where the streamlines are displaced above equilibrium, either upstream (B) or downstream of the ridge. Two possible examples are shaded. (Courtesy of Dr Dale Durran.)

When there are large mountains, or weak winds more complicated wave patterns can occur. Sometimes sudden changes in the streamlines of the air flow can resemble the 'hydraulic jumps' seen in rivers when water flows over a stone. In many atmospheric situations the complexity of the terrain which generates the waves can result in waves of different amplitude and horizontal extent exisiting simultaneously.

The density of the atmosphere decreases exponentially with height and this causes a

gravity wave that propagates high into the atmosphere to grow in amplitude. In conjunction with other changes in the background atmosphere it is possible for the wave to begin to break. In the process of breaking an orographic wave transfers momentum from the surface to higher up. Throughout the atmosphere this momentum deposition acts as a force on winds and in the upper atmosphere is essential in driving circulations.

This effect has been recognised as important for a number of years by climate modellers who use sophisticated numerical models to mimic the atmosphere. These models can be used to help understand the atmosphere as well as to assess the impact of anthropogenic activities such as global warming. To be able to solve numerically the complex physical equations which describe the motions in the atmosphere general circulation models (GCMs) break the globe into large blocks of air. Each of these blocks is known as a gridbox and is allowed only one value at each time step for each of the variables which describe the atmospheric state (e.g. wind, temperature and pressure). In the current generation of GCMs used for long term climate modelling the horizontal size of each of these gridboxes is hundreds of kilometres.

While the approximation of using large gridboxes allows for good reproduction of the large scale features of the atmosphere, many physical processes occur on scales which are much smaller than this resolution. One example is clouds, which can range in size from less than a kilometre to hundreds of kilometres. Another is many of the gravity waves that exist in reality. Models are unable to resolve much of the orography that generates small gravity waves, and the actual motions of these waves. Because they are unable to resolve the waves they are also unable to represent both any orographic cirrus that might be generated, or any effect on the winds due to wave breaking.

To circumvent the problem of unresolved gravity waves on atmospheric winds modellers parameterise their effect. This involves developing a separate physical model that attempts to describe the average effect of orographic gravity waves on the gridbox wind. The waves are generated by using subgrid scale information about the orography. Orographic gravity waves always act as a drag on atmospheric winds and thus help to decrease the speed of westerly winds simulated by models (*Palmer et al.*, 1986). In a similar way clouds are parameterised so that a gridbox is not simply cloudy or clear. Instead fractional cloud cover is allowed based on the gridbox values of humidity, temperature and pressure.

Despite the existence of both orographic gravity wave and cloud parameterisations in GCMs they are currently considered independent of each other and so do not interact. The fact that there is no reason for this to remain so leads to one of the objectives of this thesis. A modified gravity wave scheme that is capable of calculating explicitly the vertical displacement of air parcels from their equilibrium levels by unresolved gravity waves can couple this information to an existing cloud parameterisation and produce orographic

clouds. In a sense information from one parameterisation can be adapted to improve another parameterisation with relatively little computational expenditure. Two processes that are intricately linked in the real atmosphere can become linked in the climate model!

1.3 Outline

It is necessary to introduce in chapter 2 some background information needed to study orographic clouds. This includes the classification of cloud types, the microphysics of cloud formation and the effect of clouds on radiation in the Earth's atmosphere. Otherwise the general strategy of the thesis is to establish an impression of the nature and distribution of orographic wave clouds by beginning with observations of such clouds, before progressing to the more theoretical understanding needed to develop a parameterisation.

As a case study region, large orographic wave clouds over New Zealand are considered in chapter 3. This brings together previous observations by other authors as well as using satellite images to qualitatively elucidate the significance of orographic cirrus.

For a number of years satellites have also been used to study clouds quantitatively from space. Cirrus has generally been observed to be more frequent over mountainous regions when compared to oceans and flat land. Chapter 4 will consider in detail the cirrus cloud observations of the International Satellite Cloud Climatology Project (ISCCP) both globally and over New Zealand.

The thesis then begins to address the issues of parameterising orographic wave clouds in a climate model. To this end a limited review of the necessary theory of orographic gravity waves is given in chapter 5. The GCM used in this thesis is the Unified Model(UM) of the United Kingdom Met Office and a description of the model is given in chapter 6. The theory of the parameterisation is developed in detail in chapter 7. In order to validate the parameterisation, and to help understand its behaviour, a simplified testbed is introduced. Finally the results of ten year simulations of the UM with and without the parameterisation are presented in chapters 8 and 9.

As well as presenting a useful parameterisation of orographic cloud this thesis aims to draw attention to an area of relative neglect in atmospheric science.

Chapter 2

Clouds

This chapter aims to provide some of the necessary background information needed for studying clouds. It begins with the descriptive classification of clouds before focusing more specifically on the theory of orographic cloud formation. Orographic cirrus is considered in detail because of its ability to cover large areas and its relative radiative importance. The issues of cloud and its interaction with radiation are also discussed.

2.1 Cloud Classification

Clouds were originally described by their general appearance, colour, and shape, which led to them being categorised using a visual classification scheme. The basis for this scheme was produced by the English naturalist Luke Howard in 1803 (*Shaw*, 1996). In this standard scheme, cloud types are given descriptive names based on Latin root words:

Cumulus - heap or pile

Stratus - to flatten out or cover with a layer

Cirrus - a lock of hair or tuft of horsehair

Nimbus - precipitation

Altum - height

By combining these root words appropriately it is possible to classify most clouds into ten groups, which can be further combined into three height based varieties. The ten possible groups are displayed in table 2.1

In addition there are two cloud types which do not fit into this classification scheme but are important nonetheless. One is fog, which can be classified as any of the low height group clouds in table 2.1 whose base touches the ground. The other is orographically induced cloud which can form as air is uplifted over a mountain. These clouds will be discussed in detail in the next section. However, in the broadest sense, orographic clouds can take the form of any of the types of cloud listed in table 2.1.

Cloud Type	*Height Group*	*Height Range*
Cumulus	*Low*	
Cumulonimbus	*Low*	
Stratus	*Low*	*below* $2km$
Stratocumulus	*Low*	
Nimbostratus	*Low*	
Altostratus	*Middle*	$2-4km$
Altocumulus	*Middle*	
Cirrus	*High*	
Cirrostratus	*High*	$5-13km$
Cirrocumulus	*High*	

Table 2.1: Groups of clouds identified visually.

The five types of low cloud listed in table 2.1 can be broken into two groups. Cumuliform clouds are those which involve rapidly rising air, giving them a bubbling and towering nature and stratiform clouds which are broad stable sheets of cloud.

A brief outline of each standard cloud type will now be given in terms of its visual features as described by *Houze* (1993). All of these cloud types can also be seen in figure 2.1.

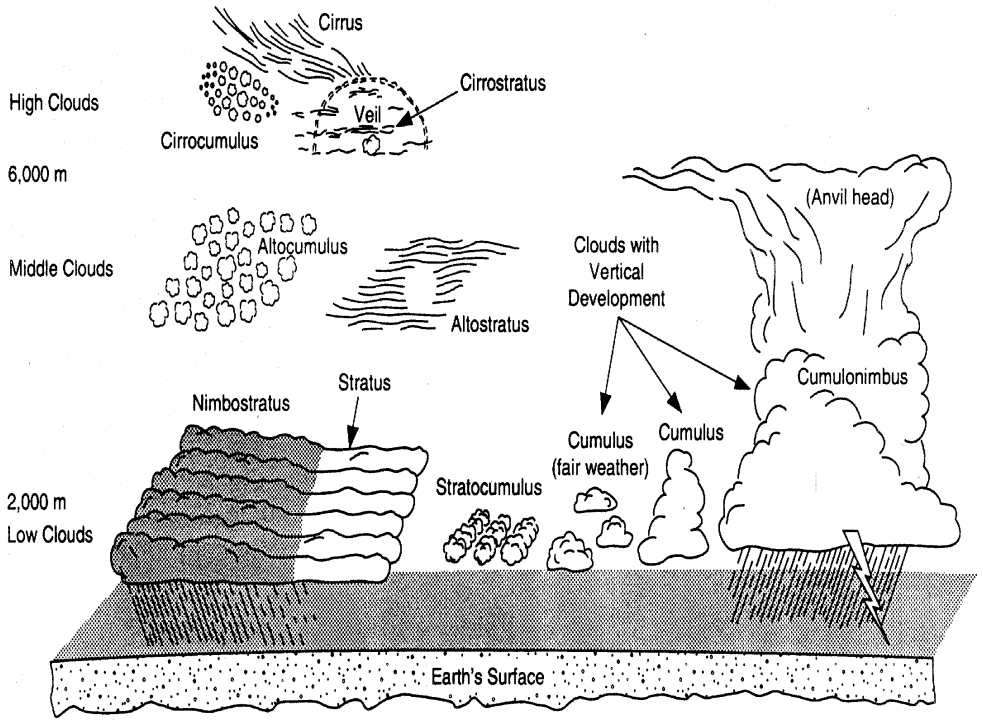

Figure 2.1: Illustration of different cloud types and their division into three main height bands. From *Shaw* (1996).

Cumulus clouds are dense clouds with sharp outlines. They can be a variety of sizes and often reach considerable heights. Their bulging upper part can often resemble a cauliflower.

Cumulonimbus is an advanced stage of cumulus development, consisting of large towers with precipitation at the base. They may form thunderstorms and can create hail storms at their bases. The tops of these clouds can reach to the tropopause, where they will form anvil heads.

Stratus is a layer cloud which is generally relatively thin. It has a well defined base which may give drizzle. A single cloud can be hundreds of kilometres in horizontal extent.

Stratocumulus is much like stratus in that it is is often a low overhanging blanket of cloud, however it is usually distinguishable due to the presence of obvious clumps. These clumps may be darker masses, or rolls, but are never fibrous. This type of cloud is often found in association with stratus.

Nimbostratus is also a large grey cloud layer but is distinguished by the presence of more or less continuously falling rain or snow. This type of cloud is also much thicker than stratus and can extend through much of the troposphere. Its upper layers may be composed of ice.

Altostratus is a grey cloud sheet but differs from stratus in that its base is at a much higher altitude. The sun's outline is often still visible through such a cloud. Any precipitation does not reach the ground.

Altocumulus is also a middle level cloud, but its distinguishing characteristic is that unlike altostratus it has distinct elements, which can be anything from small clumps to long rolls. It is often similar in appearance to stratocumulus.

Cirrus are high altitude clouds which are very thin and form patches or narrow bands. They are often described as having a fibrous appearance.

Cirrostratus is like cirrus only covering a large portion of the sky. It generally produces a 'halo', a ring of light around the sun when it is viewed through such a cloud. The halo is created by the refraction of sunlight through hexagonal prisms of ice.

Cirrocumulus is a high altitude counterpart of altocumulus and often has many of the same characteristics. It consists of a thin sheet of cloud which has small elements in the shape of grains or ripples.

2.2 Orographic Clouds

In the lowermost atmosphere the air flowing over the Earth's surface must follow the terrain. Hence, where a large mountain is present, air may be forced to rise a considerable distance from sea level. As the air ascends over the upwind side of the mountain, it may cool sufficiently for the water vapour in it to condense and form a cloud or even to precipitate as rain. It is these clouds, described as 'orographic' clouds, which will be the focus of this section. Some common, specific orographic clouds are:

Cap cloud is a simple type of cloud that remains stationary over the peak of an isolated mountain.

Crest cloud is the same as a cap cloud only for a whole mountain ridge.

Föhn wall cloud refers to a bank or wall of cloud which forms upwind and along the ridge of a mountain range. Usually associated with warm, strong, winds on the lee side of the mountain known as a Föhn wind.

Lenticular cloud, or lenticularis, is a lens shaped cloud that forms over or in the lee (downwind) of a mountain barrier. These clouds usually form in the crests of a lee wave, which is a wave that is forced by the atmospheric conditions to continue oscillating downwind.

Orographic cirrus is an orographic cloud that can form in the wave that propagates above a mountain. Because it consists of ice the cloud can be advected hundreds of kilometres downwind of the mountain over which it is created. Such large clouds can significantly influence the local radiative balance of the atmosphere and are the focus of this thesis.

Comprehensive reviews on different types of orographic cloud are given in *Smith* (1979), *Cotton and Anthes* (1989) and *Houze* (1993). The next section will simply discuss briefly how water and ice form in orographic clouds, but will not consider orographic precipitation.

2.2.1 Water vapour in air

There are numerous ways of describing the water vapour content of atmospheric air, and the ones used in this thesis need to be considered. The most fundamental is to express the vapour concentration as a *vapour pressure*, which is given the symbol e. Water vapour in most situations behaves as an ideal gas (*Bohren and Albrecht*, 1998) so the vapour pressure can be found from the vapour density, ρ_v, also known as *absolute humidity*, using

the ideal gas law for vapour

$$e = \rho_v R_v T \tag{2.1}$$

where R_v is the gas constant for water vapour. More commonly dimensionless quantities are used. The *specific humidity*, q, is defined as the ratio of the vapour density to the density of the dry air (ρ_d) and vapour (i.e. $\rho = \rho_d + \rho_v$)

$$q = \frac{\rho_v}{\rho} \tag{2.2}$$

If water vapour is slowly added to air, at a fixed temperature, a point will eventually be reached where the rates of evaporation and condensation are in equilibrium. This is called the saturation point and in the above definitions corresponds to a saturation vapour pressure, e_s, or a saturation specific humidity, q_s. This idea allows for the construction of another useful dimensionless quantity called the relative humidity, RH. Confusingly the relative humidity can have two definitions: as the ratio of vapour pressure to saturation vapour pressure

$$RH = \frac{e}{e_s} \times 100\% \tag{2.3}$$

or as the ratio of specific humidity to saturation specific humidity

$$RH = \frac{q}{q_s} \times 100\% \tag{2.4}$$

It is worth showing that both definitons are approximately equivalent. Using 2.1 the specific humidity can be rewritten as:

$$q = \frac{e}{\rho R_\nu T} \tag{2.5}$$

Expanding ρ into its components gives

$$q = \frac{e}{\rho_d R_\nu T + e} \tag{2.6}$$

$$= \frac{\epsilon e}{\rho_d R_d T + \epsilon e} \tag{2.7}$$

where $\epsilon = \frac{R_d}{R_v}$ and R_d is the gas constant for dry air. The ideal gas law can be applied to dry air to show that the dry air pressure, p_d, is

$$p_d = \rho_d R_d T \tag{2.8}$$

Then 2.7 can be expressed in terms of the total pressure of the moist air, $p = p_d + e$, as

$$q = \frac{\epsilon e}{p - e(1+\epsilon)} \tag{2.9}$$

Dividing through by the saturated specific humidity leads to

$$\frac{q}{q_s} = \frac{e}{e_s}\left(\frac{p - e_s(1+\epsilon)}{p - e(1+\epsilon)}\right) \tag{2.10}$$

Because $p \gg e(1+\epsilon)$ in the atmosphere the two definitions for relative humidity are approximately equal. For consistency in this thesis relative humidities will be calculated from the specific humidities.

2.2.2 Condensation

The properties of any particular cloud are controlled by the many factors that determine the process by which water vapour condenses to form liquid drops. The two methods of nucleation of water droplets from vapour are homogeneous nucleation and heterogeneous nucleation. The former involves the idea that vapour molecules in the air may come together by chance collisions, while the latter refers to the collection of molecules onto a foreign substance often referred to collectively as cloud condensation nuclei (CCN). An example of such nuclei are the myriad aerosol particles (e.g. dust) that exist in our atmosphere.

Once a drop has formed it may continue to grow through vapour diffusion towards the drop. This is known as condensation and only dominates over the opposite process of evaporation if the amount of vapour contained in the air is greater than its saturation level. The details of these microphysical processes will be considered only briefly here.

The saturation vapour pressure is found to be dependent only on temperature by the equation:

$$\frac{de_s}{dT_s} = \frac{L_c}{T_s(\alpha_v - \alpha_l)} \tag{2.11}$$

where T_s is the temperature at saturation, L_c is the latent heat of condensation and α_l and α_v represent the specific volumes at temperature T_s of the liquid and vapour phases of water respectively. This is known as the Clausius-Clapeyron equation after its two discoverers and a derivation can be found in *Rogers and Yau* (1989). Under normal atmospheric conditions the specific volume of vapour is much larger than that of liquid so $\alpha_v \gg \alpha_l$ and equation 2.11 becomes

$$\frac{de_s}{dT_s} = \frac{L_c}{T_s\alpha_v} \tag{2.12}$$

Also to a good approximation water vapour follows the ideal gas law (2.1) so:

$$e_s = \frac{R_\nu T_s}{\alpha_v} \tag{2.13}$$

The equation for the change in saturation vapour pressure with temperature reduces to

$$\frac{1}{e_s}\frac{de_s}{dT_s} = \frac{L_c}{R_\nu T_s^2} \tag{2.14}$$

By assuming that the latent heat of condensation is constant with temperature it is possible to integrate 2.14. Despite this assumption being strictly not true it leads to a solution that is not significantly in error over the range of tropospheric temperatures.

$$e_s = C \exp\left(-\frac{L_c}{R_\nu T_s}\right) \tag{2.15}$$

where C is a constant. Clearly then e_s is an exponential function of temperature. The higher the temperature the greater the average molecular kinetic energy, which leads to more evaporation and hence a greater saturation vapour pressure. Air parcels are usually lifted over orography rapidly enough for the ascent to be considered adiabatic. Under this assumption there is no exchange of energy with the surroundings and as it ascends an air parcel will expand and cool. The temperature of such a parcel falls according to

$$T_{\text{parcel}} = T_0 \left(\frac{p}{p_0}\right)^{\frac{R}{c_p}} \tag{2.16}$$

where T_0 and p_0 are the initial temperatures and pressures, R the gas constant and c_p the specific heat at constant pressure. This drop in temperature leads to a decrease in e_s as given by equation 2.15. However, because e also decreases it is necessary to show that it decreases more slowly than e_s. If the mass of vapour in the air parcel, m, is assumed to be constant then the vapour pressure for the parcel can be expressed as (*Andrews*, 2000)

$$e_{\text{parcel}} = \frac{mp}{\epsilon} \tag{2.17}$$

and combining this result with equation 2.16 gives

$$e_{\text{parcel}}(T) = \frac{mp_0}{\epsilon}\left(\frac{T}{T_0}\right)^{\frac{c_p}{R}} \tag{2.18}$$

For conditions in the Earth's atmosphere substitution of the appropriate values into equations 2.15 and 2.18 show that the saturation vapour pressure decreases more rapidly than the vapour pressure of the air parcel and with sufficient cooling an air parcel will reach

saturation. At this point condensation will occur faster than evaporation and a cloud will start to form. However, it should be noted that once saturation has been exceeded and water starts to condense there is a release of latent heat. This complicates any further considerations of ascent.

2.2.3 Ice formation

In the atmosphere liquid drops usually form on cloud condensation nuclei. Aerosols which are suitable for acting as CCN are usually abundant in the atmosphere. In a similar way liquid water does not necessarily freeze when its temperature drops below about 0°C (the freezing point of water depends only weakly on pressure for the atmospheric range) without the presence of ice forming nuclei (IN). However, unlike CCN, there are much fewer substances which can act as IN in the atmosphere. As a result the atmosphere regularly contains clouds consisting of liquid water at temperatures less than 0°C, which is referred to as supercooled water.

Another interesting feature of ice formation appears when the behaviour of the saturation vapour pressure curves is studied below 0°C. Figure 2.2 is the saturation vapour pressure over ice (dashed line) and the saturation vapour pressure over supercooled water (solid line). The curve for saturation vapour pressure over ice can be derived by replacing L_c in the Clausius-Clapeyron equation (2.11) with L_s, the latent heat of sublimation. Below 0°C the two lines diverge with the vapour pressure over supercooled water always being greater than that for ice at the same temperature. This is obviously a result of the inclusion of the larger L_s and is consistent with the idea that water would be expected to evaporate more easily from the surface of a liquid particle than an ice one. As a consequence air that is lifted in an orographic wave can reach saturation over ice before it reaches saturation over water. However the lack of IN means that ice will not usually form directly in the atmosphere without liquid water first condensing. If there were sufficient IN in the atmosphere this would not be the case!

There are two aspects of ice formation in clouds that need to be considered. The first is the formation, or seeding, of an ice nucleus. The second is the mechanisms by which that ice nucleus can subsequently grow or decay.

Below 0°C ice can form heterogeneously on IN. This can occur directly from the vapour phase onto an IN aerosol (*deposition nucleation*) or also from supercooled water colliding with an IN (*contact nucleation*). Subtly different is *immersion nucleation* where an aerosol immersed in a liquid drop becomes an ice nucleus through an environmental change such as a fall in temperature. Because of this process clouds can often contain both ice and liquid water. However, there is a limit to which liquid water can be supercooled. This limit, sometimes called the Schaeffer point, is somewhat uncertain but is generally

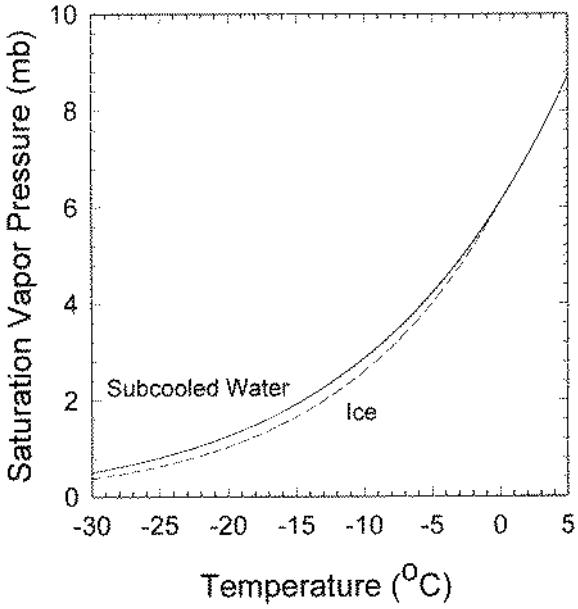

Figure 2.2: The saturation vapour pressure over water (solid line) and over ice (dashed line) for temperatures less than 0°C. From *Bohren and Albrecht* (1998).

observed in the atmosphere to be somewhere between -35°C and -40 °C. Supercooled water is very rarely observed beyond this point as it will freeze homogeneously. As with li water molecules can randomly align to form an ice embryo, which at such cold temperatures causes the rest of the droplet to rapidly freeze. Ice is not homogeneously frozen directly from vapour.

Once formed, ice can grow or decay through a number of mechanisms. The process by which ice grows by the diffusion of vapour towards an embryo is called *deposition* and results in an *ice crystal*. The reverse decay process is deemed *sublimation*. *Condensation* and *evaporation* can also be used to describe the same processes. A crystal may also grow through *riming*, where it collides with supercooled drops that subsequently freeze. Also since the saturation vapour pressure over water is always higher than that over ice in a supercooled environment, ice crystals will grow at the expense of the drops due to a flux of water vapour directly from the drop to the crystal. This process is known as the *Bergeron-Findeison process* and has an important role in the formation of precipitation.

Clumping or *aggregation* is where a crystal grows through collision with other crystals. The product is a *snowflake*. If riming progresses for long enough a crystal will grow to be an irregular *graupel* particle or even further to be a *hail particle*. Crystals can also be broken up into smaller crystals by collision or shattering during freezing from liquid water and this is known as *splintering*. Splintering leads to the formation of more ice crystals than might be expected from the number of IN present and is also known as the *Hallet*

Mossop process (*Pruppacher and Klett*, 1997).

2.2.4 Lifting condensation levels

Some orographic clouds, such as a Föhn wall, are created by the direct lifting of air adjacent to a mountain's surface (*Banta*, 1990). For these types of clouds there are two important thermodynamic parameters that reveal information about whether cloud formation is expected and what type it will be. These are the lifting condensation level (LCL) and the level of free convection (LFC). The LCL is the more straightforward of the two and is simply the level that air at a given height must be lifted adiabatically to become saturated. The LFC is the level to which an air parcel must be lifted, once saturated, to become positively buoyant. This implies that a layer of previously stable air has been raised sufficiently high for it to become conditionally unstable. By measuring the thermodynamic variables of an upwind mountain flow at different heights both the LCL and LFC can be calculated as functions of height.

Obviously, whether a cloud forms is then determined by how much lifting actually occurs. This can be described by the so called orographic lifting function, L(z), which determines the maximum lifting a parcel will undergo when flowing over a mountain. Figure 2.3 shows how L(z) is obtained for potential flow over a semi-cylinder.

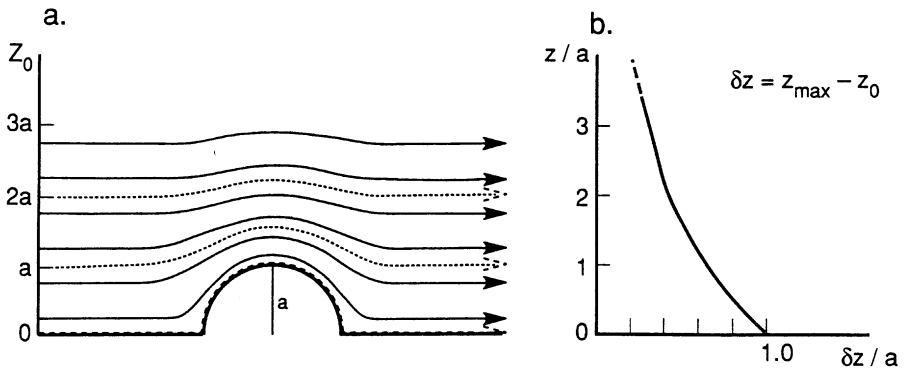

Figure 2.3: Lifting function for the potential flow over a semi-cylinder. a) shows the predicted streamlines of the flow and b) the maximum lifting, δz, experienced by a parcel which starts at a level z_0; i.e. $\delta z = z_{max} - z_0$ and variables are normalised by the maximum height of the obstacle, a. From *Banta* (1990)

By superimposing the lifting function for an idealised mountain on the LFC and LCL curves for an appropriate atmospheric flow in figure 2.4 it can be seen that it is now possible to get an idea of the cloud distribution that will form. In this example air which starts off more than 5.5 km above sea level is not lifted high enough to form any cloud. Below this height all of the air at different levels is lifted above the LCL and will form

stable stratiform cloud. A small fraction, at about 3.5 km, will even be lifted sufficiently to reach the LFC and hence convective (cumulus) clouds will be produced.

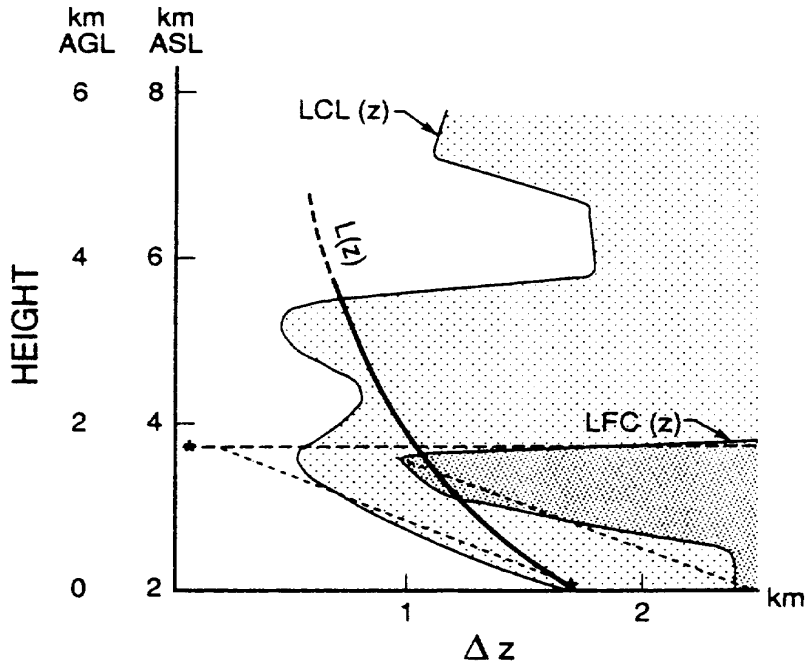

Figure 2.4: LCL and LFC curves functions from an atmospheric sounding superimposed on the L(z) for a semi-cylinder. Asterisks represent the mountain height on both the Δz axis and the height axis (shown in km above ground level, AGL, and km above sea level, ASL). The lightly shaded area shows the region in which stable stratiform clouds will form and the darkly shaded area shows where cumulus clouds will form. From *Banta* (1990)

2.3 Clouds and Radiation

Clouds play two important roles in the radiative balance of the atmosphere. By reflecting solar radiation (shortwave) incident on the Earth they act to cool the planet. However, they also absorb radiation emitted by the Earth's surface (longwave) and then re-radiate part of this energy to space at a lower temperature known as the cloud top temperature. This reduction in the longwave flux to space causes a net warming of the underlying atmosphere.

The way in which clouds re-radiate longwave radiation vertically is highly dependent on the cloud top height, whether it is liquid or ice, and finally a quantity called the cloud optical depth, τ. The optical depth is a measure of how much a cloud will absorb radiation of a particular wavelength. Clearly this depends on the physical thickness of the cloud,

L, as well as the mass extinction per unit length, k_ν, which itself is dependent on whether the cloud particles are liquid water, ice or a combination of both. In the case of a cloud with constant extinction and density, ρ,

$$\tau = k_\nu \rho L \tag{2.19}$$

More generally the extinction coefficient varies with height due to changes in cloud properties so that the optical depth for radiation of frequency ν in a cloud of density $\rho(z)$ and with extinction coefficient $k_\nu(z)$ is

$$\tau = \int_{z_1}^{z_2} k_\nu(z)\rho(z)dz \tag{2.20}$$

The optical depth of the entire atmosphere requires integrating from the Earth's surface to the top of the atmosphere.

From a satellite in space the radiative effects of cloud can be measured by comparing the upward clear sky radiation with the upward radiation observed from cloudy areas. In the longwave this radiation is emitted by clouds and the surface. In the shortwave it will be solar radiation directly reflected from clouds and the surface. As long as the measurements come from comparatively close locations the effect of other atmospheric constituents can be eliminated. The difference between the two is defined as cloud radiative forcing (*Harrison et al.*, 1990). Thus the longwave cloud radiative forcing (CRF_{LW}) in terms of the cloudy flux (F_{LW}) and the clear sky flux ($F_{LWclear}$) is

$$CRF_{LW} = F_{LWclear} - F_{LW} \tag{2.21}$$

Similarly the shortwave cloud radiative forcing (CRF_{SW}) is

$$CRF_{SW} = F_{SWclear} - F_{SW} \tag{2.22}$$

These quantities, measured from the top of the atmosphere, give an indication of the potential sensitivity of the longwave and shortwave net downward fluxes at the top of the atmosphere to any changes in clouds (*Webb et al.*, 2001). In general low and middle level clouds have a net cooling effect on the atmosphere. An upper level cloud, consisting of cirrus, may have mostly a warming effect (*Khvorostyanov and Sassen*, 2002) but this is highly uncertain and will be discussed further in the next section.

2.4 Orographic Cirrus

The processes which lead to the formation of orographic cirrus are considerably more complicated than those of section 2.2. For the purposes of this thesis it is useful to first consider cirrus in general before discussing its generation through orographic mechanisms.

Because of the wide use of the morphological cloud classification scheme outlined in section 2.1 the correct use of the word cirrus is restricted to a small class of optically thin ice clouds. However, the word cirrus is often used in the literature to mean any high ice cloud which is not associated with lower level optically thick cloud. When considering cloud modelling in GCMs it has been suggested (*Lynch*, 2002) that it would be more useful to identify clouds simply by their phase. For instance it is worth noting that currently, while all cirrus clouds are composed of ice, not all ice clouds are cirrus. Considering this, it is perhaps more appropriate to think of this section as being broadly concerned with all types of orographic ice clouds. In the context of this thesis cirrus will generally refer to high level ice cloud with a range of optical thickness. Table 2.2, adapted from *Sassen* (2002), shows the alternative cirrus types used in this thesis as classified by optical thickness and visual appearance.

Category	τ range	Description
Subvisible	< 0.03	Invisible against the blue sky
Thin	0.03-3.0	Visible but retains blue tinge
Thick	> 3.0	Disk of sun becomes indistinct

Table 2.2: The definition of cirrus types by their optical thickness.

Cirrus clouds have an important role in many aspects of the Earth's climate. Cirrus clouds have an influence on the water budget. Water vapour in the upper troposphere is highly sensitive to the distribution and microphysical properties of ice crystals (*Stephens*, 2002). Since ice crystals can fall considerable distances while evaporating, they are very effective at redistributing water. Additionally they are important in initiating, or simply increasing, precipitation processes.

Cirrus clouds in the upper troposphere also play an important role in the radiative balance of the Earth system. Because of their high altitudes, cold cirrus clouds are very effective at trapping outgoing longwave radiation. However they can also be strong reflectors of incoming shortwave radiation. Which process dominates has been shown to be highly dependent on macrophysical properties such as the optical thickness of the cloud which in turn depends on microphysical properties such as the crystal size (*Stephens et al.*, 1990). This uncertainty has consequences for studies of climate change. All GCM simulations of climate change agree that in a warmed atmosphere a more active hydrological cycle results in more transport of water vapour into the upper troposphere (*Sundqvist*,

2002). Yet the predictions of changes in cirrus amount, and whether there is a resulting positive or negative feedback on temperatures, are widely varied. Improvements in the representation of both the dynamical and microphysical properties of cirrus in climate models is needed.

According to *DelGenio* (2002) there are a number of reasons why cirrus clouds are such a large uncertainty in GCM simulations of the long term climate change. These include uncertainty in radiative properties and the sensitivity to the model water vapour distribution. However, one of the primary ones is also that the dynamic processes that create cirrus are poorly resolved by current GCMs and different in different parts of the globe. The mechanisms for cirrus generation in the real atmosphere are:

1. A variety of synoptic scale disturbances. These include jet streams and frontal lifting. The common aspects are the relatively weak vertical lifting and the growth of the cirrus clouds from the top downwards.

2. Anvil cirrus is created by strong thunderstorm updrafts

3. Cold trap cirrus inhabits much of the cold tropical tropopause and is possibly maintained by vapour injected by convection.

4. Contrail cirrus is created when water vapour enriched aircraft exhausts are injected into an ice saturated environment.

5. Orographic wave cloud cirrus, which is induced by orographic gravity waves, forms as a result of relatively high induced vertical velocities and rapid cooling.

Orographic cirrus clouds are a diverse subject in themselves. The nature of the waves that produce them, as described in chapter 1, and the sensitivity to the water content of the upwind air lead to a variety of shapes and sizes. Small lenticular (lens shaped) cirrus clouds can form in small amplitude disturbances above mountains. It is quite common for such lenticulars to be stacked one above the other, representative of a banded humidity structure in the atmosphere.

There are two conditions which can lead to the formation of large cirrus clouds. Over high mountains strong winds can generate very large amplitude vertically propagating waves. The vertical parcel displacements induced by these waves can be large enough for ice crystals of significant size to grow in the rapid updrafts. These crystals can be advected by the wind for a considerable distance before they evaporate. Secondly some regions of the troposphere are regularly supersaturated with respect to ice but not with respect to water. Any ice which is created due to ascent in an orographic wave will not evaporate when the air returns to its original level (*Queney et al.*, 1960).

The ability of small hills to produce significant cirrus clouds in this way was first identified by *Ludlam* (1952). He presented several case studies which showed that ridges or hills in Britain of only about 300m must be able to vertically displace air in the upper troposphere by up to 700m to produce the large cirrus clouds observed. Similarly, *Brown* (1983) used observational research flights to show that orographic cirrus generated over Britain were caused by hydrostatic vertically propagating gravity waves. *Conover* (1964) pioneered the use of satellite imagery to study the size of orographic cirrus clouds and the nature of the waves that create them.

Reid (1975) described large orographic clouds over the large mountain ranges of New Zealand. He attempted to show that the cloud formation could be explained using the linear hydrostatic gravity wave theory of *Queney* (1948). *Hewson* (1993) identified from satellite images orographic cirrus clouds forming off Iceland and the Faeroe islands in otherwise clear air. He described the cirrus streaming off the mountains as resembling a flame or flag blowing in the wind.

Durran (1986b) showed that orographic cirrus clouds could be generated by small amplitude waves described by linear hydrostatic gravity wave theory. However, he also showed that the formation of cloud can have a strong feedback into the vertical structure of the gravity wave itself. For large amplitude waves nonlinear effects also become important.

2.4.1 Microphysical observations of orographic cirrus

Small orographic cirrus clouds offer many advantages for studying the formation of ice. They are usually nonturbulent and almost never involve precipitation processes. As such there have been many recent field campaigns, most using special instrumented aircraft and occasionally balloons, to study the formation of ice in such clouds. While these studies have been interested in many properties of the clouds, such as crystal shape and size, this brief review focuses on the parts relevant to a general mechanism for orographic cirrus formation.

Field et al. (2001) studied a number of small mountain wave clouds over Scandinavia as part of the INTACC (INTeraction of Aerosol and Cold Clouds) experiment. Their six flights observed clouds in the temperature range -12 °C to -40 °C. In any cloud trajectories that remained warmer than -35°C heterogeneous ice nucleation was found to dominate, while for colder trajectories homogeneous nucleation was dominant. In five of the six clouds there were no significant ice concentrations until after liquid had formed in the wave, despite high supersaturations with respect to ice. This indicated a very low concentration of effective deposition nuclei in these five clouds. Additionally the most significant ice growth was observed to occur in the downdraught part of the wave, after the drops had reached their maximum size and were in the process of evaporating. The

conclusion drawn from these observations was that the two possible mechanisms for the heterogeneous nucleation were immersion and contact nucleation. These findings were supported by modelling work by *Cotton and Field* (2002). The deposition mechanism was clearly ineffective due to the need for liquid water to form before ice nucleation could occur. Ice was observed to survive downstream of the wave for a considerable distance, while all liquid water cloud evaporated by the time the air returned to its original height.

Cooper and Valli (1981) found similar results for large orographic clouds over the Wyoming-Colorado region of the Rocky Mountains. The clouds studied were in the temperature range of -18°C to -27°C. In the four case studies most of the ice crystals appeared to form within 1-2 km of the upwind cloud edge. The sharp increase in crystal concentration was associated with the formation of liquid water. They went on to show that contact nucleation was the most likely mechanism with nuclei of < 0.01 μm required.

Heymsfield and Miloshevich (1993) and *Heymsfield and Miloshevich* (1995) consider three experimental campaigns. WAVE89 and WAVE90 used aircraft measurements of orographic cirrus clouds near Boulder, Colorado. These clouds were in the temperature range of -31°C to -56°C. Their frequent observation of liquid water in clouds at temperatures of -30°C to -35°C, which were devoid of significant crystal ice concentrations, led them to the conclusion that condensation nuclei were sufficiently scarce for heterogeneous nucleation to play only a small part. Both theoretically, due to the cold temperature, and in terms of the observed ice growth rates, it was concluded that ice was forming from the homogeneous freezing of liquid water. FIREII (the First ISCCP Research Experiment, phase II) was conducted near Coffeyville Kansas in 1991. Similar results to the WAVE campaigns were observed. Additionally, very high supersaturations with respect to ice were seen within the clouds.

Strom and Heintzenberg (1994) studied the evolution of two orographic clouds over the Alps using multiple aircraft flights. For these cold clouds (-55°C) their focus was on growth rates. They found that cirrus crystals could have a long lifetime at these temperatures and be advected hundreds of kilometres downstream of their origins.

More recently orographic wave clouds were also investigated as part of the Subsonic Aircraft: Contrail and Cloud Effects Special Study (SUCCESS). These were also cold clouds at temperatures between -35°C and -41°C and were dominated by homogeneous nucleation. *Heymsfield et al.* (1998) present upwind profiles for these clouds, including one from off the coast of California. All cases exhibited a high degree of ice-supersaturation before the formation of any wave cloud, particularly for air of maritime origin.

All of these studies highlight the varied microphysical nature of orographic cirrus clouds, which reflects the conditions in which they form. Certainly it would be expected that cirrus forming in continental air could have a considerably different nature to cirrus that forms in air of recent maritime origin. Over the oceans the upper troposphere is

observed to be deficient in aerosols and so is more regularly supersaturated with respect to ice (*Jenson et al.*, 2001).

Chapter 3

Orographic Clouds Over New Zealand

This chapter investigates orographic clouds over New Zealand, which form a dramatic part of the meteorology of the region. The Northwest Arch phenomena is an example of a large cloud which is generated by gravity waves, and is explored in detail. However, it would be misleading to think of this cloud as unique to the region. As will be shown it is the orographic cirrus part of the Northwest Arch that is advected significant distances and appears dramatically in satellite images. Similar orographic cirrus can be observed over many mountain ranges around the world and will be discussed in the next chapter. Thus New Zealand offers an ideal opportunity to study the nature of the gravity waves involved and the subsequent formation of orographic cirrus. Figure 3.1 is a map of New Zealand indicating major towns and cities as well as the location of major mountain ranges.

The dramatic visual appearance of the Northwest Arch, when observed from the ground, was one of the main inspirations behind the work of this thesis. As such, photos of the Arch are included in appendix A. Information on New Zealand's orographic clouds has not previously been brought together. The chapter begins with a review of the state of knowledge of the Northwest Arch and other orographic clouds. Because of the lack of scientific studies most of this information is qualitative in nature. Satellite data are also used to show how the Arch appears from space, and to demonstrate a number of case studies. Finally a conceptual model of the Northwest Arch and its associated orographic cirrus, which draws on both observations and theory, is presented.

3.1 Review

3.1.1 Qualitative observations of orographic clouds

Considerable qualitative work has been done on studying wave clouds in New Zealand and the waves that create them. *Cherry* (1971) and *Cherry* (1972) undertook an extensive observational survey of the conditions necessary for wave clouds to form off the Southern Alps and the actual frequency of occurrence. He discussed forecasting strong northwest events using the upstream wind velocity profile. *Reid* (1975) focused more exclusively on the nature of the Northwest Arch. Observations of arch clouds are described and dimensions of some arches are estimated. One cloud was observed to have a leading edge

Figure 3.1: Map of New Zealand indicating major towns and cities as well as the location of major mountain ranges.

800 km in extent and to continue up to 200 km away from the mountains. The height of the cloud base was estimated as being about 10 km. A simplistic representation of the flow was attempted using the theory of *Queney* (1948). *Sturman* (1980) conducted a case study of lenticular lee waves which were observed to be generated by Banks Peninsula. He used soundings from Christchurch airport to consider the 'undisturbed' stability and condensation levels. *Revell* (1982) presented satellite images of New Zealand showing extensive areas of lenticular clouds. Examples are shown where these lee wave clouds resulted from northerly, westerly and southerly airflows. *Auer* (1993) reported briefly on a long lee wave train ($>$ 310 km) which occurred off the South Island.

The best observations of the wave structure come from glider pilots, who regularly use the Arch wave to reach record altitudes, and distance travelled, in gliders. *Hamilton* (1992) described flying in a Northwest Arch wave on July 19^{th} 1992. He found some turbulence at low levels before striking strong lift of about 500 m per minute, at about 1100 m. The base of the Northwest Arch was reached at 7600 m and he was able to continue to climb on the leading edge of the cloud up to a height of 9150 m. The flight was terminated at this point despite still experiencing a lift of 75 m per minute even at this height. An image of the Arch as seen that day from ground level can be found in figure A.5. Hamilton commented on the incredible smoothness of the lift with very little turbulence experienced. He also noted the still calm conditions at ground level during the flight.

Lyons (1996) described a Northwest Arch type wave cloud over the east coast of the North Island in the Napier area. He used the associated wave to successfully fly 1000 km in a little over seven hours. He described being in an extraordinary amount of lift of 600 m per minute while in the wave. He also noted that the 'magnificent lenticular' had a base at about 5800 m with tops at 10000 m plus.

Harrison (1997) did not fly through the Arch wave but described observing a massive Arch while flying over the Southern Alps. The cloud stretched from Blenheim to Waimate and he estimated the base of the cloud to be at about 6700 m.

The only scientific attempt to make observations of the Northwest Arch is that of *Rankin* (1990) who flew a BAC 167 Strikemaster jet through a Northwest Arch on the 12^{th} March 1990. The synoptic situation at noon on the 12^{th} is shown in figure 3.2. Clearly a significant northwest flow existed ahead of an approaching cold front. Figure 3.3 is a schematic diagram of Rankin's flight through the Arch cloud. The dashed line represents the actual flight path taken by the plane while the dotted line shows the path that was intended to be flown but was abandoned because of mechanical faults.

Using the limited instruments on board the jet he attempted to determine the streamlines of the wave. These are also shown in the diagram as the solid lines. The bottom of the cloud was found to be fairly flat at a height of 7 km. The wave structure in the base

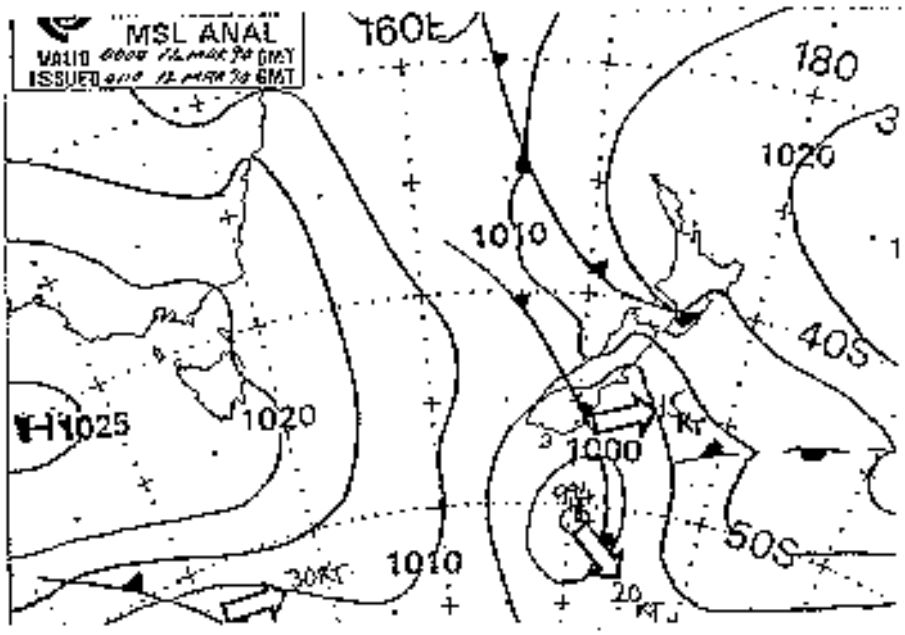

Figure 3.2: Mean Sea Level Analyses for the 12^{th} March 1990 (0000 GMT). From *Rankin* (1990).

of the cloud was confirmed to be the result of a long wave with wavelength of about 50 km but the streamline was otherwise fairly flat downstream. Unfortunately Rankin did not fly ahead of the wave cloud and thus there is no information about the lift generating the cloud. The main edge was found to lie directly over the Cragieburn ranges (directly west of Christchurch). A photograph of the cloud studied by Rankin can be found in Appendix A as photo A.2.

Rankin (1990) suggests, from considerable personal observation, that what is considered to be a Northwest Arch can actually be broken into four main regimes:

1. Arch cloud only

2. Combined roll cloud and Arch

3. Contoured Arch with roll cloud

4. Contoured Arch without roll cloud

The evolution of a Northwest Arch usually begins with type (1) at very high levels. At this stage the cloud will usually consist predominantly of cirrus (see photo A.1). It is often a sign of a more spectacular arch to follow and is usually observed in a pre-frontal situation. As the front approaches, this cloud may thicken down to lower levels and as the winds at the surface go more northwesterly, classical roll clouds may form at the altitude of the mountain tops. This is type (2) and can be seen in A.2. When the winds are

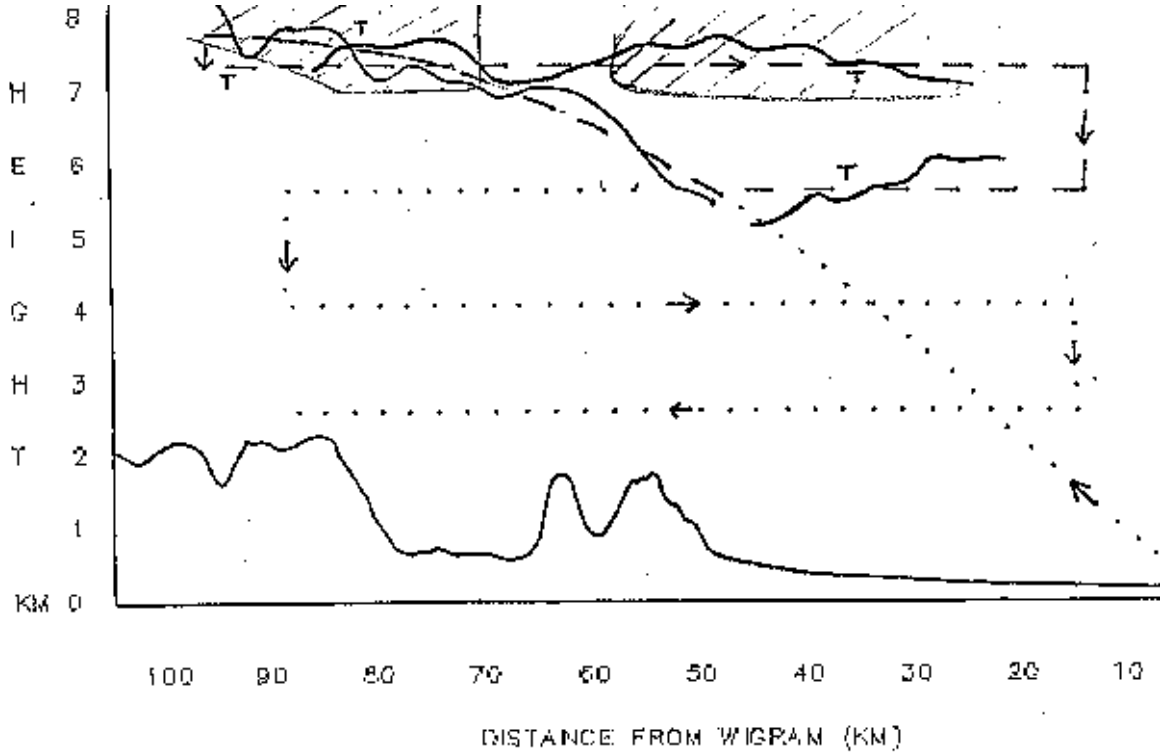

Figure 3.3: The planned (dotted line) and actual (dashed line) flight path of Rankin's jet on 12^{th} March 1990. The qualitatively inferred wave structure is shown by the solid line. The lower line represents the terrain while shaded areas indicate the location of cloud and the letter T areas of turbulence. From *Rankin* (1990).

particularly strong the lower levels of the Arch may show evidence of wave crests. This is what *Rankin* (1990) refers to as a contoured arch (types (3) and (4)). These waves are often clearest when they are emphasised by the setting sun and provide dramatic cloud cover. Occasionally the lower level rotor clouds will be significant enough to reach up and join lenticular clouds above them. While the arch might be considered a lenticular cloud it does not exhibit the classical definition as there is no significant downdraft in which the cloud dissipates.

3.1.2 Modelling of the Northwest Arch

A limited number of authors have also undertaken high resolution modelling studies to investigate the nature of the gravity waves generated over New Zealand. Unfortunately none of these studies have included moist physics and thus been able to simulate orographic clouds. It is still possible, however, to identify areas of potential cloud formation using these studies.

In his thesis, entitled 'Observations and Numerical Modelling of Air Flows over New

Zealand', *Ridley* (1991) used the Colorado State University model (CSU) to simulate large amplitude vertically propagating gravity waves over New Zealand. His interest was primarily in the initiation of so called 'southerly busters', where there is a sudden change on the east coast of the South Island to gusty southerly winds often accompanied by sudden temperature changes. He showed that the initiation of these events is synoptic but the progress of such phenomena is strongly modulated by the cross mountain flow. In the process of this work he simulated strong northwest flows over the South Island using both two dimensional (2D) and three dimensional (3D) versions of the CSU model. The 3D simulations were computationally limited and were run at a coarse resolution of 10 km by 25 km in the horizontal and 18 levels up to a height of 12 km. Their main purpose was to simulate the southerly buster and ascertain the validity of the 2D simulations.

The 2D simulations were performed for three transects across the South Island, which were chosen to represent some of the variability in the terrain seen over the length of the South Island. An envelope orography, similar to the one which will be described in section 6.3.2, was employed to ensure the full blocking effect of the mountains was represented. The domain size was 500 km with an even grid spacing of 5 km. There were 31 levels in the vertical up to a height of 12 km. The model was hydrostatic and employed a radiative upper boundary condition.

Figure 3.4 are the potential temperature curves of the three transects for a 2D simulation with constant flow of 20 ms^{-1} in the left hand column and 10 ms^{-1} in the right. The results presented are after 16 hours of simulation time. The dashed line represents the height of the boundary layer, while the dots indicate grid points where the models vertical mixing scheme was activated. If it is assumed that the motion of the air in gravity waves such as these is adiabatic then it can be assumed that air parcels move along contours of potential temperature. This derives from the fact that potential temperature is always conserved during an adiabatic process (*Holton*, 1992).

Where streamlines of constant potential temperature are deflected above their upstream heights previously cloud free air may form a cloud if the humidity is high enough. Areas in the lee of the mountain ranges which satisfy this criterion have been shaded. It should be noted that in cases where considerable cloud existed upstream it may well also be expected to exist downstream. Thus a Northwest Arch type cloud may appear in places not shaded in the plot.

The 20 ms^{-1} simulation clearly shows the presence of a low level jump in the streamlines at all three locations despite the considerably different orography. The propagation of the jump towards the coast is at different stages in the figures. There is considerable blocking of the upstream flow in all three cases. Simplistically, this is caused by air which does not have enough kinetic energy to flow over the mountain and so stagnates. The shaded areas, although considerable, occur directly over the lee slope of the mountains

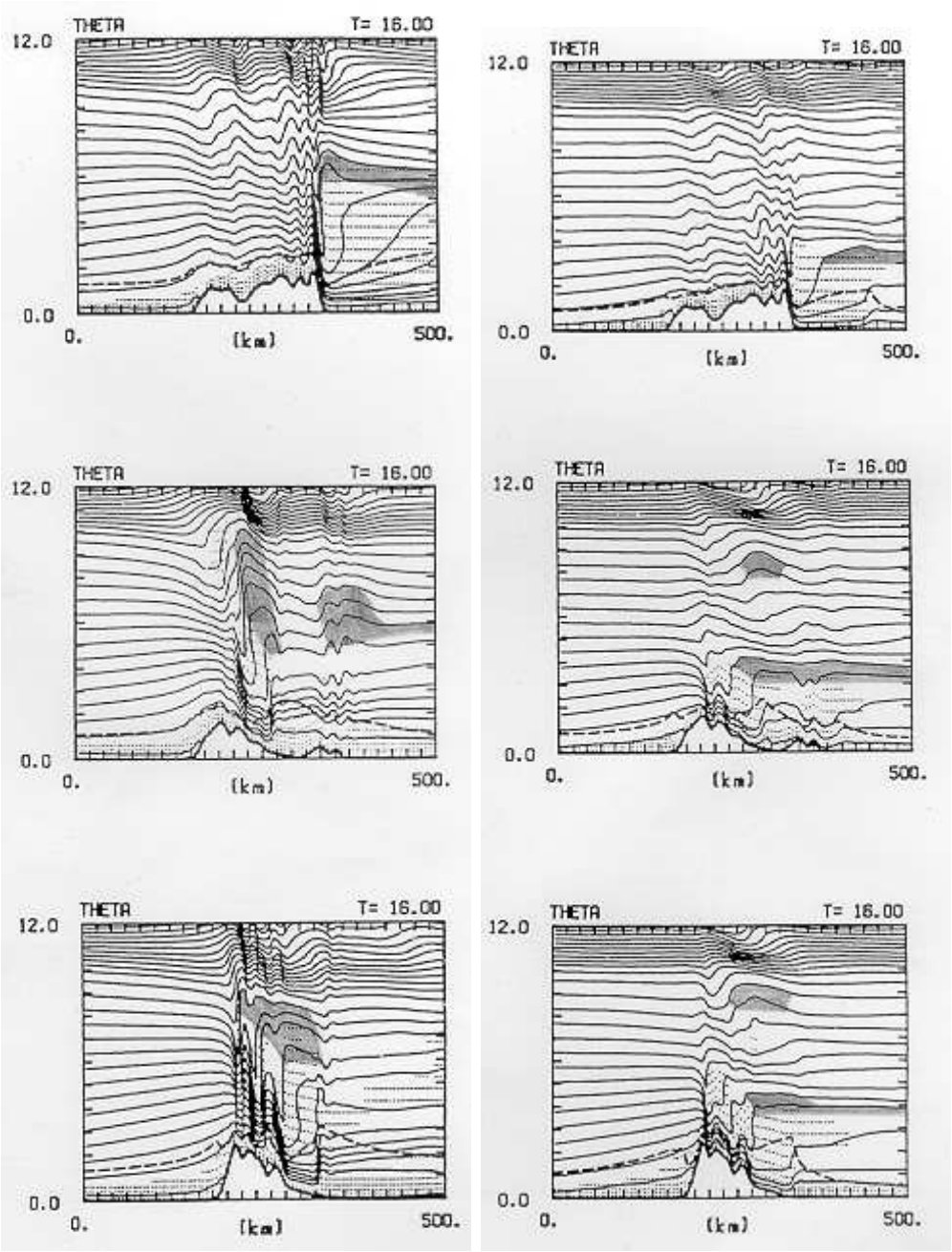

Figure 3.4: In the left column are 2D simulations of potential temperature for a uniform 20 ms^{-1} flow over three different transects across the South Island. In the second column are the same 2D transects only for a uniform 10 ms^{-1} flow. All figures are from *Ridley* (1991) but shaded areas have been added to indicate where potential temperature lines have been displaced above their upwind heights. Axes are in kilometres.

at heights of 6-9 km and are not associated with the propagating jump below, but rather with the vertically propagating gravity wave. This can be clearly seen in the full time evolution of the simulations presented in *Ridley* (1991).

In the right hand column of figure 3.4 are simulations in which the wind speed was

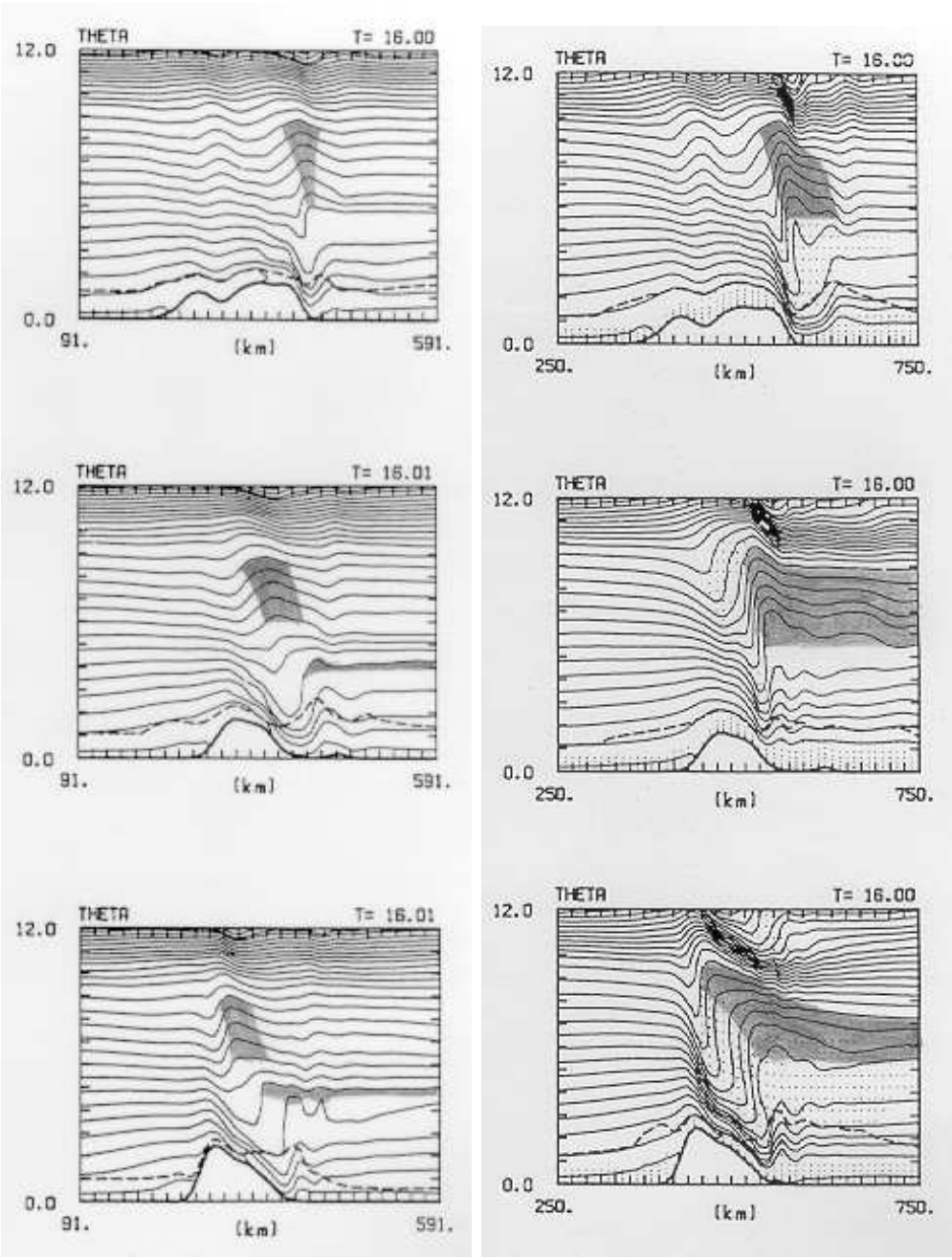

Figure 3.5: In the left column are the same three transects as figure 3.4 but taken as sections from the fully 3D simulations. The simulations of potential temperature are at a coarse resolution, revealed by the smoothed topography. In the right hand column are the results achieved for a 2D simulation which uses the coarser orography of the 3D simulation. In both cases a uniform flow of 20 ms^{-1} was used. Again shaded areas have been added to indicate where potential temperature lines have been displaced above their upwind heights. From *Ridley* (1991).

reduced to a uniform flow of 10 ms^{-1}. Wave breaking now occurs at much lower levels and the jump, while still present, does not extend so high into the atmosphere. The heights

at which shaded areas can be seen are much lower (about 3-4 kilometres in all three transects), and are associated with the jump. Although this is lower than the heights that are observed for a Northwest Arch, it is suggestive of the possibility of a cloud form which is associated with a low level propagating jump.

None of the results presented here are particularly realistic reproductions of the type of flows that occur over the New Zealand mountains. In reality there will be both vertical and horizontal shears in the wind speeds. Ridley did perform a simulation that had 5 ms^{-1} winds at ground level increasing to 10 ms^{-1} at 1500 m and then linearly up to 40 ms^{-1} in the stratosphere. The effect of this was to suppress all wave breaking in the troposphere and subsequently for no hydraulic jump to appear. Since he obtained a similar result for a constant 5 ms^{-1} Ridley concluded that it was the strength of the wind near mountain top height and below that was critical in the formation of a jump.

In the left hand column of figure 3.5 are the same three transects for a large scale flow of 20 ms^{-1} for Ridley's 3D simulations. The orography of the mountains is now at a much lower resolution, but by comparing these simulations with 2D ones of similarly low resolution (right hand column of figure 3.5) Ridley confidently concluded that for the same initial conditions the jump decreased in strength in 3D and propagated more slowly away from the mountains. In both the 2D and 3D simulations the areas with the biggest displacement are in the middle to upper troposphere and are associated with the stationary large amplitude gravity wave which propagates vertically above the mountains.

Other important findings made by Ridley were that the strength of the hydraulic jump was enhanced by the steepness of the lee slope. His only reference to any orographic cloud was a personal observation that supported the simulations showing a propagation of his jump like feature towards the coast. He observed that over Christchurch the jump could be seen to move from the mountains across the plains to the coast through the passage of the leading edge of a wave cloud. A second observation was that the inclusion of moisture in the model equations could potentially have a significant effect on the wave patterns simulated.

Richard Turner, at NIWA Wellington, has used the Regional Atmospheric Modelling System (RAMS) to simulate northwesterly flows over New Zealand (*pers coms*). A range of experiments forced with climatological, real and idealised sounding data were undertaken to investigate preferred locations for wave breaking over the Southern Alps. One particular event was simulated for the day of Oct 6^{th} 1996, in which a commercial airliner experienced extreme turbulence. The run was initialised using analyses from the European Centre for Medium Range Weather Forecasting (ECMWF). Figure 3.6 is a 2D cross section of the simulation. The horizontal velocity is shown by the solid lines and the dashed lines are potential temperature. These isentropes show significant upward deflection downstream of the mountains. From 6 kilometres and higher the isentropes are deflected a kilometre

upwards. This could potentially form high level orographic cloud. Whether a Northwest Arch was actually present is unknown.

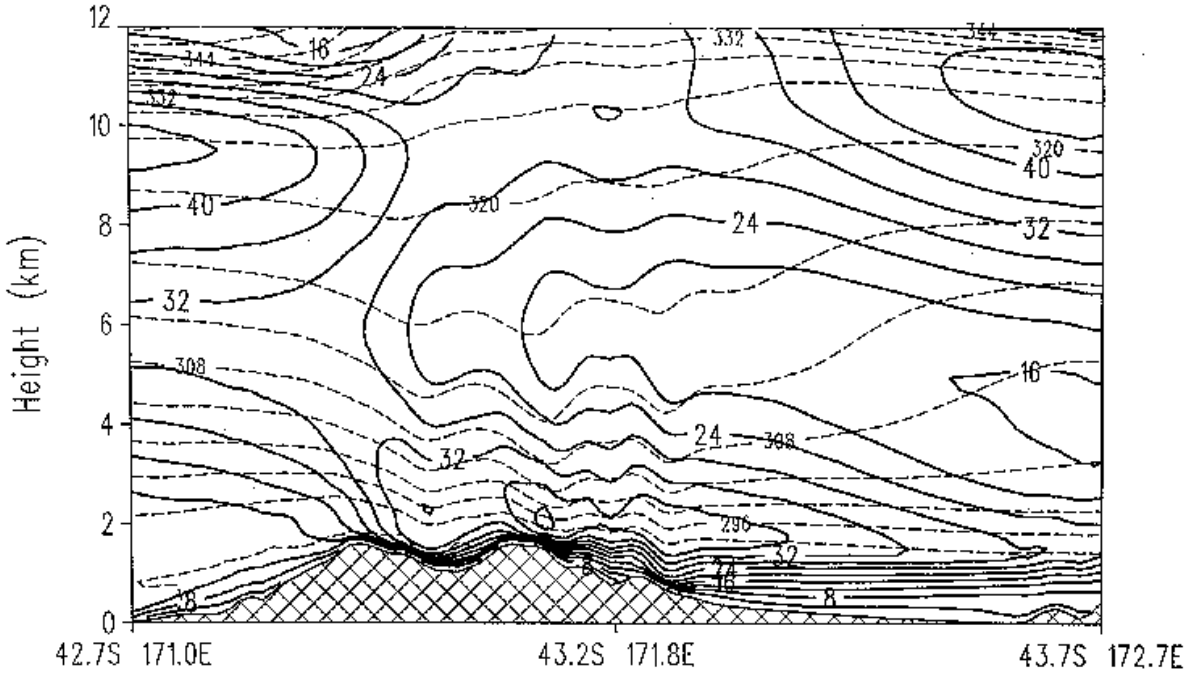

Figure 3.6: Transect of a 3D simulation over New Zealand of October 6^{th} 1996 using RAMS. Solid lines are for horizontal velocity (ms^{-1}) and dashes lines for potential temperature.

Numerical modelling was also performed by Katzfey (*Katzfey*, 1995a,b) using a mesoscale model of New Zealand. While the model did explicitly resolve a mountain wave, the focus of the work was on the enhancement of precipitation by orography and considered only high rainfall case events. No direct cloud information was presented although the effect of different resolutions on the flow was explored in detail.

Lane et al. (2000) presented a paper which covered observations and numerical modelling of extensive lee waves observed during the Southern Alps Experiment. The presence of numerous lenticular clouds and atmospheric data enabled an extensive comparison of theoretical, numerical and observational predictions for this particular event.

3.2 Satellite Data

In addition to numerical modelling, important information about orographic clouds can be ascertained from satellite observations. Specific case studies can also be used to infer information about not only the clouds but also some characteristics of the waves that generate them.

The only useful high resolution climatological cloud data over New Zealand retrieved from satellite data are presented in *Uddstrom et al.* (1999) and *Uddstrom et al.* (2001). This complex algorithm, known as SRTex, uses high resolution AVHRR data (Advanced Very High Resolution Radiometer) from NOAA (National Oceanic and Atmospheric Administration) polar orbiting satellites to calculate a 'no cloud frequency' which is the complement of a cloud amount frequency. It is also able to break the cloud cover down into 13 standard classes of cloud type. Due to the computational demands of the algorithm the data analysed were only for 1995 and derived from the daily mid afternoon (local time) overpass of the NOAA14 satellite. Unfortunately the algorithm is unreliable at determining low level cloud amount over high or complex orography and so some of the results that follow have masked areas where the surface is higher than 750 m above sea level. This does not affect the retrieval of mid or high clouds.

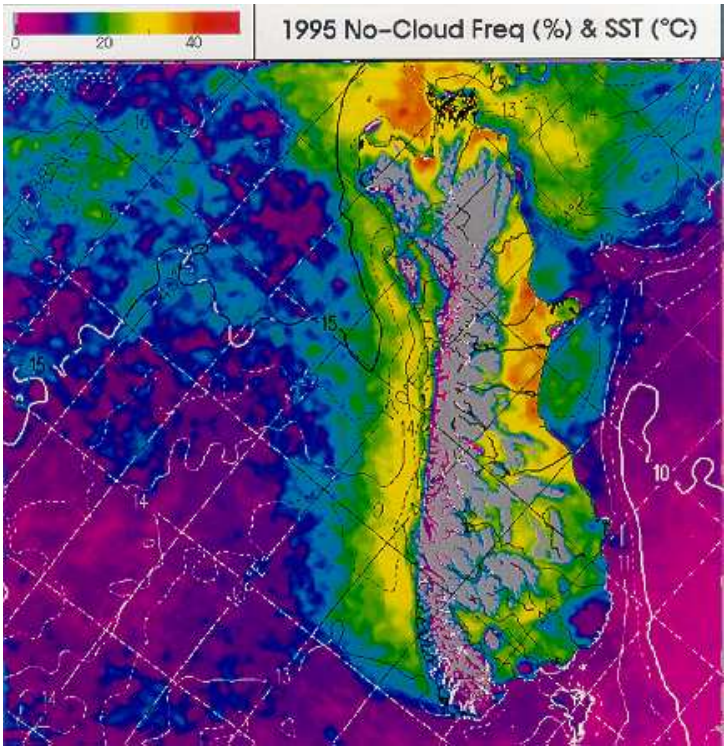

Figure 3.7: Total no-cloud frequency (all cloud types) expressed as a percentage and averaged over the year 1995 for the South Island region. White contours are sea surface temperatures in °C. From *Uddstrom et al.* (1999).

Figure 3.7 shows the no-cloud frequency for the entire year. The notable feature is the overall decrease in cloud over New Zealand from the surrounding ocean by about 20% (from 10% no-cloud up to 30% no-cloud). There is evidence of low amounts of cloud over the Canterbury plains and the Nelson region. An unexpected result is the lower levels of cloud seen over the ocean off the West Coast. *Uddstrom et al.* (1999) were unable to offer an explanation for this phenomenon as they found that there was no correlation with sea surface temperatures.

Uddstrom et al. (1999) also presented quarterly no-cloud frequencies to study the seasonal variation of cloud cover. January to March showed the lowest frquency of cloud occurrence with 45% for east of the Southern Alps, over the land and for some way out to sea. The cloudiest months were July to September, although there was still a considerable decrease in cloud in the east. In October to December the east coast was at its cloudiest, although still clearer than the surrounding oceans.

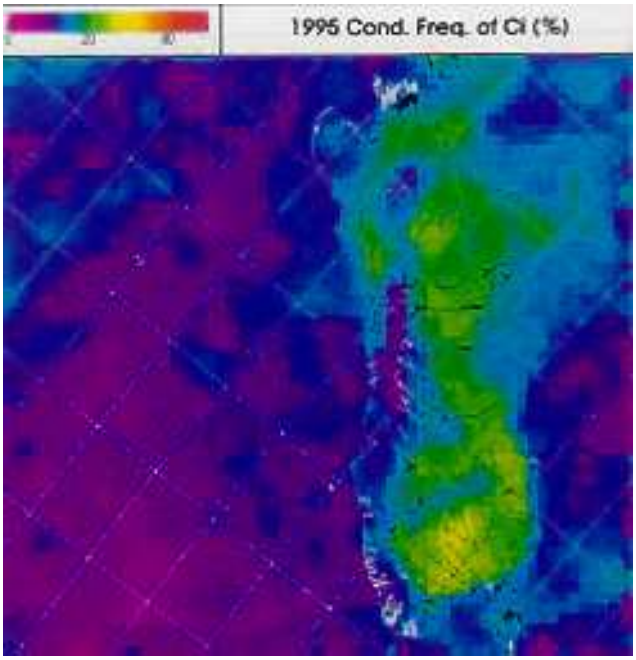

Figure 3.8: Frequency of cirrus expressed as a percentage for the year 1995. From *Uddstrom et al.* (1999)

In terms of cloud types, the most useful presented is that for cirrus (transmissive) reproduced here as figure 3.8. This illustrates that significant increases of cirrus compared to the surrounding oceans are seen over the mountains and for a considerable distance over the oceans to the east. In fact an increase from a frequency of about 10% to about 25% is seen over a large area. Results for the seasonal variation of cirrus are also presented which show a fairly consistent 25% frequency of occurrence east of the Southern Alps, with the cirrus extending over the largest area in the October to December period.

3.2.1 Case studies

Another source of observational data is raw satellite imagery. A number of example days have been collected from different satellites and some of these will be discussed now. In one case the synoptic situation is considered by the use of a Mean Sea Level (MSL) pressure chart.

2^{nd} December 2000

Figure 3.9 is the synoptic situation at 1200 GMT. A synoptic high lies to the west of New Zealand with a cold front advancing up the South Island. A moderately strong northwest flow precedes the front with a southerly flow behind it. These northwest flow ahead of the front would have provided ideal synoptic conditions for orographic wave cloud: strong winds flowing perpendicular to the mountain ranges.

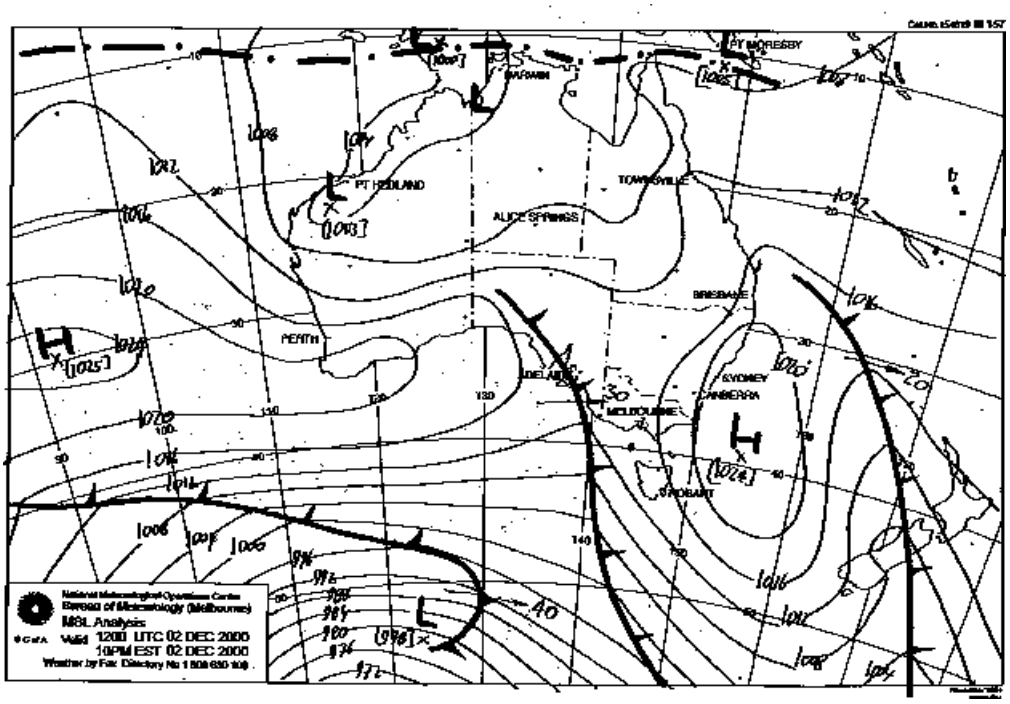

Figure 3.9: Mean Sea Level Pressure Analysis for 2^{nd} December 2000, 1200 hours (GMT).

Figure 3.10 shows the infrared image from the Japanese Meteorological Agency (JMA) geostationary satellite for 0027 GMT (i.e. 11.5 hours earlier than the analysis presented). The image is not reprojected onto a regular grid and hence horizontal distances are progressively more foreshortened to the right of the image. The cloud associated with the frontal band is visible stretching from Australia, across the Tasman Sea to the lower South Island. Although hard to distinguish from the background, the most interesting feature is the bright cloud seen in the lee of the Southern Alps extending for hundreds of kilometres.

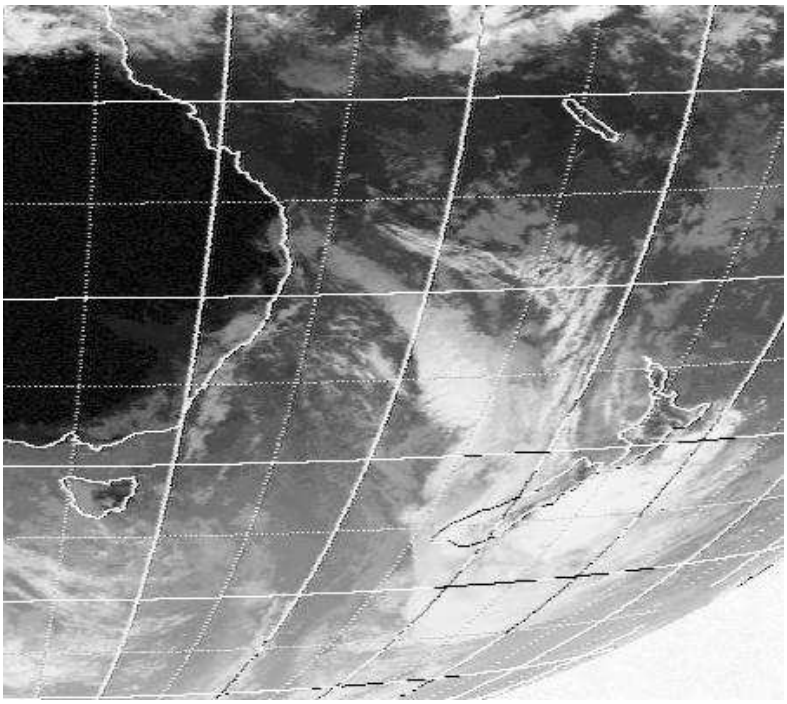

Figure 3.10: An infrared image from the JMA geostationary satellite for the 2^{nd} December 2000, 0027 hours (GMT).

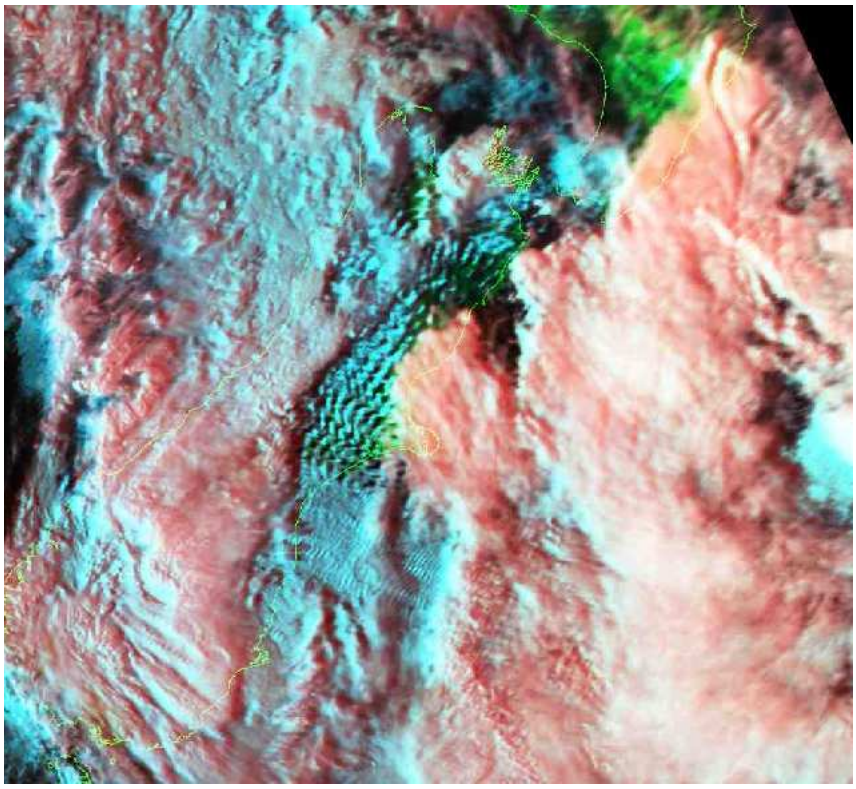

Figure 3.11: Image from NOAA-14 on a day pass for 2^{nd} December 2000 at 0623 (GMT).

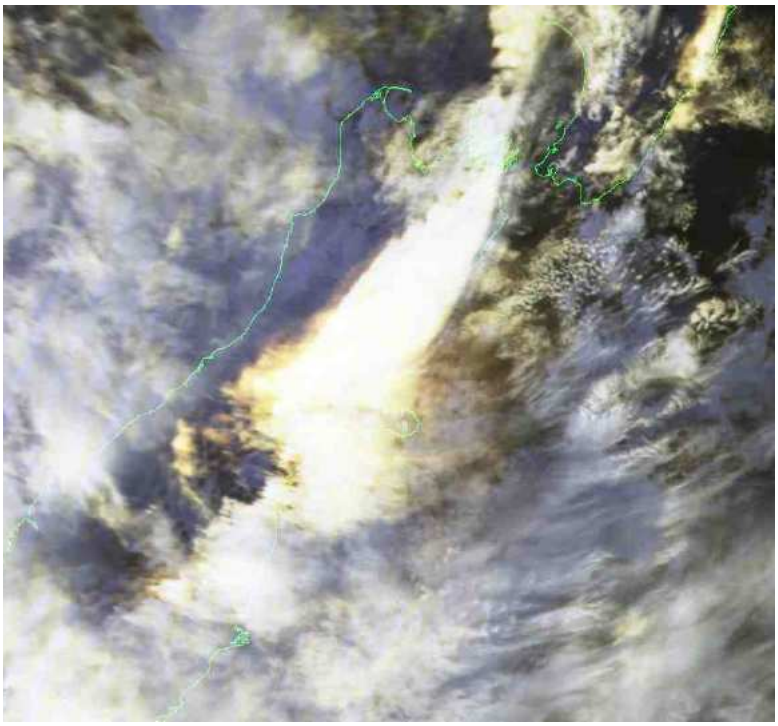

Figure 3.12: Image from NOAA-12 on a nighttime pass for 1^{st} December 2000 at 1618 (GMT).

Figure 3.11 is from the NOAA-14 polar orbiting satellite, courtesy of Landcare New Zealand, for the time 0623 GMT. It is on a regular grid and has been cropped for presentation. The daytime Landcare images such as this one are a composite of 3 of the 5 AVHRR bands for which the satellite observes. Band 1 (visible), 2 (near infrared) and 4 (micron infrared) are displayed as blue, green and red respectively after calibration. Band 4 is calibrated to brightness temperature with black being warm and white cold. The overall effect is for vegetation to turn up green, and dense cold (high) clouds as white. Thin cirrus cloud, which is semi transparent at visible wavelengths, appears red while warmer low clouds will have a blue tint. Depending on ground temperatures snow may also have a bluish tint.

This particular image shows the warm frontal cloud in blue stretching across the lower South Island with some associated upper level cirrus in red. There is a clear Föhn gap just in the lee of the Southern Alps with low level trapped lee wave clouds (blue) visible in this gap. There is also a large amount of dense high cold cloud with overlying cirrus at the highest levels. Both appear to extend a long way downstream of the mountains. It is clear however that there has been a significant increase in cirrus at least.

Figure 3.12 is a nighttime pass of the NOAA-12 satellite at 1600GMT on the 1^{st} December 2000. Nighttime images such as this one are a composite of the AVHRR bands 3,4, and 5 which are all infrared bands and displayed as blue, green and red respectively.

All three infrared bands are calibrated to temperature so that black is warm and white is cold. The resultant image is usually a grey thermal image where different emissivities can appear as colour tints. Thus the figure described earlier shows the initial formation of an orographic cloud that is at a much colder temperature than the surrounding or upwind cloud.

4^{th} October 1999

Unfortunately no synoptic situation is easily available for this date but because of the similar image time this case study illustrates how an arch in a NOA-14 image appears in a geostationary image. Figure 3.13 shows clearly an arch cloud observed at 0426 GMT. Figure 3.14 is the geostationary image for 0627 GMT by which time the cloud will not be expected to have evolved significantly. One feature of this arch cloud that is again worth noting is the upper level ice cloud that is clearly advected away from the mountains.

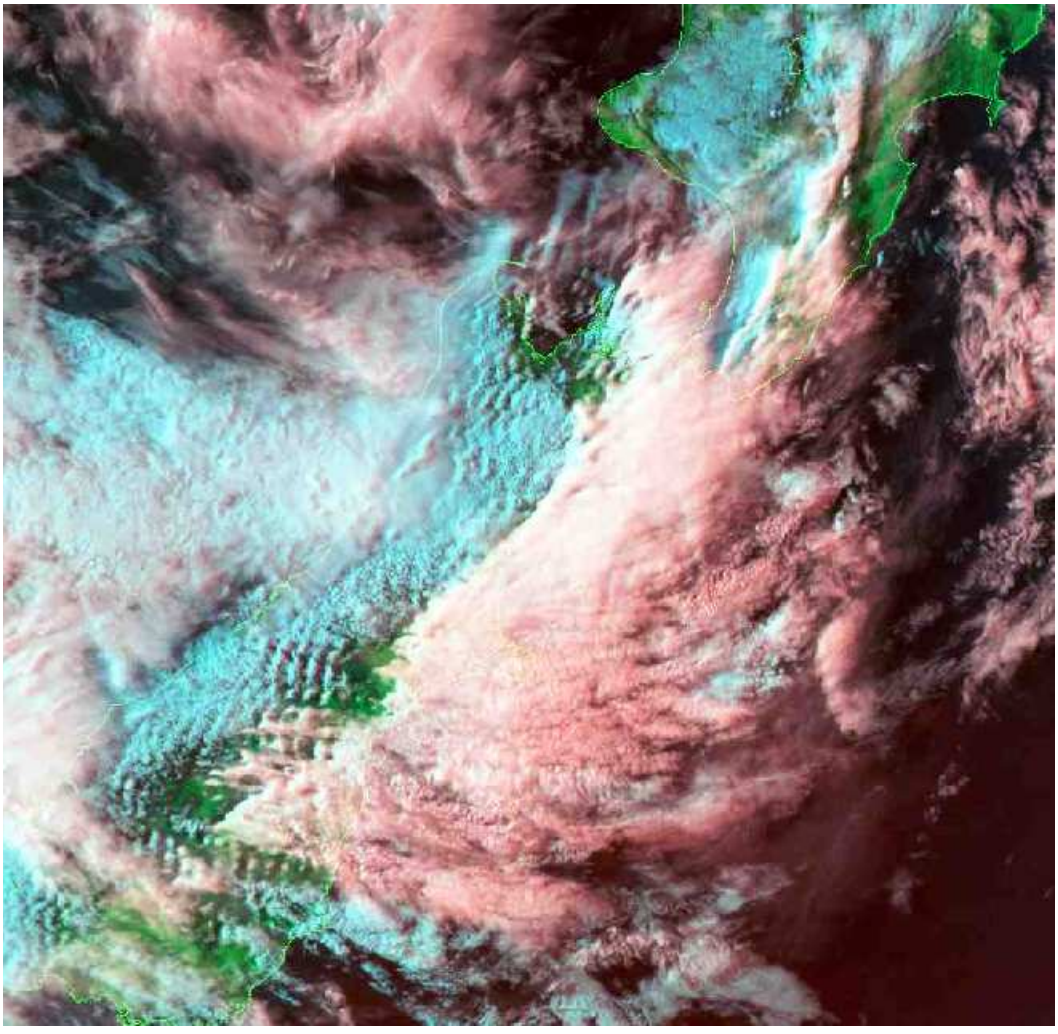

Figure 3.13: An image from NOAA-14 for the 4^{th} October 1999 at 0426 (GMT).

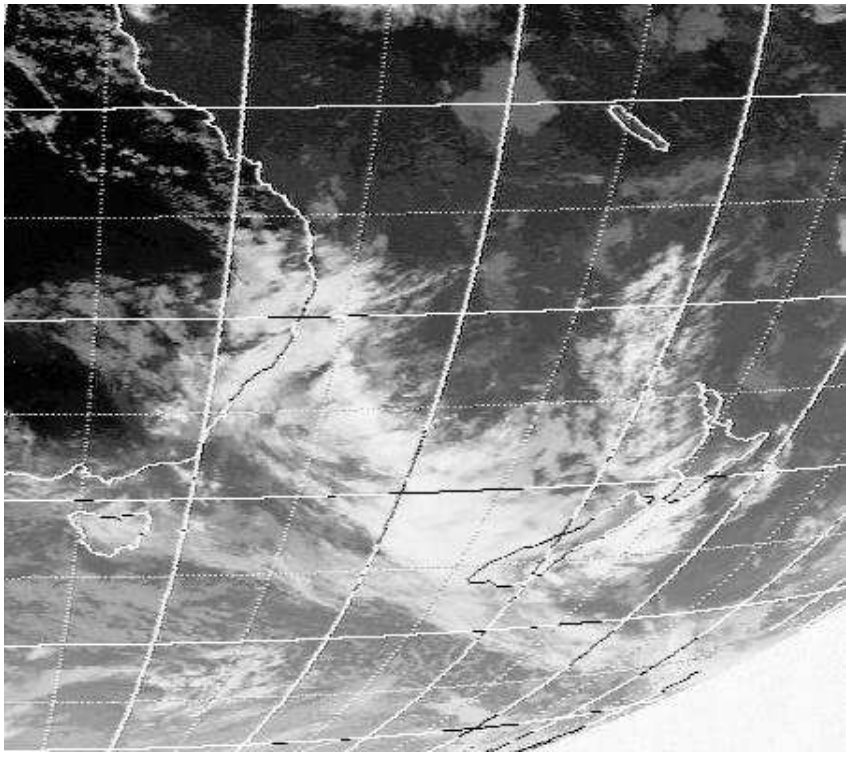

Figure 3.14: An infrared image from the JMA geostationary satellite for the 4^{th} October 1999, 0027 hours (GMT). The data have not been tranformed onto a regular grid.

1^{st} July 1999

The single AVHRR image of figure 3.15 is a superb example of how high level ice cloud streams away from the mountains for a considerable distance before evaporating. There is no similar high level cloud upstream of the mountains, only warm low clouds (blue). The edge of the wave cloud can be seen to be positioned well over the main mountain range.

It should be noted that all of these images give only an instantaneous impression of the Northwest Arch. To study the evolution of a Northwest Arch would require satellite images with regular frequency. Only geostationary satellites can provide this.

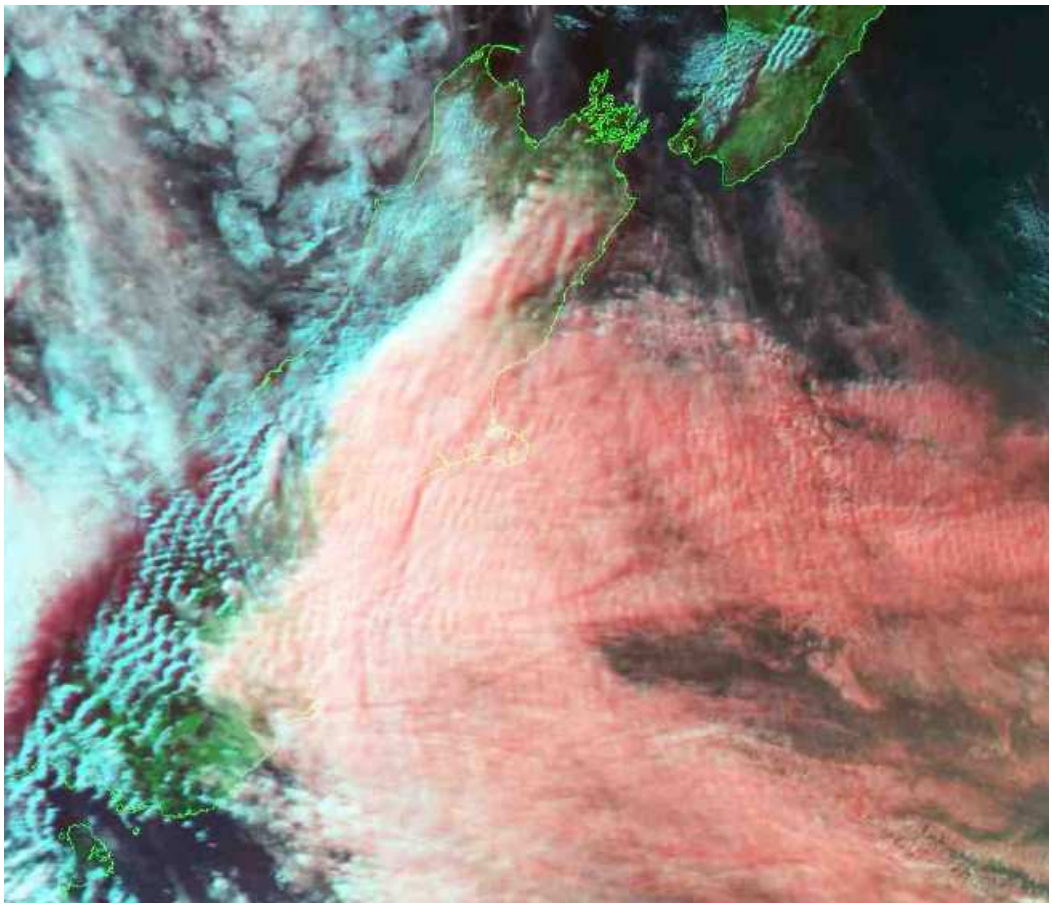

Figure 3.15: A cool NOAA-14 day pass image from the 1^{st} July 1999 showing high cloud streaming off the South Island. The cloud is clearly wave induced.

3.3 Conceptual Model of the Northwest Arch

Despite the mostly anecdotal nature of these observations it is important to bring them together to form a conceptual model of the Northwest Arch, and more generally orographic cirrus. This can then be used to help formulate an orographic cloud parameterisation.

From ground observations and satellite images the base of the cloud is seen to be liquid. From temperature considerations this is most likely true, as in a standard atmosphere the temperature at 6km (a low Arch base) is about -10°C and water rarely freezes in the atmosphere at this temperature. From satellite observations the top of the cloud is certainly ice (see figure 3.15). This ice is generated in a dramatic uplift of air seen over the mountains in which gliders have achieved lift speeds of over 8 m/s. The smoothness of the wave and the modelling of *Ridley* (1991) suggest that the uplift is associated with a smooth upper level wave, which is distinct from any low level hydraulic jump or low-level trapped lee wave phenomenon. However, the work of *Doyle et al.* (2000) has shown that hydraulic jumps have been simulated by numerous models over other mountain ranges that can fill the troposphere. Such a jump cannot be discounted as contributing to the Northwest Arch at low levels, either through mixing of air, or the possibility of a small overshoot of the streamlines.

In the upper levels of the Northwest Arch liquid water freezes to ice and this is then advected downstream by the cross mountain winds. The exact height at which ice begins to form in the orographic lift is unknown, which leaves both possible ice formation mechanisms. Either homogeneous nucleation of ice acts to freeze the liquid where trajectories reach about $<$ -35°C, or the immersion/contact heterogeneous nucleation mechanisms act before this. Which of these dominates will depend on the number of Ice forming Nuclei (IN) present. There seems at the current time to be a very limited understanding of the distribution of ice nuclei with geographical location and altitude (*Heymsfield*, 1993).

According to *Hobbs* (1993) some of the more common ice generating nuclei are various biogenic materials derived from decaying plants and the ocean surface, clay particles, some combustion products and some pollutants from industry such as metal oxides. Apart from the small amount of organic material, the oceans are not a source of IN and thus there is an expectation that IN are likely to be higher over continental masses. There is also some suggestion of this in *Field et al.* (2001) who calculated back trajectories for the six orographic clouds they observed over Scandinavia. They found that the five clouds with ice present had air of continental origin, while the one without originated from the North Atlantic. Thus there is an expectation that with the air over New Zealand being of marine origin that there may well be a lack of IN. During a northwest airflow the nearest source of land sourced IN would be Australia and it is possible that in some situations IN will remain aloft across the Tasman (*Don Grainger,pers coms*). However it is still likely that

there may well be a degree of supersaturation with respect to ice upwind of the orography due to a lack of IN.

Ice crystals, once formed will grow rapidly in any updraft, and may well continue to do so in any downdraft as well, especially if liquid water is evaporating (see section 2.4.1). The component of the cloud which survives far downstream of the mountains is shown by the satellite images (e.g figure 3.15) to be ice. This is due to the slow evaporation rate of ice in a near saturation environment compared to water. *Strom and Heintzenberg* (1994) provide some indicative evaporation rates calculated from the sublimation rate equations of *Pruppacher and Klett* (1997). This table is reproduced in an abbreviated form as table 3.1.

Temperature	Saturation over ice (%)	Evaporation time (s)
-55°C	90	8185
	50	1565
	30	1170
-40°C	90	1665
	50	330
	30	240

Table 3.1: Evaporation times in seconds for a 50 μm ice crystal to decrease to 1 μm

It is possible from these numbers to do a quick estimation of how far a 50 μm ice crystal might be advected. During the Northwest Arch of 12^{th} Dec studied by *Rankin* (1990) the wind at 10 km altitude was measured by radiosonde as 46 ms^{-1}. At this altitude the standard temperature would be close to -55°C. Therefore if this wind speed was maintained downstream, an ice crystal of 50 μm in a relative humidity of 90% would be advected a distance of 376 km. In this time such a small crystal will have fallen less than one kilometre assuming no vertical atmospheric velocities (*Pruppacher and Klett*, 1997). This crude calculation does highlight the possiblity for ice to survive hundreds of kilometres downstream of the wave even when the air upstream of the mountains is cloud free.

If clear upwind air was supersaturated with respect to ice but not water prior to cirrus formation, then when the air returns to its original altitude downstream, the supersaturation over ice will reduce to the saturation point, due to the new availability of ice embryos. However, any liquid cloud will quickly evaporate. As the ice is now in equilibrium in terms of evaporation and growth, the ice may survive for even greater distances than it would in a subsaturated environment like the previous calculation.

3.4 Conclusions

The prime requirements for a large Northwest Arch cloud, with associated cirrus, are strong northwesterly winds which blow moist air from the subtropics perpendicular to the main mountain range. Qualitative observations from pilots and researchers have emphasised the smooth nature and dramatic lift velocities of the gravity wave that generates the upper level orographic clouds over New Zealand. Modelling studies have shown that it is likely that a stationary large amplitude gravity wave is responsible for the lift and subsequent cloud formation in the upper atmosphere at least. Satellite case studies emphasised that the dramatic trailing clouds result from the high level cirrus, which is created by the wave, being advected by the background wind anything from tens to hundreds of kilometres.

While this chapter has focused on the dramatic Northwest Arch the climatology of *Uddstrom et al.* (2001) showed that high level cirrus exists over and in the lee of the South Island at all times of year with a frequency of about 25%. Cirrus amounts were higher around the equinoxes, when the westerlies were strongest. The large increase in cirrus observed at all times cannot be explained exclusively by large Northwest Arches. Instead smaller orographic cirrus clouds must also be generated regularly by weaker winds and smaller amplitude gravity waves.

Worldwide there are many mountain ranges that create strong lee side Föhn winds and downslope windstorms such as those often experienced in New Zealand. Although the Northwest Arch cloud is perhaps a dramatic example, similar clouds have been documented. An example is the Chinook Arch cloud seen in Alberta Canada (*Holmes and Hage*, 1971). The similar appearance and associated weather conditions described by *Holmes and Hage* (1971) suggest that the Chinook Arch is created by similar mechanisms. The Chinook Arch occurs in conjunction with a Föhn wind called the Chinook and occurs at similar heights in the troposphere.

This chapter has emphasised the importance of the cirrus that is generated by a large amplitude stationary gravity wave. Since even small amplitude gravity waves from relatively small mountains can produce cirrus clouds (*Brown*, 1983), there are many less spectacular clouds worldwide which may be of a fundamentally similar nature.

Chapter 4

Global Observations of High Cloud

Before considering the simulation of global cirrus cover in a climate model it is both instructive and necessary to explore the available observational evidence. For the purposes of this chapter the fifteen year cloud dataset of the International Satellite Cloud Climatology Project (ISCCP) has been analysed to investigate cirrus, and more generally high cloud, over New Zealand and globally.

As with many problems in atmospheric science, it is difficult to claim with certainty that a single physical process is responsible for what is observed. In looking at the ISCCP high cloud it will be useful to understand in advance which cloud areas might be potentially of orographic origin. This a priori knowledge of orographic cloud formation can be gained by considering where and when gravity waves might be generated.

Figure 4.1 is a coloured image of the Earth's land and sea floor topography. The land altitudes are derived from the Global Land One-km Base Elevation (GLOBE) topographical dataset. Clearly there are a number of mountain ridges over many parts of the Earth capable of generating large amplitude gravity waves, but it only in conjunction with information about the winds speed and direction over these mountains that we can say anything about wave generation. Therefore, the first part of this chapter analyses winds from the European Centre for Medium-Range Weather Forecasts (ECMWF) 15 year reanalysis project (known as ERA-15) in conjunction with a topographic dataset. By calculating the component of the climatological wind that is perpendicular to the ridge alignment, it is possible to get an idea of the potential gravity wave activity and the direction in which high cloud might subsequently be advected.

4.1 ERA-15

The aim of the ERA-15 project was to produce a long time-series of consistent meteorological analyses. The method used was to assimilate observations from a variety of sources into a single version of the ECMWF model (*Gibson et al.*, 1999). This model had a terrain following coordinate system and a horizontal spectral resolution of T106. Observations for winds were diverse and globally well spread. These are outlined in *ECMWF* (1995) as:

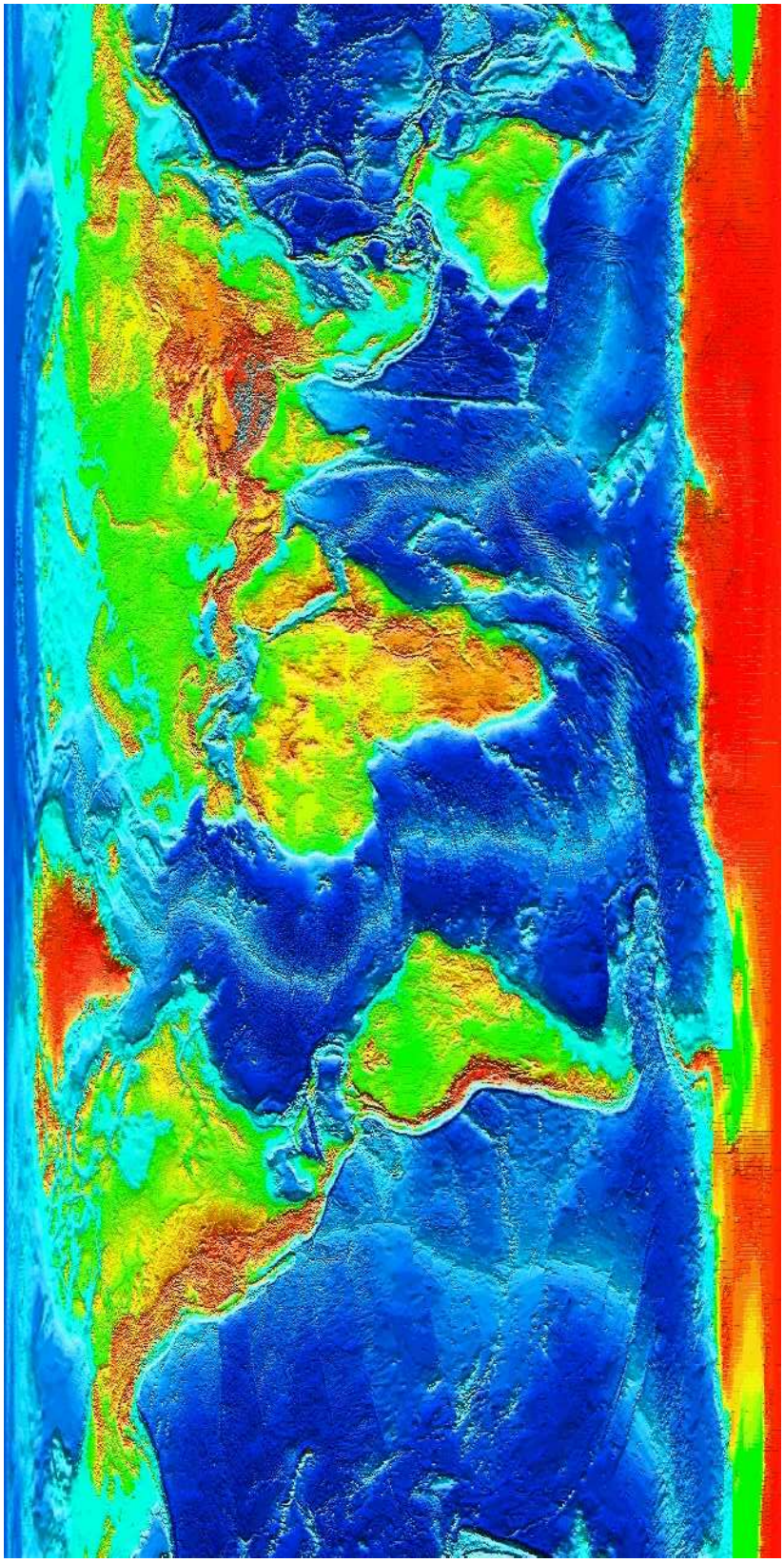

Figure 4.1: Image of the Earth's topography. Obtained from the US National Geophysical Data Centre, http://www.ngdc.noaa.gov

- Cloud motion wind data from geostationary satellites (limited to between 50°N and 50°S globally and 20°N to 20°S over land).
- Reports from surface platforms, such as meteorological weather stations.
- Reports from ships including automatic and abbreviated reports.
- Aircraft data including pilot reports.
- Radiosondes (always over land and mainly in the northern hemisphere).
- Drifting ocean buoys.
- Constant level balloons.

The version of the data used in this analysis was interpolated onto a regular 2.5° by 2.5° grid with 19 pressure levels. It spans the years 1979 - 1993 and was provided by the British Atmospheric Data Centre (BADC).

The mean orographic height data used was those from the ECMWF model at 2.5° by 2.5° resolution. However, values for the squared deviations of the gradients, σ_{xx}, σ_{xy} and σ_{yy} are calculated from the US Navy 10' global topographic dataset using the method outlined in section 6.3. These are needed for the calculation of the ridge alignment. It should be noted that these data were not at the same resolution as the standard climate version of the UM used elsewhere in this thesis.

4.1.1 Analysis method

The fifteen years of ERA-15 winds were averaged to give climatological monthly zonal and meridional wind components. One necessity of the analysis is to determine at what height to select the wind for each gridbox. Obviously this needs to be away from the surface effects, but low enough to be a height at which air is still directly lifted over the orography. Due to the terrain following coordinate of the model having been interpolated onto pressure levels, it was decided that the best compromise would be the level corresponding to the height of the mean orography plus half the height of the subgrid scale orography. The height of the subgrid orography is taken to be $2\sigma^{\frac{1}{2}}$, where σ is the variance. In practice the closest pressure level to this elevation is used, where the pressure has been calculated using a simple scale height relationship.

Using the theory which will be outlined in chapter 7 the squared deviations can be used to assign both an amplitude and a directional alignment to the orography in a gridbox. The component of the wind which is perpendicular to the alignment can then be calculated for the assigned level. The ridge alignments calculated by this method were

found to be in reasonable agreement with those determined by *Bacmeister* (1993), who used a much more complicated filtering algorithm.

There is a caveat to the validity of this analysis method: non climatological winds may be responsible for generating climatological cloud. In essence results may be distorted by first averaging the wind rather than averaging the projected wind. Since this study is only illustrative, this should not be critical.

4.1.2 Results

It is both informative and simpler for interpretation to look specifically at New Zealand first. Figure 4.2 is a time series of the component of the climatological wind which is perpendicular to the orientation of orography in the southernmost New Zealand grid box. It should be noted that throughout this thesis the year 1976 is used in figures to indicate that the data are climatological and thus the mean of a number of years. The fact that the wind values are positive at all times indicates that in the mean westerly winds dominate. Peaks in the wind component are seen in January, April, May and October. The increases in October and April are most likely related to the mid-latitude increase in the westerlies at the equinoxes. The reasons for the January maximum are less obvious, but must be related to the summer climatological circulation.

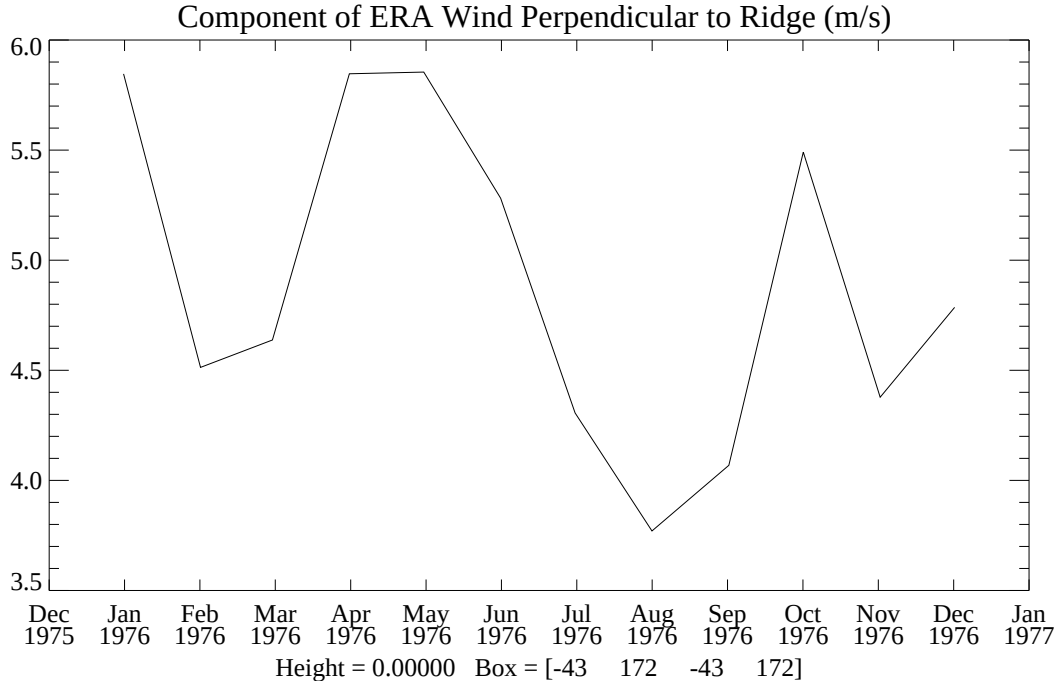

Figure 4.2: Component of the climatological wind (ms^{-1}) perpendicular to the ridge orientation for all months. The grid box is the southern most New Zealand land point seen in figures 4.3 and 4.4. The year 1976 indicates that the data are climatological.

Figures 4.3-4.4 are the component of the climatological wind perpendicular to the ridge alignment over the entire globe for the four months of January, April, July and October. These four months are chosen to be representative of the seasons. The colour indicates the magnitude of the projection, while the sign gives an indication of whether the original wind had a westerly or easterly component. For example, a ridge that is aligned exactly north-south will appear green to red (positive) if there is a westerly wind and blue (negative) if it is an easterly wind.

A number of mountain ranges around the globe are highlighted at different times of the year. In general westerly winds intercept ranges at midlatitudes, sometimes very strongly, while easterly and westerly winds project weakly onto ranges in equatorial regions. The major mountain ranges picked out strongly by the analysis are:

- The Andes on the western edge of South America.
- The tip of South Africa.
- The Australian Alps which form the southern part of the Eastern Dividing Range in Australia.
- The North Island and South Island of New Zealand.
- The Antarctic Peninsula which lies beneath South America.
- The Trans Antarctic Mountain Range adjacent to the Ross Sea.
- The Rocky Mountains stretching through western Canada and the USA.
- The Appalachian mountains in the eastern USA.
- The Kjølen mountains of Norway and Sweden.
- The Zagros Mountains of Iran.
- The Ural Mountains in Russia.
- The Himalayas.
- The Japanese islands.
- The Altai Range in Mongolia.
- The Sikhote Alin Range in Siberia.
- The Ethiopian Mountains.

The forcings seen over Greenland are a known aberration in this type of analysis and are a consequence of the massive drop in altitude at the edge of the Greenland ice plateau. This has an inappropriate effect on the calculation of the squared deviations. The strong forcing over the Himalayas is unexpected. In this region strong westerlies are expected to be incident on predominantly east-west orientated mountain ranges (*Bacmeister*, 1993). Closer examination reveals that the forcings are seen over a only a small area of the Himalayas and mainly on the eastern edge of the range. Qualitative comparison with topographical maps suggested that this is not unreasonable.

All of the regions show significant seasonal variability. Making a broad generalisation, the strongest forcings at midlatiudes are seen in the middle of winter and the weakest in the summer. There are exceptions to this and figure 4.2 illustrates that New Zealand is one of these. The tendency for wave activity to be strongest in the winter months for both hemispheres is probably due to stronger winds rather than more favourable orientation. Equatorial regions show relatively little forcing, the exceptions being in July for India, Thailand and Ethiopia. This month is associated with the Asian monsoon which is possibly producing the favourable winds.

4.1.3 Conclusions

A number of areas of potential gravity wave activity have been identified. However, there are limits to the interpretation of these results. For instance, atmospheric stability has a profound effect on whether gravity waves are able to propagate vertically and the distribution of water vapour in the upper troposphere will have a strong impact on any subsequent cloud formation. Thin cirrus clouds can be generated from both small and large mountain ranges by light winds if the atmospheric humidity is high enough. Such light winds will not appear very strongly in this analysis.

More information on the forcing of orographic gravity waves could be provided by re-doing this analysis so that the wind projection is calculated at the full temporal resolution of the data before averaging. Additionally, the ECMWF's own fields for the orientation of the orography could be used to determine the sensitivity of the findings to the orientation parameter.

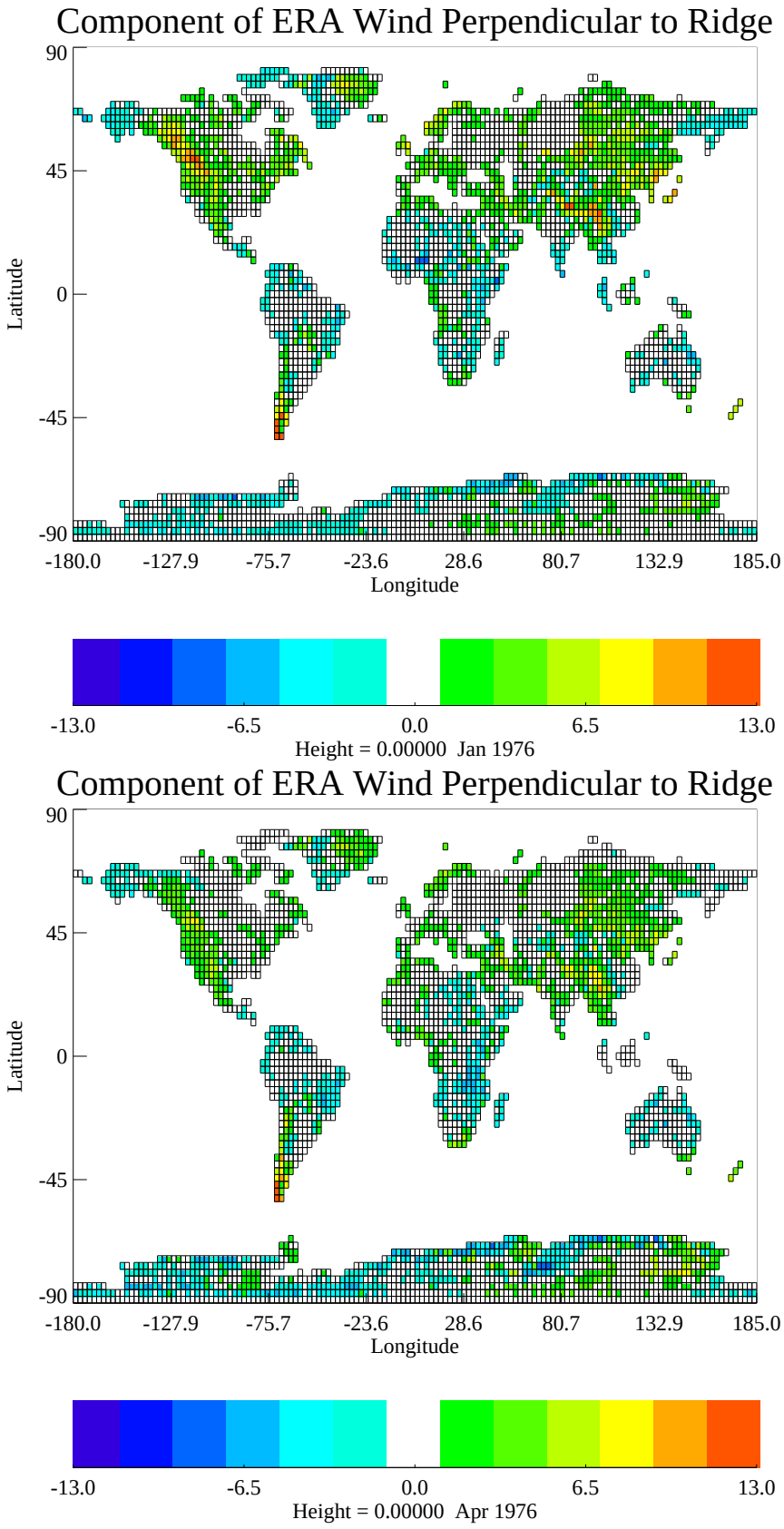

Figure 4.3: Component of the climatological wind (ms^{-1}) perpendicular to the ridge orientation for January (upper figure) and April (lower figure). Blue indicates a wind with an easterly component and green/red a westerly.

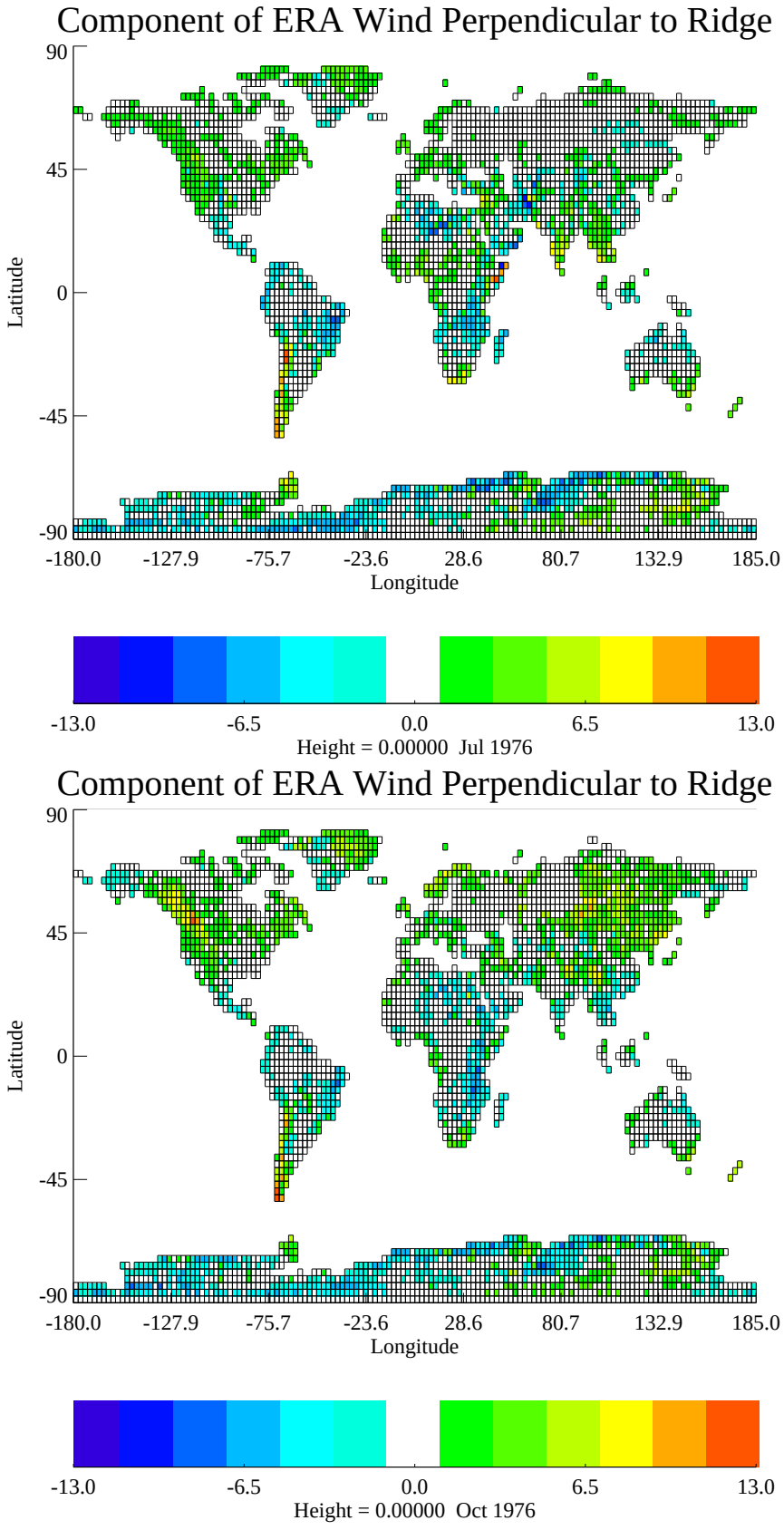

Figure 4.4: Component of the climatological wind (ms^{-1}) perpendicular to the ridge orientation for July (upper figure) and October (lower figure). Blue indicates a wind with an easterly component and green/red a westerly.

4.2 Global Cloud Datasets

There are many attributes which are required of a cloud dataset suitable for comparison with a climate model. The first is that it covers a number of years, so that interannual variability can be accounted for. Secondly the spatial coverage must be as close to global as possible. While high resolution spatial and temporal sampling would be ideal the amount of data that can be realistically analysed requires the adoption of constraints. It is generally accepted that sufficient information can be gleaned from monthly means which have, at a minimum, the same horizontal resolution as the climate model. Other requirements include that the dataset is well validated and thus believable. In the modelling community these ideas have led to the use of a small number of datasets which are based on satellite instruments, rather than ground based observations. Algorithms of diverse natures are used to calculate cloud amounts from changes in the radiances observed from space at certain wavelengths, from single or multiple instruments.

The most widely used and validated dataset is that of the International Satellite Cloud Climatology Project (ISCCP) as detailed in *Rossow and Schiffer* (1999) and *Rossow et al.* (1996). ISCCP combines satellite measured radiances in the visible and infrared, from up to five geostationary and two polar orbiting satellites, with the TIROS Operational Vertical Sounder (TOVS) temperature-humidity datasets. This allows ISCCP to obtain information about both clouds and the surface. ISCCP provides the longest temporal coverage with data from 1983 to 2000.

The stage D1 product gives data every three hours and averages pixel level data of 30km resolution to create global coverage at 280km resolution. These data are usually then transformed onto a 2.5° by 2.5° equal angle grid. The stage D2 product is simply the average of the D1 data over each month. This includes averages for each individual time as well as over all eight observation times. The D level datasets are an improved and extended version of the original C level datasets, which similarly included a C1 and C2 product. The D level algorithm incorporates a number of improvements from the original. Regarding cirrus detection the most prominent of these is the lowering of the threshold for detection of thin cloud over orography and a more complicated model of ice microphysical properties. Both of these lead to an increase in the detection of thin cirrus.

A number of studies have been performed to analyse the ISCCP results and compare them to models. One that focused on high cloud is *Fowler and Randall* (1999), who compared the ISCCP D2 data with the Colorado State University general circulation model to study the simulation of upper tropospheric clouds. They found reasonable agreement except for cirrus ($\tau < 3.6$), which was dramatically underpredicted. They also found that the model simulated upper tropospheric clouds in the tropics more successfully than at midlatitudes. This was primarily caused by the model's failure to simulate upper tropo-

spheric clouds over the continents, especially over high plateaus and mountain ranges.

Webb et al. (2001) compared the ISCCP C1 data with the Unified Model, ECMWF climate model and the Laboratoire de Météorologie Dynamique (LMD) atmospheric model. Their analysis focused on oceanic only regions that represented different cloud regimes. Compared to ISCCP, they found too much high cloud over the tropical warm pool in the Unified Model, but too little over the midlatitude northern Pacific.

Another dataset that is more accurate for upper tropospheric clouds is that derived from the High-resolution Infrared Sounder (HIRS), which has flown on a number of the NOAA polar orbiting satellites. Eight years of HIRS data have been collected and are detailed in *Wylie and Menzel* (1999). HIRS uses a CO_2 slicing method, which involves using multispectral radiance channels in which partial CO_2 absorption is occurring. *Jin et al.* (1996) compared ISCCP C1 data with HIRS and found that the HIRS dataset reports about 12% more cloud cover than ISCCP due to its higher sensitivity to thin cirrus. They also found that 1/3 of the Earth is covered by high cloud at any time and that more than 2/3 of this high cloud is cirrus.

Cloud data have also been derived from the Stratospheric Aerosol and Gas Experiment (SAGE) II (*Wang et al.* (1996)). HIRS and SAGEII have been compared by *Wylie and Wang* (1997) who found that SAGE-II observed even more high cloud than HIRS, primarily through an even higher sensitivity to thin cirrus caused by a limb viewing perspective. *Liao et al.* (1995) also found that when compared to SAGE-II, ISCCP misses about 1/3 of high level clouds, most of which is very thin cirrus.

An additional dataset that has not been so well studied in the literature but may provide useful information in the future is that from the TOVS Pathfinder datasets. The dataset and retrieval algorithms are described in *Stowe et al.* (1999) and *Jacobowitz* (1999).

4.3 ISCCP

The observational dataset used in this thesis is the ISCCP D2 dataset, which will now be considered in more detail.

The pixel level data are produced through a multiple step process. Each pixel is labelled as cloudy or clear based on whether the radiance measured is sufficiently different (preset threshold) from an initially determined and refined clear sky radiance. Thresholds are specified for the different channels using four different surface types:

- type 1 = open water,
- type 2 = near-coastal water, sea ice margin and sea ice,
- type 3 = open land,

- type 4 = near coastal land, high topography, snow and ice covered land.

The evaluation of the clear sky radiance is inferred from a statistical analysis of radiance variations and also uses separate surface type classifications. There are four different surface categories in the infrared and eleven different categories in the visible. The total cloud amount is then calculated by counting the number of cloudy pixels and dividing by the total number of pixels in that cell. This includes observations from both night and day.

Once daytime pixels are classified as cloudy or clear they are compared to radiative transfer model calculations designed to simulate spectral radiance measurements of the instruments. Using this model cloud top temperatures and optical depths are retrieved from the cloudy pixels. Surface quantities are also retrieved from the clear pixels. Each pixel is then given a cloud type based on the idea that different cloud types can be characterised by their optical depth (τ) and cloud top pressure (P_c).

The definitions used by ISCCP can be seen in figure 4.5. While the minimum optical

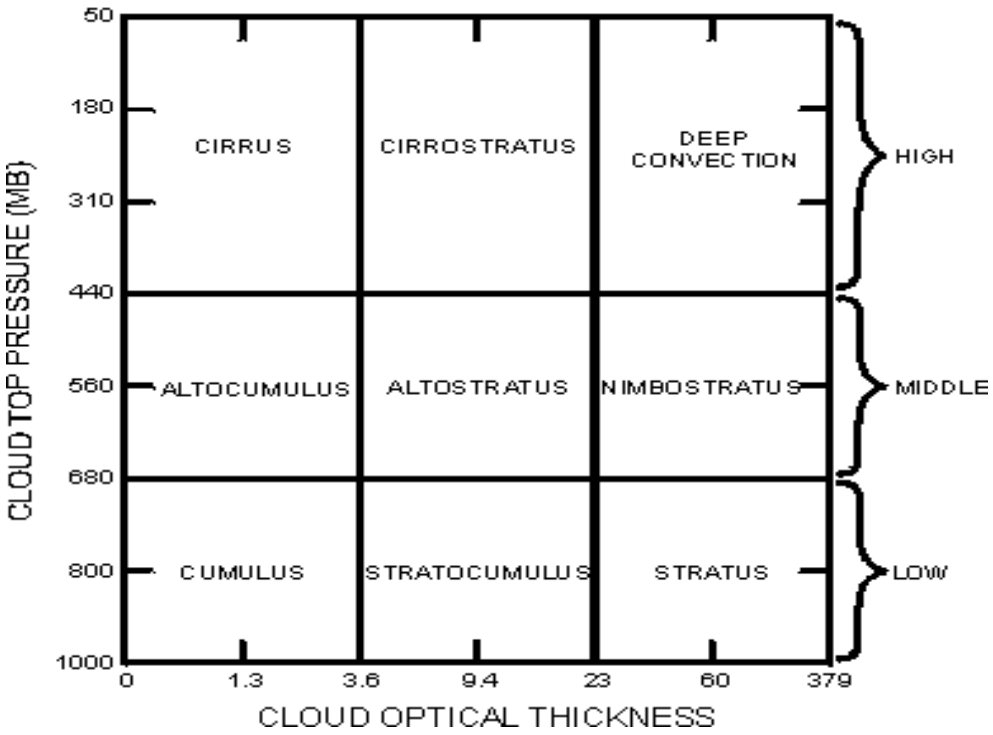

Figure 4.5: Cloud types as defined by optical depth and cloud top pressure for the ISCCP cloud dataset. From http://isccp.giss.nasa.gov/.

depth is displayed as zero, in practice the analysis is not sensitive enough to detect clouds with optical depths of less than 0.1. The six low and middle cloud types are also further subdivided into liquid and ice leading to a total of 15 different cloud type categories. The pixels in a cell are then assigned to cloud amounts in each of the categories. As an

example, cirrus is defined as a cloud type which is optically thin, constituted of ice and with a top in the upper troposphere. However, it is clear that in using this method thin cirrus that happens to overlie thick low level cloud, such as will often happen as air is lifted over orography, could be classified as cirrostratus or deep convective. In fact it is neither of these in the usual classification of clouds.

In the dataset information is included which labels each grid cell as being either land, water or coast. Land must occupy at least 65% of a grid cell for it to be labelled as such. Any cell with 35% or less land coverage is considered to be ocean. Any cell that falls between these limits is considered to be coast. In the analysis that follows figures with overlayed grids are indicating both coast and land cells.

4.3.1 Problems with ISCCP

According to *Rossow and Schiffer* (1999) detection errors are the largest source of systematic error in the ISCCP results. This occurs when pixels are classified as cloudy when they are not or when they are classified clear when they are in reality cloudy. Cloud amounts (calculated by adding up pixels) can be significantly in error if the variability of a viewing scene is greater than the pixel resolution. The accuracy of the detection thresholds has shown a strong sensitivity to the solar zenith angle (*Rossow and Schiffer*, 1999). ISCCP can also miscalculate optical depths and cloud top pressures when optically thin cirrus overlies low level cloud.

Because of the reliance on visible channels ISCCP is unable to retrieve cloud types during the polar night. Also the inherent difficulty in retrieving thin cloud over ice and snow at low temperatures with weak solar illumination makes measurements in polar regions highly uncertain even during summer. As described earlier, a number of studies showed that the ISCCP C1 dataset under-detected thin cirrus compared to other datasets. The D2 dataset thus included a new lowered detection threshold for cirrus over land and a microphysical ice model.

Analysis of the C1 dataset also showed that there were significant systematic global changes in cloud when changing from one AVHRR instrument to the next. Regional discontinuities were also present in the areas observed by adjacent geostationary satellites. A number of techniques, including normalised calibration, have been introduced into the D2 datasets to try to decrease all of these errors. *Norris* (2000) found that these changes were not completely successful, while other independent literature which comprehensively analyses the D2 datasets is yet to appear.

4.3.2 Analysis of ISCCP high cloud

For this analysis, ten years of the ISCCP D2 dataset from 1984 to 1993 has been used to study clouds with cloud top pressures smaller than 400 hPa. At midlatitudes this corresponds to clouds above an altitude of about 7.3 km and temperature of -25 °C for a standard atmosphere. For the sake of consistency with the ISCCP definition 'cirrus' will refer to the cloud amount in the optical depth range $0.1 < \tau < 3.6$, as defined in figure 4.5, while 'high cloud' refers to the total cloud amount of all three cloud type categories. Thus cirrus is a subset of high cloud.

New Zealand

While the ISCCP data over New Zealand are at a very low resolution they are still capable of providing insights into how well ISCCP identifies orographic cloud and will assist in interpreting the global data.

The solid line in figure 4.6 is the climatological cirrus amount (percentage of a grid box covered by cloud) for each month over a New Zealand land point. The dashed line shows the same thing for the adjacent sea point to the west and the dash-dot line for the adjacent sea point to the east. Since the ERA analysis showed that the winds are westerly, in the average, these points will also be referred to as upstream and downstream respectively. The vertical bars on the solid line indicate one standard deviation either side of the mean. The standard deviation is calculated from the ten months used for each data point.

In all months there is a considerable increase between the upstream point and the land point, with a maximum change of 12 (120% increase) seen in April and a minimum of 4 (44% increase) seen in July. An increase is also seen downstream, which is about half that of the land point in summer, and about the same in winter. In general the upstream point tends to have slightly higher cirrus amounts during the summer, suggesting that moisture availablity plays a role in the higher cirrus amounts seen over land in the summer compared to winter. It is also possible that the synoptic situation is more favourable for general uplifting in the summer.

Figure 4.2, from the ERA analysis, showed the wind component perpendicular to the New Zealand mountain range. The months with the strongest perpendicular winds were January, April, May and to a lesser extent in June and October. Reassuringly peaks in cirrus changes for figure 4.6 are seen in January and April, and also in May for the downstream point. However, there are no secondary increases for June or October. The matching of these peaks suggests gravity waves play a role in the increase in cirrus observed over the orography and in the lee.

Figure 4.7 shows the same three grid points only for high cloud amount. The seasonal

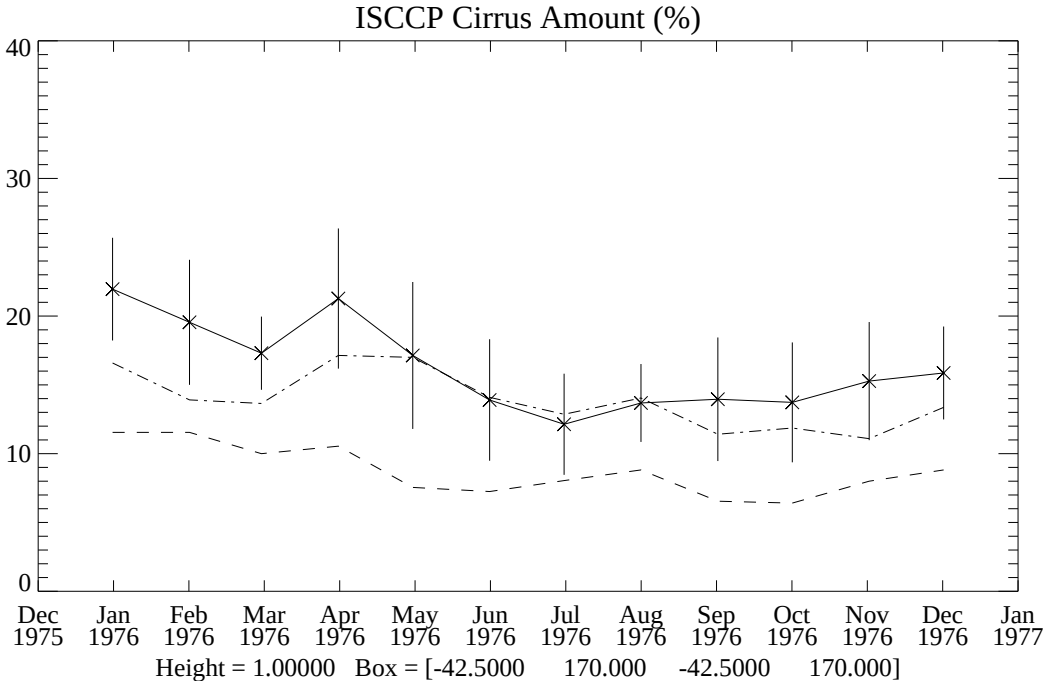

Figure 4.6: Climatological ISCCP cirrus amount for the central New Zealand gridbox (solid line) located at 42.5°S and 170°E. The dashed line is the cirrus amount for the adjacent sea point to the west and the dashed-dot line for the point to the east. Vertical bars indicate one standard deviation either side of the mean.

pattern is a little different here with a clear maximum in the middle of summer and a minimum in winter. While all three lines have much higher amounts of cloud than in figure 4.6 (just cirrus) the difference between the land point and the upstream point remains the same for each month. This suggests that the changes in high cloud over the orography are primarily attributable to an increase in the cirrus component of the high cloud amount - there is not much change in the convective or storm generated cloud over land compared to the surrounding sea.

To explore the question of ice advection downstream of the New Zealand mountains, figure 4.8 is a longitudinal slice across the same New Zealand gridbox as earlier. The land point can be found at 170 degrees. Clearly there is a significant increase in cirrus for up to three gridboxes downstream of the land. The signal is stronger for January through to June. Upstream cirrus amounts are reasonably constant apart from an increase in January.

Figure 4.9 shows the same slice but for high cloud. Here there is considerable increase in cloud in the lee for all months, with the stronger increases being mid summer and mid winter. It is clear that these increases can not be entirely due to changes in cirrus amounts. There are two possibilities suggested by this: The first is that some of the ice

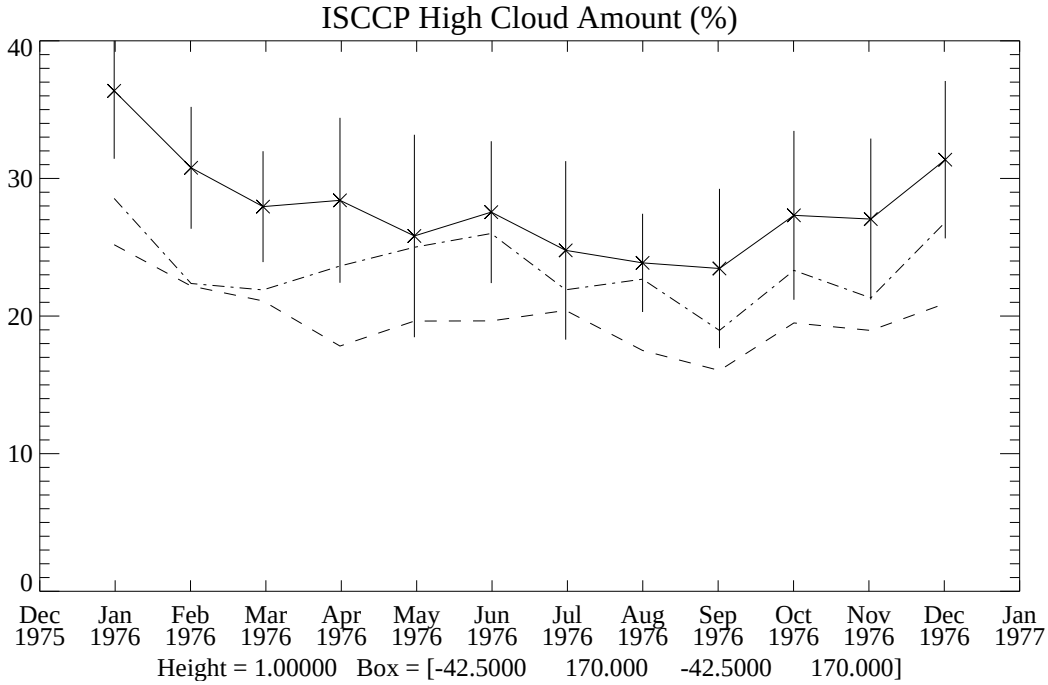

Figure 4.7: Climatological ISCCP total high cloud amount for the southern most New Zealand gridbox located at -42.5°S and 170°E.The dashed line is the high cloud amount for the adjacent sea point to the west and the dashed-dot line for the point to the east. Vertical bars indicate one standard deviation either side of the mean.

cloud generated by gravity wave activity is detected as optically thick, either through being actually thick or through simply being associated with underlying cloud. The other is that different weather conditions are leading to more thick high cloud being generated in the lee. This seems unlikely however and could be tested by examining total cloud cover. Previous work by *Uddstrom et al.* (2001) suggests that in fact a decrease in total cloud is usually seen in the lee of New Zealand.

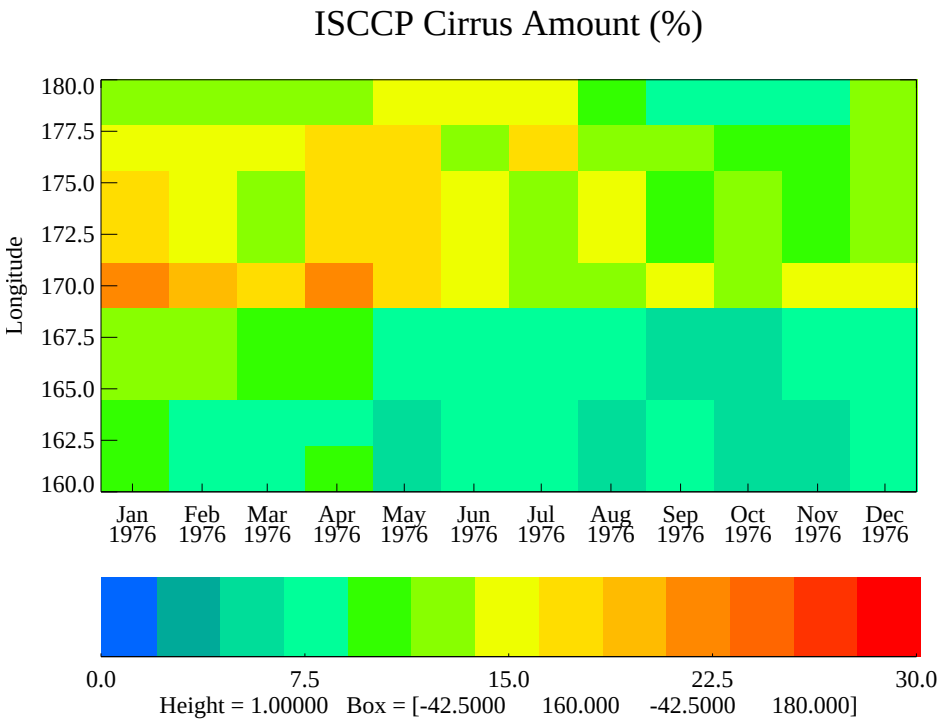

Figure 4.8: Longitude slice across the southern most New Zealand gridbox of climatological ISCCP cirrus amount. The land point lies at 170°E.

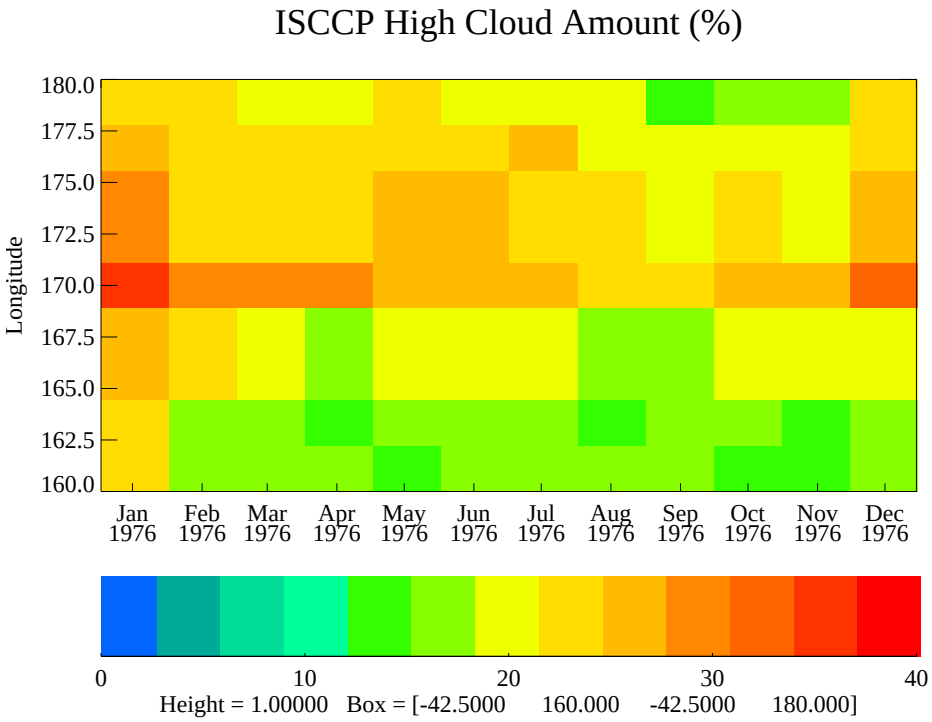

Figure 4.9: Longitude slice across the southern most New Zealand gridbox of climatological ISCCP high cloud amount. The land point lies at 170°E.

Globally

Figure 4.10 is the global cirrus cloud amount, averaged over all months for the ten years. Also shown is the standard deviation for the cirrus climatology. It is apparent that the global cirrus amount is dominated by two features: Firstly the large cirrus amount of 30-40% seen over the equatorial Indian and Eastern Pacific Oceans, most of which is likely to be from the detection of large anvils created at the top of convective towers. Secondly the increase in cirrus seen over much of the worlds orography, when compared to the surrounding oceans. It is this increase which is of more interest to this study.

Over nearly all land areas, except for Antarctica and North Africa, there is at least a small increase compared to the ocean. The areas of larger increases will now be explored separately in conjunction with figure 4.11, which is for total high cloud amount. By looking at high cloud as well as cirrus it is possible to gain more information about the source of cirrus. For instance areas of conflict exist where high cloud of convective origin might be thought to be generated over both plains and orography. By looking at the cirrus component and high cloud together it is possible to gain an insight into the impact of convective towers. This is because convective towers always produce optically thick high cloud in conjunction with cirrus.

The two areas of central South America and central Africa show cirrus amounts of 20% and 30% respectively. The most likely source of this cirrus is again convective anvils. Strong convection can be expected over equatorial land masses and these areas were seen to not be places of strong orographic wave activity in figures 4.3 to 4.4. Indeed the even greater amounts of high cloud support this. This is because these areas are also associated with optically thick high cloud, such as would be generated by convection.

North America is another area of cirrus where the large land mass might be expected to contribute some convective activity. However there was strong wave activity seen here in the ERA analysis and the plot of high cloud shows little increase due to components other than cirrus. This is suggestive of a strong orographic cirrus influence.

The bottom of South America also shows increases over both the orography and the adjacent ocean, which could potentially be caused by advected ice. However, unlike North America, there is a big increase in high cloud in this region compared to the cirrus component. Thus, there is either a convective component present, or this is one region in which the waves generated are of such large amplitude that optically thick ice cloud is generated.

These same arguments apply to the area of increased cirrus seen over the Himalayas which was identified as an area of very strong wave activity in the ERA analysis. The changes over northern Asia and the tip of South Africa are also easily linked to the gravity waves seen there.

A region that is counter to the source ideas used in this analysis is Australia, where there are significant cirrus amounts of 20% to 30%. Australia, much like northern Africa, is primarily desert and has only small mountain ranges, mostly in the east. That the high cloud here is made up of almost entirely the thin cirrus component implies that there is little convective activity. The summer origin of this cirrus suggests that there is either a small lifting of relatively dry air in the upper troposphere by the synoptic situation or convection is acting, but in a moisture sparse environment. Injection of dust capable of acting as ice nucleii into the upper atmosphere is also a possibility. This summer cirrus feature over Australia was not seen in the HIRS cirrus climatology (*Wylie and Menzel*, 1999) and would require further investigation before it could be elimnated as a detector anomaly.

Areas of strong gravity wave activity that were identified in the ERA analysis but show no increase in cirrus or high cloud in the ISCCP climatological mean data are Scandinavia and the Antarctic Peninsula. It is possible that this is due to problems with the ISCCP retrieval at these high latitudes or simply that any orographic cirrus clouds in these areas are not climatologically significant. As is shown by New Zealand, areas with reasonable changes in cirrus compared to the ocean may be lost in these figures because of the dominance of the major cirrus regions.

Another feature is that there is almost no cirrus over the northern most latitudes while only small amounts are detected over the southern most latitudes. The regular pattern of cirrus increase seen at 70 degrees south is suggestive of errors in the cloud detection due to a complex interplay between the orbits, the solar angle and the surface characteristic. The high standard deviations seen at this latitude are also indicative of this and similar spurious patterns were identified in the D2 dataset by *Norris* (2000). The inherent problem of detecting thin cirrus over snow means that polar data are less reliable.

By looking at the cirrus for four months selected from the different seasons, in conjunction with the same months from the ERA analysis, further insights into the global cirrus areas identified earlier can be gained. Figures 4.12 and 4.13 are the months of January, April, July and September. Unlike New Zealand, where there was good correlation in the seasonal trends between ERA and ISCCP cirrus amounts, there is a poor correlation globally. Cirrus amounts for potentially orographic areas in both hemispheres are greatest in summer and weakest in winter. This is the converse of the general pattern seen in the ERA data. This emphasises the importance of other factors in cirrus generation over land than simply wave activity. These may include the possibility of orographic convection as well as the seasonal availability of moisture and IN in the upper atmosphere.

Localised areas do show independent behaviour. For instance, over Canada cirrus is stronger in April and October, while over the USA it is stronger in July. This may indicate

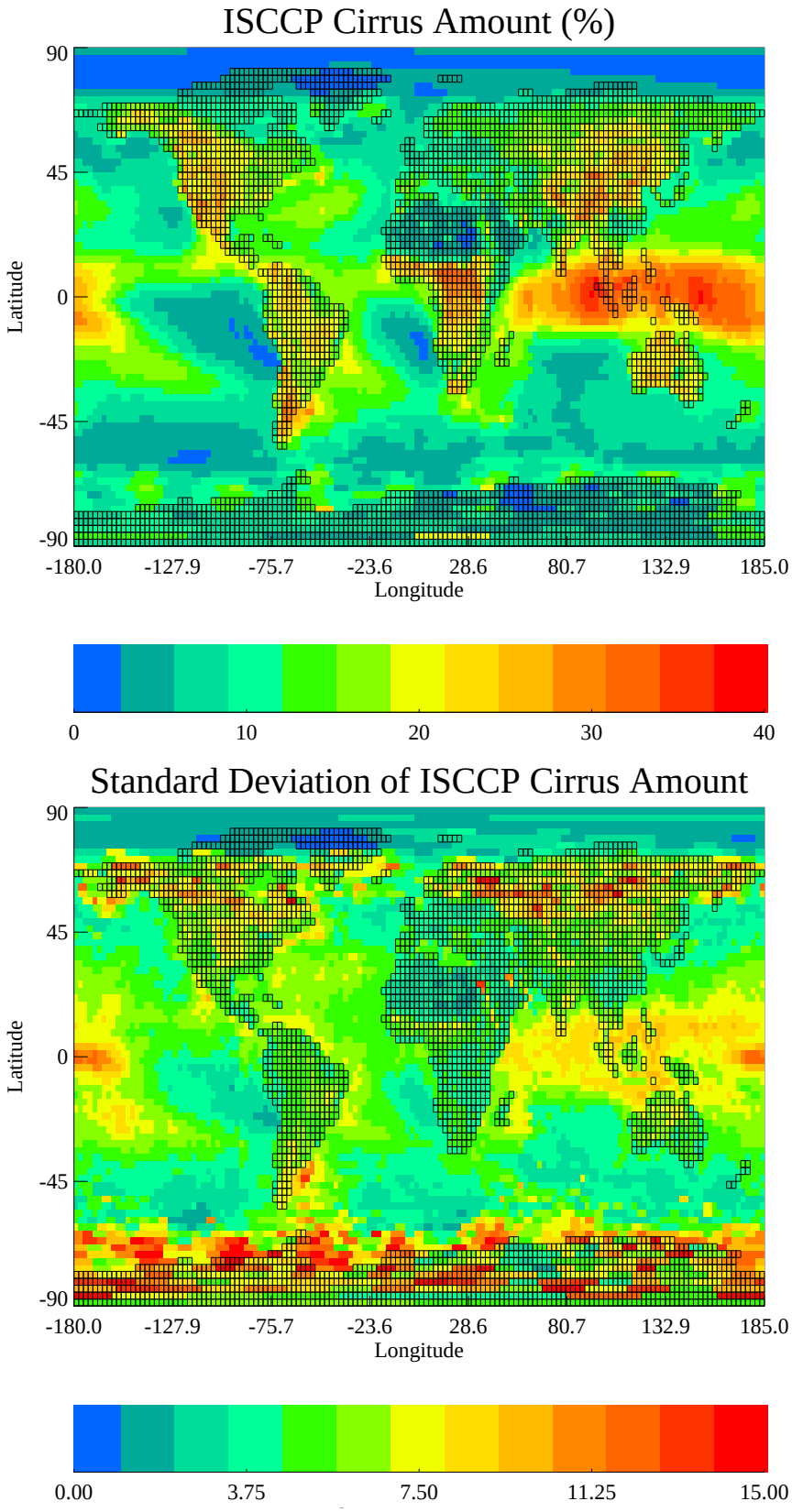

Figure 4.10: Global climatological ISCCP cirrus amount (upper figure) and the standard deviation of cirrus amount (lower figure).

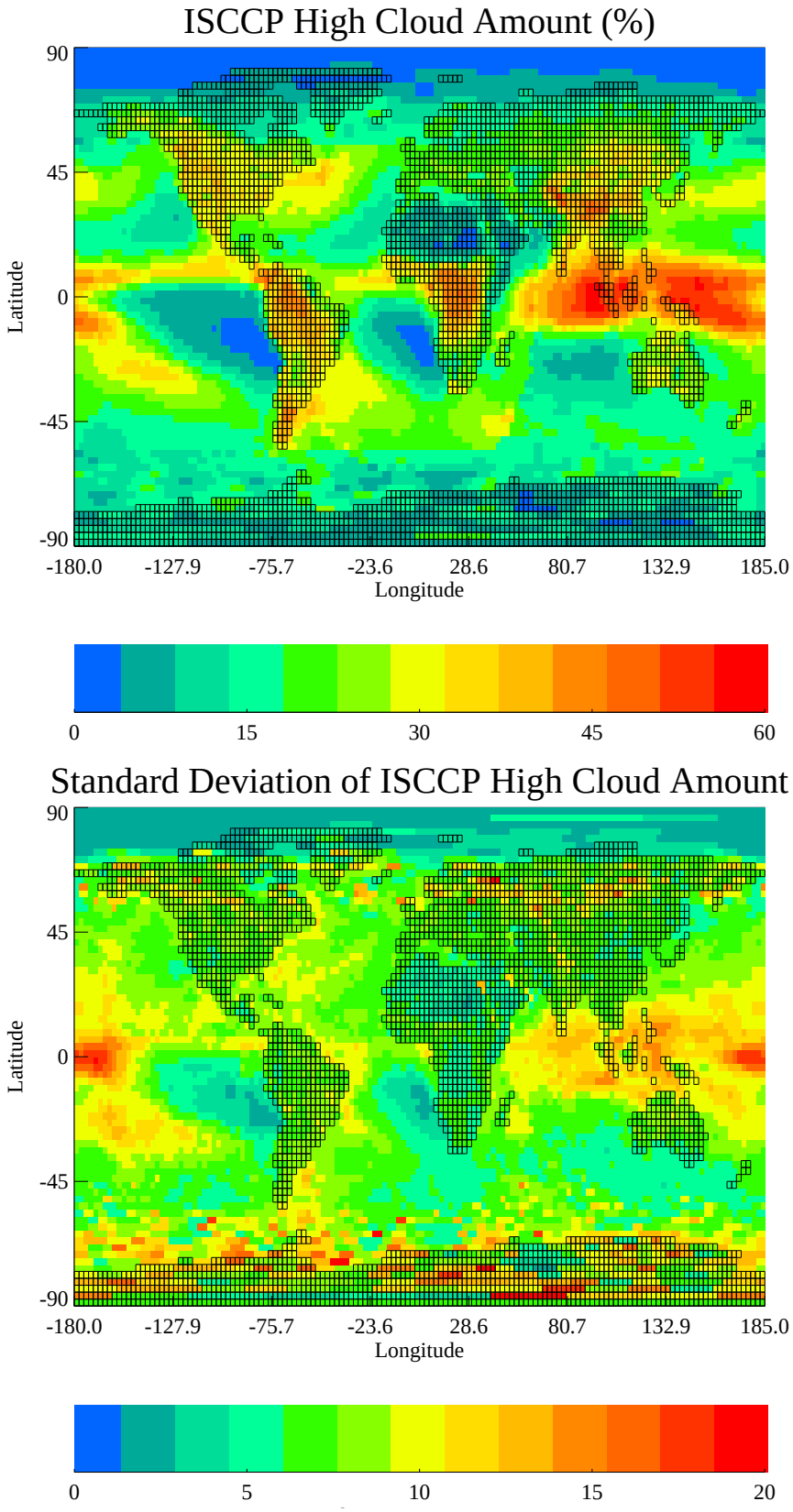

Figure 4.11: Global climatological ISCCP high cloud amount (upper figure) and the standard deviation of high cloud amount (lower figure).

greater contributions from other sources such as convection over the USA. The ERA analysis predicted strong gravity wave activity over Canada and the USA in January and October, which agrees for October, but unfortunately the satellite is unable to measure cirrus amounts over Canada in January. There is a hint of high cirrus at the edge of the available data but this could easily be a retrieval error.

Northern Asia was expected to be strong in all months except July, while in the observations the cirrus amount was strong in all months. The Himalayas were also expected to be strongest in January and in fact do show the clearest increase at this time compared to the surrounding land mass.

4.4 Conclusion

The ISCCP analysis showed significant increases in cirrus over land compared to the oceans in general. The strongest of these changes show a good qualitative correlation with areas of gravity wave forcing identified by the ERA analysis, which picked out many of the Earth's major mountain ranges. However, in general the changes in forcing with the seasons were, if anything, anti-correlated with the cirrus changes. This is probably due to the importance of humidity, stability and other cirrus generating mechanisms.

Over New Zealand there was a significant increase in cirrus at all times of year and peaks in this increase were well correlated with peaks in the ERA analysis. That the increase seen in high cloud was primarily due to the cirrus component gives confidence in the cirrus increase being primarily due to orographic gravity waves and not convection.

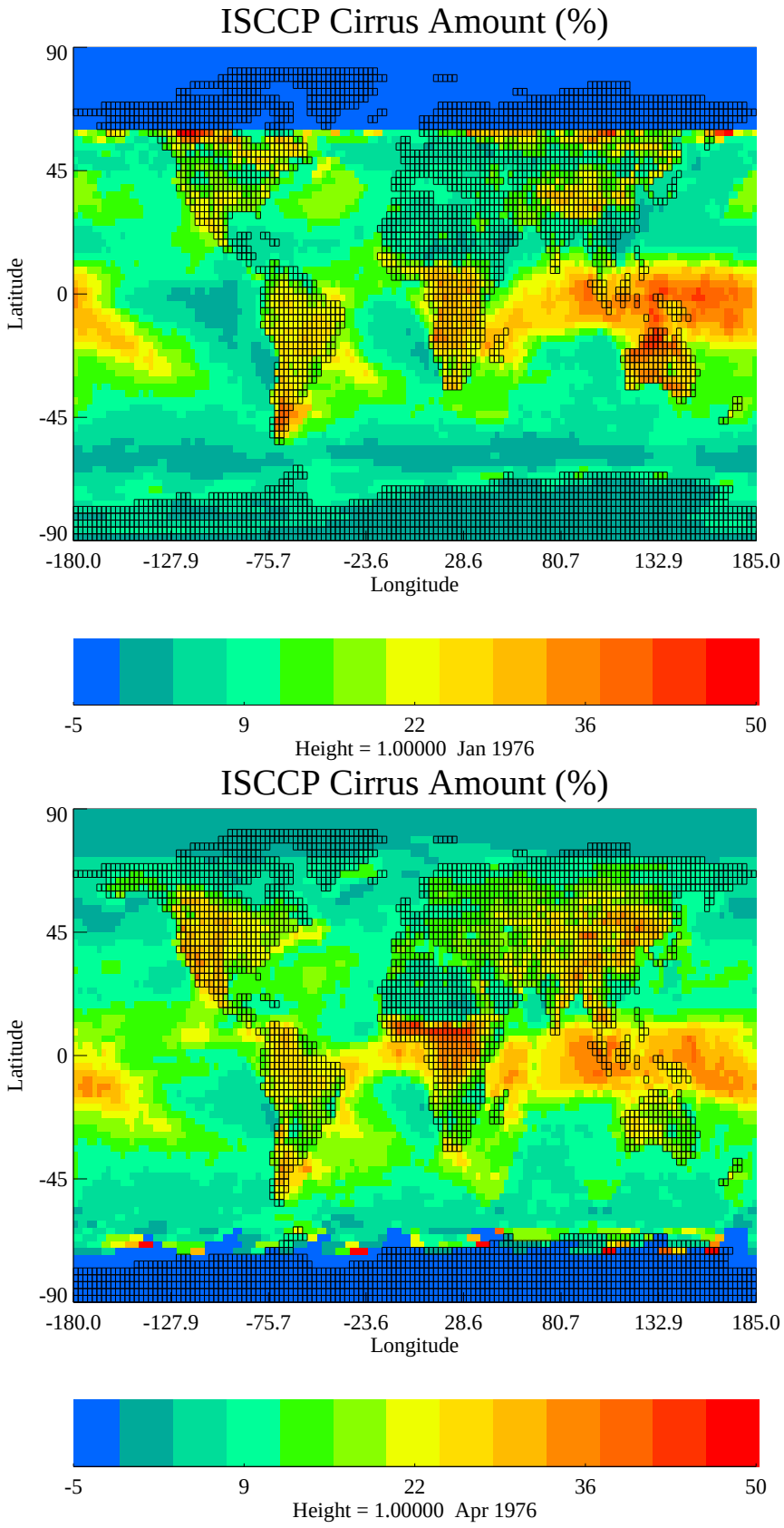

Figure 4.12: Global climatological ISCCP cirrus cloud amount for January (upper figure) and April (lower figure). The range is extended to -5 so that missing data are indicated by blue.

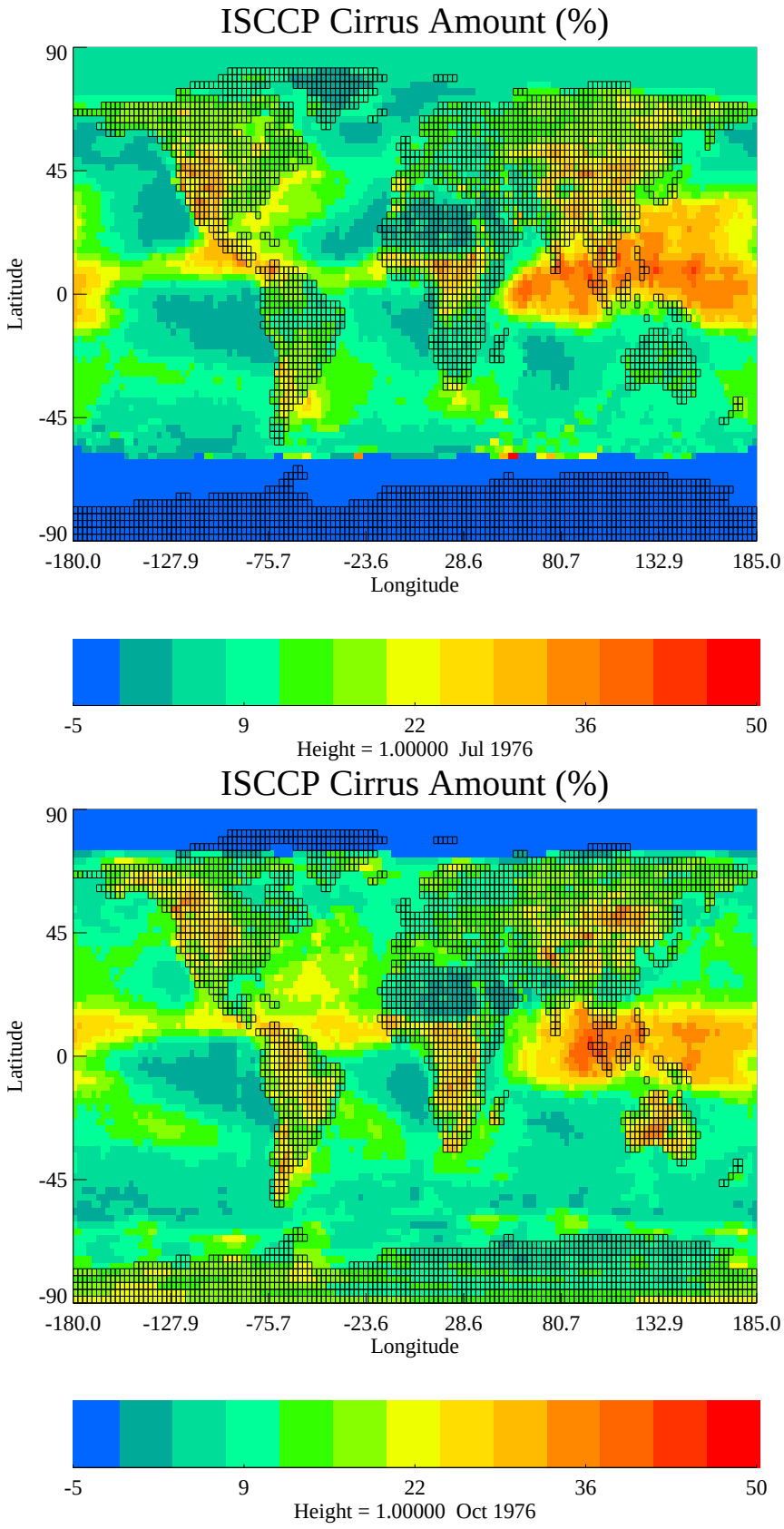

Figure 4.13: Global climatological ISCCP cirrus cloud amount for July (upper figure) and October (lower figure). The range is extended to -5 so that missing data are indicated by blue.

Chapter 5

Dynamics of Orographic Wave Clouds

When the atmosphere has a stable stratification, surface air which is forced to move over topography experiences buoyancy forces. These forces will cause the air to oscillate in response to the terrain forcing. This disturbance in the air flow is known as an *orographic gravity wave* and under certain atmospheric conditions these waves can propagate high into the atmosphere.

The lifting and mixing processes inherent in such waves can result in the formation of clouds which would otherwise not occur, or alter the extent of those that already exist. It is thus worthwhile to consider the dynamics of orographic gravity waves before considering the possibility of any cloud formation.

This chapter attempts to review the theory for mountain induced waves as the necessary precursor to the development of an orographic gravity wave parameterisation. Linear solutions are explored for a series of increasingly more complex atmospheric situations, before non-linear effects such as hydraulic jumps are discussed briefly. This review is not intended to be a complete consideration of the subject but simply to cover the background theory utilized in later chapters of this thesis.

5.1 Review

Work on the theoretical dynamics of mountain waves began with the work of Queny and Lyra in the 1940s. Since then much work has been done on this linear theory and a number of reviews have been published. *Queney et al.* (1960) gives an extensive and detailed review of the important theoretical and observational studies on airflow over mountains before 1960. *Smith* (1979) updates and extends this work and provides detailed mathematical coverage of theory for both basic and more complicated large scale waves. He also discusses the effects of orography on precipitation and breaks down a number of observational studies into regional and type classifications. In *Smith* (1989) the next ten years of development are reviewed including the introduction of theories pertaining to nonlinear effects in hydrostatic flows, which can lead to features such as downslope windstorms. More recent theory, including further development of nonlinear regimes, are included in a review by *Wurtele et al.* (1996). These reviews cover the theory in depth and the next sections will try to only briefly cover the essential ideas. The theory for

linear waves is developed primarily from *Durran* (1986b), *Durran* (1990), *Holton* (1992) and *Gill* (1982) with some extension where the details have been omitted by the authors.

5.2 Linear Theory for Mountain Waves

Initially consider that there is motion only in the x-z plane and that the waves are small enough in scale that the Coriolis force can be neglected. For simplicity the Boussinesq approximation is used, in which density is treated as a constant except where it is coupled with gravity in any buoyancy term. Then the horizontal and vertical inviscid momentum equations are,

$$\frac{\partial u}{\partial t} + u\frac{\partial u}{\partial x} + w\frac{\partial u}{\partial z} + \frac{1}{\rho}\frac{\partial p}{\partial x} = 0 \tag{5.1}$$

$$\frac{\partial w}{\partial t} + u\frac{\partial w}{\partial x} + w\frac{\partial w}{\partial z} + \frac{1}{\rho}\frac{\partial p}{\partial z} + g = 0 \tag{5.2}$$

where u is the horizontal wind velocity, w the vertical wind velocity, p the atmospheric pressure, ρ the density and g the acceleration due to the Earth's gravity. The equation of continuity is

$$\frac{\partial u}{\partial x} + \frac{\partial w}{\partial z} = 0 \tag{5.3}$$

We will also initially assume that the air is dry and will discuss qualitatively the effect condensation has on any flows. The first law of thermodynamics is

$$c_p\frac{DT}{Dt} - \alpha\frac{DP}{Dt} = \frac{DQ}{Dt} \tag{5.4}$$

where T is temperature, α the specific volume, c_p the specific heat at constant pressure and $\frac{DQ}{Dt}$ is the rate of heat exchange with the surroundings (i.e. the diabatic heating rate). Equation 5.4 reduces to the conservation of potential temperature, θ, if adiabatic motion is assumed (i.e. $\frac{DQ}{Dt} = 0$) then

$$\frac{D\theta}{Dt} = \frac{\partial\theta}{\partial t} + u\frac{\partial\theta}{\partial x} + w\frac{\partial\theta}{\partial z} = 0 \tag{5.5}$$

These four equations are then linearised to make it possible to find solutions to the equation set. It is assumed that variables can be considered to always consist of a background value, indicated by an overbar, plus a small deviation from this background, indicated by a prime i.e.

$$u = \overline{u} + u'$$

$$w = w'$$

(i.e. that $\overline{w} = 0$ and there is no background vertical velocity)

$$\rho = \overline{\rho} + \rho'$$

$$\theta = \overline{\theta} + \theta'$$
$$p = \overline{p} + p'$$

It is also necessary to assume that the background variables are spatial functions of z only. The exact details of the procedure can be found in *Holton* (1992), but essentially by assuming that any deviations from the background are small any terms that are the products of perturbation variables can be neglected. After factoring out mean terms, the equations are then

$$\left(\frac{\partial}{\partial t} + \overline{u}\frac{\partial}{\partial x}\right) u' + w'\frac{\partial \overline{u}}{\partial z} + \frac{1}{\overline{\rho}}\frac{\partial p'}{\partial x} = 0 \tag{5.6}$$

$$\left(\frac{\partial}{\partial t} + \overline{u}\frac{\partial}{\partial x}\right) w' + \frac{1}{\overline{\rho}}\frac{\partial p'}{\partial z} - \frac{\theta'}{\overline{\theta}}g = 0 \tag{5.7}$$

$$\frac{\partial u'}{\partial x} + \frac{\partial w'}{\partial z} = 0 \tag{5.8}$$

$$\left(\frac{\partial}{\partial t} + \overline{u}\frac{\partial}{\partial x}\right) \theta' + w'\frac{\partial \overline{\theta}}{\partial z} = 0 \tag{5.9}$$

Now consider solutions to the above set of equations for a steady state flow, i.e. solutions which are stationary with respect to the ground. This is only plausible for a limited time in the real atmosphere but any time derivatives are now removed:

$$\overline{u}\frac{\partial u'}{\partial x} + w'\frac{\partial \overline{u}}{\partial z} + \frac{1}{\overline{\rho}}\frac{\partial p'}{\partial x} = 0 \tag{5.10}$$

$$\overline{u}\frac{\partial w'}{\partial x} + \frac{1}{\overline{\rho}}\frac{\partial p'}{\partial z} - \frac{\theta'}{\overline{\theta}}g = 0 \tag{5.11}$$

$$\frac{\partial u'}{\partial x} + \frac{\partial w'}{\partial z} = 0 \tag{5.12}$$

$$\overline{u}\frac{\partial \theta'}{\partial x} + w'\frac{\partial \overline{\theta}}{\partial z} = 0 \tag{5.13}$$

Combining these equations is now done in detail since in the literature the result is always assumed. Differentiate equation 5.10 with respect to z and subtract equation 5.11 differentiated with respect to x

$$\overline{u}\frac{\partial^2 u'}{\partial z \partial x} + \frac{\partial \overline{u}}{\partial z}\frac{\partial u'}{\partial x} + \frac{\partial w'}{\partial z}\frac{\partial \overline{u}}{\partial z} + w'\frac{\partial^2 \overline{u}}{\partial z^2} - \overline{u}\frac{\partial^2 w'}{\partial x^2} + \frac{\partial}{\partial x}\left(\frac{\theta' g}{\overline{\theta}}\right) = 0 \tag{5.14}$$

Substituting from equation 5.12 this can be reduced to

$$\overline{u}\frac{\partial^2 u'}{\partial z \partial x} + w'\frac{\partial^2 \overline{u}}{\partial z^2} - \overline{u}\frac{\partial^2 w'}{\partial x^2} + \frac{\partial}{\partial x}\left(\frac{\theta' g}{\overline{\theta}}\right) = 0 \tag{5.15}$$

Differentiating equation 5.12 with respect to z and substituting into 5.15

$$\overline{u}\frac{\partial^2 w'}{\partial z^2} - w'\frac{\partial^2 \overline{u}}{\partial z^2} + \overline{u}\frac{\partial^2 w'}{\partial x^2} - \frac{g}{\overline{\theta}}\frac{\partial \theta'}{\partial x} = 0 \tag{5.16}$$

Now using the last of the four equations, 5.13, to substitute for $\frac{\partial \theta'}{\partial x}$ gives

$$\overline{u}\frac{\partial^2 w'}{\partial z^2} - w'\frac{\partial^2 \overline{u}}{\partial z^2} + \overline{u}\frac{\partial^2 w'}{\partial x^2} + \frac{gw'}{\overline{u}}\frac{\partial \ln\overline{\theta}}{\partial z} = 0 \tag{5.17}$$

which can be written as

$$\frac{\partial^2 w'}{\partial z^2} + \frac{\partial^2 w'}{\partial x^2} + l^2 w' = 0 \tag{5.18}$$

if l is the Scorer parameter defined as

$$l^2 = \frac{N^2}{\overline{u}^2} - \frac{1}{\overline{u}}\frac{\partial^2 \overline{u}}{\partial z^2} \tag{5.19}$$

and

$$N^2 = g\frac{\partial \ln\overline{\theta}}{\partial z} \tag{5.20}$$

is the square of the Brunt Väisälä frequency. From equation 5.20, N^2 is a measure of the static stability of the atmosphere. If θ increases with height then $N^2 > 0$ and the atmosphere is statically stable, while if θ decreases with height then $N^2 < 0$ and the atmosphere is statically unstable.

5.2.1 Solutions with constant N and $\overline{u}$

If the approximation is made that both N and $\overline{u}$ are constant with height then, given appropriate boundary conditions, solutions can be found to the simplified governing equation:

$$\frac{\partial^2 w'}{\partial z^2} + \frac{\partial^2 w'}{\partial x^2} + \frac{N^2}{\overline{u}^2}w' = 0 \tag{5.21}$$

Infinite Ridges

For simplicity, first consider the steady state flow over an infinite series of periodic ridges of the form

$$h(x) = h_m \cos(kx) \tag{5.22}$$

where h_m is the peak elevation of the topography. The bottom boundary condition is chosen so that the component of velocity normal to the lower boundary vanishes. This is the so-called 'free slip' boundary condition.

$$w'(x,0) = \left(\frac{Dh}{Dt}\right)_{z=0} \approx \overline{u}\frac{\partial h}{\partial x} = -\overline{u}kh_m \sin(kx) \tag{5.23}$$

The upper boundary condition is simply a radiation condition that implies that there is no component of the flow that radiates energy downwards. Using both conditions leads to solutions of 5.18 of the form

$$w'(x,z) = \begin{cases} \overline{u}kh_m e^{-\mu z}\sin(kx) & \overline{u}k > N \\ \overline{u}kh_m \sin(kx+mz) & \overline{u}k < N \end{cases} \tag{5.24}$$

where $m = ((N^2/\overline{u}^2) - k^2)^{1/2}$ is the vertical wave number and $\mu = (k^2 - (N^2/\overline{u}^2))^{1/2}$. The two possible solutions are illustrated in figure 5.1. In the first the waves decay

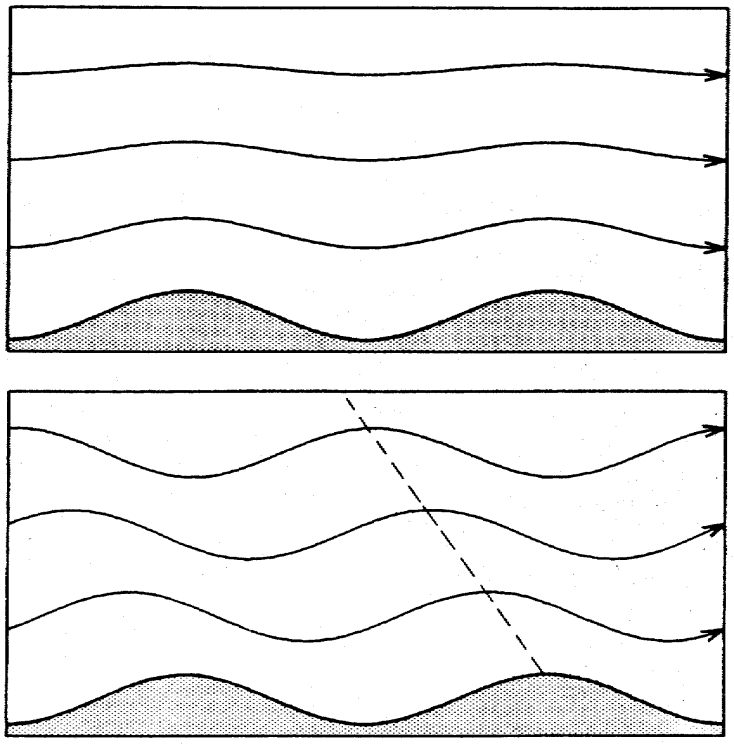

Figure 5.1: Solutions to the wave equation when the terrain is a series of infinite sinusoidal ridges. In the upper diagram the atmosphere cannot support wave propagation and the waves decay exponentially. In the lower case the waves propagate vertically away from the mountain. From *Durran* (1990).

exponentially since if the intrinsic frequency $\overline{u}k > N$ the air parcels try to oscillate faster than the maximum frequency (N) supported by the air. This corresponds to ridges that are closely spaced together or very strong winds. In the reverse case of ridges which are more widely spaced with weak winds, so that $\overline{u}k < N$, the atmosphere supports air parcel oscillations along a path slanted off the vertical at an angle $\phi = \cos^{-1}(\overline{u}k/N)$.

Isolated topography

Such an idealised sinusoidal terrain profile does not exist in reality, where isolated ridges must be considered instead. To do this it is mathematically convenient to use Fourier transforms, which allow the ridge shape to be constructed from an infinite sum of sines and cosines. The Fourier transform of the perturbation vertical velocity field, $\tilde{w}(k,z)$, is defined as

$$\tilde{w}(k,z) = \frac{1}{\pi}\int_{-\infty}^{\infty} w'(x,z)\mathrm{e}^{-ikx}dx \tag{5.25}$$

Each component of the Fourier transform of the vertical velocity must satisfy the Fourier transform of the governing equation 5.18,

$$\frac{\partial^2\tilde{w}}{\partial z^2} + \left(\frac{N^2}{\overline{u}^2} - k^2\right)\tilde{w} = 0 \tag{5.26}$$

To solve 5.26 a radiation condition is applied at the upper boundary, while the bottom boundary is again governed by the condition that the flow must follow the topography. In this formulation this requirement leads to

$$\tilde{w}(k,0) = \overline{u}(0)ik\tilde{h}(k) \tag{5.27}$$

Here $\tilde{h}(k)$ is the Fourier transform of the topography. The usual ridge shape considered is the bell shaped mountain, or 'Witch of Agnesi', defined by

$$h(x) = \frac{h_m a^2}{a^2 + x^2} \tag{5.28}$$

where h_m is the maximum ridge height and a the half width. This shape has the advantage of providing a realistic idealised ridge as well as having a simple analytic Fourier transform:

$$\tilde{h}(k) = h_m a\mathrm{e}^{-ka} \tag{5.29}$$

For this case it turns out to be more mathematically convenient to solve directly for the vertical displacement of a streamline, $\eta(x,z)$, which is related to the vertical velocity perturbation by

$$w' = \overline{u}\left(\frac{\partial\eta}{\partial x}\right) \tag{5.30}$$

Despite the choice of such a simple mountain shape the solution for 5.26 can only be found easily for the two limiting cases of $al \gg 1$ or $al \ll 1$. For a narrow mountain with strong winds and weak stability al is small and the solution is,

$$\eta(x,z) = \frac{h_m a(a+z)}{(a+z)^2 + x^2} \tag{5.31}$$

In this limit the buoyancy force is not important and no waves are generated in the flow. For a wider mountain with higher stability and weaker winds, as is characteristic for mountains in the atmosphere, buoyancy effects dominate and the flow is approximately hydrostatic. The appropriate solution is,

$$\eta(x,z) = \frac{h_m a(a\cos lz - x\sin lz)}{a^2 + x^2} \tag{5.32}$$

The flow predicted by this result is shown in figure 5.2, and is taken from the original paper of *Queney* (1948). Clearly a hydrostatic vertically propagating wave exists above

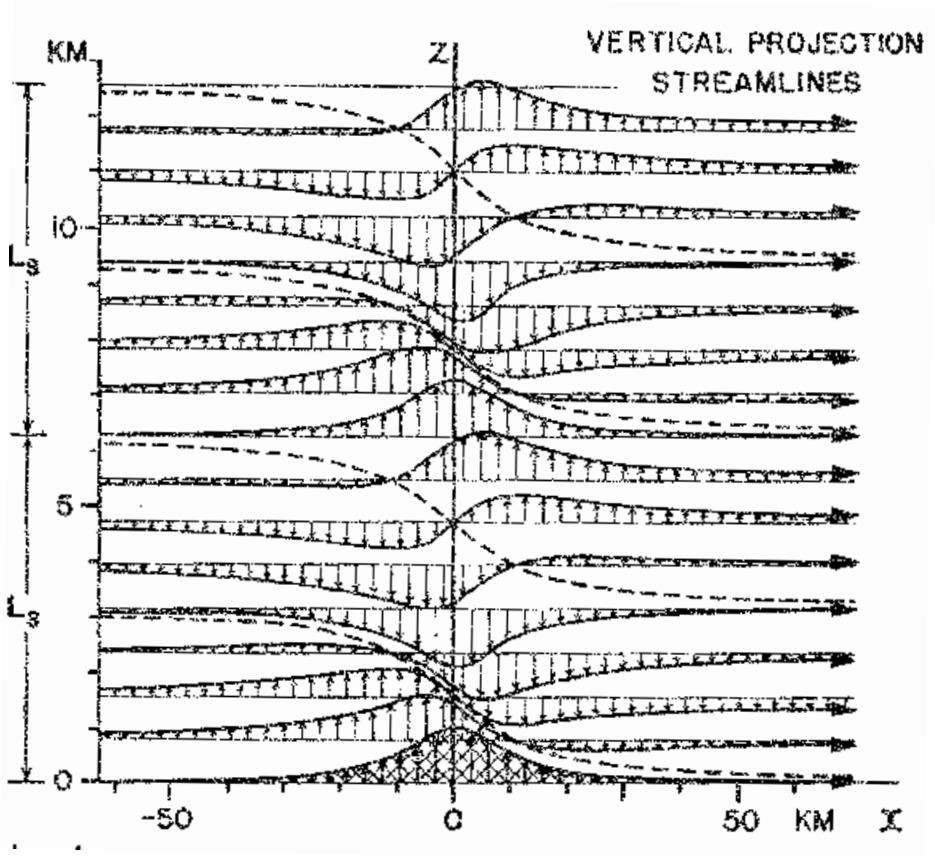

Figure 5.2: Streamlines for the flow across a wide, bell shaped mountain with constant N and $\overline{u}$ in the vertical. From *Queney* (1948).

the mountain, with no dispersion downstream. The flow is periodic such that after one vertical wavelength ($\lambda = \frac{2\pi U}{N}$) the shape of the mountain is repeated. The upward pointing arrows indicate the areas where air is ascending. If the constraint of dry air is removed then, according to *Banta* (1990), as the air is lifted and cooled the saturation point of the air may be reached, at which point cloud will start to form. Of course whether a cloud actually forms is also a function of the upstream humidity and thermodynamic state of the atmosphere.

However, as *Smith* (1979) points out, making the Boussinesq approximation at the beginning of this analysis results in the removal of important terms. The full linearised continuity equation (5.8) should be:

$$\frac{\partial u'}{\partial x} + \frac{\partial w'}{\partial z} + w' \frac{\partial \ln \overline{\rho}}{\partial z} = 0 \tag{5.33}$$

This results in three extra terms being introduced into the governing equation 5.18. Two of these can be ignored as making only a very small contribution, but the third

$$\frac{\partial \ln(\overline{\rho})}{\partial z} \frac{\partial w'}{\partial z} \tag{5.34}$$

cannot be ignored, even if it is very small, as it will always result in an amplification of the disturbance in the far field. Physically it is accounting for the growth in the amplitude of any wave disturbance due to any changes in density with height, so if we are interested in the wave at a large distance from the mountain it needs to be included. In the full derivation it is neatly accounted for by introducing a new dependent variable,

$$\hat{w} = \left(\frac{\overline{\rho}(z)}{\overline{\rho}(0)} \right)^{\frac{1}{2}} w' \tag{5.35}$$

which produces equation 5.18 in its complete form as

$$\frac{\partial^2 \hat{w}}{\partial z^2} + \frac{\partial^2 \hat{w}}{\partial x^2} + l^2 \hat{w} = 0 \tag{5.36}$$

Thus the solution 5.32 needs to undergo this transformation to be complete:

$$\eta(x,z) = \left(\frac{\overline{\rho}(z)}{\overline{\rho}(0)} \right)^{\frac{1}{2}} \frac{h_m a (a \cos lz - x \sin lz)}{a^2 + x^2} \tag{5.37}$$

For the case of $al \approx 1$ *Smith* (1979) shows, using a complicated analysis, that the solution consists of both a hydrostatic component above the mountain and dispersive, nonhydrostatic, waves in the lee.

Long (1955) has also shown that since the linear solutions derived before hold for arbitrary amplitude the equations governing the wave motion can be reformulated so that a nonlinear boundary condition can be applied. This removes the requirement for small mountains. This is known as Long's model but will not be discussed further here.

5.2.2 Solutions with non-constant N and $\overline{u}$

While the previous examples provide insight into the way waves behave, it is important to consider the possibility of variations in $\overline{u}$ and N for real atmospheric flows.

Trapped lee waves

Scorer (1949) used linear theory to show that trapped waves arise as a result of vertical variations in N and $\overline{u}$ in the atmosphere over a mountain. Such waves are illustrated in figure 5.3 and are confined to the lower troposphere on the lee side of the mountain. Scorer considered a two layer atmosphere in which l was constant but different in each of

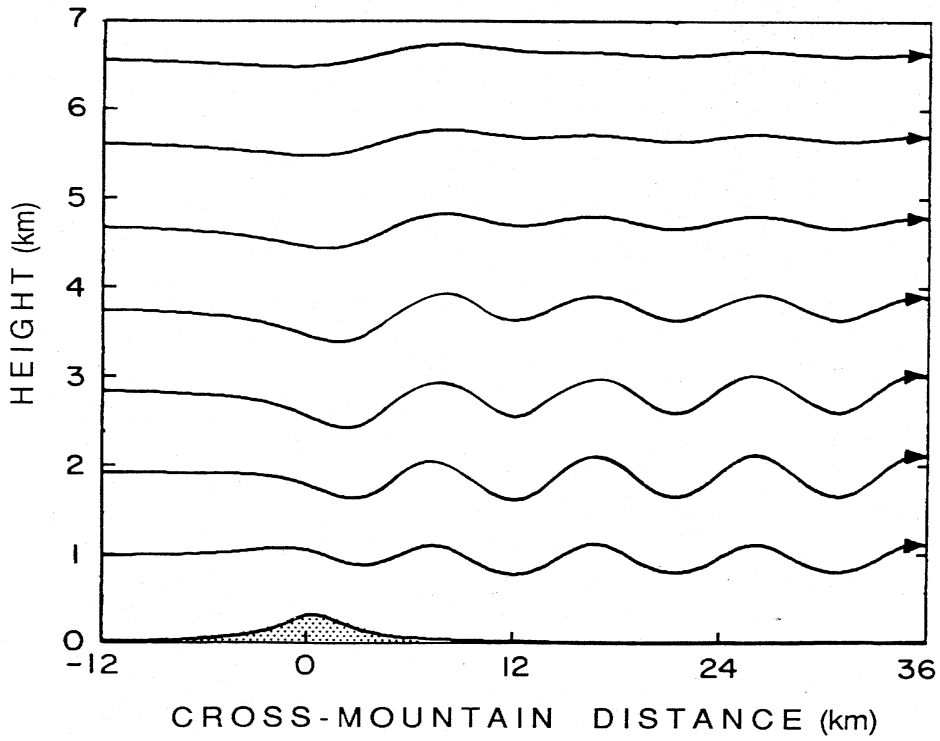

Figure 5.3: Streamlines for the flow across a mountain ridge when variations in the Scorer parameter allow trapped lee waves to occur. From *Durran* (1990).

the two layers. He then showed that the condition for the existence of trapped lee waves in such a situation is that

$$l_L - l_U > \frac{\pi^2}{4H^2} \tag{5.38}$$

where l_L and l_U are the Scorer parameters in the lower and upper layers respectively and H is the depth of the lower layer. Physically this condition is simply requiring that waves propagate in the lower layer but decay exponentially in the upper. The reason for the lack of tilt in the waves is that the wave energy is repeatedly reflected at the boundary of the two layers and the ground, thus resulting in the superposition of both upward and downward propagating waves.

The type of clouds that form in trapped lee waves are often called lenticularis due to taking the shape of a lens. There have been many observations of such clouds as they can be easily identified in satellite images because of their band like appearance. Linear theory

has been applied in a number of papers to give reasonable estimates of the horizontal wavelength, however prediction of the wave amplitude has been less successful (*Smith*, 1979). An important issue with such studies is that condensation reduces the stability of the atmosphere via the release of latent heat and according to *Banta* (1990) and *Durran* (1986b) this increases the wavelength of the mountain waves from those predicted by the above theory. In sufficient quantities it can destroy the lee waves altogether.

5.2.3 Additional effects

When $\overline{u}$ and N are complicated functions of height it becomes very difficult to solve 5.18. Numerical solutions have been derived for various atmospheric profiles by *Vergeiner* (1971) and *Sawyer* (1960) which show the coexistence of various wave types. *Sawyer* (1960) found that with the inclusion of a stable stratosphere 'leaky waves' could be found downstream at lower levels while at higher levels the vertically propagating wave dominated.

However, if l^2 varies slowly with height then it is possible to make use of the so called WKBJ approximation (alternatively called Liouville-Green after its original discoverers). This is based on the idea that if $\overline{u}$ and N vary slowly enough with height then it can be expected that locally the solution to 5.18 will behave like the solution for constant l^2. This implies that variations are slow enough for internal reflections to be absent. More detail can be found in *Gill* (1982).

A full derivation of the solution for a hydrostatic wave over a bell shaped mountain is presented in appendix B, as the derivation has not been found elsewhere in the literature. The solution derived is

$$\eta(x,z) = h_m a \left(\frac{\overline{\rho}(0)N(0)\overline{u}(0)}{\overline{\rho}(z)N(z)\overline{u}(z)}\right)^{\frac{1}{2}} \frac{a(a\cos\int_0^z l dz - x\sin\int_0^z l dz)}{a^2+x^2} \tag{5.39}$$

It can be seen immediately that the wave amplitude will be reduced in areas of high wind shear such as the tropospheric jetstream. This behaviour has been observed over the Rockies by *Smith* (1979). High stability, such as exists in the stratosphere, will also reduce amplitude growth. In the troposphere $\overline{u}$ will often vary considerably in magnitude over one vertical wavelength but it has been found that the WKBJ solution is sturdier than might be expected (see *Laprise*, 1993).

5.3 Non-linear Effects

The wave theory discussed so far suffers from three problems when applied to the real atmosphere. The assumption of linearity implies small amplitude disturbances so cannot be confidently applied to large mountains or where the winds are very weak. In these situations nonlinear effects will become important. However, small amplitude waves can

still produce impressive cloud formations (*Durran*, 1986b). Rapid changes in l^2 will also cause partial vertical reflections which are ignored. Finally if the component of the wind perpendicular to the ridge becomes zero at some height then a singularity occurs in 5.18. This is traditionally called a critical level. *Bretherton* (1969) showed that little if any of the wave can propagate through a critical level and *Klemp and Lilly* (1978) show through numerical simulations that wave reflection at critical levels can be important. Much of the research into addressing these questions has used numerical simulations. For a review of the analytical literature see *Maslowe* (1986).

Research into large amplitude mountain waves has focused on the so called 'downslope windstorm', which is observed in the lee of mountain ranges such as Boulder Colorado. Spectacular roll clouds are seen to form in these waves usually at, or slightly above, mountain height. High cloud will often also form in association with the upper part of the wave.

While far from complete theories, three possible mechanisms have been suggested by recent work to explain the development of large amplitude waves. These are:

1. The qualitative similarity of the flow to the hydraulic jump observed when immiscible fluids flow over an obstacle.

2. The reflection of waves by layers in the atmosphere leading to a resonance situation.

3. The resonant reflection of waves at a critical layer created by wave breaking.

The three theories are now explained in more detail.

5.3.1 Hydraulic jump

Long (1953) first suggested the qualitative analogy to the hydraulic jump that is observed in two or more immiscible fluids flowing over a barrier. He suggested that the mechanism creating these jumps is similar to that which creates strong downslope winds in the atmosphere. In this theory a homogeneous fluid with a free surface is allowed to flow over a ridge like obstacle. The shallow water equations then lead to the idea that the surface of the fluid can either rise or fall depending on the magnitude of the Froude number, Fr, defined as

$$Fr = \frac{u^2}{gD} \tag{5.40}$$

where u is the upstream velocity, D the depth of the fluid and g the gravitational acceleration. The three regimes for water flowing over an obstacle are shown in figure 5.4.

In the case $Fr > 1$ (supercritical) the fluid thickens and slows down as it crosses the top of the obstacle. For the case that $Fr < 1$ (subcritical) the fluid thins and accelerates

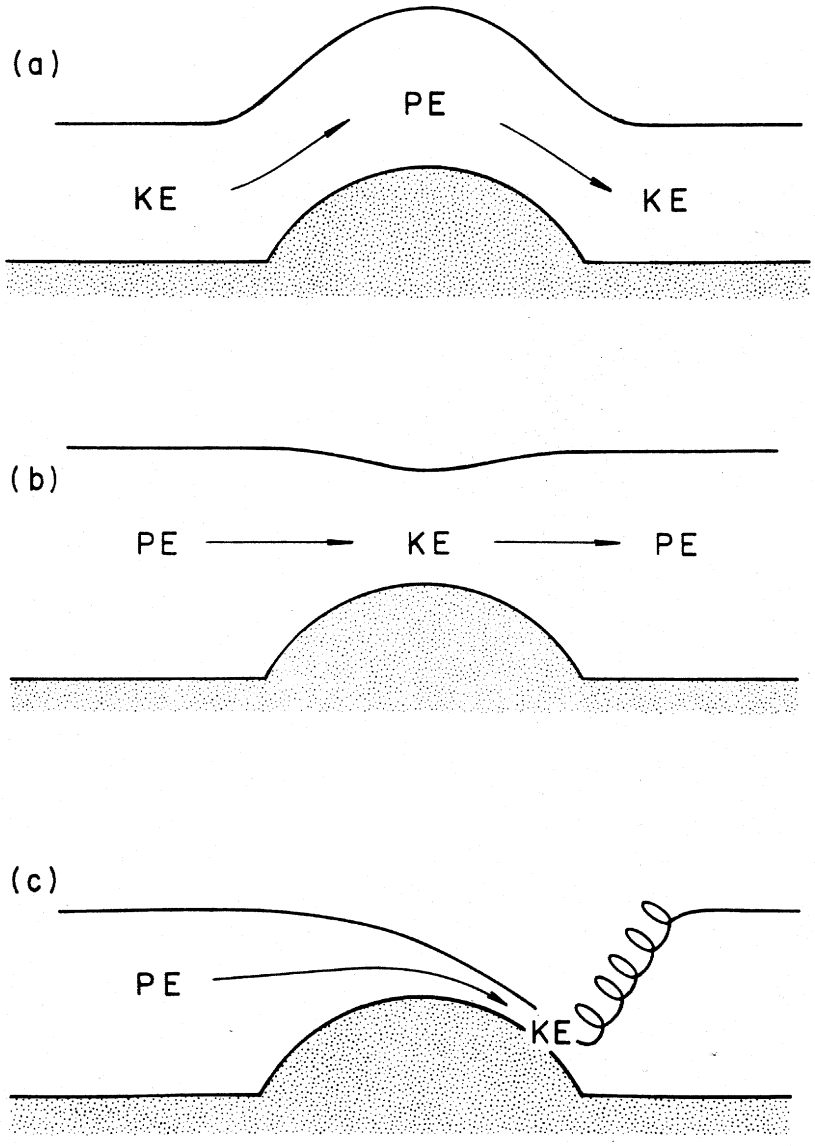

Figure 5.4: Behaviour of shallow water flowing over an obstacle: a) the flow is supercritical at all stages, b) the flow is subcritical at all stages, c) the flow is subcritical up to the peak but undergoes a change to supercritical flow down the lee slope before returning to ambient conditions in a turbulent hydraulic jump. From *Durran* (1990).

as it crosses the top, reaching a maximum speed above the mountain crest. In supercritical flow nonlinear advection dominates the pressure gradient and the forces are only balanced if the fluid accelerates in the same direction as the gravitational force, thus converting kinetic energy (KE) to potential energy (PE) as it ascends the obstacle. In subcritical flow the pressure gradient dominates and the force balance is only maintained when the fluid parcels accelerates in the opposite direction to the gravitational force. Thus as the free surface drops PE is converted to KE. In the third figure of 5.4 is the situation that

can occur if there is a sufficient increase in velocity and decrease in thickness as the fluid ascends towards the crest. In this case a transition to supercritical flow can occur which results in the fluid continuing to accelerate as it flows down the mountain. It eventually recovers to the ambient downstream conditions in a turbulent hydraulic jump.

The problem with applying these ideas to the atmosphere is that there is no free surface (or rigid lid as in some formulations). In the atmosphere gravity waves can propagate energy away from the mountain to great heights.

5.3.2 Reflection of upward propagating waves

The observation that waves could be reflected by changes in the atmosphere suggested a second theory due to *Klemp and Lilly* (1975), who examined the behaviour of linear waves in a multi layer atmosphere with constant stability and wind shear in each layer. They used the work of *Eliason and Palm* (1960), who showed that when a propagating gravity wave encounters a region in which the Scorer parameter changes rapidly then some of its energy may be reflected back into a downward propagating wave. Klemp and Lilly suggested that downslope wind storms occur when the atmosphere is tuned so that partial reflections at a number of layers occur to cause the superposition of upward and downward propagating waves.

5.3.3 Self-induced critical layer

The third explanation for downslope winds is that of Peltier and Clark (*Peltier and Clark* (1983), *Peltier and Clark*, 1979). They used comprehensive numerical simulations to show that a considerable increase in downslope wind speeds occurs when vertically propagating waves become unstable and break. This results in a high level reversal in the flow, which acts as a 'self-induced critical layer'. They proposed that this critical layer could reflect vertically propagating waves and, like Klemp and Lilly's theory, if the cavity between the mountain and the critical level was suitably tuned then a resonant wave would form that would amplify linearly in time.

5.3.4 Smith's theory

Smith (1985) also incorporated hydraulic theory to develop a theory in which a divided streamline (at height H_0) creates a turbulent and well mixed layer of depth δ_c i.e. the existence of a wave breaking region is assumed. This simple model for a strong downslope wind results in a solution under the dividing streamline that is identical to that of Long's equation for flow beneath a stagnant well mixed layer (see *Long*, 1955). Using both the assumption that the density is conserved along the dividing streamline and Bernoulli's theorem, Smith shows that for a given H_0 it is possible to determine a minimum mountain

height, such that a large deflection occurs in the streamlines. Smith then shows that his values for the parameters are consistent with documented cases. The dividing streamline is usually assumed to equate to a critical level and the theory relies on N and u being constant with height. Figure 5.5 is a schematic of the idealised configuration as hypothesised by Smith.

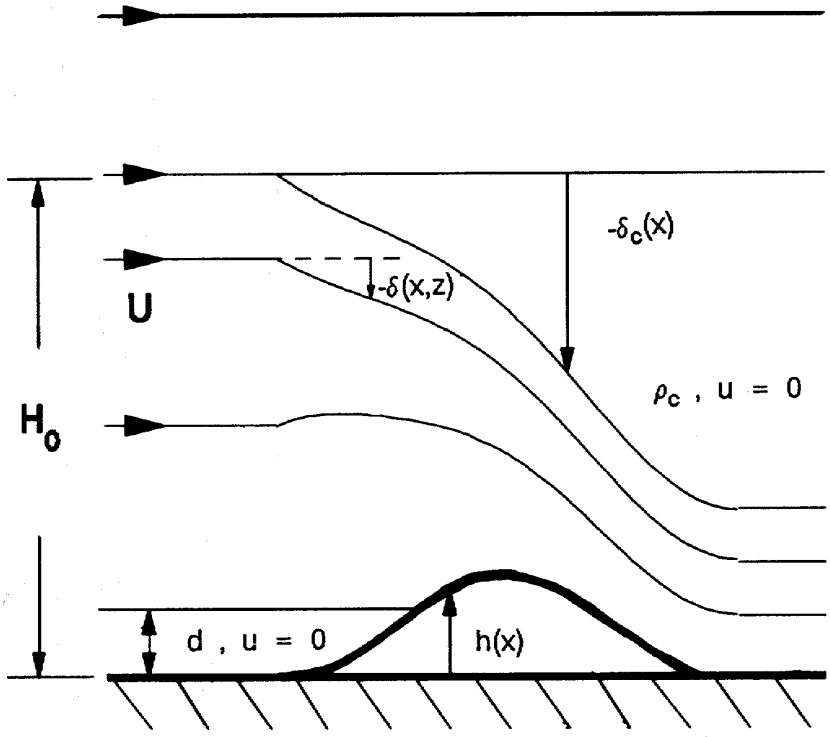

Figure 5.5: The idealised severe wind state proposed by *Smith* (1985). The upstream fluid speed u and stability N are uniform and the upstream fluid has a blocked layer of depth d.

The theory allows for an expression for the nondimensional critical streamline height,

$$\hat{H}_0 = \hat{H} - \hat{\delta}_{cm} + \arccos\left(\frac{\hat{H}}{\hat{\delta}_{cm}}\right) + n2\pi \tag{5.41}$$

where n=0,1,2,..., $\hat{H}$ is the maximum mountain height and

$$\hat{\delta}_{cm} = -\left[\frac{\hat{H}^2}{2} + \frac{\hat{H}\left(\hat{H}^2+4\right)^{\frac{1}{2}}}{2}\right]^{\frac{1}{2}} \tag{5.42}$$

A circumflex over a quantity implies that the quantity is nondimensionalized with the length scale u/N. This expression is valid for $0 < \hat{H} \leq 0.985$ but Smith suggests that

flow blocking occurs when $\hat{H} > 0.985$ resulting in a blocked layer which has a depth $\hat{d} = \hat{H} - 0.985$.

A number of authors have attempted to validate this work including *Durran and Klemp* (1987) who used numerical simulations to consider the theories of Smith, and Clark and Peltier. They found that changes in the critical layer height and mountain height resulted in changes in the simulations that were in good agreement with Smith's theory but not Clark and Peltier whose simulations they found to be valid in only a narrow range of values. They also compared Smith's theory to shallow water theory and showed that an analogous Froude number could be used to describe the transition to different flow states.

Rottman and Smith (1989) compared Smith's theory with a number of numerical simulations, as well as experiments which used tanks containing linearly stratified fluids. They determined that for certain values of the Froude number and ridge shapes a well mixed region of fluid formed above the ridge and was usually observed to occur in conjunction with strong downslope flow on the lee sides of the ridges. Unfortunately their tank simulations are designed to study the wave breaking regions and their streamlines do not indicate the low level dynamic processes. Their wave breaking region was also far from the theoretical one considered by Smith as it was found to be highly disturbed by lee waves and always occurred downstream of the ridge.

Unfortunately while both the theories of Smith and Clark and Peltier highlight the importance of a critical level, their theories provide little insight into the downstream flow behaviour, or help in forecasting such events.

Chapter 6

The Unified Model

This chapter provides an introduction to the climate version of the Unified Model (UM). It would be impossible and unnecessary to discuss all of the complicated physics that make up the many aspects of the model. Instead the focus will be on those parts that have some relevance to the development of a parameterisation of orographic cloud for incorporation into the UM. These include the physics routines for cloud, precipitation, radiation and gravity waves.

6.1 Description

The UM derives its name from its ability to be run at a variety of different temporal and spatial scales. It can be used for high resolution mesoscale modelling and weather forecasting, as well as for low resolution climate studies. Even within the climate version there are a number of possible configurations. These include an atmosphere-only model, a coupled atmosphere-ocean model, or a configuration with an atmosphere model and a simplified ocean known as a 'slab ocean'. The model version used in this thesis is known as HadAM3 and consists of an atmosphere only model with prescribed sea surface temperatures.

The Unified Model simulates the atmosphere by numerically solving the set of primitive equations which govern atmospheric dynamics. There are six equations for six variables: the three wind components (u,v,w), potential temperature (θ), specific humidity (q) and geopotential(Φ). The equations are the usual three momentum conservation equations, the continuity equation, an energy equation and an equation of state. Coriolis terms due to the rotation of the Earth are also included. For all large scale flows the hydrostatic approximation is made. i.e. there are no vertical accelerations. The exact form of the equations is discussed in *Cullen et al.* (1993).

The equations are modified to conform to a spherical coordinate system and discretized on a regular latitude longitude grid. For HadAM3 the resolution of this horizontal grid is 2.5° in latitude and 3.75° in longitude. This results in a grid which is 96 points by 73 points.

The UM uses a pressure based hybrid coordinate in the vertical. The coordinate system is purely terrain following at the surface and purely pressure in the top few layers.

This means that model levels flatten out away from the surface. In the standard HadAM3 configuration there are 19 levels in the vertical, which are chosen so as to give increased resolution in the lower atmosphere and less resolution higher up (see figure 6.1).

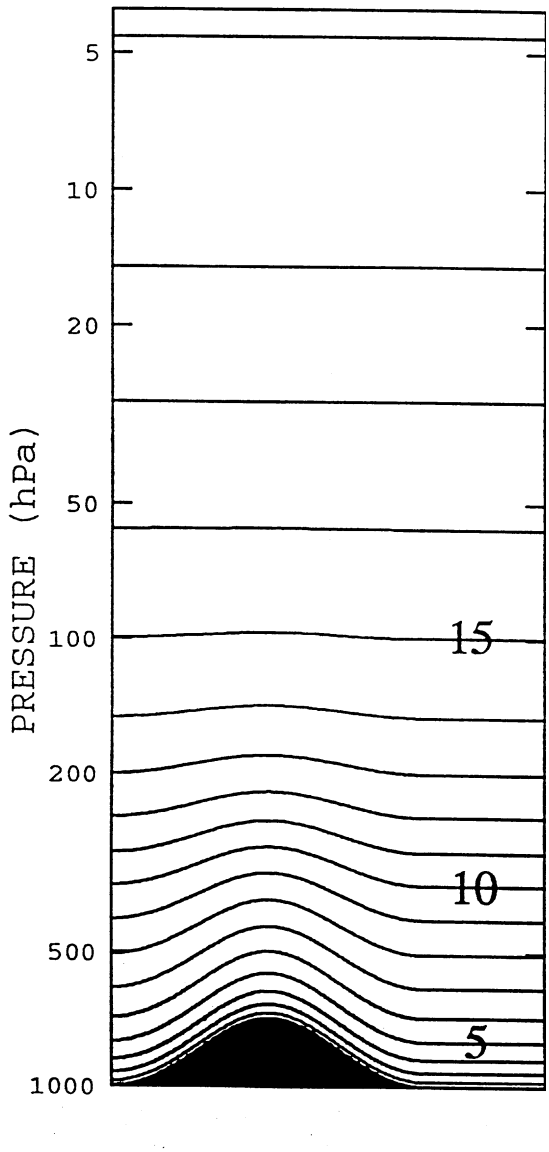

Figure 6.1: Standard 19 level model showing how the levels might look over a ridge.

The vertical coordinate is given the label η, which is defined in terms of the pressure at a given level, p, and the surface pressure, p_*, by $\eta = \frac{p}{p_*}$. Thus at the surface, where p is always equal to p_*, $\eta = 1$. For a given surface pressure the pressure at each of the model levels can be calculated using the equation

$$p_k = A_k + B_k p_* \tag{6.1}$$

where k is an integer index that represents the different levels and A_k and B_k are predetermined constants for each level. These are carefully chosen using a standard atmosphere with a standard surface pressure to give suitable seperation between model levels.

When the UM is run at standard climate resolution the grid points can be about 300 km apart. There are a number of processes in the real atmosphere that operate on scales that are much smaller than this and these processes must be parameterised. This assumes that the gross effects of these processes on resolved scales can be predicted using a modelling scheme which uses the large-scale fields in the model (*U.K. Met Office*, 1998). The routines in the UM which represent such subgrid-scale physical parameterisations are:

- Cloud Scheme
- Radiation
- Boundary Layer
- Sulphur Cycle
- Precipitation
- Convection
- Land Surface and Vegetation
- Gravity Wave Drag

Some of these will now be discussed, the level of detail reflecting the importance to an orographic cloud parameterisation.

6.2 Parameterisation of Cloud

This section begins by discussing the general concepts behind cloud parameterisation before addressing in detail the ways in which clouds are parameterised in the UM.

Water can be undergoing many different processes in a cloud. In order to maintain the essential physics of these simultaneous processes it is convenient to group the various forms of water by their specific ratios, and to then include parameterisations of how each changes from one to the other. A reasonable number of groups might be:

q_v = water vapour
q_l = cloud liquid water
q_d = drizzle
q_r = rainwater

q_f = cloud ice
q_s = snow
q_g = graupel
q_h = hail

In a numerical model water continuity equations are used to account for the different types of particles and sizes. Ideally each category of water listed above has an equation describing any change through the action of sources and sinks, labelled S_i:

$$\frac{Dq_i}{Dt} = S_i \quad i = 1..n \tag{6.2}$$

Then the total water amount, q_t, is given by the sum of the amounts of water in the different categories:

$$q_t = \sum_{i=1}^{n} q_i \tag{6.3}$$

Two general strategies have been developed to formulate the source terms on the right hand side of equation 6.2. In *bulk* models liquid and ice are grouped into categories according to particle type only while in *explicit* models the particles are further divided according to size. This second method obviously requires considerably more computational time. More detail can be found in a variety of articles on parameterisation of changes of state in clouds, but useful are the reviews of *Houze* (1993) and *Rogers and Yau* (1989).

6.2.1 Practical implementation

Because of the small scale of clouds and the computational demands for their simulation, climate models create clouds through a variety of simplified mechanisms which attempt to capture some of the physics just described. The simplest is that of large scale saturation which may be explicitly determined through prognostic cloud water variables carried by the models, or diagnosed as occurring when the relative humidity exceeds a critical value. Originally a model grid was assumed to be either fully cloudy or fully clear. More recently, however, models have been extended to allow for empirical estimates of varying cloud fractions. Another method by which cloud can be formed is through the parameterisation of cumulus convection. Finally, boundary layer cloud can also be parameterised separately, but this is only rarely included in climate models.

Table 6.1 lists the models studied in *Weare and Mokhov* (1995) as part of the Atmospheric Model Intercomparison Project (AMIP) and shows the names of the modelling groups, their addresses, abbreviations, the horizontal and vertical resolution of the model, an indicator of the moist convection scheme used in the model, an indicator of how the convective cloud fraction is determined and an indicator of how the stratiform cloud frac-

tion is determined. This table gives an idea of the diversity of mechanisms that are used in climate models. Full details of each scheme can be found in a number of papers. For a review the reader is referred to an excellent article by *Sundqvist* (1993) on parameterisation of clouds in large scale numerical models.

Modeling group or observation set	Address	Abbreviation	Resolution[a]	Convection[b]	Convective cloud fraction[c]	Stratiform cloud fraction[d]
International Satellite Cloud Climatology Project		C2	2.5° × 2.5°			
Nimbus-7 Cloud Project		N7	4.5° × 4.5°			
Meteor		Meteor	5° × 5°			
Bureau of Meteorology Research Centre	Melbourne, Australia	BMRC	R31L9	Kuo, Tiedtke	*Q*(RH)	*Q*(RH)
Canadian Climate Centre	Victoria, Canada	CCC	T32L10	MCA	*Q*(RH)	*L*(RH)
Centre National de Recherches Météorologiques	Toulouse, France	CNRM	T42L30	Bough, Gel	*L*(precipitation)	*Q*(RH), 50% max.
Center for Ocean–Land–Atmosphere Studies	Calverton, Maryland	COLA	R40L18	Kuo, Tiedtke	*F*(precipitation)	*Q*(RH)
Commonwealth Scientific and Industrial Research Organization	Mordialloc, Australia	CSIRO	R21L9	AS, Gel	fixed	*Q*(RH), 50–70% max.
Colorado State University	Fort Collins, Colorado	CSU	4° × 5° L17	AS, MCA	100% if convection	100%, RH > threshold
Dynamical Extended Range Forecasting	Geophysical Fluid Dynamics Laboratory, Princeton, New Jersey	DERF	T42L18	MCA, Tiedtke	*L*(precipitation)	*L*(RH)
Department of Numerical Mathematics	Moscow, Russia	DNM	4° × 5°L 7	Kuo	Smag	Smag
European Centre for Medium-Range Weather Forecasting	Reading, England	ECMWF	T42L19	Tiedtke	*F*(precipitation)	*Q*(RH)
Geophysical Fluid Dynamics Laboratory	Princeton, New Jersey	GFDL	R30L14	MCA	100% if convection	100%, RH > threshold
Goddard Institute for Space Studies	New York, New York	GISS	4° × 5° L9	DGY	*F*(convection)	prognostic CW
Goddard Laboratory for Atmospheres	Greenbelt, Maryland	GLA	4° × 5° L17	AS	conical anvils	80%, RH > threshold
Goddard Space Flight Center	Greenbelt, Maryland	GSFC	4° × 5° L20	AS	*F*(AS)	100%, RH > threshold
Institute of Atmospheric Physics	Beijing, China	IAP	4° × 5° L2	AS	100% if convection	100%, RH > threshold
Japan Meteorological Agency	Tokyo, Japan	JMA	T42L21	Kuo, Tiedtke	100% if convection	*Q*(RH)
Laboratorie de Météorologie Dynamique	Paris, France	LMD	3.6° × 5.6° L11	MCA, Kuo	*F*(convection)	prognostic CW
Main Geophysical Observatory	St. Petersburg, Russia	MGO	T30L14	Kuo, MCA	*F*(precipitation)	*Q*(RH)
Max Planck Institute for Meteorology	Hamburg, Germany	MPI	T42L19	Tiedtke	prognostic CW	prognostic CW
Meteorological Research Institute	Ibaraki-ken, Japan	MRI	4° × 5° L15	AS, MCA	fixed	100%, RH > threshold
National Center for Atmospheric Research	Boulder, Colorado	NCAR	T42L18	Hack	20% < *F*(precipitation) < 80%	*f*(RH, –, precipitation)
National Meteorological Center	Camp Springs, Maryland	NMC	T40L18	Kuo	*F*(precipitation)	*Q*(RH)
Naval Research Laboratory	Monterey, California	NRL	T47L18	AS, Tiedtke	*F*(convection)	*Q*(RH)
State University of New York at Albany	Albany, New York	SUNYA	R15L12	MCA	*F*(convection)	95%, RH > threshold
State University of New York at Albany/NCAR	Albany, New York; Boulder, Colorado	SUNYANC	T31L18	KP	*F*(precipitation)	*Q*(RH)
University of California, Los Angeles	Los Angeles, California	UCLA	4° × 5° L15	AS	100% if convection	100%, RH > threshold
UK Universities Global Atmosphere Modelling Programme	Reading, England	UGAMP	T42L19	BM	*F*(precipitation)	*Q*(RH)
University of Illinois, Urbana—Champaign	Urbana, Illinois	UIUC	4° × 5° L7	AS, MCA	*F*(RH, convection)	prognostic CW
United Kingdom Meteorological Office	Bracknell, England	UKMO	2.5° × 3.75° L20	GR	*F*(precipitation)	prognostic CW
Yonsei University	Seoul, Korea	YON	4° × 5° L5	AS	*F*(convection)	*Q*(RH)

Table 6.1: Global climate models and the cloud schemes they use:
a Spherical harmonic truncations: R - rhomboidal, T - triangular, L - levels.
b Largely following the work of : Initials stand for authors but not listed here.
c Treatment of convective clouds: L(precipitation) - linear function of precipitation rate; Q(RH) - quadratic function of relative humidity; F(precipitation,convection,RH) - functions of convective precipitation, convective mass flux or relative humidity; conical anvils - amount proportional to anvil size.
d Treatment of stratiform clouds generally following: Q(RH)-quadratic function of relative humidity; L(RH)-linear function of relative humidity; prognostic CW-prognostic cloud water with empirical cloud fraction; f(RH,-,precipitation)-function of relative humidity,vertical velocity, stability and precipitation rate; xx%, RH>threshold - cloud fraction fixed at xx% if RH exceeds a threshold.
From *Weare and Mokhov* (1995).

6.2.2 The UM

The UM attempts to deal with two different types of cloud using separate routines. These are convective cloud and large scale cloud. In terms of the calculation of the cloud fraction both these routines are semi-prognostic in that, while the values are overwritten at each timestep, they are passed on to additional routines. In the radiation scheme convective and large scale clouds are also treated separately as input is taken from the two separate cloud routines (see *Ingram et al.* (1997) for details). However, the final total cloud fraction in a gridbox can be output which takes account of the presence of both types of cloud. Figure 6.2 shows the subroutines in the model configuration used in this study that have some connection with cloud, and the the order in which they are calculated.

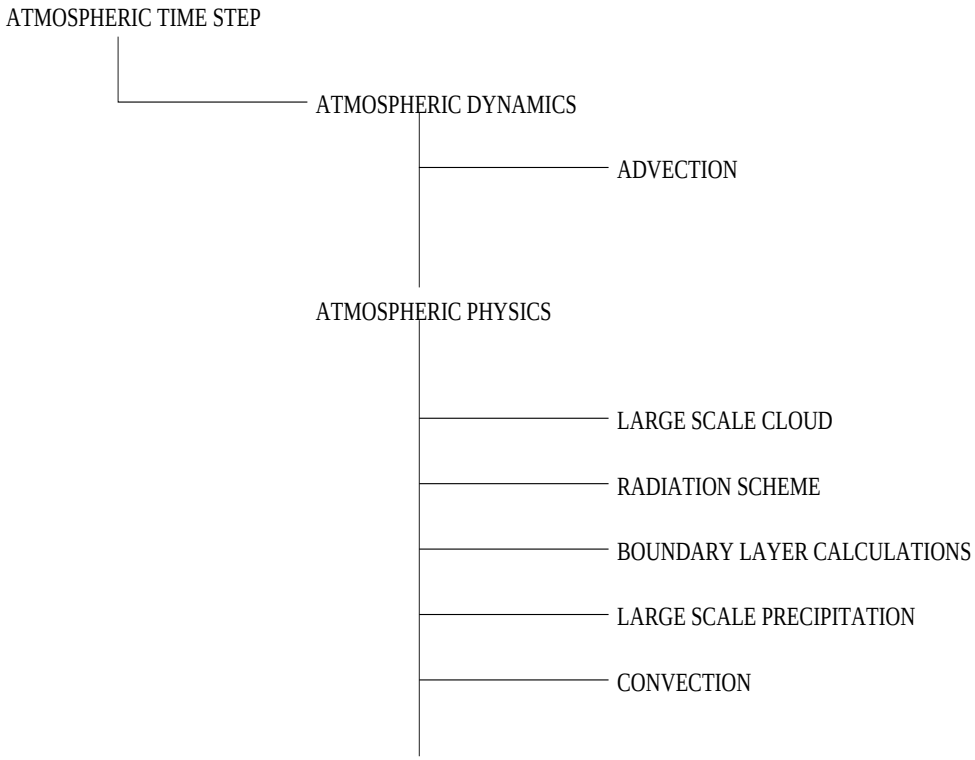

Figure 6.2: The subroutines in an atmospheric time step which are involved in the calculation of cloud, or use the output of such routines in some way. Adapted from *U.K. Met Office* (1998)

6.2.3 Large scale clouds

There are a number of different large scale cloud schemes available in the UM, each with an appropriate choice of precipitation scheme. Table 6.2 provides a summary of the possible combinations, and an explanation of their characteristics will follow. The 1A scheme is the oldest scheme and will be considered first. Modifications included in 2A and 2B will

then be discussed. As the most sophisticated of the schemes it is 2B that has been used in this thesis.

Cloud Scheme	Precipitation Scheme
1A - Original, ice diagnosed by temperature	2X - Bulk conversion scheme
2A - Prognostic ice, with ice and liquid cloud	3B - Mixed phase precipitation
2B - Like 2A but with RHcrit parameterisation	3B - Mixed phase precipitation

Table 6.2: Cloud and precipitation schemes available in the Unified Model (HadAM3). X indicates multiple possibilities.

6.2.4 The 1A cloud scheme

The scheme is only slightly modified from that proposed by *Smith* (1990) and the details of its inclusion in the UM can be found in *Smith et al.* (1997). Also *Slingo* (1998) presents an excellent review of the basics of the scheme and discusses its primary flaws.

The parameters calculated by the model are the fractional cloud cover for a grid box, C, and the total cloud water content, q_c. Technically q_c is composed of two parts; the liquid water content, $q_c^{(l)}$, and the frozen ice content, $q_c^{(f)}$, such that $q_c = q_c^{(l)} + q_c^{(f)}$. A simple function of temperature is used to partition the condensate into liquid and ice when necessary. If the temperature is warmer than 0 °C the cloud is assumed to be all water. If it is colder than -15°C then it is all ice, and between these limits it is a linear combination. Rather than calculating the cloud amount and cloud water content from the temperature and specific humidity the UM uses a thermodynamic variable and water content variable, which are conserved during changes of state of cloud water. These are the liquid/frozen water temperature T_L and the total water content q_t. The exact definitions are:

$$T_L = T - \frac{L_c}{c_p} q_c^{(l)} - \frac{L_c + L_f}{c_p} q_c^{(f)} \tag{6.4}$$

$$q_t = q + q_c^{(l)} + q_c^{(f)} = q + q_c \tag{6.5}$$

where L_c is the latent heat of condensation, L_f the latent heat of fusion and c_p the heat capacity of air at constant pressure. Clearly T_L is simply the temperature the air would have if all of the liquid and ice present were evaporated and q_t is the sum of the ice, liquid and vapour amounts.

The evolution of q_c can be described by the continuity equation

$$\frac{dq_c}{dt} = \left(\frac{dq_c}{dt}\right)_A + \left(\frac{dq_c}{dt}\right)_D + \left(\frac{dq_c}{dt}\right)_{TM} + \left(\frac{dq_c}{dt}\right)_S + \left(\frac{dq_c}{dt}\right)_P + \left(\frac{dq_c}{dt}\right)_{CV} \tag{6.6}$$

All of the possible sources and sinks of cloud water are shown on the RHS of equation

6.6, but in practice not all are actually included in the model. Here A denotes the rate of change due to advection; D, horizontal diffusion; TM, vertical turbulent mixing; S, stratiform cloud formation or dissipation; P, formation of large scale precipitation; CV, convection. In the UM cloud water content is not advected directly but instead the total water content is advected with other prognostic variables by a separate routine. The same applies to any diffusion.

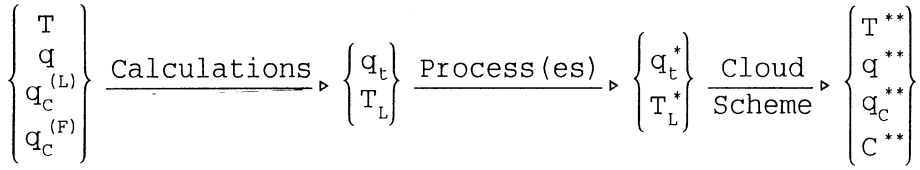

Figure 6.3: Outline of the way in which the cloud scheme is employed in the Unified Model going from the end of one timestep to the beginning of the next. The * variables indicate the situation where the conserved variables are modified by a separate routine such as advection.

Figure 6.3 shows that after the prognostic variables, T_L and q_t, are changed by the model dynamic processes the cloud subroutine is called to calculate the new cloud fraction (C), cloud water content, temperature and specific humidity. These variables are then used by other physics subroutines.

In equilibrium, the amount of cloud would be expected to depend on the difference between q_t and the saturation specific humidity q_s. However, as soon as any condensation begins, latent heat will be released, raising the temperature and decreasing the value of q_s. Thus the difference, Q_c, needs to be corrected by the inclusion of a scaling variable, a_L, which is estimated iteratively using the gradient of q_{sat} so that,

$$Q_c = a_L(q_t - q_s(T_L, p)) \tag{6.7}$$

The UM also attempts to deal with subgrid variability by assuming that the cloud conserved variables are distributed in a certain way about their means. Any suitable probability distribution function (PDF), G, must satisfy the requirements

$$\int_{-\infty}^{\infty} G(s)ds = 1 \tag{6.8}$$

$$\int_{-\infty}^{\infty} sG(s)ds = 0 \tag{6.9}$$

where s is the local deviation from the mean. The first of these constraints is simply

that the sum of all the probabilities must be 1 while the second implies that s is a deviation about zero. The UM designers pragmatically chose a distribution function which is triangular and has a standard deviation of σ_s. Thus the total width is $2b_s$ if $b_s = \sigma_s\sqrt{6}$ (figure 6.4). The mean cloud fraction is the fraction of the gridbox with cloud

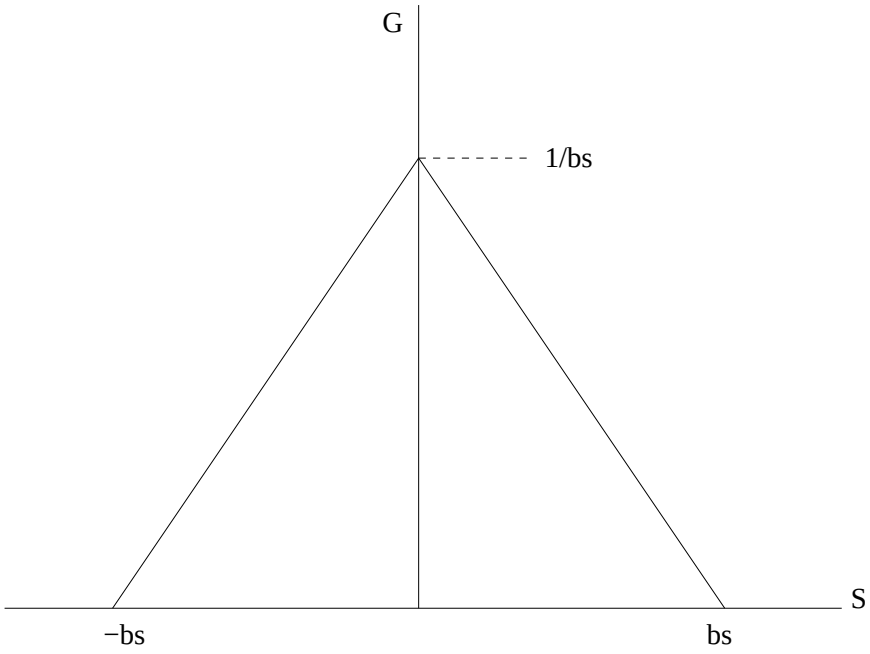

Figure 6.4: The probability distribution function used in the UM cloud schemes with standard deviation $\sigma_s = \frac{b_s}{\sqrt{6}}$.

water content greater than zero. Thus it can be found by integrating all the probabilities for the water contents greater than saturation, as given by the distribution about q_t. An example is given in figure 6.5. Note that the actual integration is performed by shifting the distribution so that it lies about zero. In terms of G the cloud fraction is

$$C = \int_{-Q_c}^{\infty} G(s)ds \tag{6.10}$$

Additionally, the mean cloud water content will be the integral of the probability of a certain amount of cloud water multiplied by that amount of cloud water for all water contents greater than saturation. Again in terms of G,

$$q_c = \int_{-Q_c}^{\infty} (Q_c + s)G(s)ds \tag{6.11}$$

Before these integrations can be done it is necessary to consider the value of b_s so that the distribution function is fully specified. The UM chooses to do this through the speci-

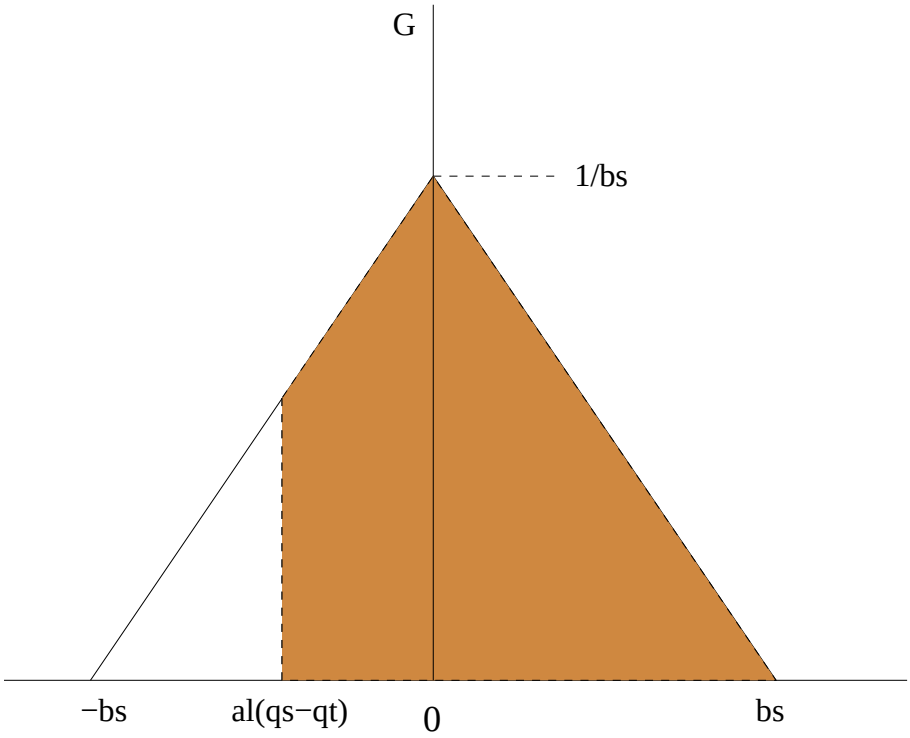

Figure 6.5: An example of how q_t is distributed about its mean value and then shifted to zero using the triangular distribution function. Integrating all the probabilities with the shifted q_t greater than $a_L(q_s - q_t)$ will give the cloud fraction.

fication of a critical relative humidity, RH_c, below which no cloud is allowed to form. To relate RH_c to b_s consider the case where clouds are just starting to form in the gridbox so that $q_t = RH_c q_s$ and thus

$$b_s = a_L(q_s - q_t) = a_L(q_s - q_s RH_c) = a_L q_s(1 - RH_c) \tag{6.12}$$

In the 1A and 2A cloud schemes RH_c is a specifiable constant for each model level and is thus open to tuning. The sensitivity of the cloud scheme to RH_c is an important issue.

The actual calculation of cloud fraction is performed in terms of a normalised distribution function, which has the advantage of eliminating a_L. For instance the grid box mean difference normalised, Q_N, is:

$$Q_N = \frac{Q_C}{b_s} = \frac{q_t - q_s}{(1 - RH_c)q_s} \tag{6.13}$$

For reference, the final equations for C and q_c are included in appendix C. It should be noted that while the cloud water content q_c is an additional prognostic variable the calculation of cloud fraction is diagnostic in the sense that it is overwritten at each time

step and not updated.

The precipitation schemes which can be used with the 1A cloud scheme are 2B, 2C, 2D and 2E, all of which are variants of a simple bulk parameterisation that converts liquid and ice water contents into precipitation. The transfer of water to rain contains both a conversion rate and allows accretion, as water is swept out by falling rain. The diagnosed ice content is allowed to fall with a parameterised fall speed and will melt if it warms to zero degrees. This limited scheme does not deal with the multitude of transfer mechanisms which change the phases of water in the real atmosphere.

6.2.5 The 2A and 2B cloud schemes

The second generation of cloud schemes is based on the inclusion of a prognostic ice variable. In conjunction with the 3B mixed phase precipitation scheme this allows for the amount of ice present to be predicted. The relevant transfer equations, or cloud microphysics, are included as part of the precipitation scheme and will be described in detail in the next section (6.2.6). With regards the cloud scheme, the predominant change is to allow for the separate calculation of an ice cloud fraction, C_{frozen}, and liquid cloud fraction, C_{liquid}.

Because of the prognostic ice variable the cloud conserved variables (6.4 and 6.5) are modified to exclude ice:

$$T_L = T - \frac{L_c}{C_p} q_c^{(l)} \tag{6.14}$$

$$q_t = q + q_c^{(l)} \tag{6.15}$$

The liquid cloud fraction and liquid cloud amount are diagnosed using exactly the same PDF approach as used in the 1A scheme. An ice cloud fraction can then be diagnosed directly from the cloud ice amount, $q_c^{(f)}$. For consistency the ice cloud fraction is found from the same equation as the liquid cloud (equation C.1). However the value of Q_N is found by inverting the equation used to find q_c (equation C.2), where q_c is now just $q_c^{(f)}$. The inverted equation can be found in appendix C.

This procedure is not independent of b_s, which has a modified definition given by

$$b_s = (1 - RH_c) q_s^{\text{ice}} \tag{6.16}$$

where q_s^{ice} is the saturation specific humidity over ice. The absence of a_l results from the fact that there is no change of state occurring and hence no latent heat release. Calculating cloud fraction in this manner for ice means that, for a given mean ice amount, the ice cloud fraction predicted is highly sensitive to the saturation point over ice and hence the temperature. The lower the saturation point the more cloud will be diagnosed. This is a consequence of trying to be consistent with the way in which liquid cloud is diagnosed.

The inversion process to find Q_N effectively assumes that it is some sort of 'q_t' which is distributed about its mean and that all the values over ice saturation give the mean ice amount. This means that if q_c^f increases then it is inferred that Q_N increases while if q_s decreases then again Q_N increases. This is fine for liquid cloud, but is perhaps less rigorous for ice which may not be in equilibrium and whose changes are explicitly resolved through transfer equations. It might make more sense to assume that the ice itself is distributed in some way about the gridbox mean q_c^f and then diagnose a cloud fraction.

To combine the liquid and frozen cloud fractions the UM uses a simple overlap assumption:

$$C_{\text{total}} = \min\left(C_{\text{frozen}} + C_{\text{liquid}}, 1\right) \tag{6.17}$$

The 2B version of the scheme is the same as the 2A scheme except that RH_c is no longer a specified constant but is instead parameterised in terms of large scale cloud inhomogeneity. The underlying principal is that there is a relationship between the subgrid variability and the resolved variability over a surrounding 3x3 grid. In this case,

$$RH_c = 1 - \frac{\sqrt{6}A(p)\sigma_{3\times3}^2}{a_L q_s} \tag{6.18}$$

where $A(p)$ is a function of pressure only and $\sigma_{3\times3}^2$ is the variability across the surrounding nine gridboxes. A fuller explanation can be found in *Cusack et al.* (1999).

6.2.6 Mixed phase precipitation and ice scheme (3B)

The original mixed phase precipitation scheme in the model (2B) simply diagnoses the amount of ice and liquid water at each timestep by using a temperature function. In the alternative scheme, 3B, liquid water is still diagnosed by the cloud scheme but ice is considered a prognostic variable. Including a prognostic ice variable in the Unified Model allows not only for the calculation of an ice cloud fraction, as described in section 2.1, but also for the introduction of ice microphysics which describe how ice is transferred from one state to another. Thus the amount of ice (QCF) in a grid box can be predicted by growing and decaying it from and to liquid (QCL), vapour (Q) and rain (RAIN). The transfer processes and the order in which they are calculated, as outlined in *Wilson* (1999) and *Wilson and Ballard* (1999), follow. Where the process is important to an orographic cloud parameterisation a little more explanation is given.

Fall of ice into and out of a layer (QCF→QCF)

The fall out of ice is calculated using a mass weighted fall velocity V_t. The proportion of ice that falls through the bottom of a layer is given by $\delta QCF = V_t QCF \delta t/\delta z$ where δt is a model timestep. The falling ice is stored as the flux SNOW. Each

layer considers ice falling in, ice falling out, and the special case where the ice has sufficient velocity to fall through an entire layer.

Homogeneous nucleation of ice from liquid (QCL→QCF)

The homogeneous mechanism simply freezes all liquid water if the temperature is less than -40.0 °C.

Heterogeneous nucleation of ice from liquid or vapour (QCL→QCF,Q→QCF)

Heterogeneous nucleation will act to seed each grid box with a number of ice nuclei assuming certain conditions are met. These are:

1. The liquid cloud fraction must be greater than 0.001 or that QCF > 0. This is simply the requirement for the microphysics scheme to be called by the model.

2. Q > $RH_{crit}Q_{satice}$. This means that the specific humidity must be greater than the saturated specific humidity over ice reduced by the subgrid variability coefficient. If this is not true then ice is decreasing through evaporation.

3. -10°C > T > -40°C. This restricts the temperature range for heterogeneous nucleation.

4. Q > $RH_{crit}Q_{satliquid}$ g(T) where g(T) is the minimum of 1 and (188.92+2.81 T/°C +0.013336 $(T/°C)^2$-10)/100. *Wilson* (1999) simply describes this as an empirical condition for cirrus formation. Upon investigation the equation for g(T) is found to originate from *Heymsfield and Miloshevich* (1995) and describes the maximum relative humidity observed in orographic cirrus clouds in strong updrafts. Its value is mostly greater than 1 and in this case the condition as a whole reverts to the requirement that the specific humidity is greater than the saturated specific humidity for liquid reduced by the subgrid variability coefficient. This matches the common observation that cirrus in the upper atmosphere often forms after liquid saturation has been reached. For temperatures less than -33°C, g(t) is less than 1 and so the constraint is weakened somewhat. This is possibly compensating for the fact that homogeneous nucleation has begun to occur at these temperatures.

If all these constraints are satisfied then the number density of nuclei produced per timestep is the minimum of 0.01exp(-0.06 T/°C) and 10^5 m^{-3}. Each nuclei is then assigned a small mass of 10^{-12} kg. The temperature function is accounting for the fact that the number of aerosols able to act as ice nuclei rapidly increases as the

temperature is decreased. The transfer of mass to ice occurs preferentially from liquid, or if there is no liquid then from the vapour.

Deposition of ice from liquid and vapour (QCL→QCF,Q→QCF)

The rate of deposition is a function of temperature and pressure as well as being proportional to the percentage supersaturation. However the mean supersaturation defined as

$$s = \frac{Q + QCL - Q_{satice}}{Q_{satice}} \tag{6.19}$$

is replaced in the final equation by

$$s = \frac{Q + QCL - Q_{satice}(RH_{crit}(1 - cf_{ice}) + cf_{ice})}{Q_{satice}} \tag{6.20}$$

where the cf_{ice} is the ice cloud fraction. The effect of the extra parameters is to increase the supersaturation and hence the deposition as the ice cloud fraction decreases. This is supposed to account for subgrid influences.

In a simple form the deposition (and evaporation) can be summed up as

$$\delta QCF = \min\left(\frac{dQCF}{dt}\delta t,\ \text{available moisture}\right) \tag{6.21}$$

Evaporation of ice to vapour (QCF→Q)

This is governed by the same equation as the deposition and occurs if the air is subsaturated.

Riming (QCL→QCF)

This term only accounts for the growth of falling ice as it collides with stationary liquid water. It freezes the amount of water contained in a cylinder of area equal to the cross sectional area of the falling particle. The collection efficiency is assumed to be equal to 1.

Capture of raindrops by ice particles (RAIN→QCF)

Capture uses similar ideas to the riming equations, but in this case the liquid available is RAIN not QCL. Both the ice and RAIN are allowed to be falling. This term is generally found to be very small.

Evaporation of melting ice (QCF→Q)

Melting of ice to rain (QCF→RAIN)

Evaporation of rain (RAIN→Q)

Accretion of water droplets by rain (QCL→RAIN)

Autoconversion of liquid to rain (QCL→RAIN)

Another advantage of a prognostic ice variable is that it can also be advected directly around the model domain rather than just as part of the total water. This should allow for the formation of trailing ice clouds in the lee of mountain ranges, as ice created in the uplift over the orography, can be advected into subsequent grid boxes by the model winds. In the UM the prognostic ice variable is advected using the tracer advection scheme, not the scheme used for the other prognostic variables.

6.2.7 Convective cloud

The UM convection scheme attempts to deal with the transport of heat moisture and momentum associated with convection in cumulus clouds. The component of the convection scheme that this review is concerned with is that which calculates the amount of cloud associated with any convective activity. The scheme uses a 'single cloud' model, based around parcel theory which is modified by entrainment and detrainment, to represent an ensemble of convective clouds with different heights and characteristics. Basically each layer of the model is tested until one is found that has buoyancy above a specified value. Then the convection process is started and the parcel is lifted, entraining environmental air and detraining cloudy air until it is no longer buoyant. The routine then calculates an associated convective cloud amount through a 'bulk' model and also the amount of resulting precipitation. Full details of the scheme can be found in *Gregory and Inness* (1996).

6.2.8 Radiation scheme

For meteorological purposes radiation can be broken into two parts, shortwave (sunlight) and longwave (re-emitted heat). The version of the UM radiation code used in this thesis (3A-radiation) treats both the longwave and shortwave using two stream equations. Full details can be found in *Edwards and Slingo* (1996) as well as *Ingram et al.* (1997). The scheme requires some cloud quantities as inputs, which include the height of a cloud's base and top, the fractional cloud cover for a grid box and the condensed water path (cwp). The only cloud quantity amongst these not discussed already is the condensed water path. For large scale layer cloud this is obtained from the cloud water content q_c and is calculated in the radiation scheme by

$$\text{cwp} = \rho q_c \Delta z \tag{6.22}$$

where ρ is the density of air and Δz is the thickness. For convective cloud this quantity is already calculated in a different way by the convection scheme.

The shortwave calculations also require the effective radius of each cloud's drop size distribution. In the configuration used in this thesis water droplets have a prescribed effective radius of 7 μm and ice particles have an effective radius of 30 μm. With ice microphysics included the phase of the water is already known.

The two cloud schemes, discussed earlier, allow for a single convective tower and a number of layer clouds in the vertical. A cloud is assumed to occupy a whole layer, or a number of layers, with its top and base at layer boundaries. Only one layer cloud can exist in any one layer, but the convective cloud may extend through layers containing layer cloud.

In large scale models which allow fractional cloud cover the assumption is usually made that layer clouds in different model layers overlap randomly. The UM can use this idea but also has the alternative option, for the longwave scheme, that clouds overlap maximally when they are in adjacent layers and randomly if there is a cloud free layer between them.

Clouds are assumed to emit at the temperatures of the layer boundaries where their base and top are i.e. they radiate only at their edges. These temperatures are linearly interpolated from the centre of a layer.

6.3 Orography in the Unified Model

The representation of orography in a global model plays a role in terms of cloud formation through its strong effect on the general dynamics, since the orography is the bottom boundary of the model. As such, this section will discuss the incorporation of orography in the UM.

6.3.1 Input orographic parameters

In a model with a terrain following coordinate there must be information about the height of the lower boundary for each grid. The simplest approach is to use a much higher resolution terrain dataset from which the mean altitude of each grid box is calculated. This gives a 'step like' lower surface. In order to reduce the effects of large discontinuities in height between adjacent grid boxes some form of smoothing algorithm can then be applied which distributes the heights more smoothly over a number of grid boxes.

The standard climate resolution in the UM is a 2.5° (latitude) x 3.75° (longitude) grid. However, the orographic heights come originally from the US Navy global 10' (1/6°) resolution dataset. Since there can be only one height value per model gridbox, the UM chooses to use a mean of the height values on the US Navy 10' dataset. The only additional

filtering occurs east-west polewards of 60° (*Webster, pers com*) with a 1-2-1 filter applied to the gridbox means. This has the effect of smoothing the heights that the model sees in an attempt to remove structure at the grid scale, which can cause contamination through noise.

The model then assigns arbitrarily the condition that at least half the points, on the 10' dataset, for a model grid box must be land before the gridbox is identified as a land point. Otherwise the gridbox height is set to zero and assigned as a sea point. This condition can have a large effect on the number of land points and their heights for islands such as New Zealand, but will have little effect on large continents. Figure 6.6 shows the entire model domain with each shaded gridbox representing a land point. It can be seen that New Zealand is represented by only three gridboxes.

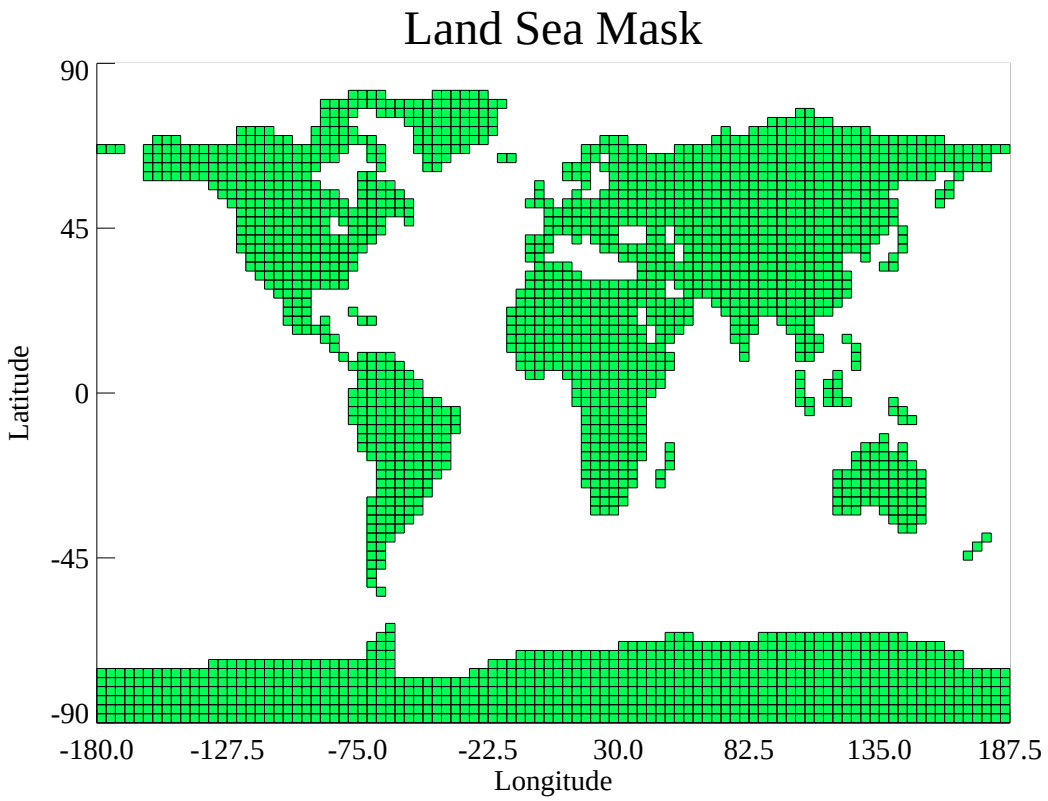

Figure 6.6: The model land/sea mask showing the model domain and the land points therein.

Geopotential is defined as $\Phi(z) = \int_0^z g\, dz$ and thus at sea level is equal to zero. However over land the geopotential will not be zero and this is how the orographic heights enter into the equations; by affecting the value of the geopotential in the bottom layer of the model. The geopotential appears in the two horizontal momentum equations which then directly affect the dynamics of the model. This can affect the surface pressure, p_*, which is a function of both the geopotential and the amount of air in the column above. While at

each timestep the surface geopotential is constant, there may be convergence or divergence of the air above.

6.3.2 Envelope orography

The UM has the non-standard option of incorporating an envelope orography method in global simulations. The following details the ideas behind this option but full coverage of the theory is given by *Wallace et al.* (1983), while *Slingo and Pearson* (1987) discuss its utilisation in UM simulations.

Not surprisingly the simple mean height of a grid box approach just described considerably smooths the true profile of the Earth's surface. Studies have shown that such a filtering results in a considerable deficiency in terms of the ability of high mountain ranges in the subgrid scale to block the large scale atmospheric flow. It was thus suggested that these effects might be parameterised in models by making these blocked valleys and basins of decoupled air, part of the the lower boundary of the terrain itself, hence the concept of an 'envelope orography'.

This simple concept is much more difficult to implement in reality, since the amount of blocking due to a mountain range changes with the wind speed, direction, and local stability. To recalculate such an effect at each timestep would be computationally demanding. In practise these changes are not taken into account and an average contribution to the blocking is assumed. This is done through adding to the mean elevation of a gridbox a height which is equal to the standard deviation of the terrain within the gridbox multiplyed by a constant, before the smoothing process mentioned earlier is applied. The advantage of this system is that the height of the terrain can be made to match the top of the mountains while the increase in terrain height is largest for rough mountain ranges which are the worst affected in the simple scheme. For large plateaus the increment is small.

The use of an envelope orography in the UM is now non-existent as the introduction of an effective orographic gravity wave parameterisation in recent years has done a better job of representing the drag on the large scale atmospheric dynamics.

6.4 Gravity Wave Drag Parameterisation in the Unified Model

Gravity waves that propagate vertically in the atmosphere can transfer wave momentum to the background flow. Instabilities in the wave, due to changes in the background atmosphere can cause energy to be dissipated through turbulence. Also if the wave reaches a critical level, where the difference between the background wind, $\overline{u}$, and the phase speed of the wave, c, approaches zero then the background atmosphere can physically no longer support the wave and it will break down completely. At this point all of its remaining

momentum is deposited in the background flow. In both cases the deposited momentum must act as a drag on the background wind. This drag can also be thought of as caused by a vertical gradient in the stress, τ, due to the wave.

General circulation models are currently run at low resolutions which cannot resolve many gravity waves. As such, models which do not incorporate a parameterisation of gravity wave drag suffer from excessively strong midlatitude westerlies (*Palmer et al.*, 1986). There are also effects on the large scale circulation and temperatures.

The UM includes a gravity wave scheme that parameterises the effect of orographic gravity wave drag. The scheme is detailed in *Shutts* (1990), while *Gregory et al.* (1998) discusses the effect of the parameterisation on the model climate. The relevant UM technical documentation paper is *Webster* (1997). Only a brief overview will be given here.

The parameterisation has a few key features which will each, in turn, be elaborated upon:

1. The calculation of a surface layer which excludes blocked air.

2. A calculation of the surface stress which uses an orographic-variance-spectrum-function which accounts for anisotropy in the subgrid scale orography.

3. A treatment of low Froude number regimes, where flow blocking can occur, by use of a hydraulic jump response.

4. A linear hydrostatic scheme that calculates the wave drag at each model level due to an orographic gravity wave. It includes the facility for determining the occurrence of trapped lee waves which predicts their wavelength and amplitude profile.

Surface Layer and Flow Blocking

One of the key aspects of the air's interaction with orography is in determining the amount of flow blocking that can occur. Flow blocking results from the fact that stratified flows tend to flow around rather than over steep terrain slopes. Air may become trapped in a valley or separate near peaks. The overall effect is to reduce the height of the orography that contributes to gravity wave generation.

In the UM these effects are considered through use of a Froude number:

$$Fr = \frac{U}{N\sigma^{\frac{1}{2}}} \tag{6.23}$$

where U is the horizontal wind speed, N the static stability and $\sigma^{\frac{1}{2}}$ the standard deviation of the subgrid scale orography (σ is the variance). This particular definition of a Froude

number can be compared with the definition 5.40 for a shallow water system. It can be seen that in a stratified system such as the atmosphere g/u is replaced by N to reflect the presence of both a buoyancy force and gravitational force.

In essence the UM uses the idea that flow contains blocked layers if $Fr \leq 1$. This result is simply derived from a consideration of potential and kinetic energy, but usually involves h, the mountain height, rather than σ. For $Fr \leq 1$ the air at the bottom of the mountain does not have enough kinetic energy to reach the top. In most cases the use of $\sigma^{\frac{1}{2}}$ instead of h is a reasonable approximation. However, in terms of flow blocking, the maximum heights may well be more appropriate and these are generally between $\sqrt{2}\sigma^{\frac{1}{2}}$ and $\sigma^{\frac{1}{2}}$.

The first action of the gravity wave scheme is to calculate the height of the surface layer of air that is lifted over the subgrid scale orography. The top of the layer, h_t, is related to the height of the orography through the standard deviation of the subgrid scale orography. i.e.

$$h_t = \min(\sqrt{2}\sigma^{\frac{1}{2}}, 750m) \tag{6.24}$$

The inclusion of the 750 m constraint is to ensure that the surface layer does not reach jet levels. Justification for this statement is not given in the literature. The bottom of the layer is simply defined to be the top of any blocked layer (h_b), which only occurs if the Froude number is less than 1 (more precisely for $Fr \leq 0.985$).

$$h_b = h_t - 0.985\frac{U}{N} \tag{6.25}$$

where h_b is evaluated using the wind and N for level 2 in the model. If there is no blocked layer then the bottom is specified as level 2. However the surface layer is further constrained to consist of whole levels and for the top to be no lower than level 3.

It should also be noted that for the lowest four levels in the UM the coordinate system is purely terrain following. From level 5 and above there is a mixture of terrain and pressure coordinates. Above sea points the four levels reach a height of about 869 mb. Obviously over terrain they can reach much lower pressures. Once the surface layer is known the average density, wind speed and N are calculated for the layer.

Surface Stress and Anisotropic Orography

The UM gravity wave scheme then calculates the surface stress caused by topography from the anisotropy of the subgrid scale orography and the surface layer Froude number. This anisotropy is measured by the standard deviation of the subgrid scale orography, $\sigma^{\frac{1}{2}}$ as well as σ_{xx}, σ_{xy}, σ_{yy}, which are the squared gradients of the elevation of the subgrid scale orography.

It is worth considering how these parameters are calculated. Interestingly $\sigma^{\frac{1}{2}}$ is not simply calculated using the differences between the points in a gridbox from the 10' US Navy dataset and the mean for the gridbox. Instead the mean slope is used by linearly interpolating adjacent grid box mean values back onto a 10' grid and then using the difference between these and the mean. This can have a large effect where there are steep slopes on the model grid. The squared gradients are defined as

$$\sigma_{xx} = \left(\frac{dh}{dx}\right)^2 \tag{6.26}$$

$$\sigma_{xy} = \left(\frac{dh}{dx}\right)\left(\frac{dh}{dy}\right) \tag{6.27}$$

$$\sigma_{yy} = \left(\frac{dh}{dy}\right)^2 \tag{6.28}$$

where $h(x, y)$ is the elevation of a point on the 10' dataset. To show how $\frac{dh}{dx}$ is calculated it is useful to use an illustration:

o1 o2 o o
•1 • •
o3 o4 o o
•2 • •
o5 o6 o o

In the above pattern the points o are the 10' dataset points and thus $\frac{dh}{dx}$ at point •1 is given by simple finite differencing as

$$\frac{dh}{dx} = \frac{1}{2} \times \left(\frac{(h(o2) - h(o1))}{(their\ separation)} + \frac{(h(o4) - h(o3))}{(their\ separation)}\right) \tag{6.29}$$

$\frac{dh}{dy}$ is simply the north-south rather than the east-west calculation. The orographic gradients are calculated at all • points. The final value for the model grid is then simply the mean of all the values that lie within a model grid box.

The Froude number is used to determine the type of regime that is invoked in the parameterisation. When the Froude number is greater than 2.5 the model invokes a linear hydrostatic regime. For Froude numbers less than or equal to 2.5 non-linear processes become increasingly more important and the regime is based on a hydraulic jump response. In this case the surface stress is assumed to be considerably higher than otherwise. Specifically for $1 \leq Fr \leq 2.5$ there is no flow blocking present but there is a hydraulic jump while for $Fr \leq 1$ flow blocking is assumed to accompany the jump. How this surface stress is distributed through the model is also effected by the choice of regime.

Hydraulic jump

Essentially the model diagnoses a height for the top of the hydraulic jump layer by using a version of the theory of *Smith* (1985) discussed in section 5.3.4. It then deposits 2/3 of the surface stress linearly up to this height. The remaining stress is then passed into the linear hydrostatic scheme for deposition through the rest of the atmospheric column.

The upstream height of the hydraulic jump layer, H_0 is defined as being the layer where

$$\int_{h_b}^{H_0} \frac{N(z)}{U(z)} dz > \frac{3\pi}{2} \tag{6.30}$$

is first satisfied. This is supposed to be equivalent to a height of 3/4 of the mean vertical wavelength of the waves and *Webster* (1997) cites *Rottman and Smith* (1989) as being the source of this assumption. The only information for such a result in this paper is reproduced here as figure 6.7. In this paper Rottman and Smith study the flow of a

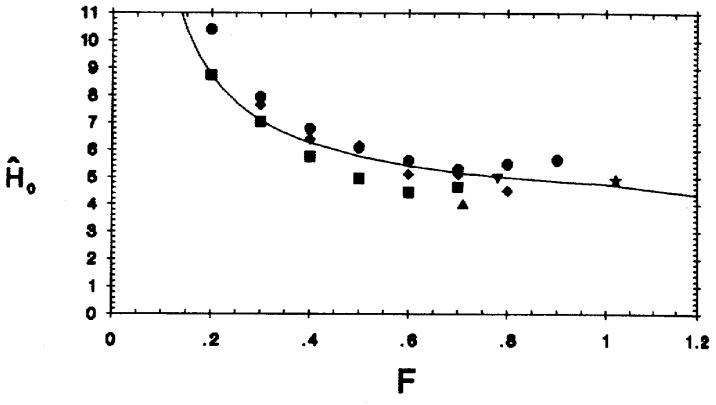

Figure 6.7: The nondimensional critical streamline height $\hat{H}_0$ is plotted against the Froude number. The experimental measurements of *Rottman and Smith* (1989) are: ■, steep ridge; ♦, intermediate ridge; •, gentle ridge. The numerical experiments are: ▼, *Peltier and Clark* (1979); ▲, *Durran* (1986a); ★, *Bachmeister and Pierrehumbert* (1988). The prediction of the theory of *Smith* (1985) is shown as the solid line. Figure from *Rottman and Smith* (1989).

stratified fluid over ridges of steep, intermediate and gentle slopes. In the figure they plot the non-dimensional height $\hat{H}_0 = (NH_0)/U$, where H_0 is the height of the wave breaking region above the base, against the Froude number, $U/(Nh)$, where h is the height of the ridge. They also plot the results of three numerical simulations and the result predicted by the theory of *Smith* (1985). Their results agreed well with the theory of Smith although they see a systematic decrease in $\hat{H}_0$ as the steepness of the ridge increases.

The vertical wavelength in a 2D vertically unbounded fluid domain is always

$$\lambda = \frac{2\pi U}{N} \tag{6.31}$$

Thus 3/4 of this would result in a height for the critical streamline of

$$H_0 = \frac{3\pi U}{2N} \tag{6.32}$$

or in terms of the non-dimensional mountain height

$$\hat{H_0} = \frac{3\pi}{2} \approx 4.71 \tag{6.33}$$

This is then obviously only an approximation since the theory of Smith predicts that $\hat{H_0}$ changes as a function of the Froude number (cf figure 6.7). The number 4.71 will be appropriate for a range in Froude numbers from 0.6 to 1.0 only. Additionally the hydraulic jump regime is activivated more regularly by the model than occurs in reality (*Stuart Webster, pers com*).

Linear hydrostatic regime

For those points with $Fr > 2.5$, and for the hydraulic jump points above the hydraulic jump height, a linear hydrostatic regime is assumed. For each model level the maximum stress, or saturation stress, that could be supported by the atmosphere is calculated. If the available stress exceeds the maximum stress then the excess is deposited in the mean flow and the saturation stress is passed upwards to the next model level.

For the case of no hydraulic jump the routine also considers the possibility of unresolved short wavelength non-hydrostatic trapped lee waves and the reflection of hydrostatic gravity waves at the tropopause increasing the stress deposition in the troposphere.

Vertically trapped lee waves depend on there being a variation in height of the Scorer parameter, as defined in equation 5.19. The atmospheric column is split in two halves of equal depth with Scorer parameters l_1 and l_2 respectively. The model then calculates H_l, the optimum height of the layer interface for trapped lee waves as well as their vertical wavenumber in the bottom layer, the inverse decay scale for trapped lee waves in the top layer, and the horizontal wavelength of the waves.

Chapter 7

Orographic Cloud Parameterisation

7.1 Introduction

This chapter will cover the theoretical development, testing and implementation of an orographic cloud parameterisation for use in climate models. As discussed in chapter 1 orographic clouds have an important role to play on both global and regional scales, particularly with regard to large cirrus clouds. At the current resolution of GCMs the waves responsible for generating these clouds, through air flowing over subgrid ridges, are not resolved and so should be parameterised. The aim of this chapter is to describe a gravity wave parameterisation which is capable of predicting wave amplitudes in the troposphere, and subsequently an inferred temperature perturbation in the air over the mountain. This temperature perturbation can then be used in the cloud parameterisation in the model to generate orographic cloud . The scheme was developed for implementation in the Unified Model described in chapter 6.

The first section will describe previous studies which have used gravity wave schemes for similar work. The important ideas behind representing the forcing of the waves by the unresolved topography will then be explored in detail: from the ideas of wave propagation to the calculation of the temperature perturbations used in the cloud scheme. The suitability of the current parameterisation of cloud microphysics in the Unified Model for the generation of orographic cirrus clouds is also considered. Finally, results from an offline testbed used in the development of the parameterisation are presented.

7.2 Previous Work

There have been previous studies which have utilised gravity wave parameterisations to calculate subgrid temperature perturbations. For example, *Carslaw et al.* (1999), considered the temperature perturbations in the lower stratosphere which can influence Polar Stratospheric Clouds (PSCs, these special clouds have a significant role in ozone depletion). Also *Butchart and Knight* (1999) used the existing gravity wave scheme in the Unified Model to calculate a temperature perturbation from the wave stress at each level. Once again the interest was in the polar stratosphere and potential areas for the formation of PSCs. The work of *Cusack et al.* (1999) notes that the subgrid PDF determined by the

RH_c parameter in the Unified Model cloud scheme attempts to compensate for unresolved gravity waves on the model clouds. *Wilson and Gregory* (2003) highlight the inadequacies of such an approach and similar ones such as that of *Xu and Randall* (1996).

Nilson et al. (2000) used a lagrangian aerosol box model to show that atmospheric waves can enhance the aerosol particle nucleation rates by up to 5 orders of magnitude due to the strong temperature fluctuations. They reccomended that this effect should be included in climate model simulations. Similarly *Karcher and Lohmann* (2002) used a box model to show that large vertical velocties have a significant influence on cirrus nucleation. They suggest that incorporation of unresolved vertical velocities from all types of waves (which are equivalent to a temperature perturbation) needs to be incorporated in GCMs for the correct nucleation of cirrus. *Lohmann et al.* (1999) incoporated the effect of unresolved vertical velocities on the nucleation rate of cloud droplets by adding a term to the resolved vertical velocity that was a function of the turbulent kinetic energy. However this approach assumes that unresolved velocities are dominated by the turbulent transports and is unable to create the geographical variations in cloud seen in observations. The orographic cloud scheme to be described next is unique in that it utilises a gravity wave scheme to explicitly calculate the temperature perturbation due to subgrid orographic gravity waves in the troposphere of a GCM and uses this to influence clouds.

7.3 New Gravity Wave Scheme

For the new gravity wave scheme it is useful to calculate an initial wave amplitude at the surface rather than a stress. In general the average valley to peak height of subgrid orography should be about $2\sigma^{\frac{1}{2}}$, where σ is the variance of all the subgrid orography about the gridbox mean height. This would be a natural first guess for the surface vertical displacement amplitude of the wave (henceforth referred to as the surface wave amplitude). However, because orography preferentially aligns as ridges, simply using this total variance would greatly underestimate or overestimate the true surface wave amplitude (depending on the surface wind direction). It is more useful to construct a variance function which describes the amount of variance in any given wind direction. This can, it turns out, be found by using a modification of the spectrum function ideas used by the UM gravity wave scheme.

As described in section 6.4, the subgrid orography is represented in the UM gravity wave scheme by a spectrum function of orographic height variance. This function is assumed to be separable in wavenumber and azimuth, with a power law dependence for the former. This spectrum function is embedded directly in the calculation of the surface drag. Essentially it modifies the surface drag by trying to estimate the variability in terrain in a grid box, for a given wind direction. The theory involved will now be explored in

some detail.

Consider an isolated mountainous region within a rectangle defined by $0 < x < X$ and $0 < y < Y$, with $h(x, y)$ the height of the orography minus the mean elevation. $h(x, y)$ is also set equal to zero at all points outside the rectangle. Then the variance of the orography is simply

$$\sigma = \int_0^Y \int_0^X \frac{(h(x,y))^2}{XY} dxdy \tag{7.1}$$

A small digression is now required. With the Fourier transform of a generic function $f(x, y)$ defined as

$$\hat{f}(k,l) = \frac{1}{4\pi^2} \int_{-\infty}^{\infty} \int_{-\infty}^{\infty} f(x,y) \mathrm{e}^{-i(kx+ly)} dxdy \tag{7.2}$$

Parceval's theorem can be derived (see *Champeney*, 1987) which relates the functions f(x,y) and g(x,y) to their Fourier transforms

$$\frac{1}{4\pi^2} \int_{-\infty}^{\infty} \int_{-\infty}^{\infty} f(x,y) g^*(x,y) dydx = \int_{-\infty}^{\infty} \int_{-\infty}^{\infty} \hat{f}(k,l) \hat{g}^*(k,l) dkdl \tag{7.3}$$

where * indicates the complex conjugate. In the special case where f(x,y)=g(x,y) this gives

$$\frac{1}{4\pi^2} \int_{-\infty}^{\infty} \int_{-\infty}^{\infty} |f(x,y)|^2 dydx = \int_{-\infty}^{\infty} \int_{-\infty}^{\infty} |\hat{f}(k,l)|^2 dkdl \tag{7.4}$$

Using this relationship 7.1 becomes

$$\sigma = \frac{4\pi^2}{XY} \int_{-\infty}^{\infty} \int_{-\infty}^{\infty} |\hat{h}(k,l)|^2 dkdl \tag{7.5}$$

This can be re-written as

$$\sigma = \int_{-\infty}^{\infty} \int_{-\infty}^{\infty} S(k,l) dkdl \tag{7.6}$$

where

$$S(k,l) = \frac{4\pi^2}{XY} |\hat{h}(k,l)|^2 \tag{7.7}$$

is the spectrum function of orographic height variance used by the Unified Model. Finally, with the idea of a directional variance in mind, it is more useful to write the spectrum function in terms of polar coordinates where $k = \kappa \cos\chi$ and $l = \kappa \sin\chi$ so that

$$\sigma = \int_{\kappa_L}^{\kappa_U} \int_0^{2\pi} \kappa S(\kappa, \chi) d\kappa d\chi \tag{7.8}$$

Here κ has been restricted to the range of wave numbers between an upper (κ_U) and a lower (κ_L) that are of relevance for the forcing of gravity waves. The values of these bounds will be considered later.

The UM assumes that the spectrum can be separated in azimuth and wavenumber *Bretherton* (1969) showed, by computing the mean of 90 one dimensional spectra for the orography in North Wales, that the wavenumber spectrum,$A_\kappa(\kappa)$, defined by

$$A_\kappa(\kappa) = \int_0^{2\pi} \kappa S(\kappa, \chi) d\chi \tag{7.9}$$

could fit a power law of the form

$$S(\kappa) = \kappa_0 \kappa^\gamma \tag{7.10}$$

where κ_0 is a constant coefficient and γ was found to have the value of -1.5. Other studies include *Young and Pielke* (1983) who measured γ as -1 for west Colorado, *Bannon and Yukas* (1990) with -1.7 in the Appalachians and *Shutts* (1995) with -1.5 for the Lake District in England. The UM chooses to use $\gamma = -1.5$ and an azimuth dependence proposed by *Shutts* (1990) to account for anisotropy. This variance spectrum is defined as

$$\kappa S(\kappa, \chi) = \left(\frac{\mu}{\kappa}\right)^{1.5} \left(a\cos^2\chi + 2b\sin\chi\cos\chi + c\sin^2\chi\right) \tag{7.11}$$

where $\mu = \kappa_0^{-1.5}$ is a constant coefficient and with $b^2 < ac$, $a > 0$ and $c > 0$ to ensure positivity. The coefficients a b and c can be rewritten in terms of the squared gradients of the topography, defined as

$$\sigma_{xx} = \frac{1}{XY} \int_0^X \int_0^Y \left(\frac{\partial h}{\partial x}\right)^2 dxdy \tag{7.12}$$

$$\sigma_{xy} = \frac{1}{XY} \int_0^X \int_0^Y \left(\frac{\partial h}{\partial x}\right)\left(\frac{\partial h}{\partial y}\right) dxdy \tag{7.13}$$

$$\sigma_{yy} = \frac{1}{XY} \int_0^X \int_0^Y \left(\frac{\partial h}{\partial y}\right)^2 dxdy \tag{7.14}$$

The practical calculation of these from a topographic dataset was discussed in section 6.3. From the definition of the Fourier transform and once again Parceval's theorem it can be shown that for σ_{xx}

$$\sigma_{xx} = \int_{\kappa_L}^{\kappa_U} \int_0^{2\pi} \kappa^3 \cos^2\chi S(\kappa, \chi) d\kappa d\chi \tag{7.15}$$

Substituting for $\kappa S(\kappa, \chi)$ and integrating leads to

$$\sigma_{xx} = \frac{\pi}{6}\mu^{1.5}\left(\kappa_U^{1.5} - \kappa_L^{1.5}\right)(3a + c) \tag{7.16}$$

Similar arguments lead to

$$\sigma_{xy} = \frac{\pi}{3}\mu^{1.5}\left(\kappa_U^{1.5} - \kappa_L^{1.5}\right) b \tag{7.17}$$

$$\sigma_{yy} = \frac{\pi}{6}\mu^{1.5}\left(\kappa_U^{1.5} - \kappa_L^{1.5}\right)(a + 3c) \tag{7.18}$$

Thus, combining 7.16 to 7.18, a b and c can be eliminated from 7.11 to give

$$\kappa S(\kappa,\chi) = \frac{3}{4\pi\kappa^{1.5}(\kappa_U^{1.5}-\kappa_L^{1.5})}\left[\left(4\cos^2\chi-1\right)\sigma_{xx}+\left(4\sin^2\chi-1\right)\sigma_{yy}+8\sigma_{xy}\sin\chi\cos\chi\right] \tag{7.19}$$

A completely new result is to recognise that this can be used in equation 7.8 to express the variance as

$$\sigma = \int_{\kappa_L}^{\kappa_U}\int_0^{2\pi}\frac{3}{4\pi\kappa^{1.5}(\kappa_U^{1.5}-\kappa_L^{1.5})}\left[\left(4\cos^2\chi-1\right)\sigma_{xx}+\left(4\sin^2\chi-1\right)\sigma_{yy}+8\sigma_{xy}\sin\chi\cos\chi\right]d\kappa d\chi \tag{7.20}$$

Upon integrating with respect to κ the variance as a function of χ is found to be

$$\sigma(\chi) = \frac{3\left(\kappa_L^{-0.5}-\kappa_U^{-0.5}\right)}{2\pi\left(\kappa_U^{1.5}-\kappa_L^{1.5}\right)}\left[\left(4\cos^2\chi-1\right)\sigma_{xx}+\left(4\sin^2\chi-1\right)\sigma_{yy}+8\sigma_{xy}\sin\chi\cos\chi\right] \tag{7.21}$$

To use this result for the forcing of the subgrid scale gravity waves the parameters κ_U and κ_L need to be chosen. *Shutts* (1990) suggests that κ_L should represent the lowest unresolved wavenumber in the numerical forecast model, while κ_U represents the highest wavenumber that is not trapped in the lower atmosphere. He suggests that this is a wavelength ≈ 25 km. Applying this to the UM, *Webster* (1997) suggests that this would mean that $\frac{2\pi}{\kappa_L} = 600$ km and that $\frac{2\pi}{\kappa_U} = 25$ km would be good choices. However, he then goes on to add that in fact these parameters are ultimately treated as tunable and are not implemented with these values. The constant coefficient part of equation 7.21 is

$$C = \frac{3\left(\kappa_L^{-0.5}-\kappa_U^{-0.5}\right)}{2\pi\left(\kappa_U^{1.5}-\kappa_L^{1.5}\right)} \tag{7.22}$$

It is necessary to consider what value C will take in the new parameterisation. Figure 7.1 shows the standard deviation, $\sigma^{\frac{1}{2}}$, for the middle New Zealand land point where

$$\begin{aligned}\sigma_{xx} &= 2.6249\times10^{-4}\\ \sigma_{xy} &= -8.2646\times10^{-5}\\ \sigma_{yy} &= 1.9320\times10^{-4}\end{aligned}$$

In this case C is calculated using the theoretical values for κ_U and κ_L suggested by *Webster* (1997).

The change in $\sigma^{\frac{1}{2}}$ with wind direction seems appropriate with maxima at 145 and 325 degrees. New Zealand's mountains are orientated roughly northeast to southwest and reassuringly the directions perpendicular to this alignment would correspond to angles of 135 and 315 degrees. The maximum deviation of 400 m at these angles would

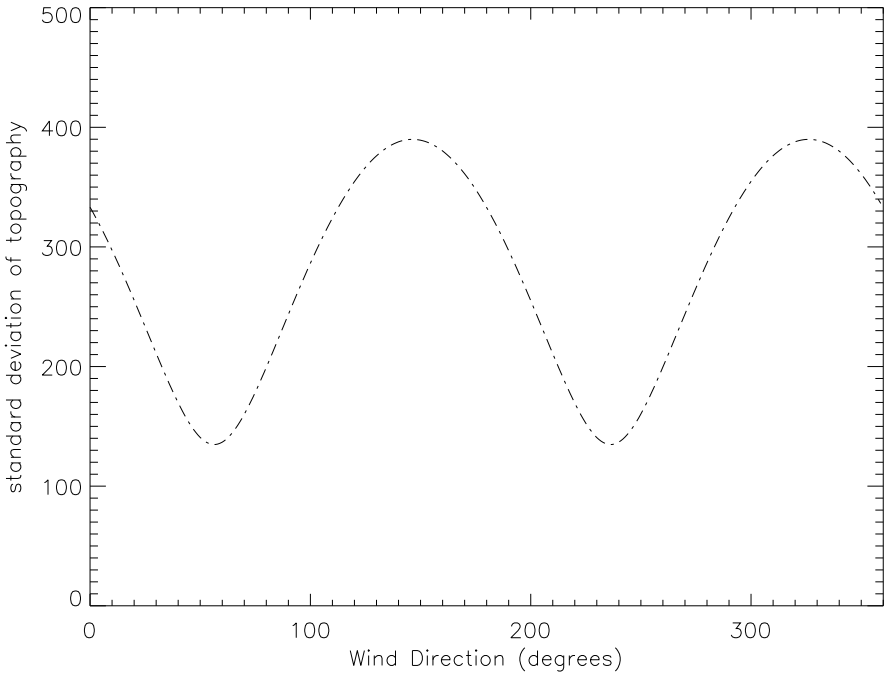

Figure 7.1: The standard deviation, $\sigma^{\frac{1}{2}}$, of a New Zealand grid point plotted as a function of direction from 0-360 degrees. Here κ_U and κ_L are given their theoretical values.

result in waves of amplitude of 800 m being launched in the parameterisation (assuming amplitude= $2\sigma^{\frac{1}{2}}$).

The mean standard deviation for this figure is 278 m. From the US Navy 10' source dataset the standard deviation for this gridbox is 518 m. This discrepancy between the predicted and calculated standard deviation is not unreasonable considering the imposition of the arbitrary wavenumber limits. It does, however, suggest that C could be scaled so that the mean standard deviation predicted matches that of the true dataset. For the new Zealand middle grid box this requires C to take the value,

$$C = 6.310 \times 10^8 \text{ m}^2 \tag{7.23}$$

Figure 7.2 is the same as figure 7.1 only with this new scaled value for C. In comparison the standard deviation now shows much bigger variation with a maximum of 720 m. This would result in waves being launched with an initial maximum amplitude of 1440 m. This value still seems reasonable for the mountains of New Zealand.

However, using one grid point only does not ensure reasonable results over the rest of the globe. Thus figure 7.3 shows the global true standard deviations as well as the average standard deviations predicted by the scaled version of equation 7.21. It apparent that

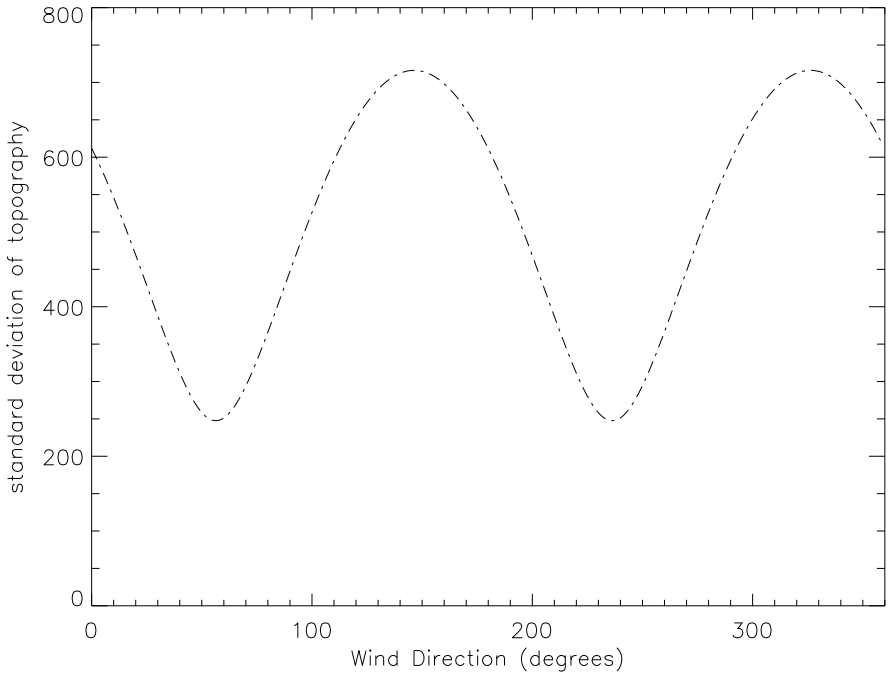

Figure 7.2: The standard deviation, $\sigma^{\frac{1}{2}}$, of a New Zealand grid point plotted as a function of direction from 0-360 degrees. Here C is given the scaled value of 6.310×10^8 m^2.

the initial scaling parameter does a good job of matching the true mean deviations over the globe. The only areas of concern would be the Himalayas and Andes which remain under-predicted.

It is still important to check that the standard deviations themselves are reasonable. As such, figure 7.4 shows the deviations predicted by a southerly wind and also those for a westerly. The scheme does a good job of predicting the north-south alignment of the Andes and the Rockies, down the west coast of the American continent. Also picked out strongly by a westerly are the Antarctic Peninsula, the Alps, and Scandinavia. Ranges that are picked up by a southerly include the Pyrenees in Spain, the Himalayas, New Guinea, and the Caucasus Mountains. The values of the deviations over the Himalayas and the Andes reach up to 1600m, which would lead to launch amplitudes of 3200 m. However, it is unlikely that waves will ever be launched of this size as further constraints implied by saturation will be accounted for.

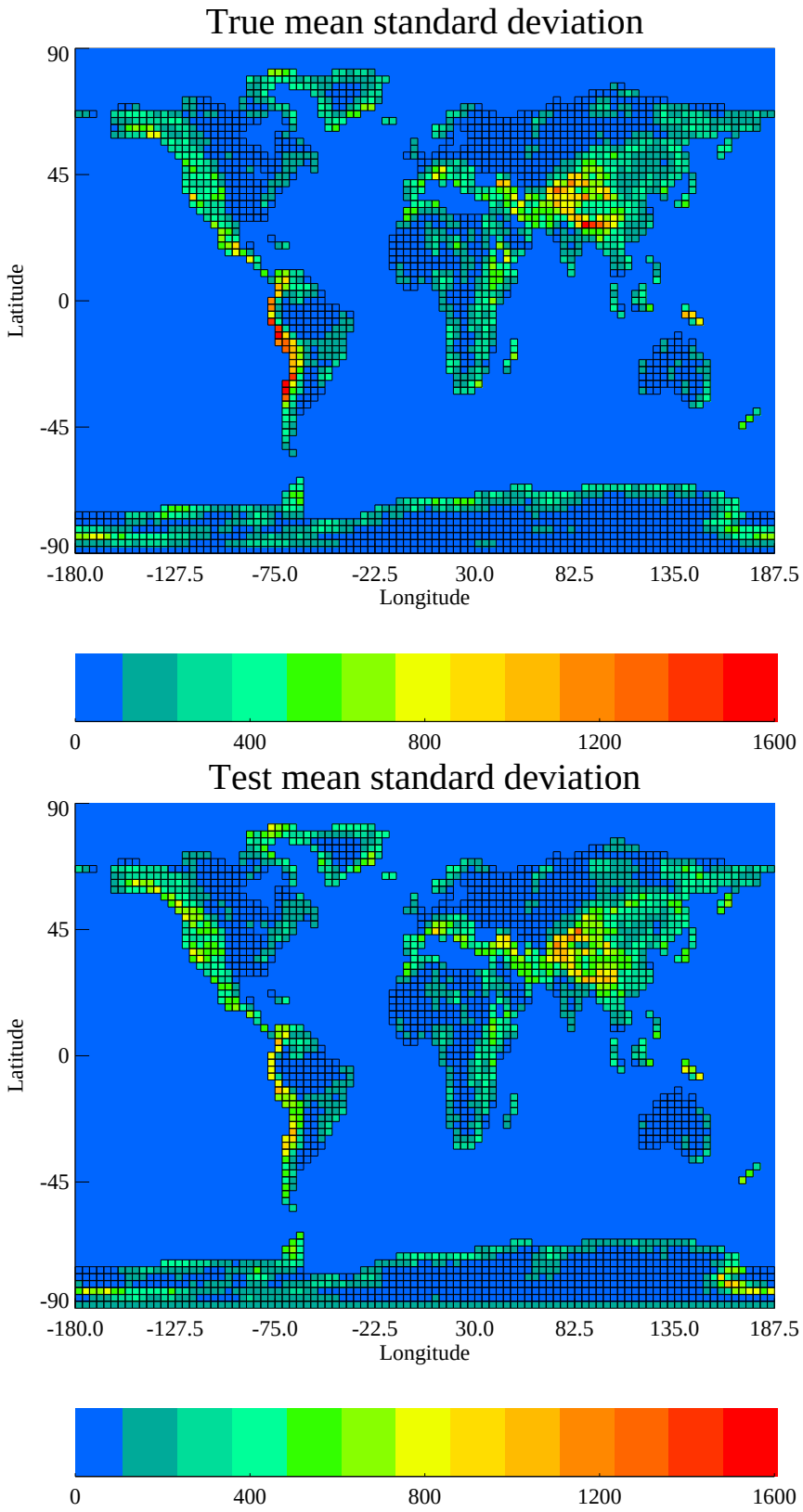

Figure 7.3: The upper figure is the true standard deviation as calculated from the UM topographic dataset. The lower figure is the average directional standard deviation calculated from σ_{xx}, σ_{xy} and σ_{yy} for each gridbox.

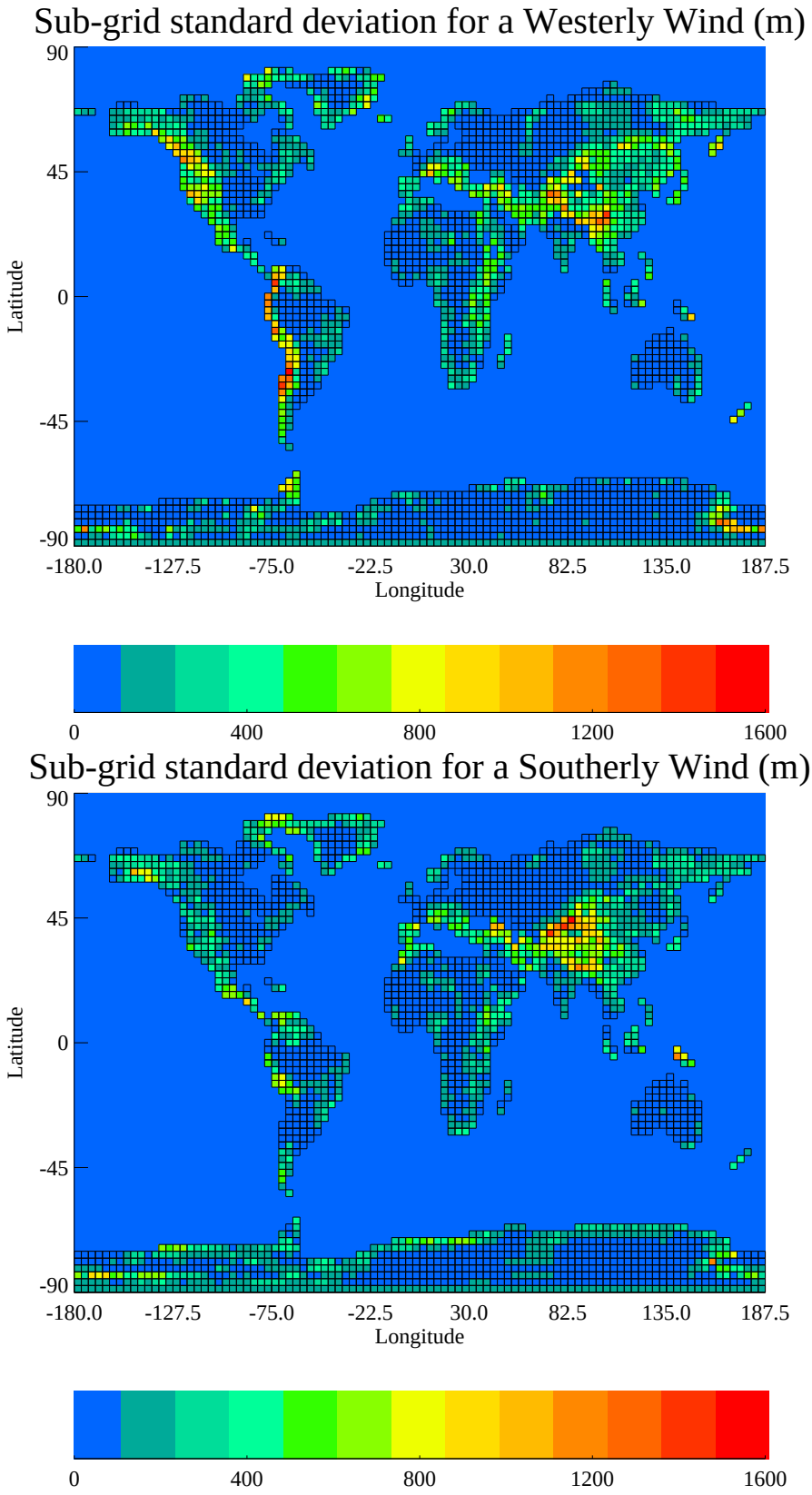

Figure 7.4: The upper figure is the average standard deviation predicted by the parameterisation for a westerly wind at every point on the globe. The lower figure is the same for a southerly wind.

7.3.1 Surface layer

To make sure that waves are being generated by the air which is actually blown over the subgrid orography the first part of the parameterisation involves defining an appropriate surface layer. Flow blocking was discussed earlier in this thesis (section 6.4) with regards to its incorporation in the existing gravity wave scheme. In that case flow blocking was allowed to occur if

$$F_r = \frac{u}{N\sigma^{\frac{1}{2}}} \leq 1 \tag{7.24}$$

The same idea will be used in this scheme but with the gridbox standard deviation from the US Navy orography replaced with the directional standard deviation calculated from 7.21. This will mean that for a given wind direction a more realistic amount of blocking will be calculated rather than always applying a 'mean' blocking. Essentially the flow blocking will account for anisotropy in the calculation of the height of the blocked layer, h_b

$$h_b = 2\sigma^{\frac{1}{2}}(\chi) - \frac{U}{N} \tag{7.25}$$

where U is the wind speed in the direction χ. In practice the model level that contains this height is taken as the bottom level of the surface layer. The top of the surface layer, h_t, is simply taken to be the level which encompasses the elevation of the subgrid orography,

$$h_t = 2\sigma^{\frac{1}{2}}(\chi) \tag{7.26}$$

A mean value for the surface wind speed U_s, direction χ_s and N_s are found by averaging across the levels defined by the surface layer. These mean values are then used in the calculation of the surface wave amplitude.

7.3.2 Vertical propagation and wave saturation

In the absence of damping, gravity waves will grow in amplitude due to the decreasing density of the atmosphere with height. Because of this growth, at some height the wave could reach amplitudes for which the wave field becomes unstable (*Lindzen*, 1981). At this point the turbulence generated would inhibit any further amplitude growth. Practically this means that the lapse rate due to the sum of the mean state and wave perturbations has become equal to the adiabatic lapse rate. The amplitude at which this process begins is called the saturation amplitude. The general Richardson number is used to describe where and when turbulence will occur and is defined as

$$Ri = \frac{N^2}{(\frac{\partial U}{\partial z})^2} \tag{7.27}$$

These ideas imply a combined negative stability, $N^2 < 0$ or that $Ri < 0$. This is usually referred to as the criterion for convective instability. However the more restrictive dynamical criterion of $Ri < 0.25$ is also sometimes used. This is based on the point at which shear instabilities will be initiated.

The local wave-modified Richardson number, Ri_m can be written in terms of the background Ri_b, U, N and wave vertical displacement amplitude, A, (*Palmer et al.*, 1986) as

$$Ri_m = \frac{Ri_b(1 - \frac{NA}{U})}{(1 + \sqrt{Ri_b}\frac{NA}{U})^2} \tag{7.28}$$

If wave breaking is said to occur for $Ri_m < 0.25$ then substituting $Ri_m = 0.25$ into equation 7.28 gives the saturation amplitude, A_s, as

$$A_s = \frac{U}{N}\left[2\left(2 + \frac{1}{\sqrt{Ri_b}}\right)^{\frac{1}{2}} - \left(2 + \frac{1}{\sqrt{Ri_b}}\right)\right] \tag{7.29}$$

For the alternative criteria that $Ri_m < 0$ then 7.28 can be used to find

$$A_s = \frac{U}{N} \tag{7.30}$$

Lindzen (1988) claims that for $0 < Ri < 0.25$ then instabilities do not necessarily set on and that if they do their growth rates are usually much smaller than for $Ri < 0$. Thus the choice of saturation mechanism employed in this scheme is for simplicity that if $A(z) \geq \frac{U(z)}{N(z)}$ then set $A(z) = \frac{U(z)}{N(z)}$ which follows *Palmer et al.* (1986). At the surface layer this also has the effect of accounting for any flow blocking on reducing the launch amplitude. This is also the condition that both *McFarlane* (1987) and *Bacmeister et al.* (1994) use in their parameterisations.

It is also necessary to account for changes in the wave amplitude due to changes in the state of the air as the wave propagates vertically. Using WKBJ theory *McFarlane* (1987) showed that the evolution of the vertical displacement amplitude of a linear wave is governed by

$$A(z) = A(0)\left(\frac{\overline{\rho}(0)N(0)U(0)}{\overline{\rho}(z)N(z)U(z)}\right)^{\frac{1}{2}} \tag{7.31}$$

This result is also apparent from the derivation of the solution for a linear wave over a bell shaped mountain derived in appendix B.

7.3.3 Wave displacement

The actual displacement generated by a wave at various heights above a mountain requires both an idea of the wave amplitude as well as the phase. For an orographic cloud

parameterisation acting in the troposphere it is useful to know where cooling and warming will occur. The approach in this parameterisation is to try to represent the average displacement across a gridbox as being generated by an ensemble of separated, bell shaped ridges.

The solution for a single bell shaped ridge with constant U and N can be seen in figure 5.2. The full solution for the vertical displacement due to the wave, $\eta(x,z)$, with slowly varying U and N as derived in appendix B is

$$\eta(x,z) = h_m a \left(\frac{\overline{\rho}(0)U(0)N(0)}{\overline{\rho}(z)U(z)N(z)}\right)^{\frac{1}{2}} \left(\frac{a\cos\left(\int_0^z l dz\right) - x\sin\left(\int_0^z l dz\right)}{a^2+x^2}\right) \tag{7.32}$$

In order to implement this solution in a parameterisation it is necessary to consider an average grid box effect. The most intuitive would thus be to use the average displacement of the streamline at any given height. In appendix B this is derived as

$$\eta_{mean}(z) = h_m a \left(\frac{\overline{\rho}(0)U(0)N(0)}{\overline{\rho}(z)U(z)N(z)}\right)^{\frac{1}{2}} \frac{\cos\left(\int_0^z l dz\right) tan\left(\frac{a}{L}\right)}{L} \tag{7.33}$$

But does this make sense in terms of the effect on any cloud formation? Consider the streamlines in figure 5.2: Some undergo only upward displacement and would potentially show only cloud formation. Others show only downward displacement and thus potential cloud evaporation. In these two cases the average displacement will give the right effect of overall potential cloud formation or destruction only if there is no hysteresis in the evaporation of cloud. This is always true for water clouds but not in the case of ice. This was highlighted in the discussion of orographic cirrus in section 3.3.

Because the upper troposphere is usually deficient in ice nuclei the air can regularly be supersaturated. If an air parcel is supersaturated with respect to ice, but undersaturated with respect to water, and during a streamline ascent it reaches water saturation, then ice will rapidly form and survive downstream of the wave. Additionally if a stream line reaches about -40°C due to displacement in a wave, then homogeneous nucleation will be initiated and ice will rapidly form which will also survive downstream of the wave. These two processes are believed to be important in the creation of very large orographic cirrus clouds and for both it is the maximum displacement of the streamline that is critically important. As such, it was decided to account for them in the parameterisation. If either condition is satisfied, using the maximum displacement as an initial test criterion, then it is the maximum displacement that is used. Otherwise the average displacement is used. The maximum displacement is derived in appendix B as,

$$\eta_{max}(z) = h_m \left(\frac{\overline{\rho}(0)U(0)N(0)}{\overline{\rho}(z)U(z)N(z)}\right)^{\frac{1}{2}} \left(\frac{\sin^2\left(\int_0^z l dz\right)}{\sin^2\left(\int_0^z l dz\right) + \left[\cos\left(\int_0^z l dz\right) - 1\right]^2}\right) \tag{7.34}$$

The inclusion of the bell shaped ridge leads to the introduction of two arbitrary parameters that describe the 'average' ridge. These are the ridge spacing, $2L$, and the characteristic half width, a. These are given the initial values of $L = 30$ km and $a = 10$ km, but are ultimately tunable. Such ridge parameters are common in gravity wave schemes which explicitly calculate amplitude (cf. α and L in *Bacmeister et al.*, 1994).

7.4 Calculation of the Temperature Perturbation

The most obvious way for the subgrid gravity wave scheme to influence the cloud in the model is by calculating the temperature change due to the wave displacement.

The definition of potential temperature, θ, comes from integrating the first law of thermodynamics and is

$$\theta = T(z)\left(\frac{p_s}{p(z)}\right)^{\frac{R}{c_p}} \tag{7.35}$$

where T is temperature, p is pressure, p_s is a reference surface pressure, R is the gas constant and c_p is the specific heat of air at constant pressure. Effectively, θ is then just the temperature a parcel of dry air would have if it was compressed or expanded adiabatically to a standard pressure p_s. The usefulness of potential temperature is that, unlike temperature, it is conserved during adiabatic ascent or descent and is also the model prognostic variable for temperature. So, if $\overline{\theta}$ is the basic state value of the potential temperature, then to first order

$$\overline{\theta}(z+\eta) \approx \overline{\theta}(z) + \frac{d\overline{\theta}(z)}{dz}\eta \tag{7.36}$$

where η is the displacement due to a gravity wave. For an adiabatic process conservation of potential temperature implies that the resulting perturbation from the background potential temperature, $\delta\theta(z+\eta)$ is

$$\delta\theta(z+\eta) = \overline{\theta}(z) - \overline{\theta}(z+\eta) \tag{7.37}$$

Using 7.36

$$\delta\theta(z+\eta) = -\eta\frac{d\overline{\theta}}{dz} \tag{7.38}$$

and 7.35 implies that the temperature perturbation at the displaced level, $\delta T(z+\eta)$, will

be

$$\delta T(z+\eta) = \delta\theta(z+\eta)\left(\frac{p_s}{p(z+\eta)}\right)^{\frac{-R}{c_p}} \tag{7.39}$$

$$= -\eta\frac{d\overline{\theta}}{dz}\left(\frac{p_s}{p(z+\eta)}\right)^{\frac{-R}{c_p}} \tag{7.40}$$

This temperature perturbation can then be passed as an input to the cloud scheme.

7.5 Modifications to the Cloud Scheme

There are no specific modifications of the cloud scheme physics. However, one important feature of the cloud scheme in the Unified Model is its role in the calculation of the temperature field used by the other physics subroutines. Since it was considered appropriate that the temperature perturbation did not cause instability in the model it was desirable that the model temperature seen by other physics subroutines remained the same. To achieve this the cloud subroutine was modified so that the temperature calculation is performed twice, one of which does not include the orographic temperature perturbation. In this way changes in temperature due to changes in state of liquid water are accounted for, but the temperature seen by the rest of the model does not include the gravity wave perturbation.

7.6 Modifications to the Microphysics Scheme

The effect of the changes to the cloud scheme result in more or less cloud being diagnosed, primarily through the change in value of the saturated specific humidity over ice and water. This results in more/less liquid being formed and carried through to other physics routines. However, the amount of ice cloud is effectively diagnosed from the ice prognostic variable so while the amount of ice cloud can change there can be no change in the amount of ice present. The subroutine which is responsible for the transfer from and to frozen water is the mixed phase precipitation and is outlined in section 6.2.6. Thus it is important that the temperature perturbation is also used in this subroutine.

While the perturbation could be applied to only the ice physics, it is useful to apply it to the the entire subroutine. This is expected to have the secondary benefit of increasing the amount of rainfall over high orography as the gravity wave scheme will produce considerable uplift adjacent to the mountains. While this will not be explored further in this thesis the parameterisation offers a way of producing more realistic precipitation over high orography compared to the more artificial precipitation thresholds currently used.

7.7 Implementation in the Unified Model

Figure 7.5 is a flow chart which describes schematically the implementation of the parameterisation in the model. The original gravity wave scheme is still included in the model to calculate the drag on atmospheric winds due to unresolved gravity waves. While the new gravity wave scheme, for calculating the temperature perturbations, could be used for this role interpreting cloud effects is initially simpler if the model is kept unchanged in all other facets.

The new gravity wave scheme is the first subroutine called by the model. This is necessary as it needs to be called before the cloud scheme. The cloud scheme is called early because of its role in the calculation of temperature from the conserved prognostic temperature, T_L, described in section 6.2.3.

The first step of the gravity wave scheme is to calculate the surface layers. It then averages the wind and stability across these layers and uses the new values to calculate the launch amplitude of the wave. The scheme then moves upwards through the rest of the model levels. The amplitude of the wave can be calculated iteratively using a modification of equation 7.31

$$A_k = A_{k-1}\left(\frac{\overline{\rho}_{k-1}N_{k-1}U_{k-1}}{\overline{\rho}_k N_k U_k}\right)^{\frac{1}{2}} \tag{7.41}$$

where k is an index for model levels. It is then necessary to check if the wave amplitude is saturated according to equation 7.30. If it is, the amplitude is constrained to remain at the saturation value. This can be summarised as:

$$A_k = \min\left[A_k, \frac{U_k}{N_k}\right] \tag{7.42}$$

Additionally if the wind component in the direction χ becomes zero at any level then the amplitude is set to zero at all levels above this. To calculate the displacement it is necessary to integrate the phase iteratively up to the current level so if

$$\phi = \int_0^z \frac{N(z)}{U(z)}dz \tag{7.43}$$

then this is approximated iteratively by using the trapezoidal rule so that

$$\phi_k = \phi_{k-1} + \frac{\Delta z}{2}\left(\frac{N_{k-1}}{U_{k-1}} + \frac{N_k}{U_k}\right) \tag{7.44}$$

where Δz is the difference in height between the layer centres. The mean and maximum

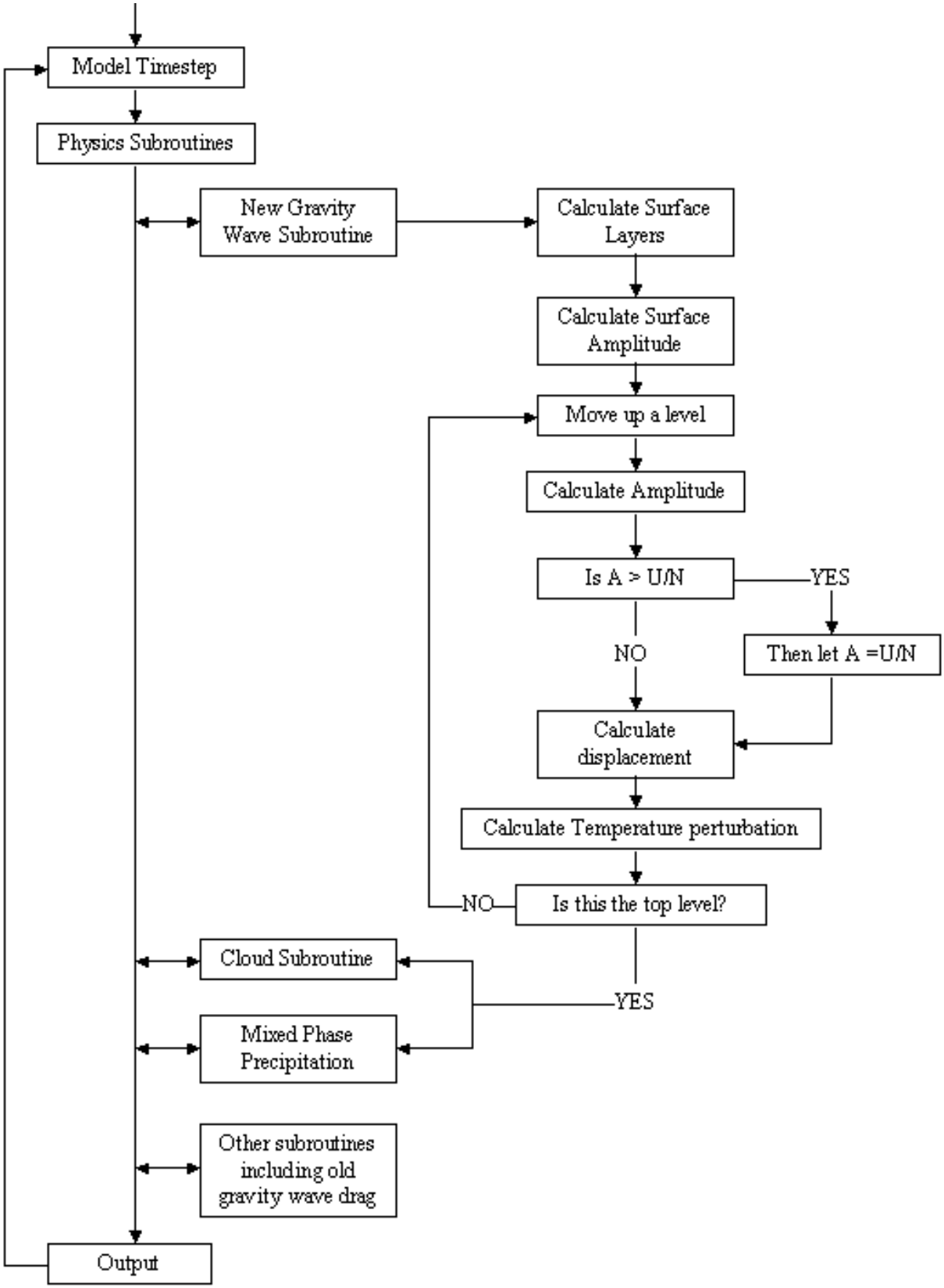

Figure 7.5: Flow chart of how the orographic cloud parameterisation is implemented in the Unified Model.

displacement for a level can then be calculated as

$$\eta_k^{mean} = A_k \frac{\cos\phi_k tan\left(\frac{a}{L}\right)}{L} \tag{7.45}$$

$$\eta_k^{max} = A_k \frac{\sin^2\phi}{\sin^2\phi + (\cos\phi - 1)^2} \tag{7.46}$$

The displacements can now be used in conjunction with the potential temperature gradient to calculate the temperature perturbation as given by equation 7.40. This is then fed into both the cloud subroutine and the mixed phase precipitation scheme. Finally the rest of the physics subroutines are called, all of which are unaffected by the temperature perturbation except for any indirect affect via cloud water and ice phase changes.

It should also be noted that in this implementation of the scheme the original gravity wave scheme is still called to calculate the stress deposition in the atmosphere. In terms of making a model as efficient as possible this is far from ideal. It would be desirable for the two gravity wave schemes to be incorporated, especially since one of the original tenants of this work was the exchange of useful information between parameterisations. Currently the original gravity wave scheme is the last physics subroutine. There is no reason why this is necessary and it would be quite possible for it to be the first called. This means that the two schemes could be incorporated to give a scheme that calculates both a stress and a temperature perturbation.

Alternatives are also suggested by the fact that wave amplitude and stress are theoretically proportional to each other. Thus a wave amplitude could be calculated directly from the stress of the existing scheme. This would be similar to the work of *Butchart and Knight* (1999). Unfortunately, information about the phase of the gravity wave would be lost, and hence whether there is a cooling or warming. The new gravity wave scheme developed also offers other advantages, primarily through the directional launch amplitude. This suggests that the stress could instead be calculated from the wave amplitude and would result in a parameterisation for stress similar to *Bacmeister et al.* (1994). This future work would be a necessary component of implementing an orographic cloud scheme for wider release in the Unified Model.

7.8 Testbed

To facilitate parameterisation development an offline testbed was used. The offline description refers to the fact that the testbed is completely separated from the Unified Model. This allows the parameterisation to be tested with idealized profiles of wind and stability as well as realistic fields output from a run of the UM. The testbed was written using the IDL package, which allows for easy graphical analysis. To study the effect of the temperature perturbation on the cloud distribution the cloud scheme in the UM was also re-written in IDL. Tests were performed to ensure that this cloud scheme gave the same result as the UM for a given atmospheric state. The complexity of the mixed phase precipitation scheme meant that this was not included in the testbed. Subsequently only single timestep simulations are meaningful, but this still reveals useful information about the gravity wave scheme. Results are presented here for tests run over the New Zealand middle gridbox.

7.8.1 Idealised profiles

Figure 7.6 shows the amplitude and average displacement of the gravity wave predicted by the parameterisation for the case of constant wind and stability; specifically $u = 20$ ms^{-1}, $v = 0$ ms^{-1} and $N = 0.01$ s^{-1}. The heights axis are shown as kilometers above the surface, specifically in this case the mean orography, which has an elevation of 476.48 m. For this wind direction at the surface the launch amplitude predicted by equation 7.6 is 1223.7 m, which is approaching the maximum value of a little over 1400 m. The maximum height that the air at the surface could reach is $u/N = 2000$ m, which means that there is no reduction in amplitude due to flow blocking.

For this case the surface layers are 2, 3 and 4 as layer 1 is always excluded. It can be seen that the amplitude of the wave remains constant through the surface layer. Above this it shows a characteristic growth due to the exponential decay of density. At the point where saturation is reached the wave amplitude becomes constrained to 2000 m until the last model level, where it is artificially fixed at zero. The displacement shows the characteristic alternation between positive and negative up to the maximum imposed by the amplitude saturation term. The theoretical vertical wavelength is $2\pi u/N = 12.566$ km and examining the plot the wavelength in the lower atmosphere complies with this exactly. It is harder to see this in the upper atmosphere as the greatly increased spacing between model levels leads to poor resolution of the wave propagation.

For comparison, figure 7.7 shows the same case but with $u = 10$ ms^{-1}. The significant difference is that the amplitude is saturated at launch and throughout the atmospheric column. The displacement shows more clearly that the theoretical wavelength for this state, $2\pi u/N = 6.283$ km, is correctly simulated.

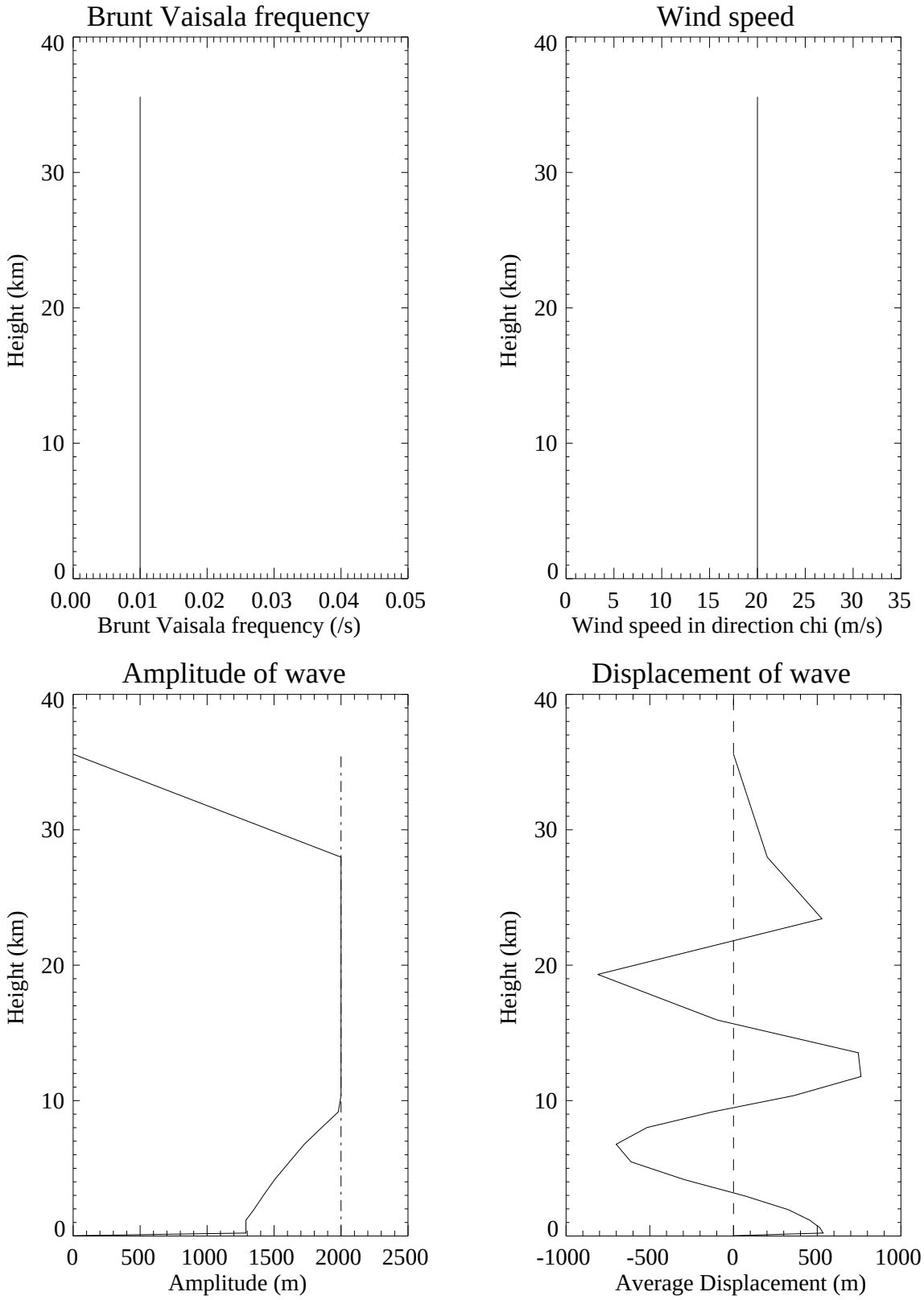

Figure 7.6: Testbed results for constant $u = 20$ ms^{-1} and $N = 0.01$ s^{-1}. The dash-dot line indicates the theoretical saturation amplitude. The heights are kilometers above the mean orography.

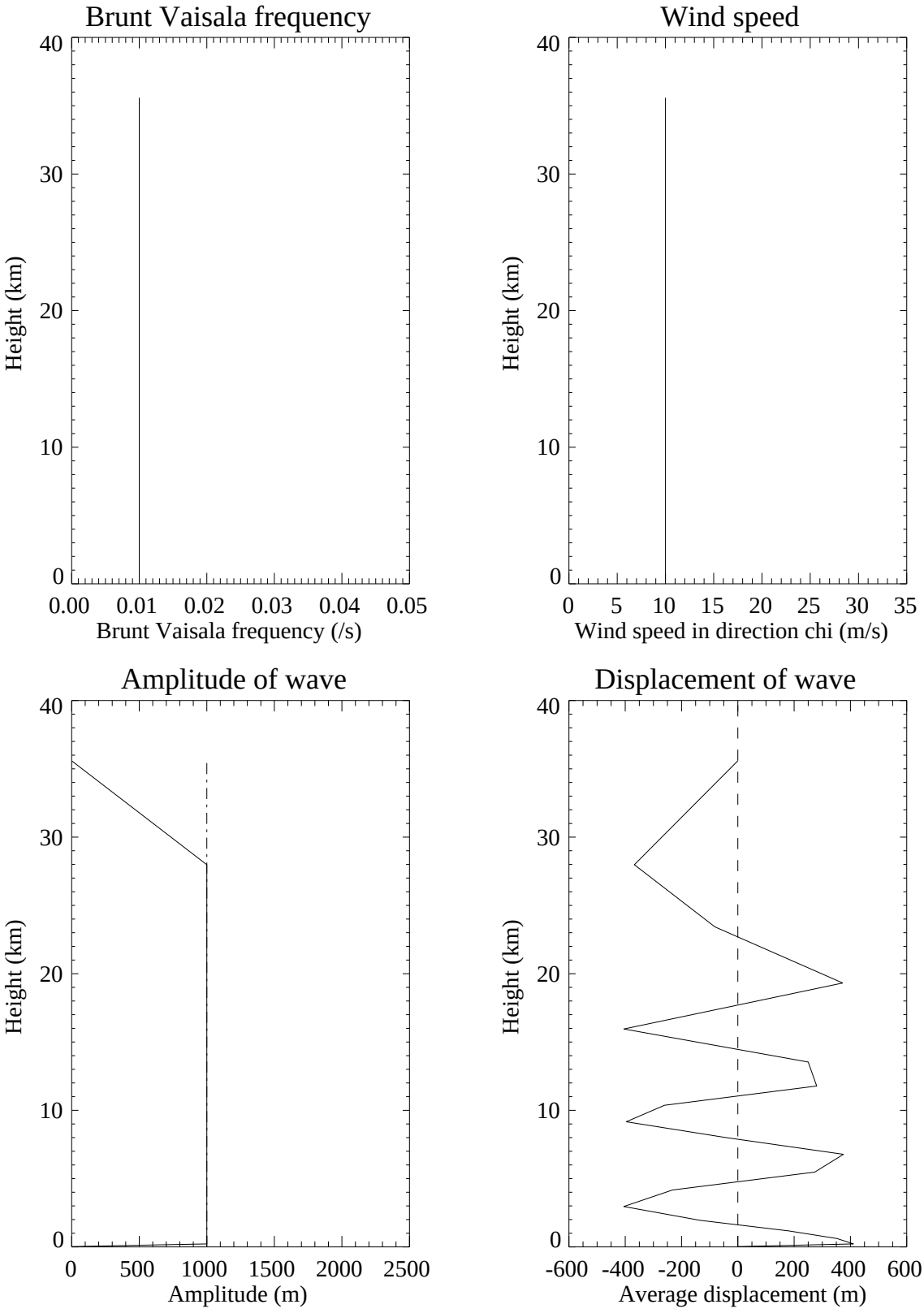

Figure 7.7: Testbed result for constant $u = 10$ ms^{-1} and $N = 0.01$ s^{-1}. The dash-dot line indicates the theoretical saturation amplitude.

7.8.2 Profile with wind shear

In order to simulate a more realistic atmosphere it is necessary to introduce vertical variations in the wind and stability. Doing this in a controlled manner, before examining real atmospheric profiles, will help in identifying how the wave amplitude is affected by the interaction with atmospheric parameters.

An appropriate two layer atmospheric model can be constructed which represents the troposphere and stratosphere as shown in this diagram:

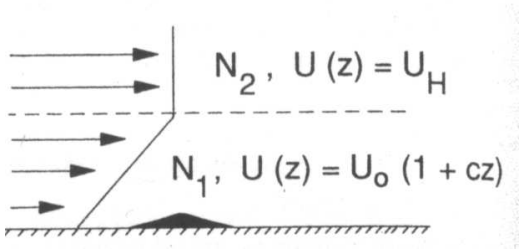

In the tropospheric lower layer the wind increases linearly with height according to $u(z) = u_0(1 + cz)$ where u_0 is the surface wind, and c is a shear parameter. In the stratosphere it has a constant value equal to the tropospheric maximum. N is constant, but different, in the two layers with a higher value in the stratosphere to represent increased stability.

Figure 7.8 shows the results for an atmosphere with a small wind shear in the troposphere (c=0.0001 m^{-1}). Interpreting the amplitude changes requires careful consideration of equation 7.41 which governs amplitude growth, as well as equation 7.42 which represents the saturation constraint. As described in the previous section the exponential decrease in density with height will cause the wave amplitude to increase with height. However, from equation 7.41 it is obvious that a positive wind shear with height will act to reduce this amplitude growth. Similarly an increase in N will also inhibit amplitude growth. It is also necessary to remember that at any given level the saturation amplitude will be greater for a stronger wind. In summary: positive wind shear acts to reduce amplitude growth but a stronger wind allows the potential for larger amplitudes!

In the troposphere of figure 7.8 the amplitude increases exponentially with height, but at a much reduced rate compare to figure 7.6, which has a constant wind. This must be caused by the wind shear because the amplitude is always well below the saturation limit (indicated by the dash-dot line). At 19 km the amplitude decreases due to the increase in N, which also decreases the saturation limit. Above this point the wave is saturated and there is no amplitude growth. In terms of the displacement, the vertical wavelength can be seen to increase upwards in the troposphere, in accordance with theory.

Figure 7.9 shows the results for a similar atmosphere with a much larger wind shear in the troposphere (c=0.0002 m^{-1}). This figure was chosen to illustrate that with sufficiently strong linear wind shear wave amplitude growth can be completely suppressed in the

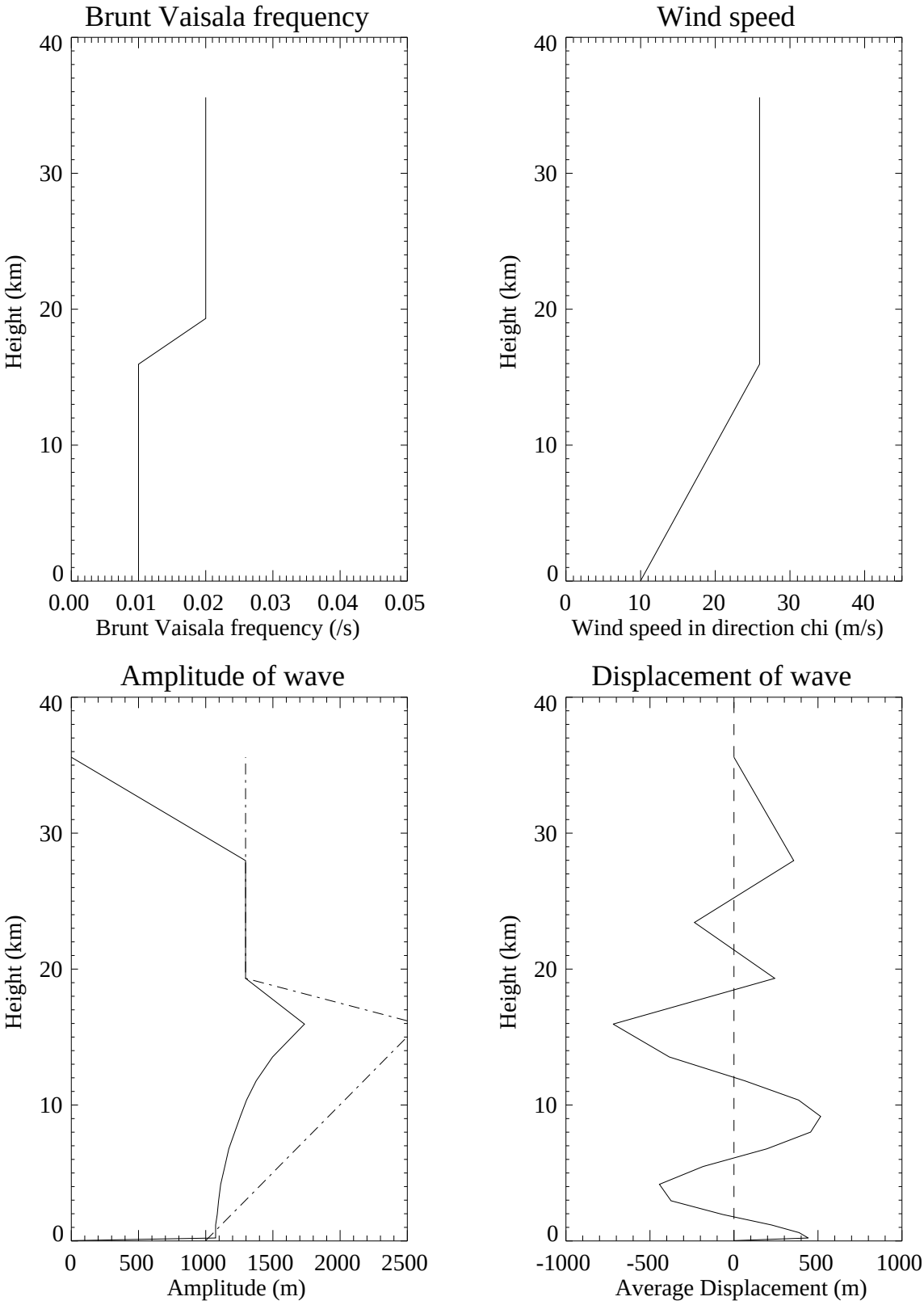

Figure 7.8: Testbed result for atmosphere with small wind shear in the troposphere ($c = 0.0001m^{-1}$) and constant u above. Stability is $N = 0.01\ s^{-1}$ in the troposphere and $N = 0.02\ s^{-1}$ in the stratosphere. The dashed-dot line indicates the theoretical saturation amplitude.

troposphere. However, because density decreases exponentially with height, the wind shear would have to increase exponentially with height to continue to suppress amplitude growth throughout the vertical domain.

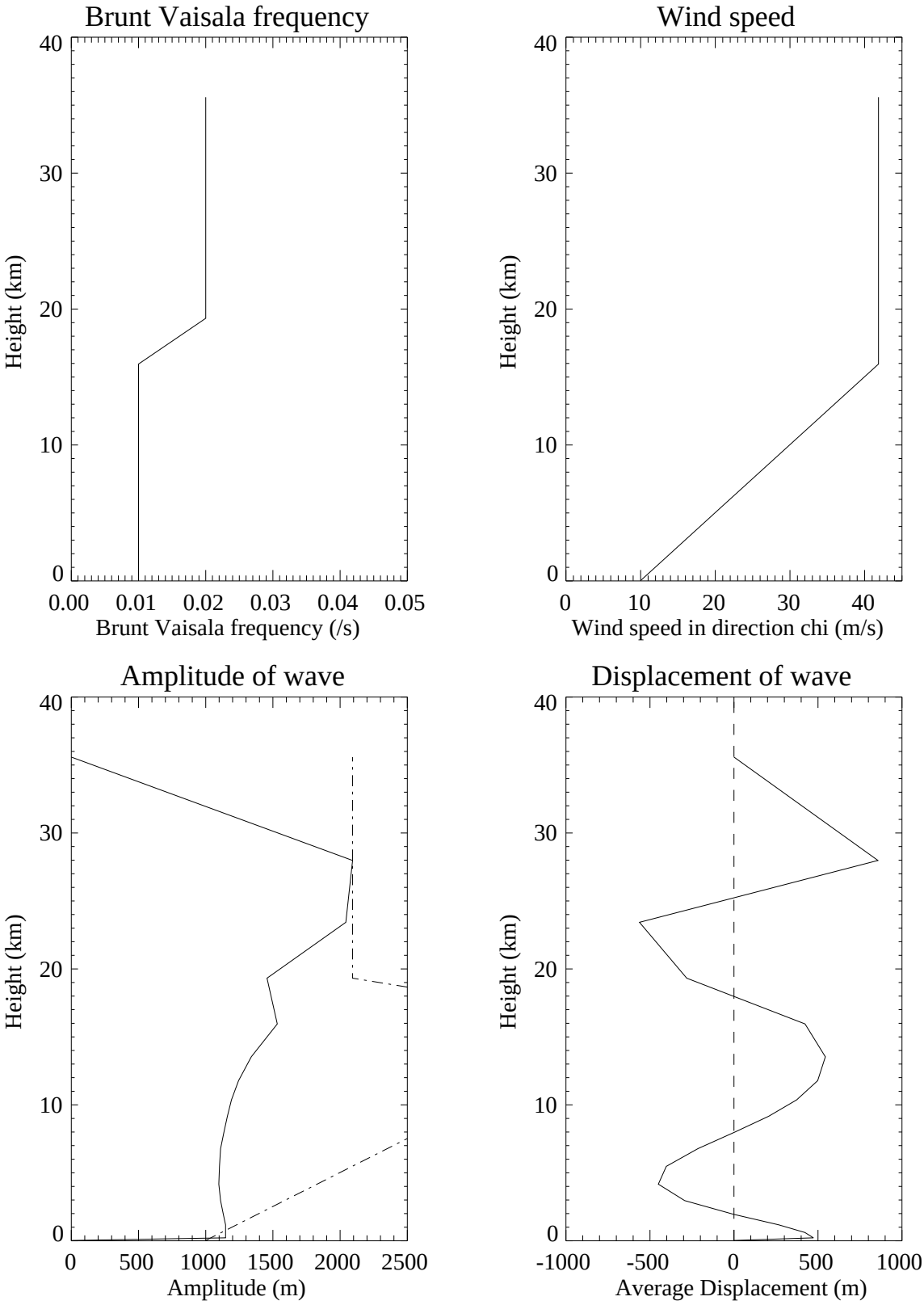

Figure 7.9: Testbed result for atmosphere with large wind shear in the troposphere ($c = 0.0002m^{-1}$) and constant u above. Stability is $N = 0.01\ s^{-1}$ in the troposphere and $N = 0.02\ s^{-1}$ in the stratosphere.

7.8.3 Realistic profile from the UM

A particular case study is presented in this section which allows for consideration of some additional aspects of the parameterisation. The input fields are taken from a selected timestep during a simulation of the UM. Figure 7.10 shows the total cloud amount as seen from the top of the model. A large band of frontal cloud can be seen stretching across

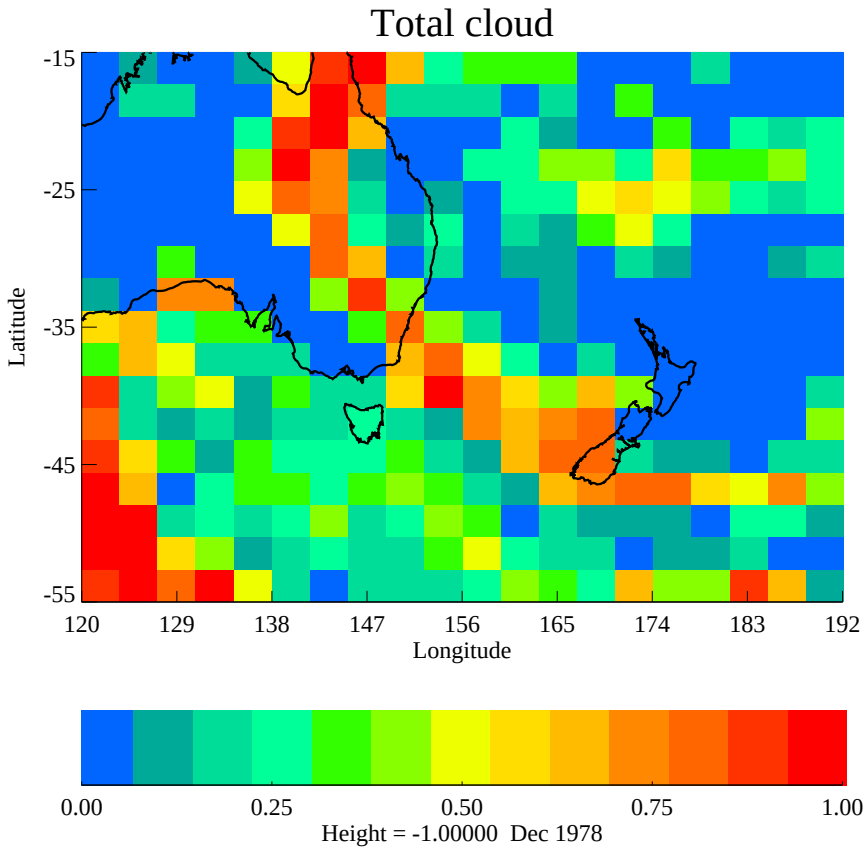

Figure 7.10: The total cloud amount(%) over the New Zealand region for the realistic testbed case.

the Tasman Sea from Australia. This is associated with northwest winds bringing moist warm air down from the tropics. Orographic cirrus is typically observed in a synoptic situation like this.

Figure 7.11 is the atmospheric state at this time over the central New Zealand gridbox. The specific humidity decreases rapidly from the surface up to a height of about 15 km. A notable feature, however, is the layer of increased humidity between 6-10 km. This makes the likelihood of high level cirrus significant. The temperature profile is relatively smooth and reveals that the tropopause lies at about 14 km. The wind speed displayed is the component of the model wind at each height which is in the direction of the surface wind. Throughout the troposphere there is the characteristic increase in wind speed which will act to reduce any amplitude growth. In the stratosphere the wind speed decreases until at

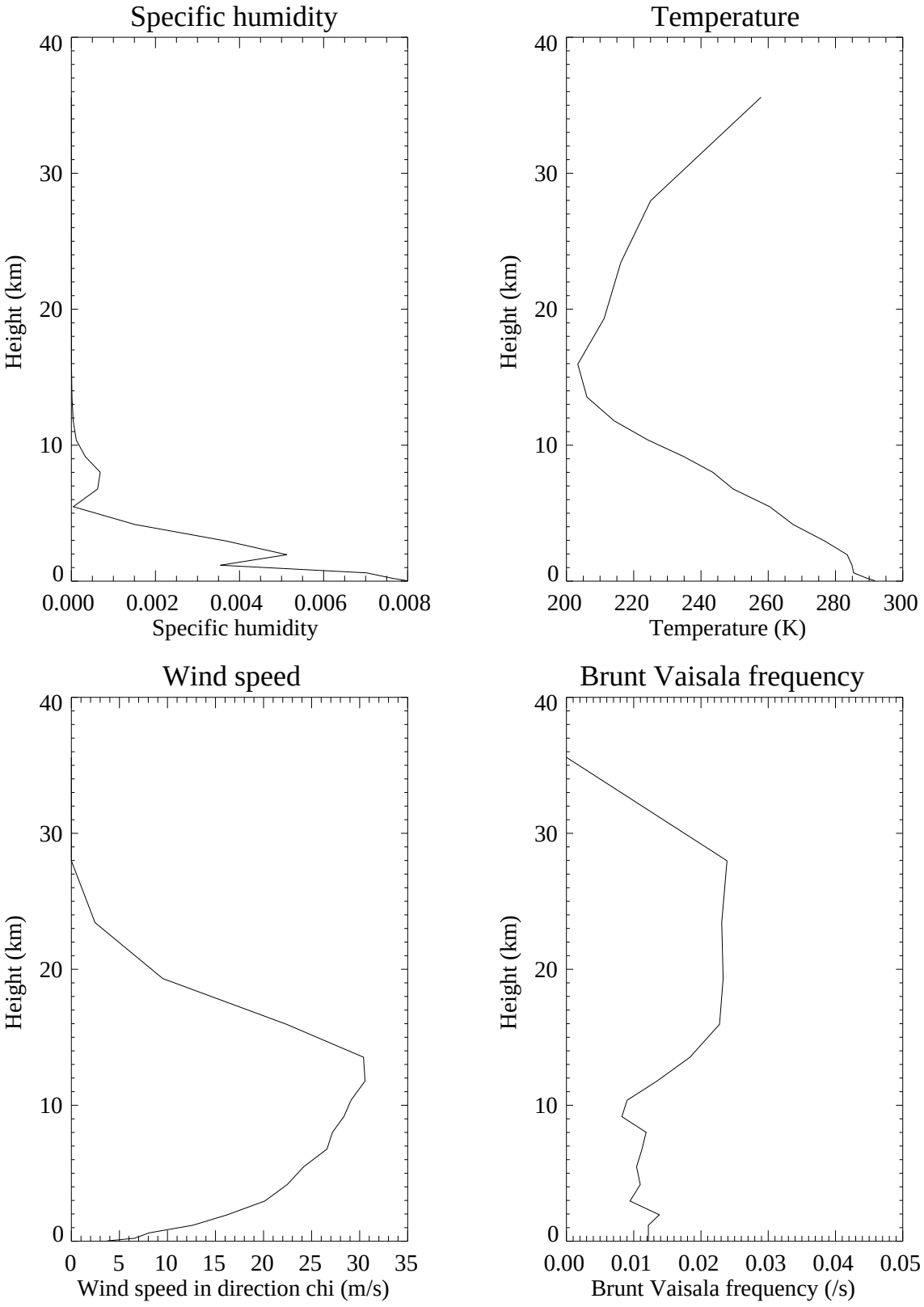

Figure 7.11: Input fields taken from a Unified Model timestep over a New Zealand gridbox.

28 km a critical level is reached where the component has become zero. Components above this point have been set to zero. The Brunt Väisälä frequency is reasonably constant at about 0.01 s^{-1} up to about 10 km, at which point it begins to increase. This will also act to reduce any wave growth.

Figure 7.12 shows the total cloud fraction (which in this case refers to liquid and ice large scale cloud) predicted by the model. Some high cloud is predicted in association with the band of humidity in the upper troposphere and a very small amount next to the surface. Considering the atmospheric conditions, however, the maximum cloud fraction of 0.05 is tiny.

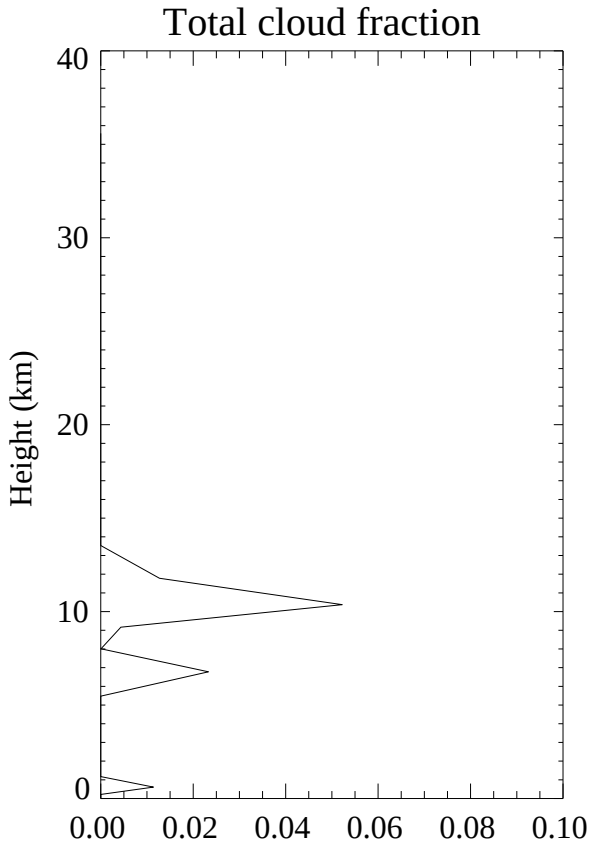

Figure 7.12: The cloud fraction diagnosed by the Unified Model cloud scheme from the input fields in figure 7.11.

Figure 7.13 shows the amplitude, displacement, temperature perturbation and change in cloud cover generated by the parameterisation. In this first case the mean displacement is used at all heights to compare subsequently with the maximum displacement criteria. The surface layer mean wind direction calculated by the scheme is 339 degrees. This is very close to being perpendicular to the main ridge alignment and a launch amplitude of 1402 m is predicted. However, the low wind speed leads to a considerable amount of blocking which reduces the launch amplitude to 798 m. The amplitude grows slowly

through the troposphere but is then relatively limited due to the increasing wind speed. Sudden increases in amplitude, such as at 9 km, are associated with decreases in N at that height. Above 17 km the amplitude drops off as the wave saturates.

The displacement shows a smooth curve with a vertical wavelength which grows steadily. The largest upward displacements are seen at the surface and about 11 km. This is encouraging for the possibility of increasing low level cloud and upper tropospheric cirrus, both of which might be expected in this synoptic situation. The displacement decreases rapidly above 20 km and goes to zero at the critical level. This is in agreement with the idea of wave breaking at a critical level.

The temperature perturbation is, as expected, anti-correlated with the displacement. The biggest change is a warming seen at 16 km. Such a result has interesting implications for studies of polar stratospheric clouds which have used similar gravity waves schemes but assumed that cooling dominates. Finally, the difference in the cloud amount with and without the parameterisation included can be considered. A small increase is seen adjacent to the ground, and a more considerable layer of cloud is generated between 8 and 13 km, reaching a maximum change in cloud fraction of 0.1. This represents a reasonable increase in orographic cirrus cover. However, considering the ideal synoptic situation a total cirrus coverage of about 0.14 is still relatively small.

Figure 7.14 shows the same as figure 7.13 except that now the maximum displacement is used when the air is supersaturated with respect to ice and the maximum displacement reaches at least -40 °C. The differences are considerable. The amplitude, of course, remains unchanged. The displacement however is now much greater between about 9 km and 14 km. This leads to a maximum cooling of about 4 °C and the creation of a large cloud layer. The change at low levels remains small. It seems likely that the maximum change of 0.4 in cloud fraction gives a good representation of orographic cloud coverage compared to the original model.

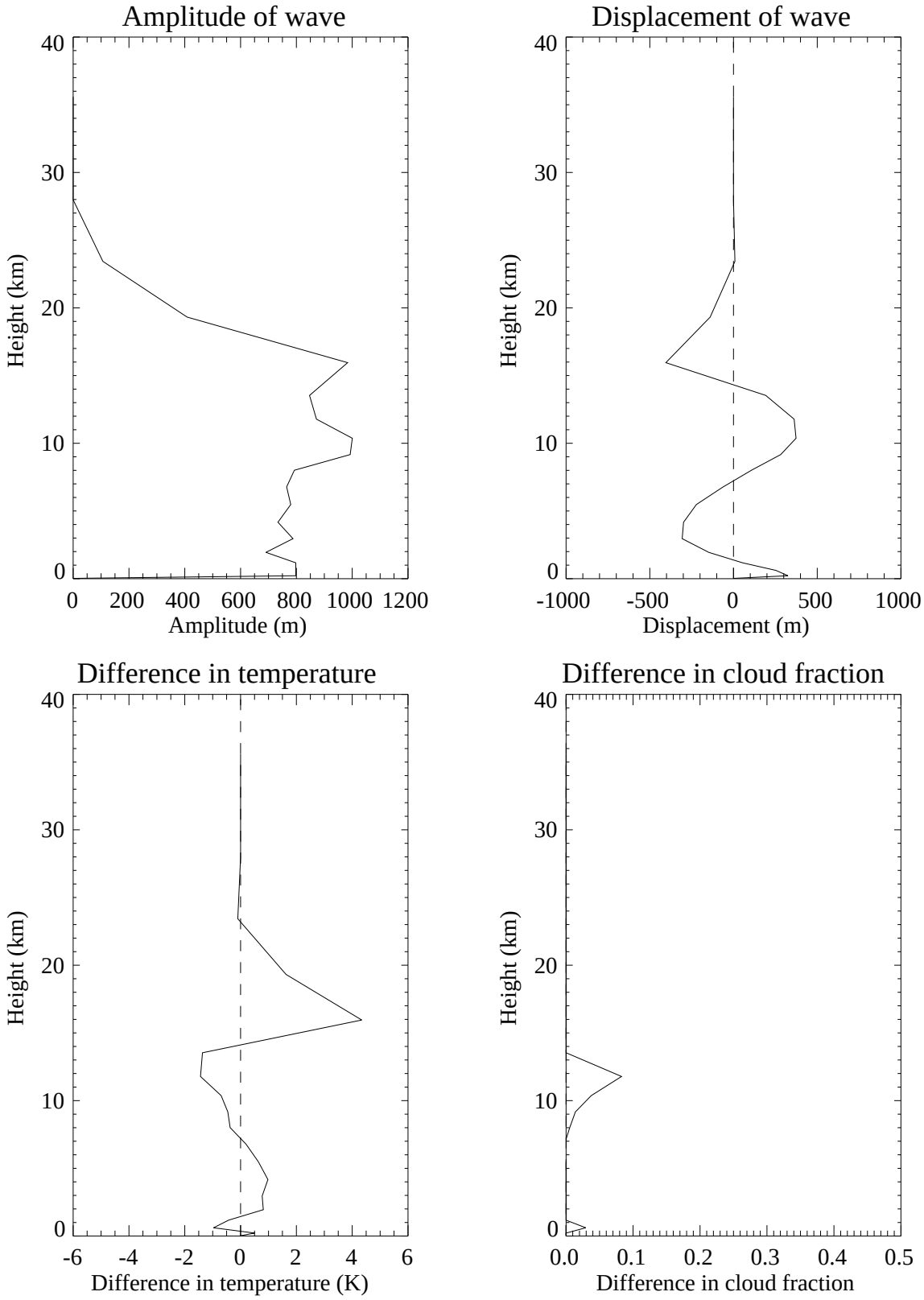

Figure 7.13: The testbed results for the atmospheric state shown in figure 7.11. The displacement is the mean displacement over the ridges. Differences are with respect to a simulation without the parameterisation included.

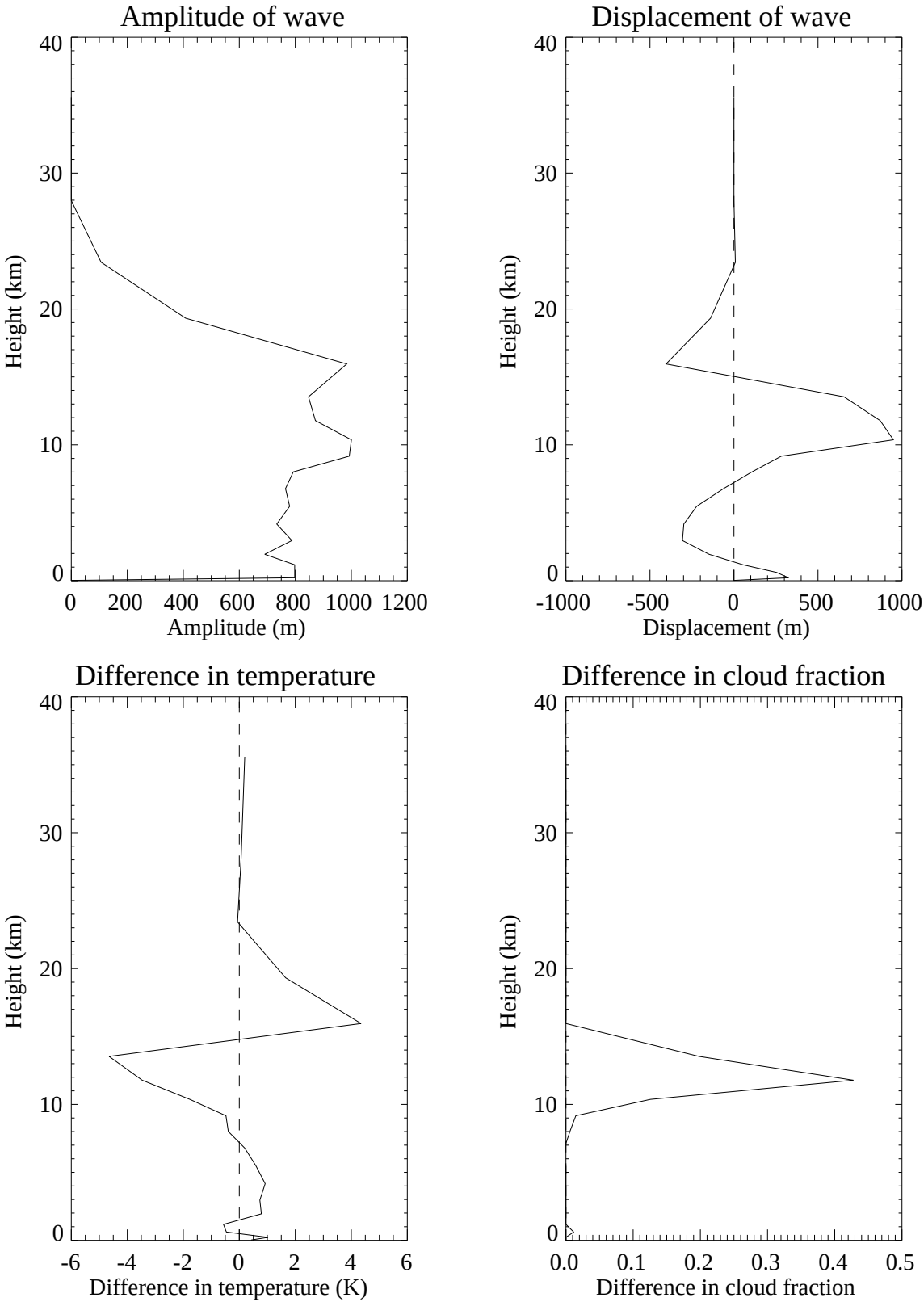

Figure 7.14: Same as figure 7.13 but the displacement is the maximum if $T + T_{max} < -40$ °C and $q > q_{satice}$.

7.8.4 Realistic profile over the Andes

Tan and Eckermann (2000) have used a two dimensional, nonlinear, high resolution, compressible model to study mountain waves over the Andes. Their simulations used realistic upstream profiles of wind and temperature to calculate the temperature perturbation due to waves in the middle atmosphere. Their aim was to compare these with the temperature profiles measured by satellites for the same time. The model uses a single transect taken perpendicular to the main axis of the Andes. Since the Andes were identified as an area of orographic cirrus generation in chapter 4 such waves are also likely to lead to cirrus generation in the troposphere. In fact photos taken by shuttle astronauts during this event showed a long band of cirrus looking cloud running along the Andean spine (*Eckermann and Preusse*, 1999). Thus their work offers an ideal opportunity to compare the temperature perturbations predicted by the parameterisation with that predicted by their mesoscale model.

It is first necessary to choose an appropriate gridbox to use for the testbed. The red line in figure 7.15 represents the zonal transect that is closest to that used by *Tan and Eckermann* (2000) for their model, transposed onto the UM domain. The gridbox highlighted in red is the one used for the testbed input parameters. Figure 7.16 shows

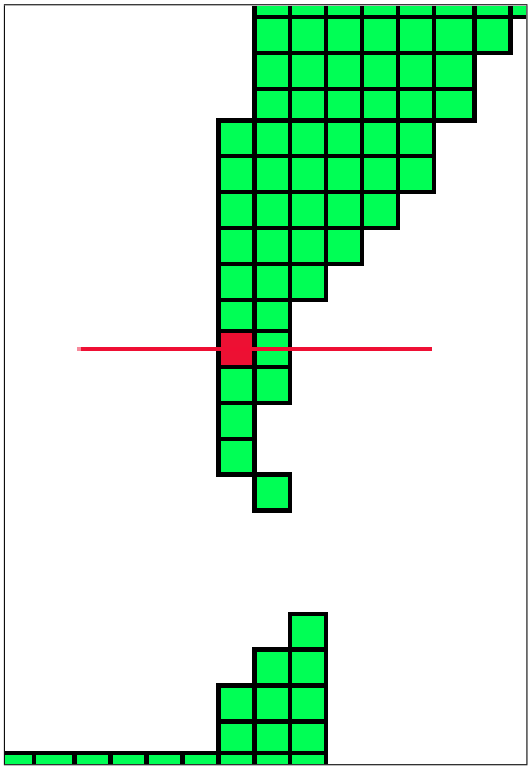

Figure 7.15: Transect across the Andes similar to that used by *Tan and Eckermann* (2000) transposed onto the UM grid. The red gridbox is one used in the parameterisation testbed.

the upstream profiles of wind speed (perpendicular to the mountains), temperature and stability using the data of *Tan and Eckermann* (2000) from NASA's Data Assimilation Office. Also shown are the profiles interpolated onto the resolution of the testbed (19 levels). The profiles are resolved reasonably well, although deviations are somewhat damped.

The results are shown as figure 7.17. Each of the pairs is for a different position along the transect, sampling across 150 km in the middle of the transect. In all plots the dotted line shows the same single result predicted for the gridbox by the testbed. In this case the testbed is using the average displacement at each level as there is no information about humidity. In the left hand column the solid line is the result predicted by the mesoscale model at full resolution. The dashed line is the prediction from the testbed. In the right hand column are the same results only with the mesoscale model output interpolated onto the same vertical resolution as the testbed.

The agreement in vertical wavelength and amplitude is excellent in all cases, especially below 20 km. The phase of the waves is more variable with good agreement for 905 km and 949 km but less so for 799 km and 849 km. The inherent dependence on the exact nature of the underlying terrain makes correct phase prediction difficult. For points further from the centre than those presented the phase correlation becomes worse. The disagreement above 20km is also not a major concern as there are only three model levels above this point. This results in very poor resolution of the wave. The most important point however is the good prediction of significant cooling in the upper troposphere by both the mesoscale model and the testbed.

An average across the four points (figure 7.18), which is essentially what the parameterisation is trying to imitate, also shows good agreement. The cooling near the surface, upper troposphere, and lower stratosphere are all well predicted and the amplitude is in excellent agreement.

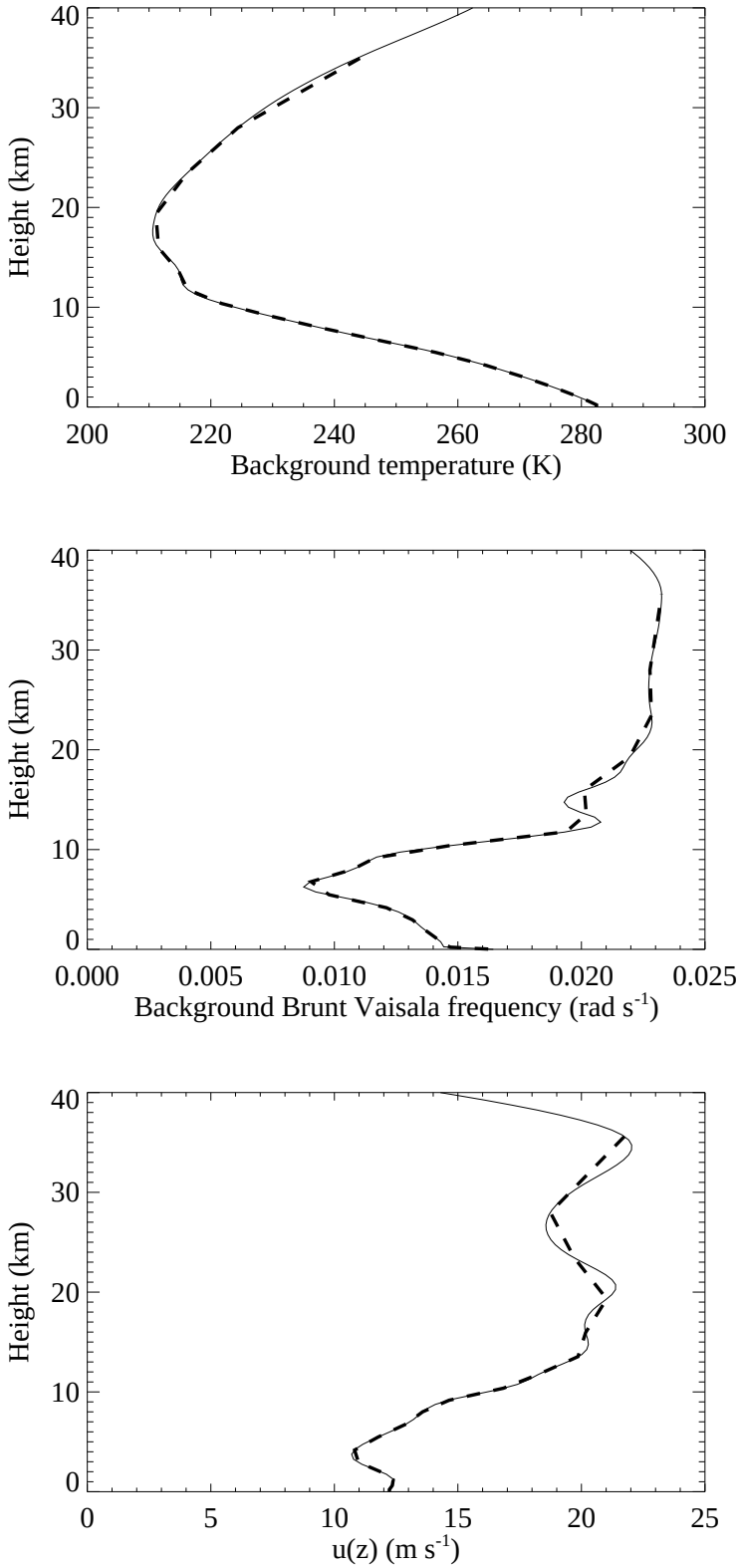

Figure 7.16: The input fields used as the upwind boundary condition for the *Tan and Eckermann* (2000) model (solid line) and the fields interpolated onto the testbed's 19 levels (dashed line).

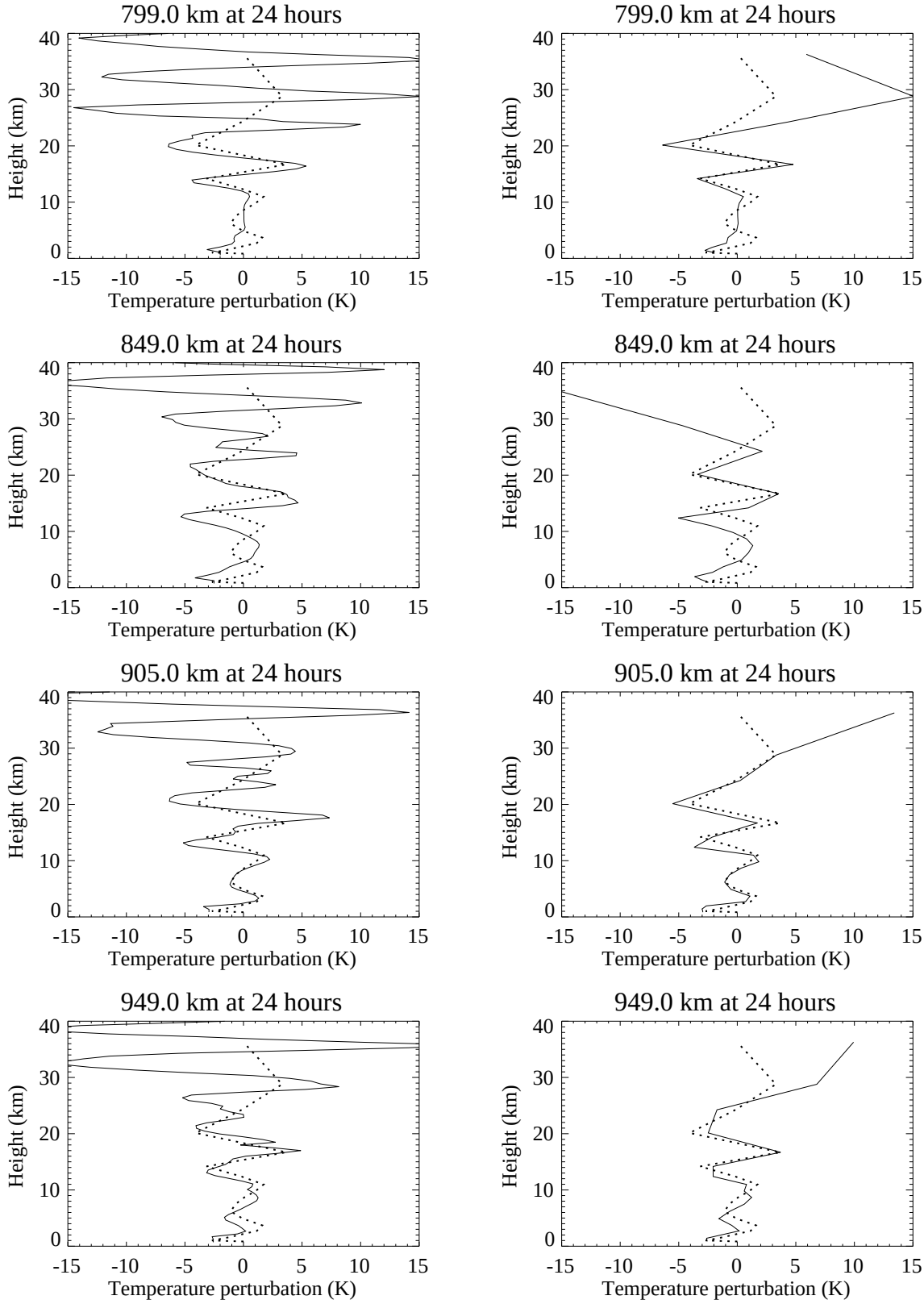

Figure 7.17: Comparison between the temperature perturbation predicted by the high resolution model (solid line) and the parameterisation (dashed line). The right hand column has the mesoscale result interpolated onto the UM grid.

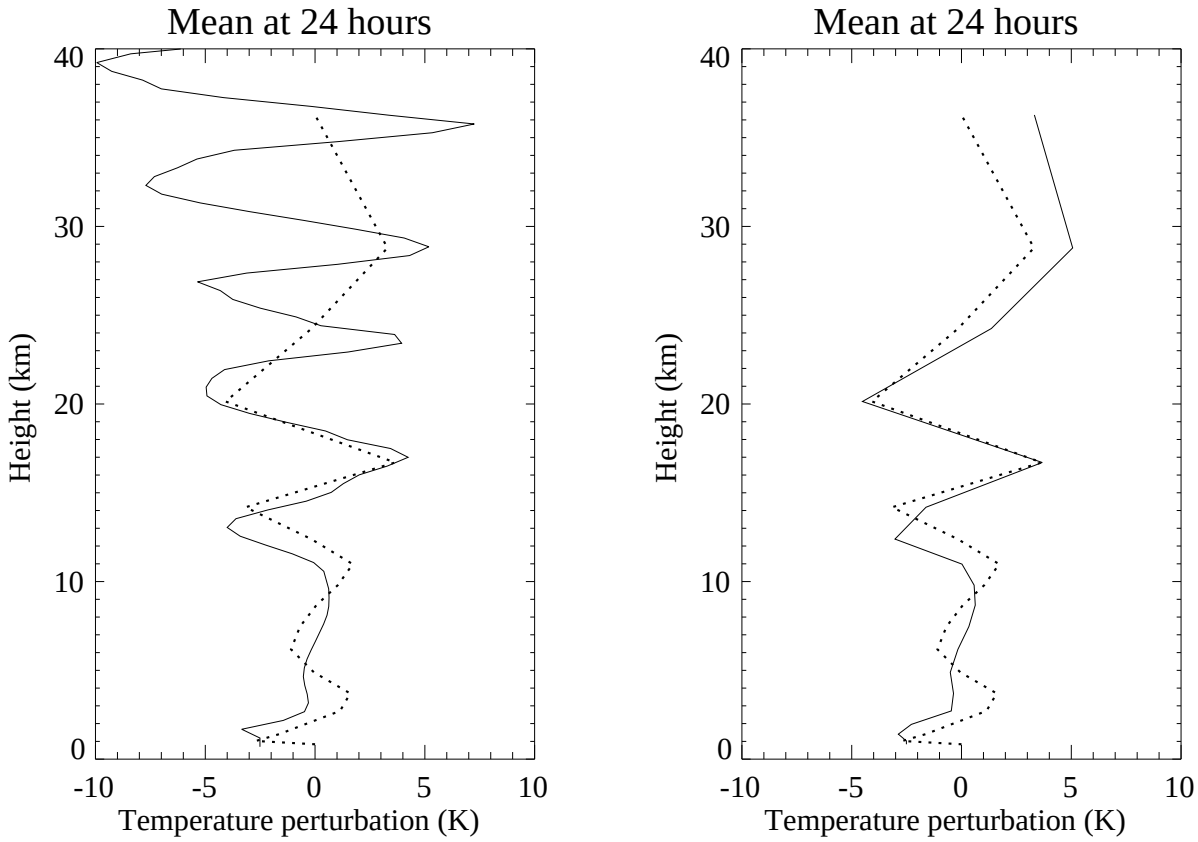

Figure 7.18: The same as figure 7.17 but for the mean of the four locations.

7.9 Conclusions

It has been demonstrated through testbed studies that a linear hydrostatic gravity wave scheme is capable of being used to generate orographic cirrus. Idealised simulations with constant u and N correctly simulate the vertical wavelength predicted by the analytical solution. In a nineteen level model the phase of the wave is poorly resolved above about 20 km. However, in the troposphere where orographic clouds form there is sufficient resolution.

When wind shear is introduced the parameterisation exhibits complex behaviour which is the result of competing effects. Positive shears in wind and stability act to reduce the wave growth due to decreasing density. The saturation mechanism was found to be more important in limiting wave growth in the stratosphere than the troposphere.

A realistic profile over New Zealand from the Unified Model showed that the parameterisation is capable of significantly increasing the amount of orographic high cloud. In a situation that is ideal for the formation of orographic cirrus, cloud cover over orography increased significantly from 0.05 to 0.4. However, a single column testbed is unable to evaluate whether even larger scale orographic cirrus will be simulated in the UM through ice advection.

Whether a linear hydrostatic gravity wave scheme is capable of reasonably reproducing the amplitude and phase of the unresolved waves that generate orographic cirrus is an important question. This was addressed by comparing the parameterisation with a nonlinear two dimensional high resolution model forced by observations. This model, which includes considerably more physical processes than the parameterisation, showed good agreement, particularly in the amplitude. For a parameterisation in a GCM where the 'average' over long time scales is ultimately the most important aspect, this result is excellent.

Chapter 8

Unified Model Control Simulation

This chapter investigates orographic cloud within the framework of the Unified Model, which was described in chapter 6. Special diagnostics have been used which allow the cloud simulated by the UM to be compared directly with satellite observations in a consistent manner. The details of these diagnostics will be considered in the first section. Two ten year control runs of the UM are then analysed to see how well orographic clouds are simulated by the GCM in its standard forms. Throughout the analysis special emphasis is given to the New Zealand region as a case study for orographic clouds.

8.1 ISCCP Diagnostics

In order to compare the model simulations in a consistent way with ISCCP data, special diagnostics were incorporated into the Unified Model. The diagnostics are those used by *Webb et al.* (2001) and are described briefly here as they are a relatively new tool for model comparisons.

The diagnostics attempt to mimic a satellite by observing the cloud from the top of the model domain. Through the impact on the radiances, the diagnostics calculate an optical depth in association with a cloud amount. The diagnostics are thus part of the radiation code, rather than the normal cloud subroutine, and only return values for the part of the Earth which is illuminated by the Sun.

Each gridbox, at a model level, is broken into ten or more sub-boxes. This allows certain sub-boxes to be identified as convective and thus part of a convective tower, while the stratiform cloud fraction for each level is distributed in a maximum-random fashion amongst the remaining sub-boxes. More explicitly this means that if there are cloudy sub-boxes in the level below, the cloudy sub-boxes for the current level are aligned with these, but are otherwise distributed randomly. The absorption is then calculated for each sub-box and progressively integrated up through all the model layers to produce an optical thickness for each of the ten 'pixels' associated with a sub-column as observed from the top of the model.

The highest level at which a sub-column is cloudy is used to calculate a cloud top pressure. Thus, in the end, each model column is described by ten pixels, each of which is identified as cloudy or clear, with an associated optical depth and cloud top pressure.

This allows a cloudy pixel to be classified as of a certain cloud type by using the ISCCP cloud type definition (see figure 4.5).

Thus, in the discussion to follow, cirrus will refer to clouds with tops at pressures lower than 400 hPa and in the optical depth range $0.1 < \tau < 3.6$. High cloud will refer to the total amount of all high cloud types, of which cirrus is a subset. These diagnostics also have the advantage of presenting clouds in terms of the way they influence the radiative forcing.

8.2 Control Run

Before considering the effect of the parameterisation on the model cloud cover it is necessary to investigate how well the model already simulates orographic high cloud. Thus the results of a ten year simulation of the Unified Model will now be discussed. The simulation included the 2B mixed phase precipitation scheme with a prognostic ice variable and the 3B cloud scheme which explicitly diagnoses an ice cloud fraction. The run is labelled as CONTROL.

8.2.1 Global results

Figure 8.1 is the difference between the climatological annual mean cirrus amount simulated by the model and that observed by ISCCP. To calculate this difference the UM data have been interpolated onto the 2.5° by 2.5° ISCCP grid. To aid in considering the magnitude of these changes, and for future reference, figure 8.2 is the actual cirrus amount simulated in the control run.

Clearly the differences are dominated by the massive lack of cirrus (dark blue) over North America, the bottom half of South America, the tip of southern Africa, central Asia and Australia. In general there is a lack of cirrus over all land and over some ocean areas, particularly to the east of the continents. Even at this low resolution one New Zealand gridbox can be seen to have too little cirrus. There is slightly too much cirrus (green) in the tropical warm pool and over the Sahara and Amazon basin..

In a similar way, figures 8.3 and 8.4 showing high cloud are presented to provide further insight. There is too much high cloud over vast amounts of the globe, including the Southern Ocean and the tropics. However, there is still not enough cloud in many of the land areas in which cirrus was missing. The magnitude of the deficiency in high cloud implies that it is caused predominantly by a lack of cirrus (cf. figure 8.1). However, considering the model predisposition to excess high cloud elsewhere, there is probably a contribution from a lack of optically thick cloud as well.

The excess in tropical high cloud seems to be associated with areas of strong convection. For comparison figure 8.5 shows the difference between the standard total high cloud

model diagnostic and ISCCP. This diagnostic is similar to the ISCCP diagnostic in using the same cutoff for cloud top height, but is sampling cloud both at night and day. The disappearance of the excess cloud in the tropics implies that the model is producing too much convective cloud, which is optically thick, during daytime hours but compensates with too little at night. The differences in the Southern Ocean remain for figure 8.5 and are harder to understand, but this has already been identified in chapter 4 as a region in which ISCCP data are unreliable.

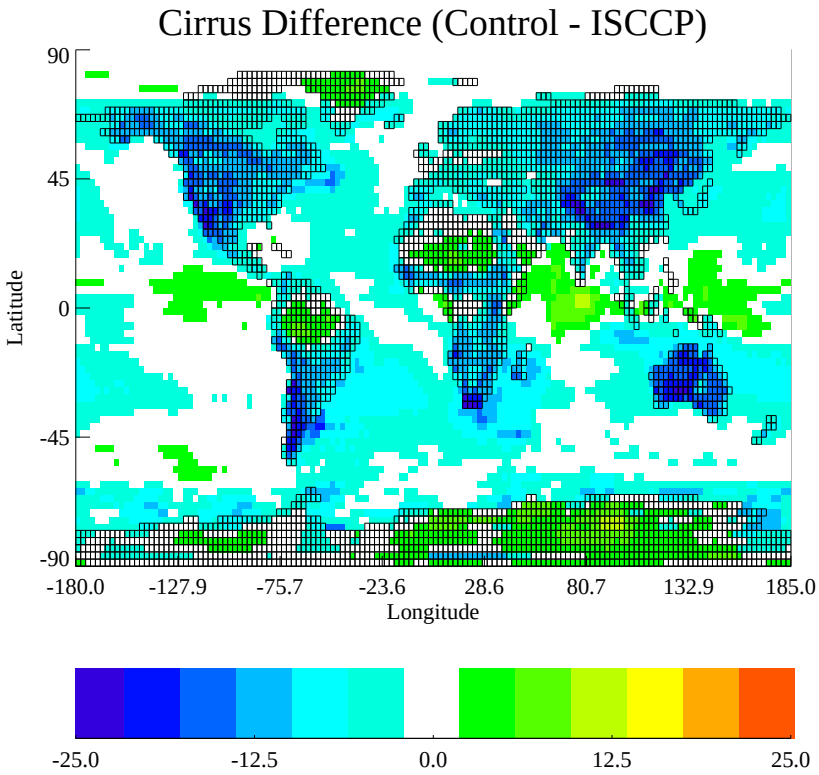

Figure 8.1: The difference in global, annual, climatological cirrus (gridbox percentage cloud cover) between the CONTROL run of the Unified Model and ISCCP observations.

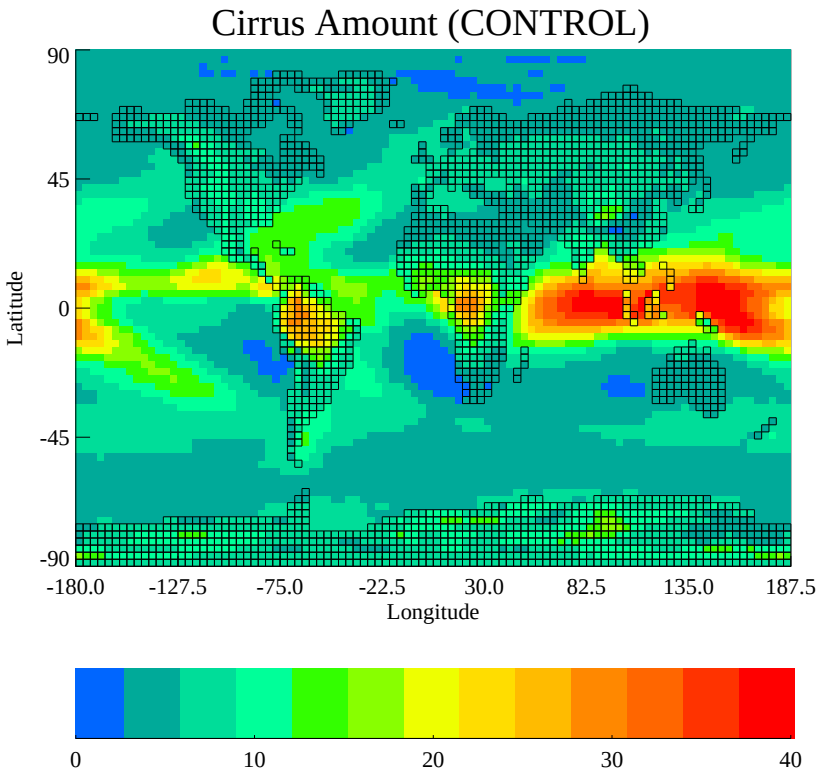

Figure 8.2: The annual climatological cirrus amount shown on the Unified Model grid. From the CONTROL run.

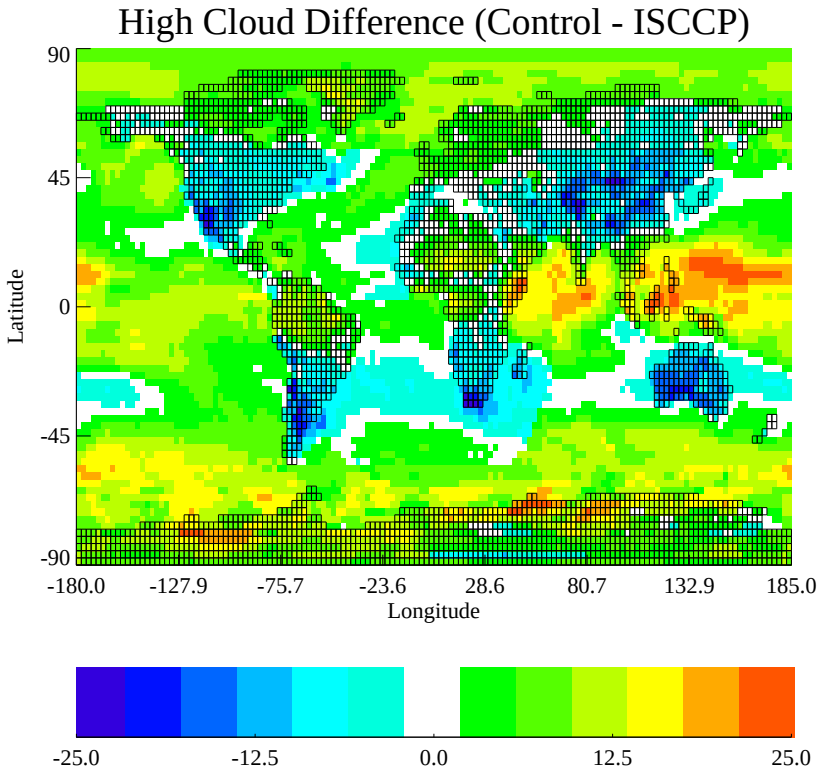

Figure 8.3: The difference in global, annual, climatological high cloud between the CONTROL run of the Unified Model and ISCCP observations.

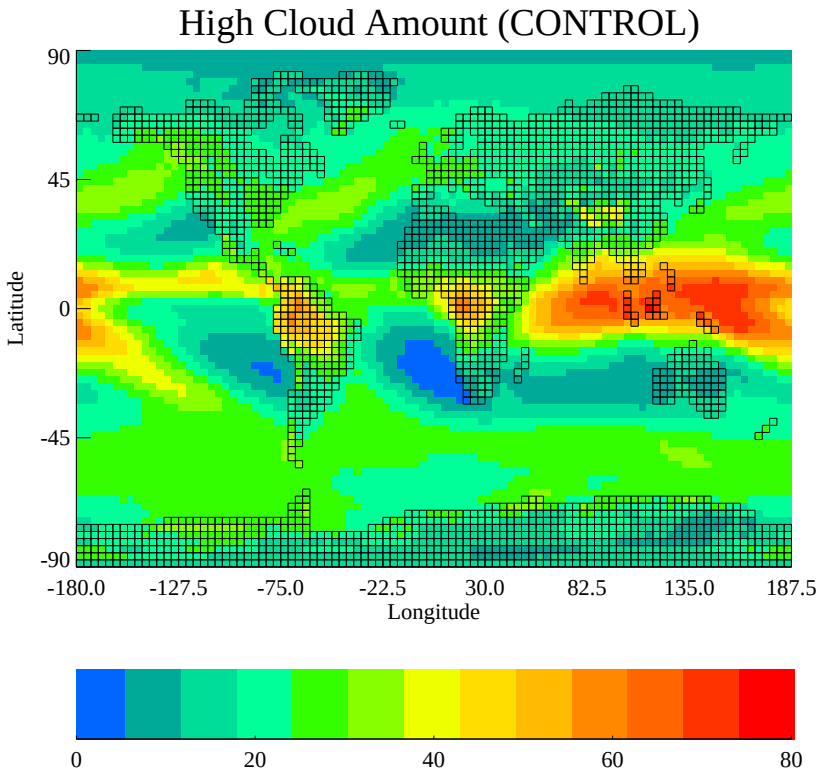

Figure 8.4: The annual climatological high cloud amount shown on the Unified Model grid. From the CONTROL run.

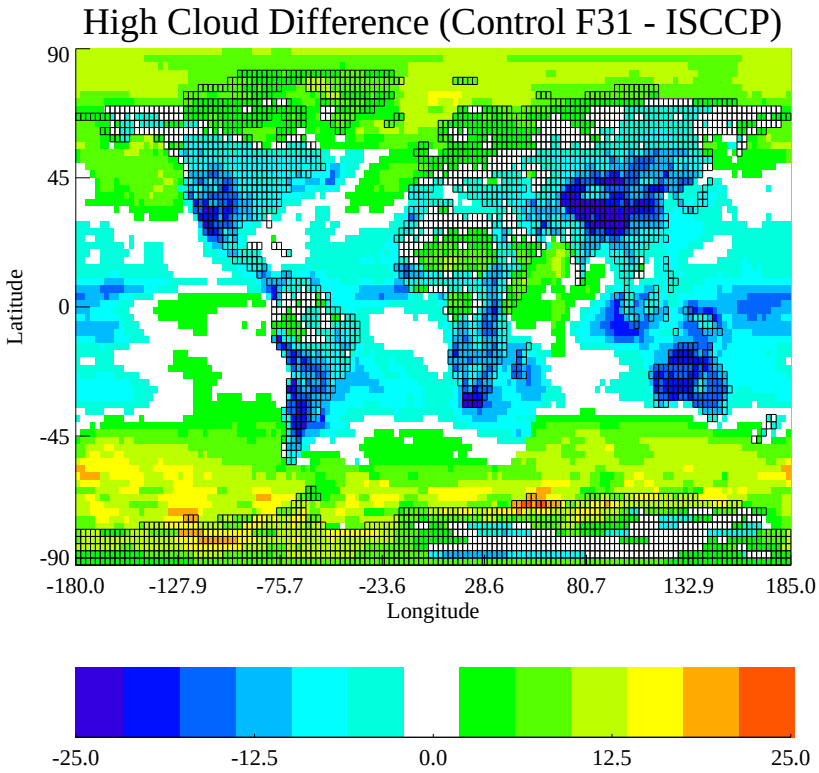

Figure 8.5: Same as figure 8.3 but in this case high cloud (F31) is the model's standard diagnostic for high cloud amount.

8.2.2 New Zealand

To help interpret the global features in cirrus and high cloud, New Zealand is used as a case study. Because it is a narrow mountainous land area situated in the midlatitude Pacific, convective activity is limited. It is also known to be a regular source of orographic cirrus (see chapter 3).

Figure 8.6 is the climatological monthly model cirrus amount for the southernmost land point (solid line) and the adjacent sea points to the west (dashed line) and east (dashed-dot line). Due to the predominantly westerly winds the later two points will also be described as upstream and downstream. The unexpected result is that the land point has about the same cirrus amount as the upstream point during the summer six months and less during the winter six months. The largest cirrus amounts are seen over the downstream point at all times. However, for all three points there is a significant lack of cirrus compared to the same plot for the ISCCP data (figure 4.6).

By taking a longer longitude slice through the same points (figure 8.7) more understanding is gained. The land point is located at the 172° tick mark. The peak in cirrus in the middle of winter is due to the increase in cirrus over the ocean upstream of the orography. Figure 4.8 shows that in the ISCCP observations this increase is seen in summer, not winter.

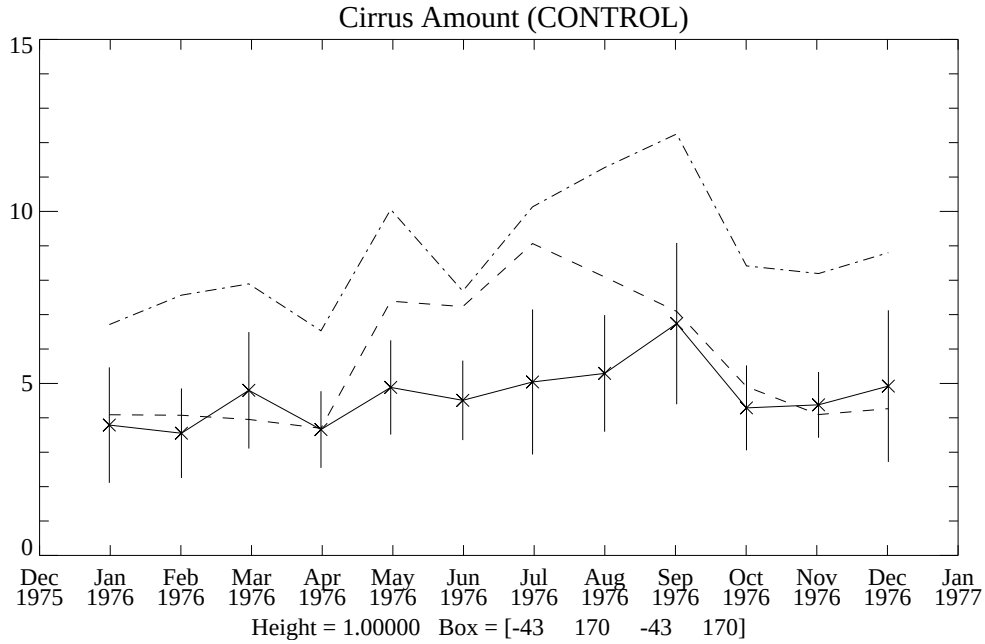

Figure 8.6: Monthly climatological cirrus amount for a New Zealand land point (solid line) and the adjacent sea points to the west (dashed line) and east (dash-dot line) from CONTROL. Vertical bars indicate one standard deviation either side of the mean. The year 1976 indicates climatological mean data.

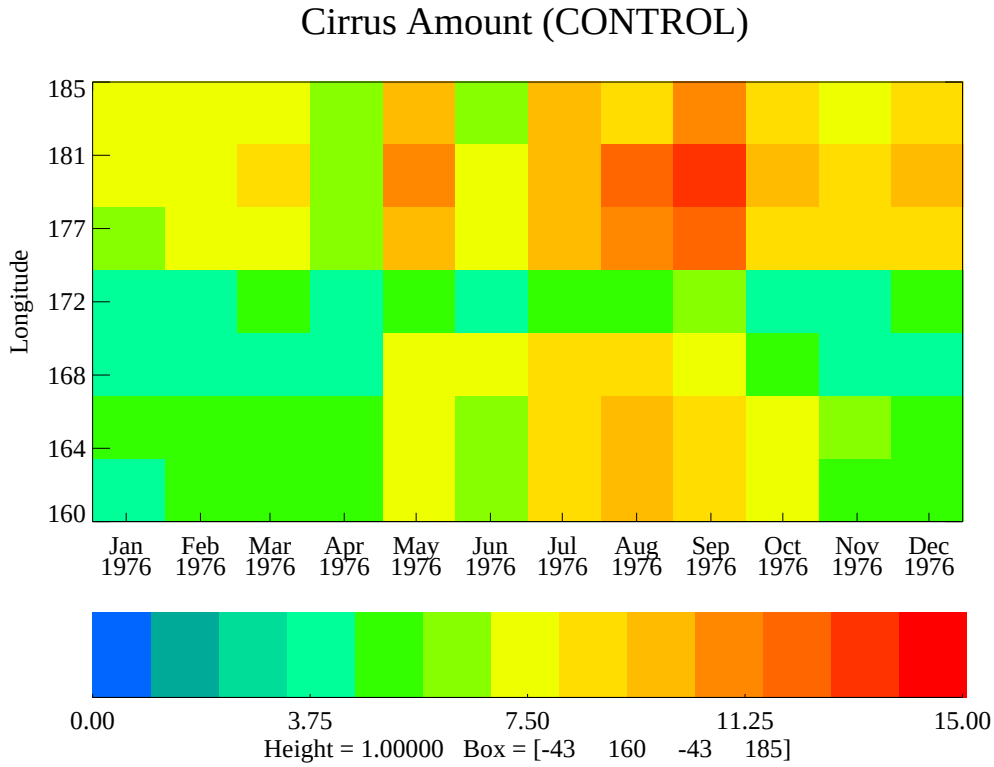

Figure 8.7: Longitude slice across the southern most New Zealand gridbox (170°E) of monthly climatological cirrus amount (CONTROL).

Complimentary to this analysis are figures 8.8 and 8.9 for high cloud. The biggest increase in high cloud is seen over the orography point where there is an increase of about 7 % cloud cover compared to the upstream point. This is about half the increase seen in figure 4.7 of the ISCCP observations. Overall the range of values over the land point is in agreement with the observations because of the slight excess of high cloud upstream. As for cirrus, the seasonal peaks are the wrong way around with the result that the model has a little bit too much high cloud in winter and not enough in summer (cf. figure 4.9).

It seems that the model does produce extra high cloud over the orography but it is optically thick cloud. Thus it is either due to a wave or convective activity over the land surface. *Davies and Brown* (2001) found that resolved gravity waves are not produced in any skillful way for mountains represented by three gridboxes or less. Thus attribution of this increase in high cloud is difficult, but unlikely to be due simply to wave processes. To ascertain more it is necessary to look at the standard model high cloud as this is calculated in the same pressure band as ISCCP but does not have any influence from low cloud. This indicates whether the cloud increase over the land point is optically thick because of an increase in underlying low cloud or if the thick cloud is all high level.

Ordinary model high cloud (figure 8.10) shows a similar pattern and magnitude to the

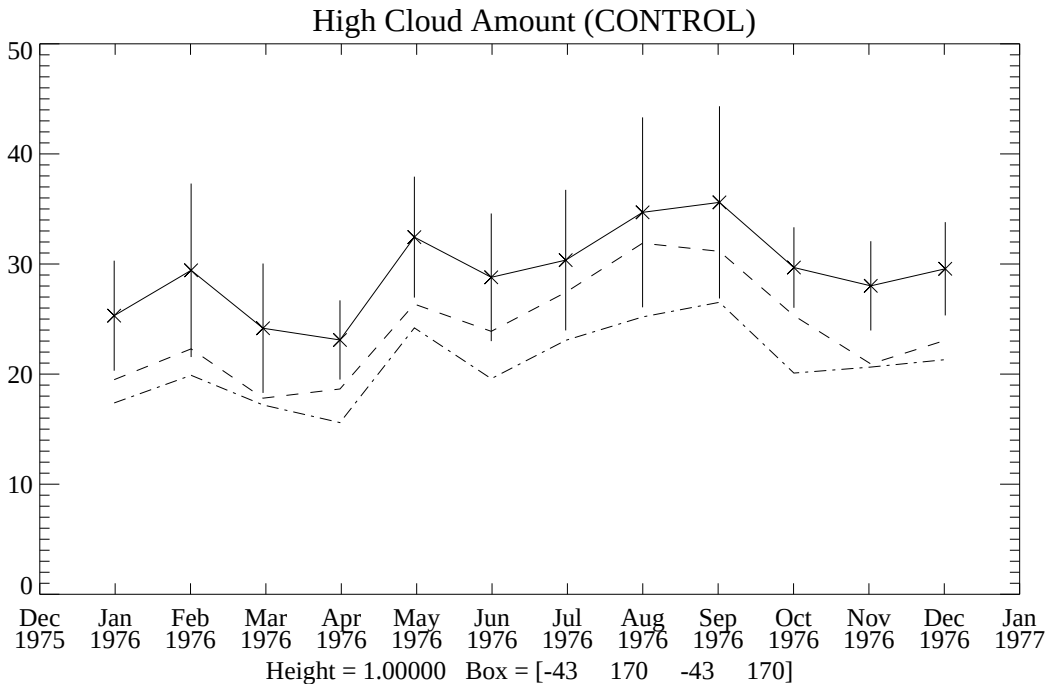

Figure 8.8: The same as figure 8.6 but for high cloud amount in CONTROL.

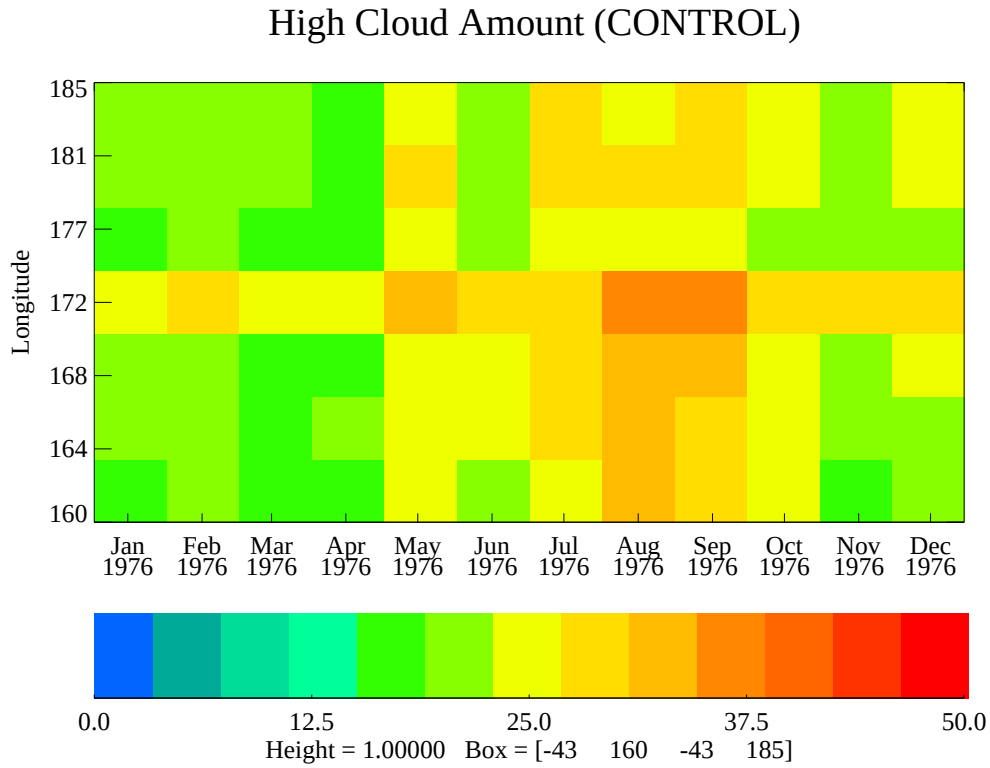

Figure 8.9: The same as figure 8.7 but for high cloud amount in CONTROL.

'ISCCP-like' high cloud. From these two plots it is possible to claim that the changes seen in the ISCCP-like high cloud over NZ cannot be primarily due to changes in the amount of low level cloud, which would force cirrus to appear in the higher optical depth categories.

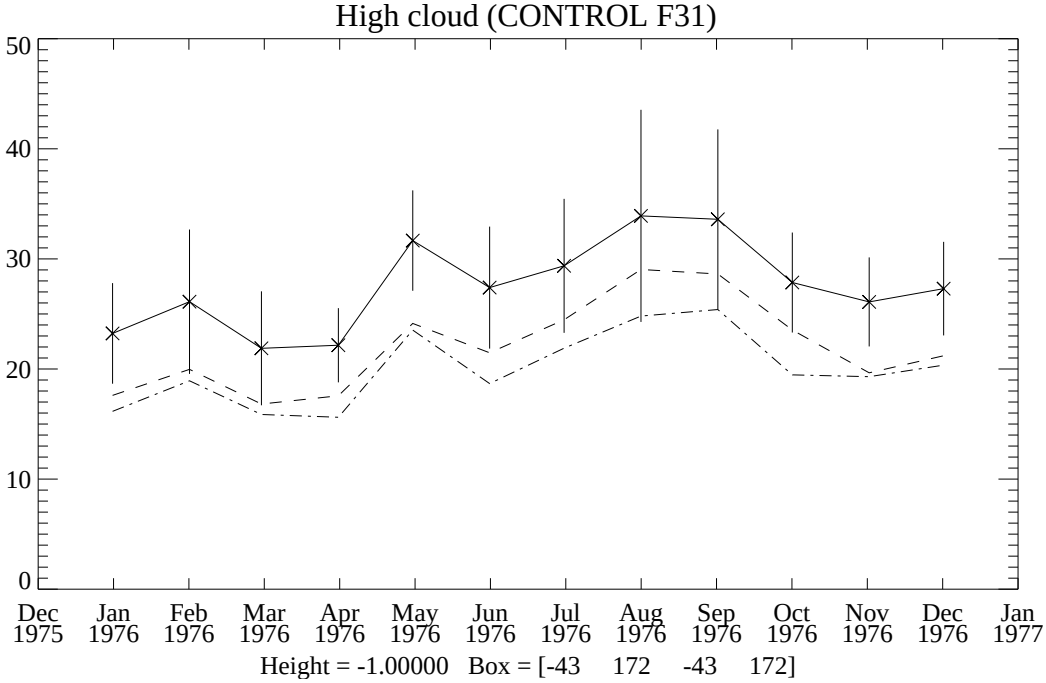

Figure 8.10: The same as figure 8.6 but for the standard model diagnostic of high cloud amount (F31) from CONTROL

However, the most notable feature of figures 8.8 and 8.9 is that there is no advection of thick cloud downstream. In fact, there must be a substantial decrease in the thick component, considering that there is an increase in the thin component (figure 8.7). It is possible that this is simply the result of a classification change.

Examining a longitude slice of low cloud (figure 8.11) it is clear that there is a considerable decrease in the amount of low level cloud in the downstream gridboxes. The standard model diagnostic was used here as the ISCCP diagnostic of low cloud does not include low cloud that is obscured by high cloud. The decrease in low level cloud will result in some cloud in the lee being classified as thin rather than thick without any change in the high cloud overall from upstream to downstream.

Of primary relevance to the advection problem is the actual amount of ice in a longitude slice plot, figure 8.12. Model level eleven ($\approx$ 300 hPa) has been selected here but

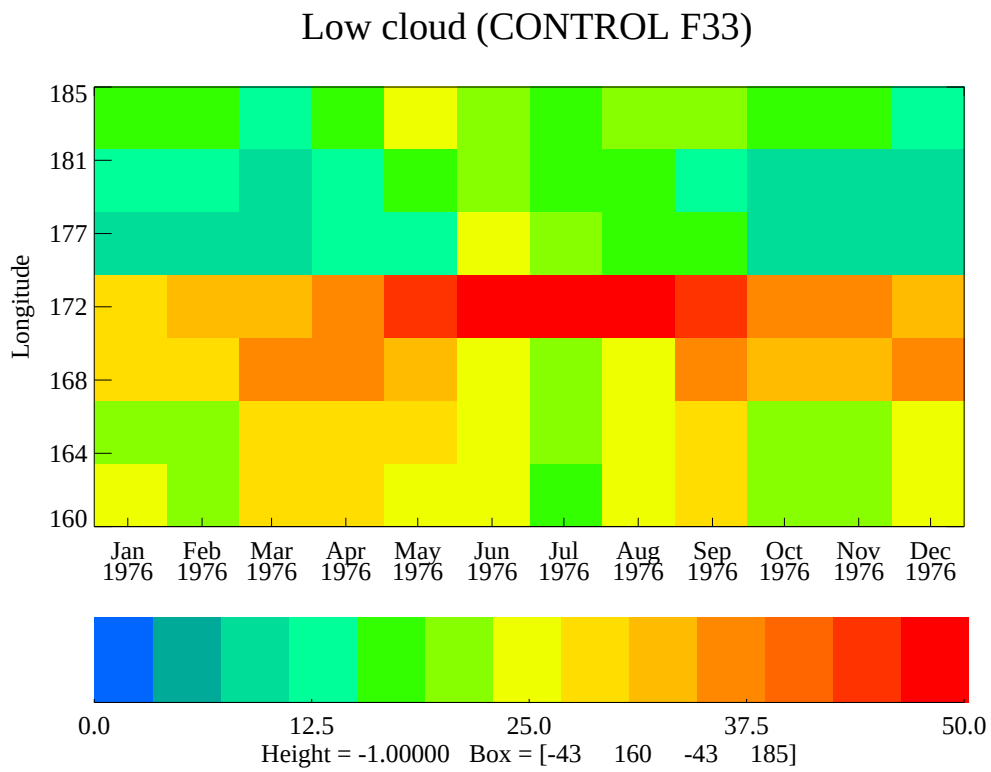

Figure 8.11: NZ longitude slice for the standard model low cloud amount (F33) from CONTROL.

other levels show a similar pattern. High cloud will normally involve all model levels ten and above but it is the lowest ones, such as ten and eleven, which have the highest moisture amounts and subsequently the most cloud. The testbed work in section 7.8 suggested that level eleven would be a height at which the parameterisation might have a strong influence.

There is a significant increase in ice amounts over the land point, and some evidence of a decrease in the adjacent downstream point compared to upstream amounts. More significantly there is no evidence of an increase in the downstream gridboxes. Why none of the extra ice over the land appears downstream is an important issue. Examining a longitude slice of temperature for level eleven, figure 8.13, shows a significant cooling over the orography. It is apparent from figure 6.1 that model level eleven is still partially terrain following and thus does not represent an isentropic surface (along which ice would be transported). Thus it is difficult to use this analysis method to claim that extra ice is generated over the orography. However, it is apparent that from figure 8.12 that if anything ice has decreased downstream of New Zealand compared to upstream. There is little evidence in figure 8.13 of any warming in the lee that might destroy any advected ice.

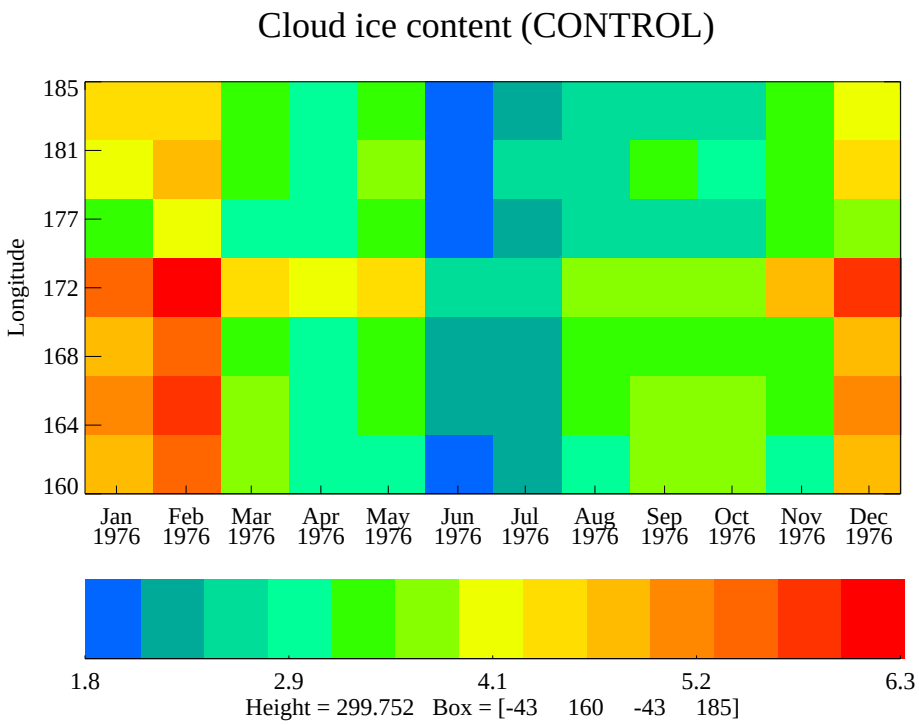

Figure 8.12: NZ longitude slice for the mean gridbox cloud ice amount in model level eleven of CONTROL. The ice amount has been multiplied by 1×10^6 for presentation.

It should be noted that while the liquid and vapour undergo an explicit diffusion process this is not the case for the prognostic ice variable (*Damian Wilson, pers com*). There may be a degree of implicit numerical diffusion as part of the tracer advection scheme, but this has been minimised as much as possible. Thus ice transport relies entirely on the tracer advection scheme.

To investigate further it is possible to generate ice diagnostics at three different stages of a model timestep and these will be identified by three letters:

- B - Before the dynamics are called. The ice amounts at the beginning of a model timestep.
- A - After the dynamics are called. The ice amounts after they have been moved around by the tracer advection scheme.
- P - After the mixed phase precipitation scheme has been called. This is the ice amount after the microphysical transfer equations have been calculated.

Figure 8.14 is the difference between ice before and after the tracer advection is used (i.e. B-A). Since this is a climatological mean plot it is hard to say how much ice is being advected by an event, but even in the mean it is clear that there is a significant increase

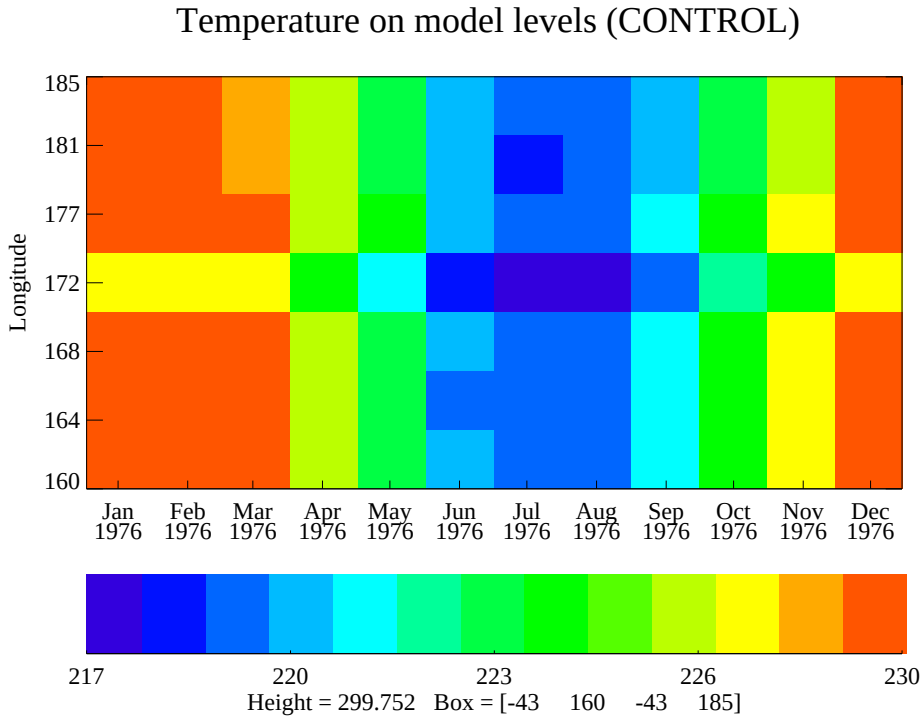

Figure 8.13: NZ longitude slice for the temperature (K) of model level eleven of CONTROL.

in ice in the first downstream grid box. As a percentage change this requires about 15 % of the ice to be advected from the landpoint and an increase of about 35 % in the downstream gridbox. There is no subsequent advection of ice into additional downstream gridboxes.

It is possible to perform a very crude calculation with some rough data: The climatological westerly wind at this height for summer months is about 25 ms^{-1}, the New Zealand gridbox is of order 305 km wide and a model timestep is 30 minutes. Thus about $\frac{25\times30\times60}{305000}\% = 14.8\%$ of the gridbox could be expected to be advected into the next gridbox, in good agreement with the percentage ice change. Cleary advection is occuring in reasonable amounts into the first gridbox at least.

Figure 8.15 is the difference between the ice before the microphysics and after the microphysics (i.e. P-A). There is a considerable decrease in ice in the downstream gridbox, implying that all the extra ice advected into the gridbox is being destroyed by the microphysics scheme. Since any temperature perturbation that existed over the land is not present downstream the ice is likely to be significantly out of equilibrium. It is reasonable that the microphysics will attempt to evaporate the extra ice and clearly it does so almost completely. This raises the question of whether there is any ability for ice hysteresis in the parameterisation due to the sublimation and deposition rates being too fast. Another cause may be simply that there is not enough extra ice generation over the land because

of the unresolved orography. It has already been pointed out that the increase in high cloud is half that compared to ISCCP so this is possible.

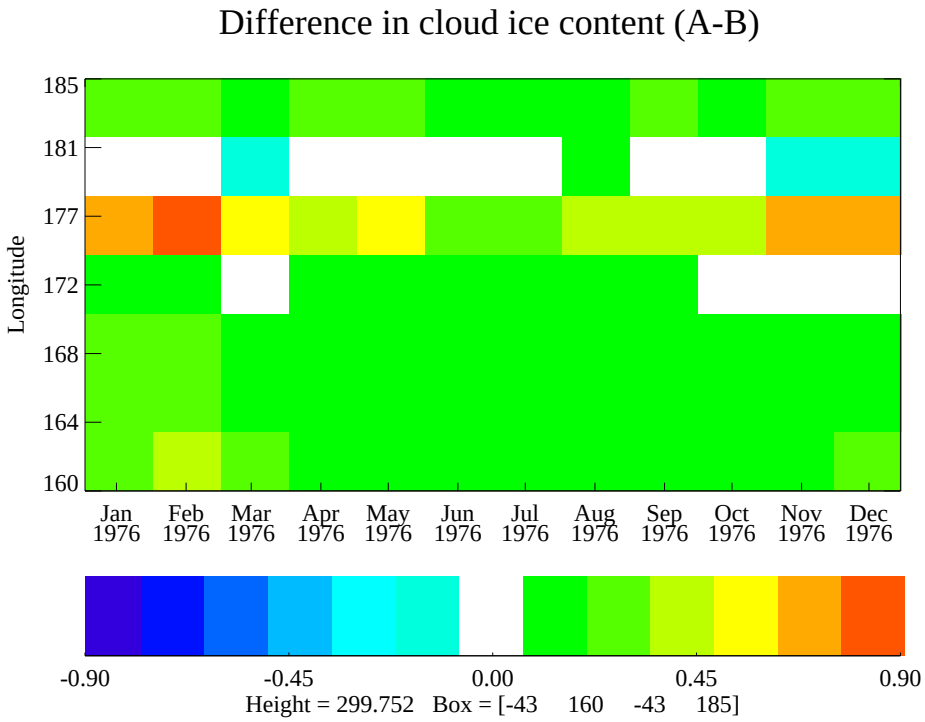

Figure 8.14: NZ longitude slice of the difference in the mean ice amount after advection (A) and before advection (B) in model level eleven.

Another issue raised by figure 8.12 is the seasonal trend. Ice water contents are high in summer months, when ice cloud fraction is low, and the reverse in the winter months. This holds true for all upper tropospheric model levels. The reason for this is the decrease in temperature in the model levels in the winter (figure 8.13). This reduces quite considerably the saturation specific humidity, q_s. As identified in section 6.2.5, the way in which the subgrid variability is accounted for in the cloud parameterisation results in the amount of ice cloud diagnosed being very sensitive to q_s. If q_s decreases then the amount of cloud will increase considerably for the same amount of ice. In summer the increased ice amounts are most likely due to the higher specific humidities in the troposphere. Conceptually it is not unreasonable to assume that a lower saturation will lead to more cloud, but observationally ISCCP showed more high cloud, particularly cirrus, in the summer months (see figures 4.7 and 4.6).

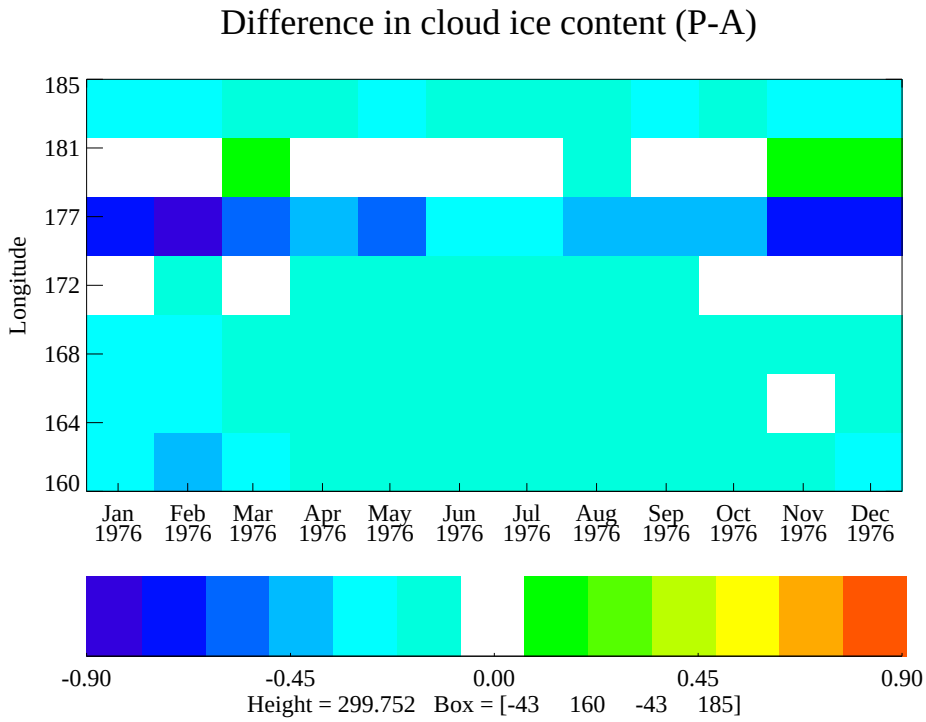

Figure 8.15: NZ longitude slice of the difference in the mean ice amount after advection (A) and after the ice microphysics (P) in model level eleven.

8.2.3 Cloud radiative forcing

It is important in any discussion of clouds to consider their radiative forcing, as this is one of the primary ways in which they influence the atmosphere. However, the Unified Model has already been studied extensively in this regard, especially using comparisons to observational datasets such as ERBE (Earth Radiation Budget Experiment). An example is *Senior* (1999) who found that while there was good agreement between the model and ERBE, comparisons of this nature give no insight into the models ability to simulate cloud-climate feedbacks. Using the same diagnostics as this thesis *Webb et al.* (2001) showed that in many areas the correct top-of-the-atmosphere forcing is simulated by the model through compensating errors in the cloud distribution. Over the midlatitude Pacific a lack of high level cloud was compensated for by increased shortwave forcing from low clouds.

The main interest in this work is to examine how the parameterisation, to be analysed in the next section, may influence the cloud radiative forcing. Thus, for future reference, the global longwave cloud forcing, figure 8.16, and the global shortwave forcing, figure 8.17, are presented. From the definitions given in section 2.3 a large positive value for the cloud longwave forcing indicates strong absorption of outgoing longwave radiation and hence a warming of the atmosphere.

Figure 8.16 shows that the cloud longwave radiative forcing is strong in the tropical warm pool and equatorial ocean as well as over the midlatitude oceans. For shortwave cloud forcing a large negative value implies more reflection of solar radiation by clouds and hence a cooling of the atmosphere. Cloud forcing in the shortwave, figure 8.17, shows a similar pattern to the longwave with the strongest forcing in cloudy areas such as the midlatitude storm tracks. Much of this shortwave forcing is through high clouds, and thus topography has a clearer influence with high shortwave forcing over some of the world's mountain ranges.

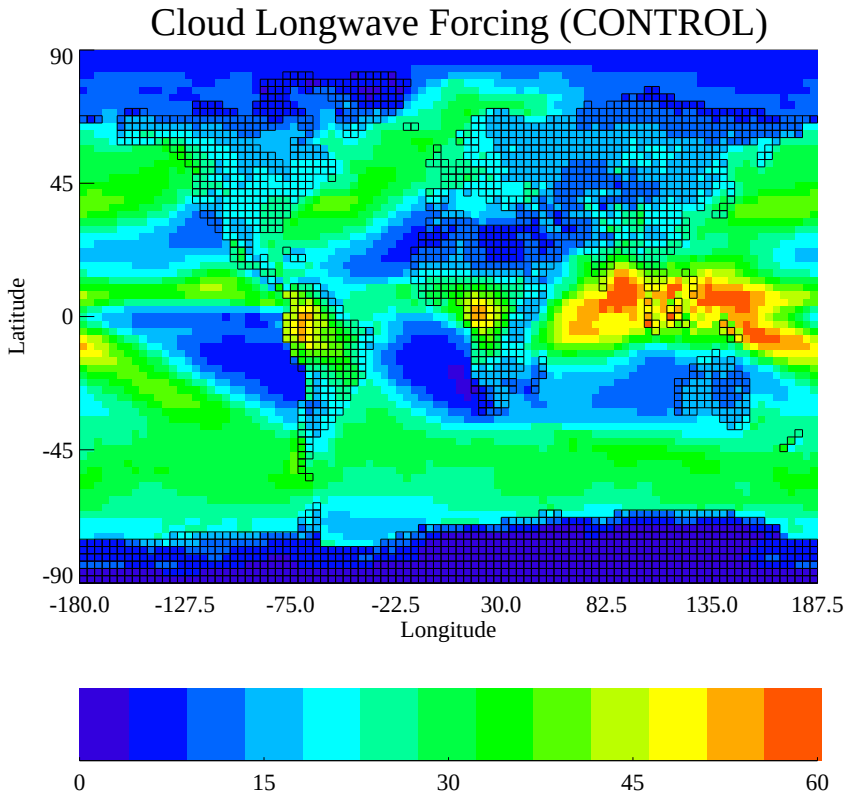

Figure 8.16: Global longwave cloud radiative forcing (Wm^{-2}).

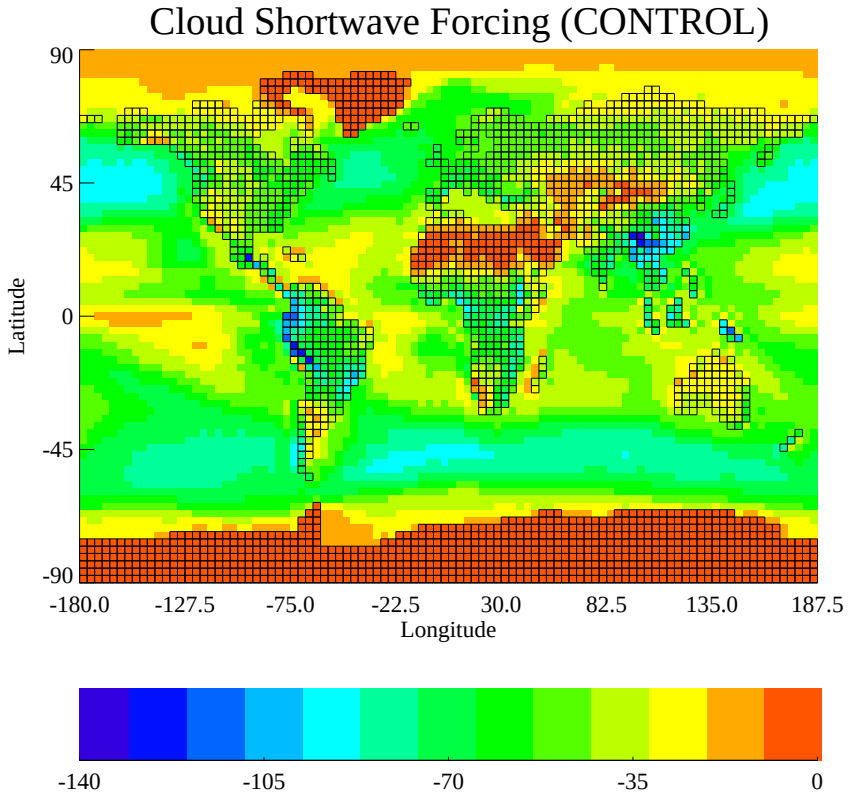

Figure 8.17: Global shortwave cloud radiative forcing (Wm^{-2}).

8.3 1A Cloud Scheme

For comparison a ten year model control run was performed which used the 1A cloud scheme and, and will thus be labelled as 1A. The 1A cloud scheme does not have a prognostic ice variable and so might be expected to lack orographic cirrus in the lee of mountains such as New Zealand. Overall, the simulation predicts more cirrus (figure

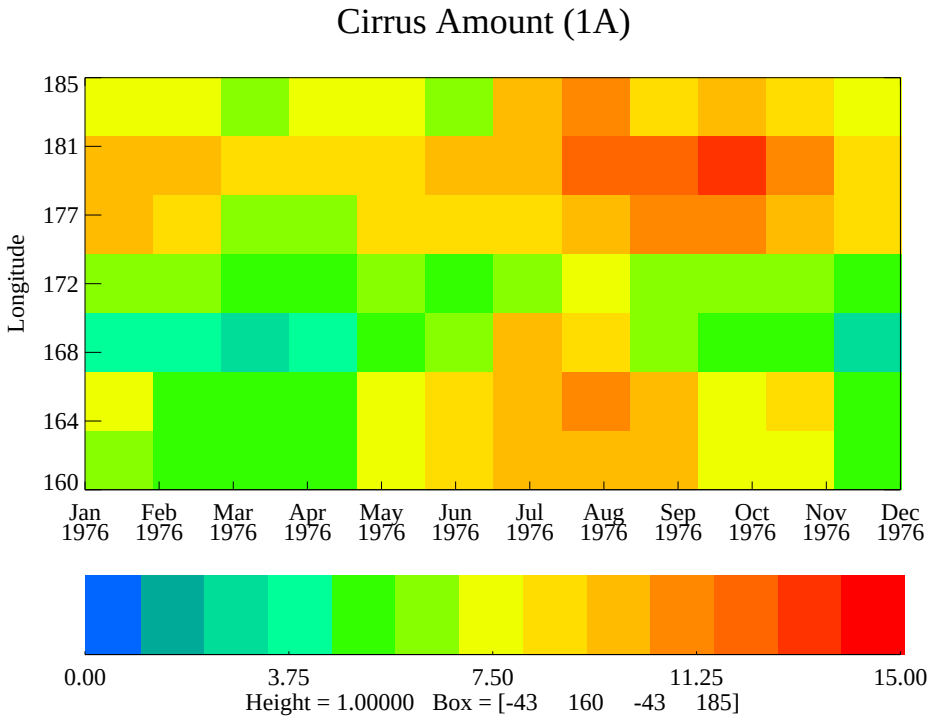

Figure 8.18: NZ longitude slice of cirrus from the 1A simulation.

8.18) and more high cloud (figure 8.19) at all times of year upstream and downstream of the mountains. For the cirrus component there is an increase in thin cirrus in the lee which is comparable to that seen in the control run. Since there is no change in high cloud in the lee this suggests that again there is a reclassification of optically thick cloud to optically thin cloud in the lee. The cause of this is the considerable decrease in low cloud (figure 8.20), which may result in cloud being seen as optically thinner in the lee.

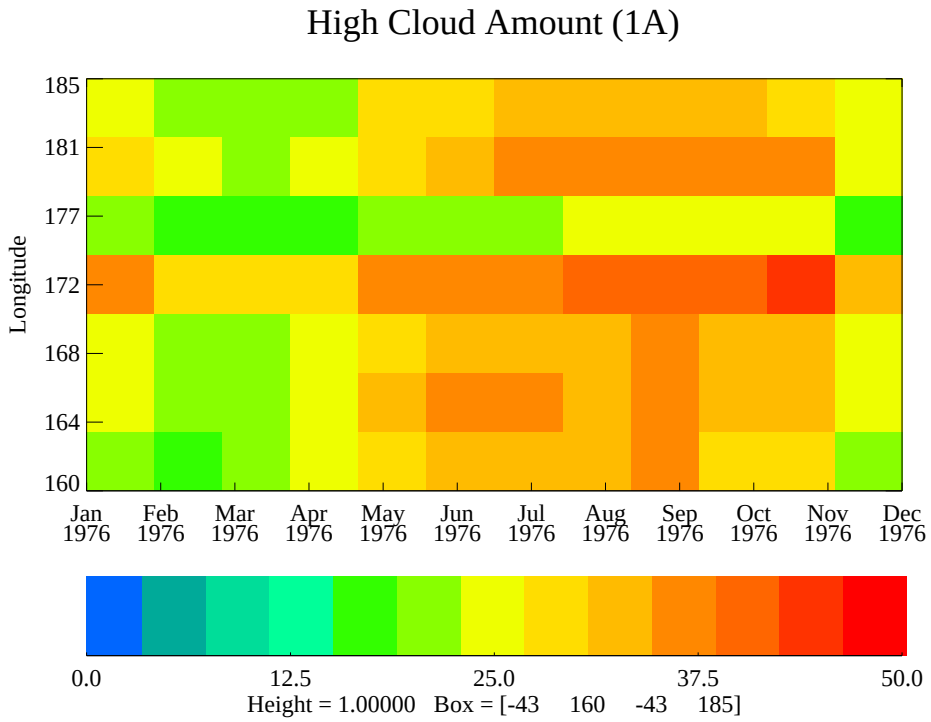

Figure 8.19: NZ longitude slice of high cloud from the 1A simulation.

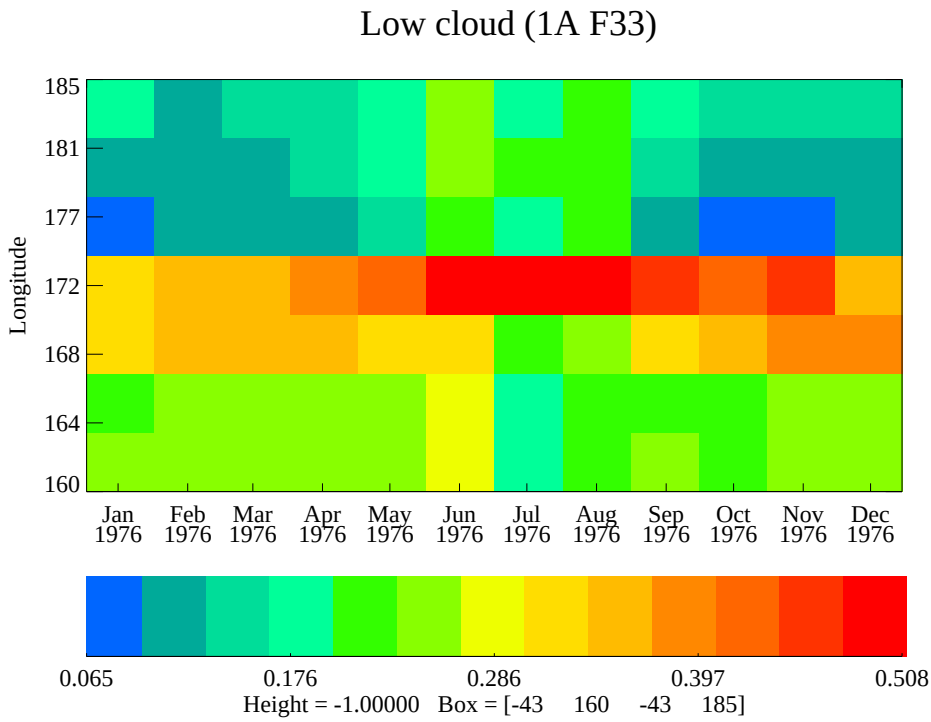

Figure 8.20: NZ longitude slice of low cloud from the 1A simulation.

8.4 Conclusions

This version of the UM is significantly lacking globally in optically thin cirrus, over both ocean and land when compared to ISCCP, despite the inclusion of a prognostic ice variable. The major deficiencies exist over high orography. While the model generally has too much high cloud over the oceans, deficiencies in high cloud still exist over mountainous areas. This is almost entirely because of the lack of cirrus.

The magnitude of the change in high cloud over New Zealand is smaller than in the observations, though the end result is close to the observations. This is because there is already too much high cloud over the Tasman sea. However, this is not the case in many other mountainous areas of the globe where high cloud is deficient. This is more evidence for a global lack of high cloud over orography, although convective processes will also play an important role in some areas.

There is no evidence of any of the additional high cloud generated over New Zealand appearing downstream. While a considerable amount of ice is advected into the first gridbox downstream of New Zealand it is evaporated by the microphysics. Thus trailing orographic clouds are not observed. It seems likely that this is also true of the global high cloud in a number of locations.

It should be noted that the UM does have a cloud area parameterisation, which gives a pseudo increase in vertical resolution. This would have had an influence on the optical thickness of the cloud calculated and thus change the categorisation of cloud type. However, it would not influence the total high cloud amount or any potential downstream advection.

Chapter 9

Unified Model Orographic Cloud Simulation

9.1 Orographic Cloud Parameterisation

The results of a ten year simulation of the Unified Model that incorporated the orographic cloud parameterisation described in chapter 7 will now be considered. This simulation will be referred to as PARAM. In all other aspects it is identical to the control run.

9.1.1 Global results

Figure 9.1 is the difference in climatological cirrus, found by subtracting the CONTROL run from the PARAM run. In this way areas where climatological mean cirrus amount has increased in the PARAM run appear as either green or red, depending on the strength of the change. Areas where cirrus has decreased will appear as a shade of blue. Only differences which are statistically significant with 99% confidence are shown. Statistical significance is established using the Student's T-statistic (or T-Test) which gives the probability that two sets of sampled data have significantly different means. The T-statistic for sample populations x and y of size N, means $\overline{x}$ and $\overline{y}$ and variances σ_x and σ_y is defined as

$$T = \frac{\overline{x} + \overline{y}}{\sqrt{\frac{\sigma_x + \sigma_y}{N}}} \tag{9.1}$$

Any gridbox difference which has less than 99% confidence is set to zero and thus appears as white in the figure. This approach is taken to attempt to mask as much as possible the internal variability in the model simulations as this dominates the small changes. Unfortunately this has the disadvantage that small, but real, changes caused over orography by the parameterisation will be lost. Alternatives would include performing an ensemble of simulations, or taking into account the more complicated statistics involved in assuming that there is an expectation for changes in certain areas (e.g. the parameterisation only acts over land).

The changes in cirrus (figure 9.1) over orography are mostly small with increases of the order of 1% cloud cover over some mountain ranges and similar decreases over others. The biggest differences are equatorial, where decreases in cirrus of the order of 5% cloud cover (beyond the plot scale used) appear over land. However, these are not in association

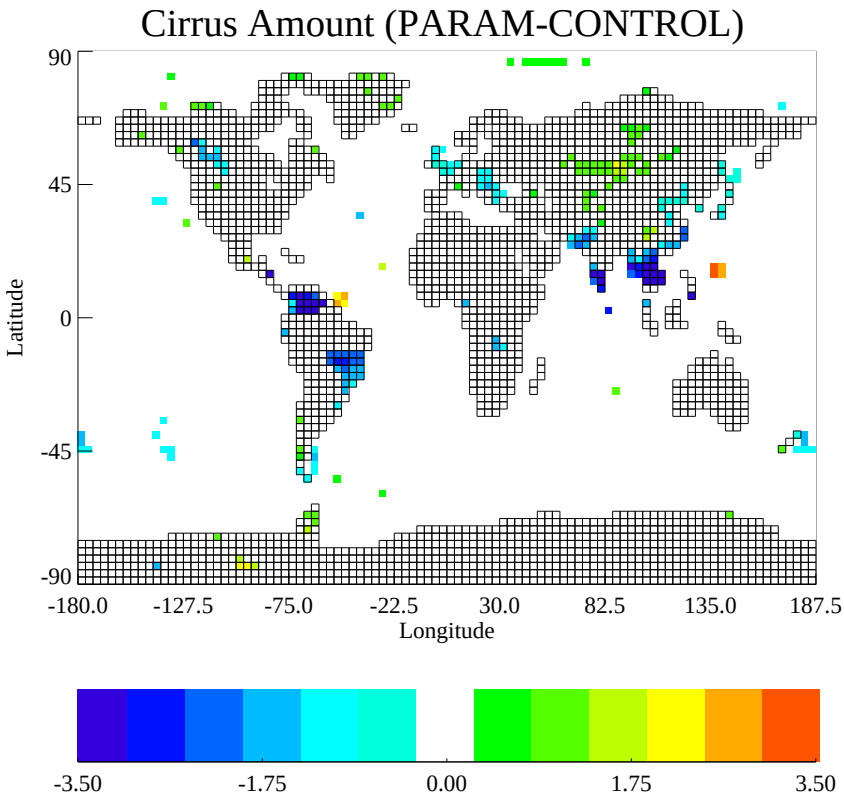

Figure 9.1: Global statistically significant difference in cirrus amount between the PARAM run and the CONTROL run (change in % cover).

with major mountain ranges. By considering figure 8.2 it can be seen that these decreases represents a loss of about one quarter of original cirrus cover.

Since there is no temperature perturbation applied over the oceans, changes in cirrus there can not have been directly forced by the parameterisation. However, the changes may be indirect through a slight change in the model climate. Along these lines increases seen over ocean to the east of the major areas of cirrus decrease in cirrus may be connected. There is also some evidence for very small decreases in cirrus over ocean in the lee of some mountain ranges such as the Andes and New Zealand.

More widespread and larger changes are seen in the high cloud amounts (figure 9.2). Here there are increases of up to 7% cloud cover seen over the Andes, the Antarctic Peninsular, the Himalayas, the Alps, the Pyrenees and New Zealand. There is also some indication of widespread increases over Russia. In comparison with figure 8.4 it can be seen that all these changes represent a climatological increase of about one fourth of the previous high cloud cover. The only area where a major decrease in high cloud is seen, is at the top of South America. In this same location there was also a decrease in cirrus.

Diagnostics that can give more information about the relationship between the changes in cloud and the parameterisation are the wave vertical displacement amplitudes, figure

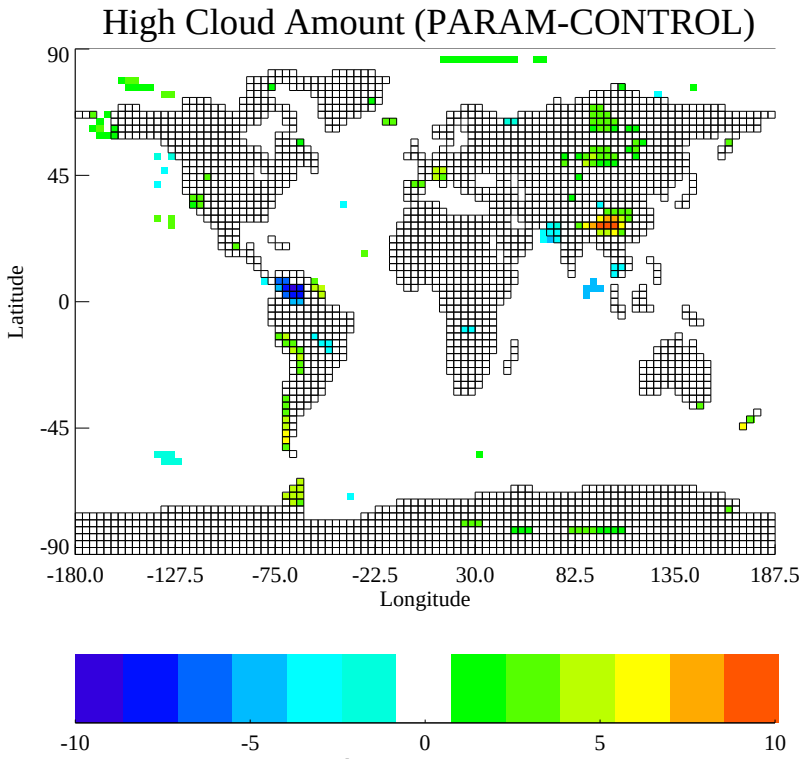

Figure 9.2: Global statistically significant difference in high cloud amount between the PARAM run and CONTROL run.

9.3, and the temperature perturbations caused by the waves, figure 9.4. For consistency with other parts of this thesis these global plots are for level eleven.

The magnitudes of the wave amplitudes produced by the parameterisation are difficult to interpret as a climatological average is dependent on the frequency of occurrence of the waves. However, comparing with the orographic cirrus areas identified in chapter 4, the distribution is excellent. The strongest temperature perturbations, which are coolings, are seen over the bottom of South America, New Zealand and the Antarctic peninsula. These are all areas in which there are significant amounts of extra high cloud. The large increase in high cloud over the Himalayas is associated with very strong cooling in higher levels of the model such as thirteen and fourteen.

Many other areas where there are changes in high cloud can be associated with weaker temperature perturbations generated by the parameterisation. However, over the Rockies no changes in high cloud are observed despite considerable subgrid wave activity generating temperature perturbations over a large area. This emphasises the importance of other atmospheric parameters in the model, such as a suitable humidity distribution in the upper troposphere.

The changes in cirrus cannot be correlated with the parameterisation. To try and understand this, and to also examine the effects of the parameterisation on the lower

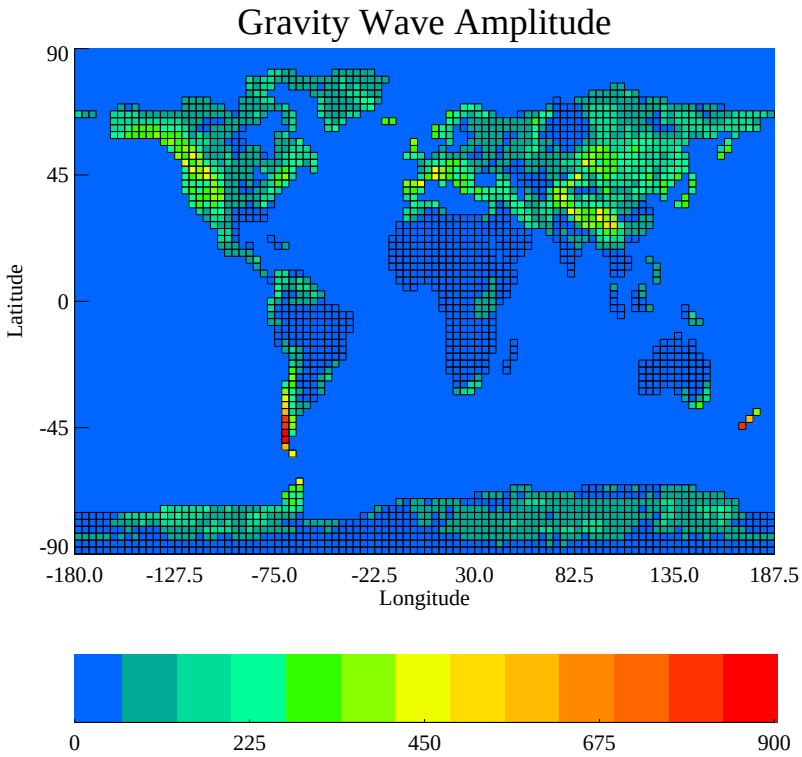

Figure 9.3: Mean amplitude (m) of the parameterised gravity waves in level eleven of PARAM

atmosphere, figure 9.5 and figure 9.6 are the statistically significant changes in low and middle cloud respectively. The parameterisation has considerably increased the low level cloud by amounts of up to 20% in cloud cover over many mountain ranges. This is expected as there will always be extra lifting generated at the surface. All the changes are easily linked directly to the parameterisation and, as well as mostly being of a similar magnitude, are widely spread. In particular Europe, South America and Asia show extensive increases in low cloud. Over some less mountainous regions there are also decreases in low cloud.

It is also apparent that some of the changes in cirrus seen in figure 9.1 are associated with big increases in low level cloud. For example consider the decreases in cirrus over India, Vietnam and the mountainous areas of Brazil for which there is no change in high cloud. It thus seems likely that the changes in cirrus in these areas are primarily caused by a re-classification of cloud into an optically thicker category.

There is also evidence of increased low cloud off the east coast of the Andes and New Zealand, both areas downstream of where the parameterisation is acting strongly. The model is capable of advecting extra water cloud into the first gridbox adjacent to orography but this should be removed by the cloud scheme due to the increase in temperature. Thus, this feature is counterintuitive and remains unexplained.

Changes in middle clouds (figure 9.6) mostly involve decreases in cloud in the areas

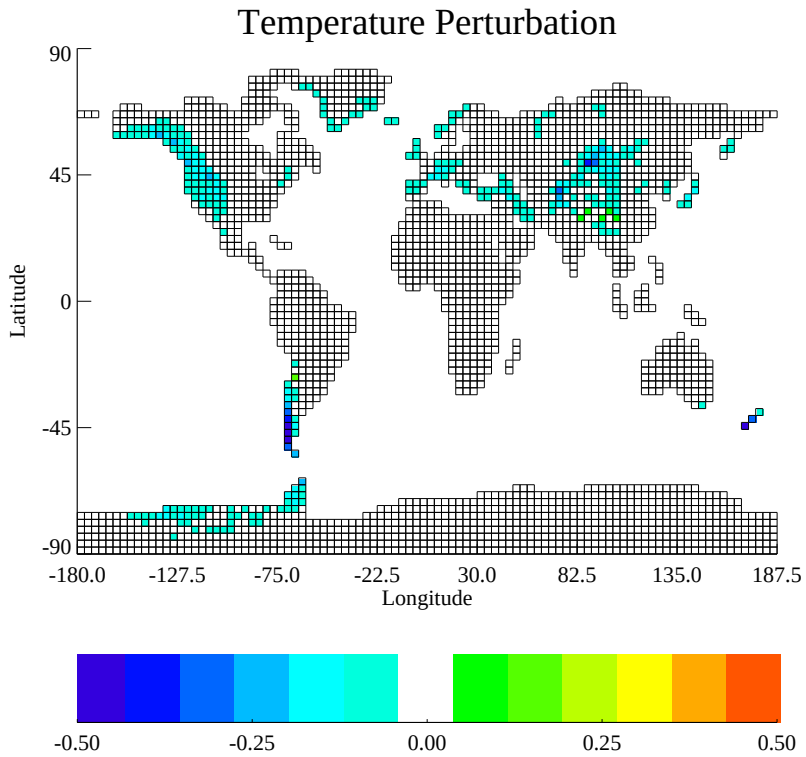

Figure 9.4: Mean temperature perturbation generated by the parameterised gravity waves in level eleven of PARAM

where increases in high cloud are seen (e.g. New Zealand and the Andes). This implies that the dominant vertical wavelength of the gravity waves over these mountains is such that descent occurs in the middle troposphere (see also figure 5.2). Generalising, it is possible to conclude that due to the predominent atmospheric conditions the parameterisation increases low level cloud, decreases middle cloud and again increases high cloud over many mountain ranges.

Considering the conclusions reached about the CONTROL run it not surprising that the extra cloud generated by the parameterisation is primarily optically thick. Any extra cloud generated by the parameterisation will suffer from the same problems as the extra cloud created by the resolved orography that result in it being optically thick. This issue emphasises that extra model levels need to be included in the upper troposphere to correctly simulate optically thin cirrus.

Like the CONTROL run, there is little evidence of significant advection of high cloud. Thus, the trailing cirrus clouds (or high clouds) seen in observations, and one of the motivations of this work, are not created. Since it is the ice that is actually advected, it is worth considering a global plot of the statistically significant difference in the level eleven ice amount between the simulations (figure 9.7). In this instance it is the ice amount after the dynamics, but before the microphysics (i.e the ice that the cloud scheme sees).

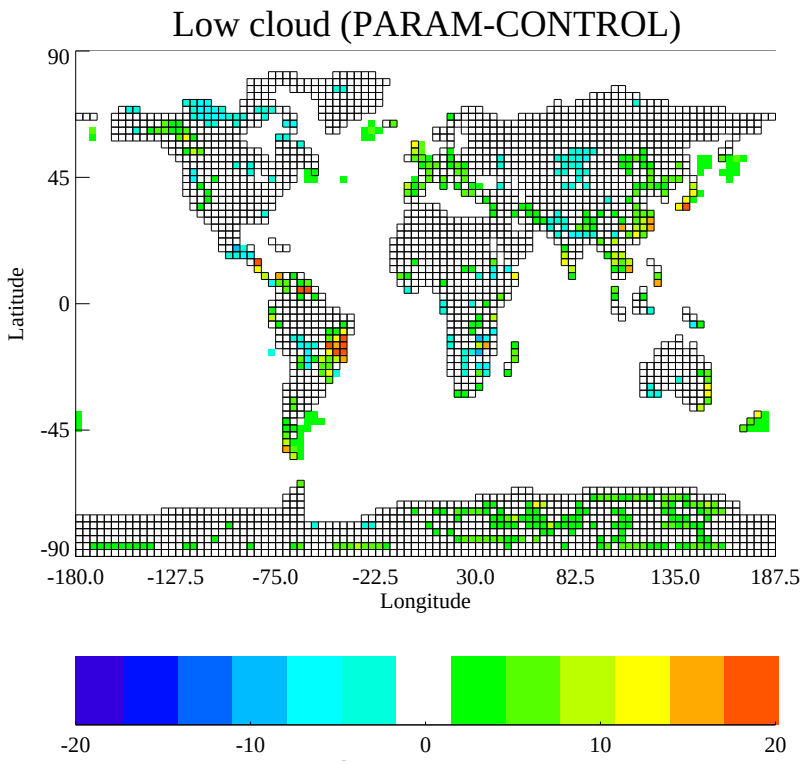

Figure 9.5: Global statistically significant difference in low cloud amount (F33) between the PARAM run and CONTROL run.

The dominant changes in ice are increases over many parts of the globe, many of which can be linked to the parameterisation. Over the Himalayas in particular the changes in high cloud can be directly linked to the large increases in ice amount. Differences can be seen over South America and New Zealand with changes also apparent in the first adjacent downstream gridbox. There is clearly some advection of extra ice, but the diagnosis of extra cloud is obviously also sensitive to whether there is a temperature perturbation. Again ice is not advected beyond the first downstream gridbox and is destroyed by the microphysics, as for the control run. From this figure it is also apparent that there have been changes in ice amounts over ocean areas due to subsequent effects. This has occurred mostly at midlatitudes.

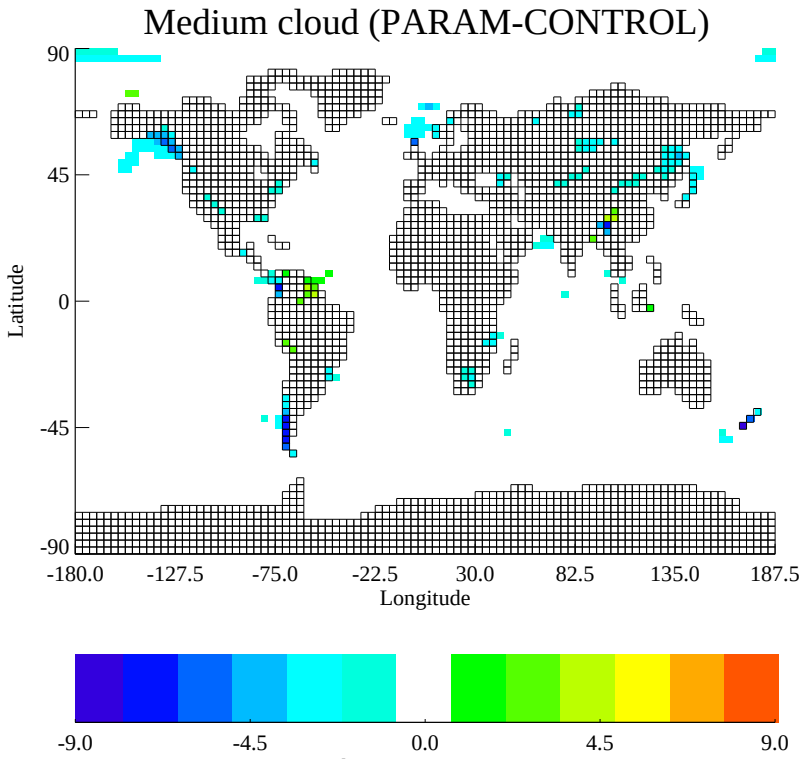

Figure 9.6: Global statistically significant difference in middle cloud amount (F32) between the PARAM run and the CONTROL run.

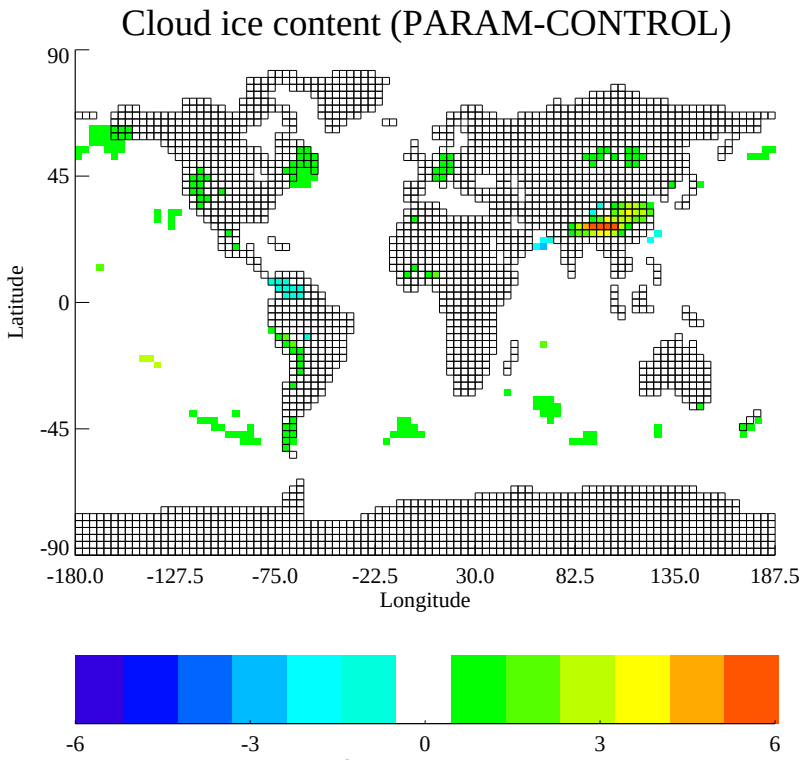

Figure 9.7: Global statistically significant difference in mean ice amount between the CONTROL run and PARAM run for level eleven.

9.1.2 New Zealand

It is again useful to consider more closely the effect of the parameterisation over New Zealand. Figure 9.8 is the change in cirrus amount over the southern most New Zealand land point (solid line), the upstream sea point to the west (dashed line) and the downstream sea point to the east (dash-dot line). This difference is simply the ordinary numerical difference between PARAM and CONTROL. Over New Zealand there is a strong expectation for both small and large changes in cloud to be generated by the parameterisation. Using the normal test for statistical significance causes some of these changes to be lost. For completeness, and to help in consideration of the global results, figure 9.9 shows which of these changes is statistically significant with 99% confidence. The two figures are the most informative when used in combination.

Over the NZ land point (solid line) there is an increase in cirrus cover ranging from 0.5%-3.0% for all months except May and September, when there is a decrease. However, only in two of the months are any of these changes statistically significant. These are over the land point in February and for the land and downstream points in October.

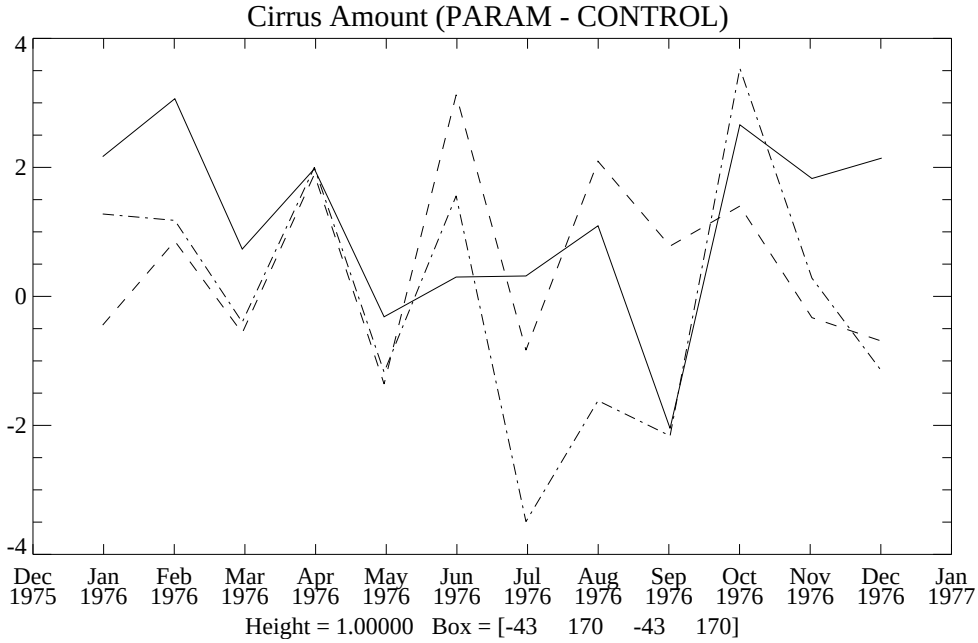

Figure 9.8: Difference in the monthly climatological cirrus amount for a New Zealand land point (solid line) and the adjacent sea points to the west(dashed line) and east (dashed-dot line) between CONTROL and PARAM. The year 1976 indicates climatological mean data.

Examining a longitude slice of simple cirrus differences (figure 9.10) reveals that the increase in June in figure 9.8 is due to a general change in the amount of model cirrus upstream. The figure also highlights that in April and October there is some evidence of

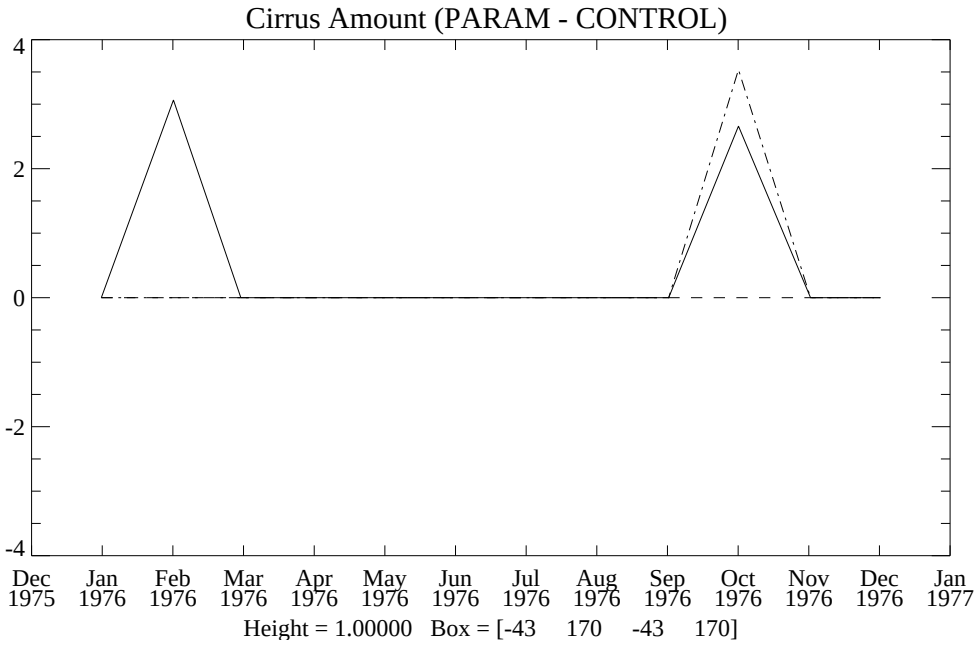

Figure 9.9: The same as for 9.8 but with only the statistically significant differences shown (99% confidence).

possible cirrus advection, although the reasons for this may be to do with low cloud, as was identified for the control run. More generally there is a decrease in cirrus downstream. All of these changes are, however, very small and unable to satisfy the deficiencies in model cirrus compared to the ISCCP observations.

Of more interest, and easier to interpret, is the change in high cloud amount over New Zealand, for both ordinary differences, figure 9.11, and significant ones, figure 9.12. It is apparent that the parameterisation increases high cloud over the land in all months except July and December, where there is almost no change. The largest changes are in April, June and October, and in these months increases are also seen over the upstream and downstream points. It is these three months, along with March and January, for which the changes over land are statistically significant. The changes downstream are statistically significant in April and June.

The average increase in the difference in high cloud over the land point compared to upstream is about 6% cloud cover. Adding this to the increase already resolved by the model leads to an average total increase of about 13% cloud cover. The magnitude of this change brings the model into good agreement with the ISCCP observations (see figure 4.7). However the changes obviously cannot solve the problems of too much high cloud upstream or the seasonal trend (see figure 8.6). Additionally the cloud is optically thick rather than thin.

A longitude slice of the simple high cloud difference, figure 9.13, reveals that the large

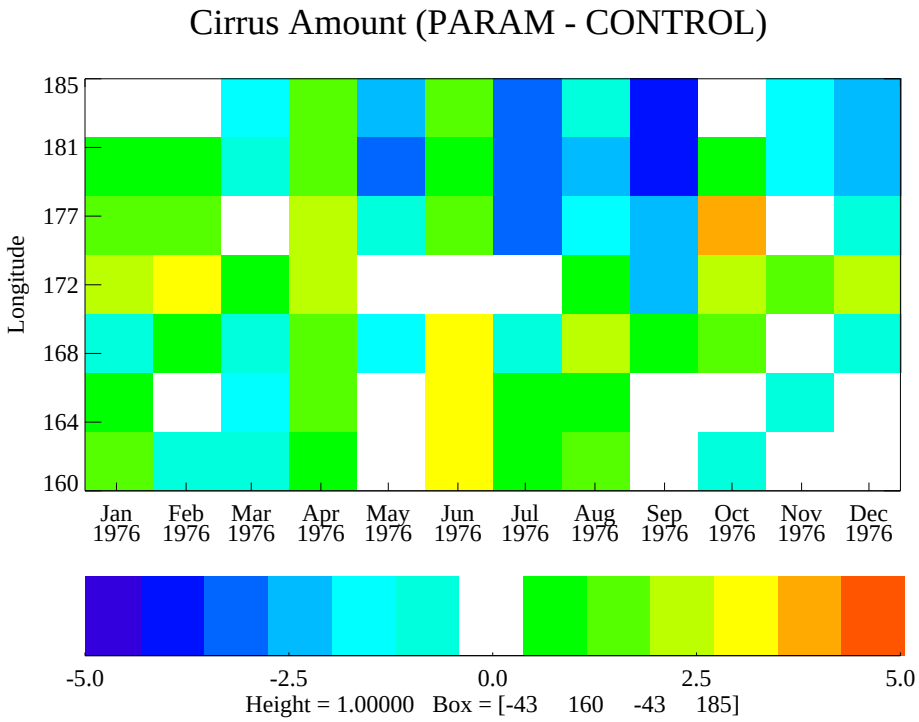

Figure 9.10: NZ longitude slice of the difference in cirrus amount between CONTROL and PARAM.

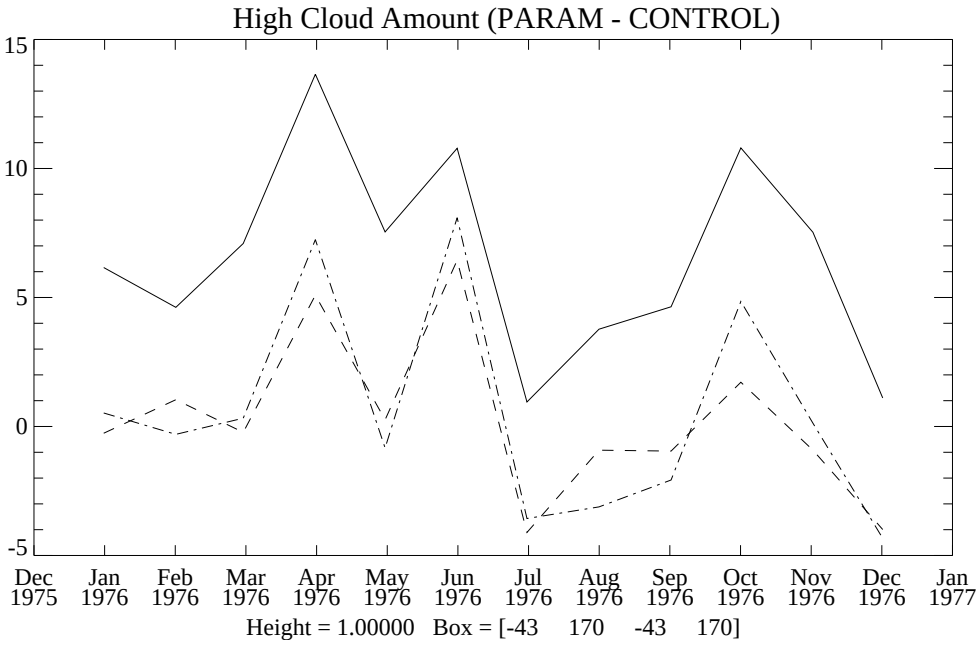

Figure 9.11: As for figure 9.8 but showing the differences in high cloud amount.

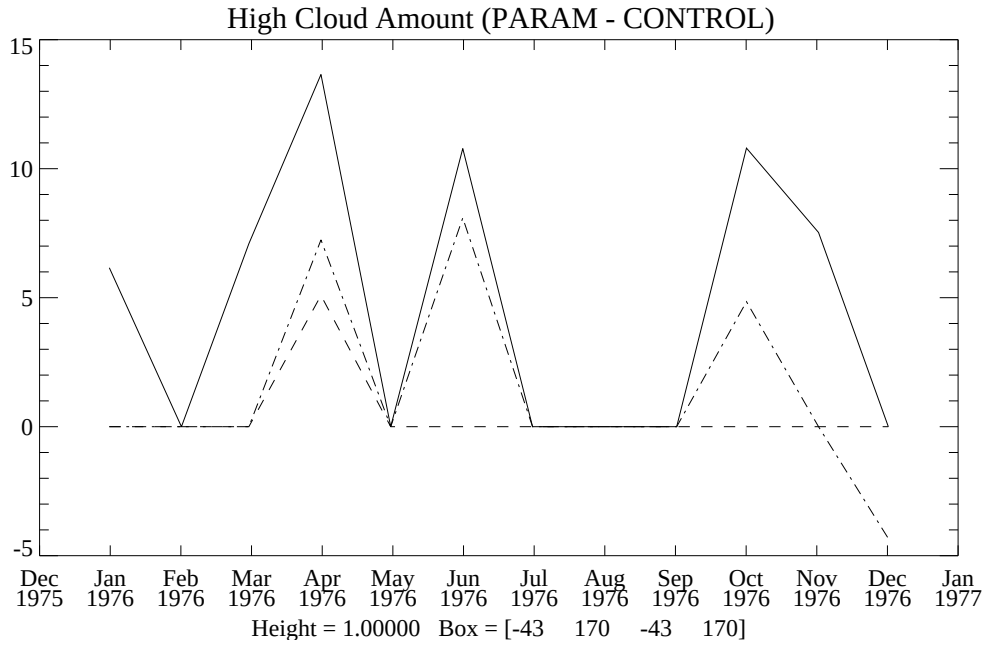

Figure 9.12: As for figure 9.11 but showing the statistically significant differences in high cloud at 99% confidence.

increase in June can again be seen to be associated with a change in the June climatological amount of high cloud upstream. While there is an increase in most months over the land point of between 5% and 15% cloud cover, only in April and October is there any evidence of trailing lee clouds. Also the slight increases in the upstream box are suggestive of the possibility that any ice generated is being significantly diffused into other gridboxes.

Figure 9.14 is a longitude slice of the change in ice amount. Ice amounts increase between 1×10^{-6} and 2×10^{-6} over the land point compared to upstream in all months except in May, July and August. It is clear that the trailing lee clouds seen in April and October are created by the increase in advected ice seen downstream of NZ. The June upstream levels of ice have increased slightly which will contribute to the extra high cloud being diagnosed in June. These results emphasise that trailing lee wave clouds are created once enough ice is generated to survive evaporation by the microphysics.

It is important to consider the behaviour of the gravity wave part of the parameterisation. As such, the climatological monthly mean amplitude of the gravity waves over New Zealand is shown in figure 9.15. The parameterisation appears to be performing well, with particularly large mean wave amplitudes around March and October. The seasonal pattern shows larger waves in the summer months compared to the winter. April shows the highest level of variability in wave amplitude. As identified in the testbed (section 7.8) the wave amplitudes will be controlled by many factors including the wind speed, wind direction and shears in the wind and stability. Strong winds perpendicular to New

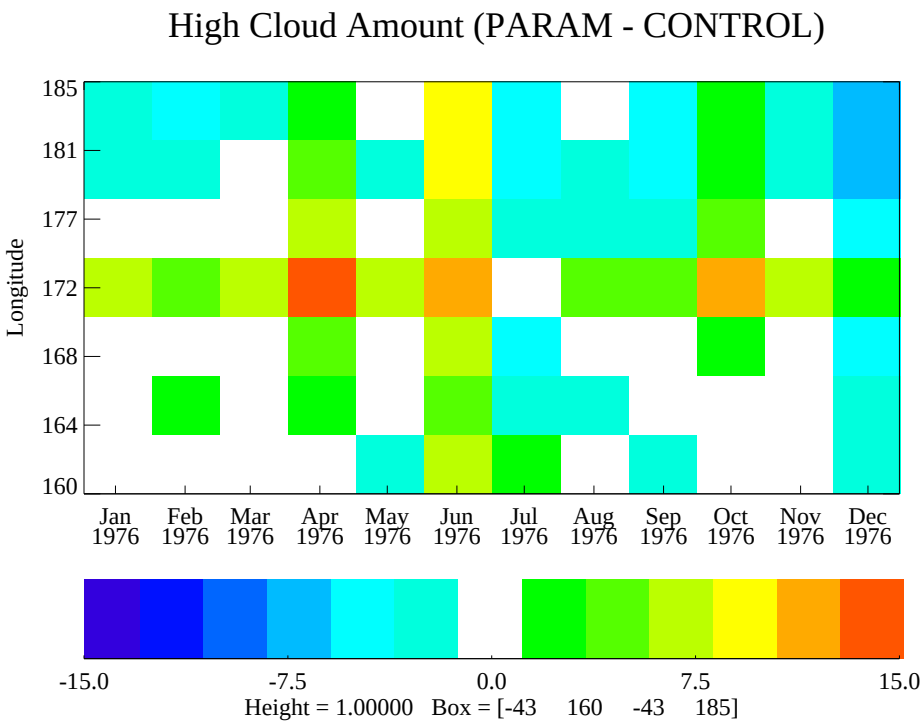

Figure 9.13: NZ longitude slice of the differences in high cloud amount between CONTROL and PARAM

Zealand mountains will reduce any flow blocking, while higher up strong winds will increase the saturation amplitude. Figure 9.16 shows the component of the model wind in level eleven which is perpendicular to the major orientation of New Zealand's mountains (325°). The similarity to figure 9.15 shows that the parameterisation is responding to the model winds.

The changes in cloud are influenced more directly by the temperature perturbation generated by the gravity waves (figure 9.17). As would be expected, a similar pattern is seen in the temperature perturbations where the coolings are strongest in Summer. Slight differences in some months may well result from the further dependence on the background temperature structure. Overall the patterns correspond well with the changes in high cloud identified in figure 9.13, though the lack of exact correspondence of the peaks further emphasises the importance of other factors such as the frequency of occurrence and the availability of water vapour.

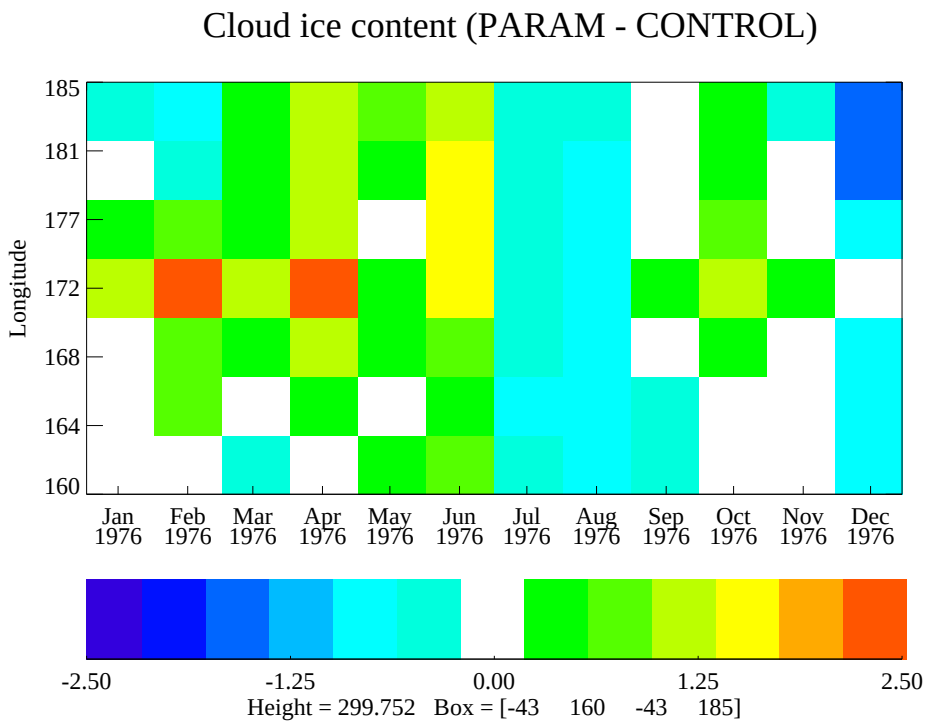

Figure 9.14: NZ longitude slice of the differences in the level eleven ice amount between CONTROL and PARAM. Ice amounts have been multiplied by 1×10^6 for presentation.

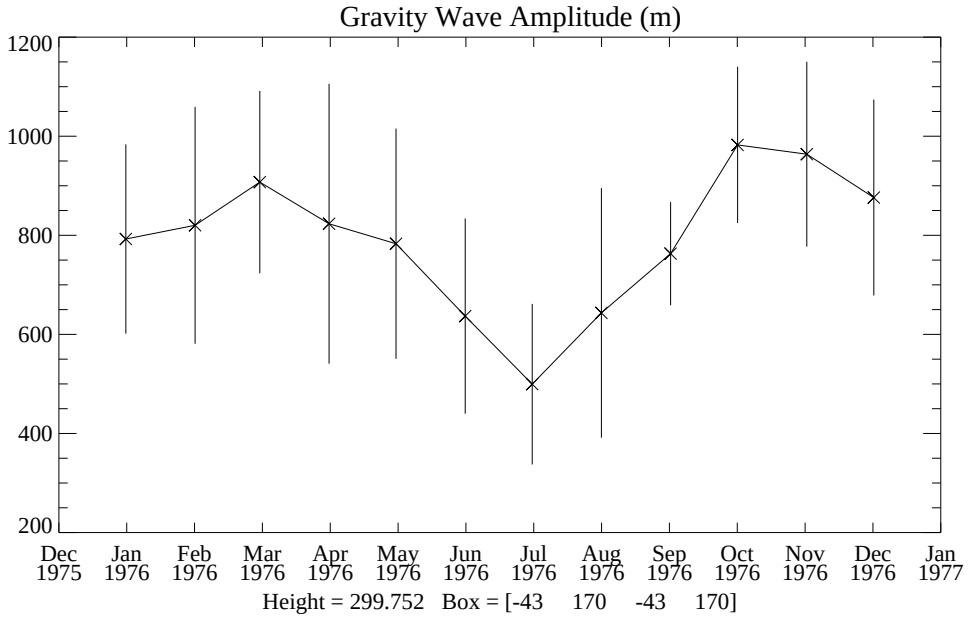

Figure 9.15: Mean amplitude (m) of the parameterised gravity waves in level eleven over NZ. Vertical bars indicate one standard deviation, with respect to the 10 months, either side of the climatological monthly mean.

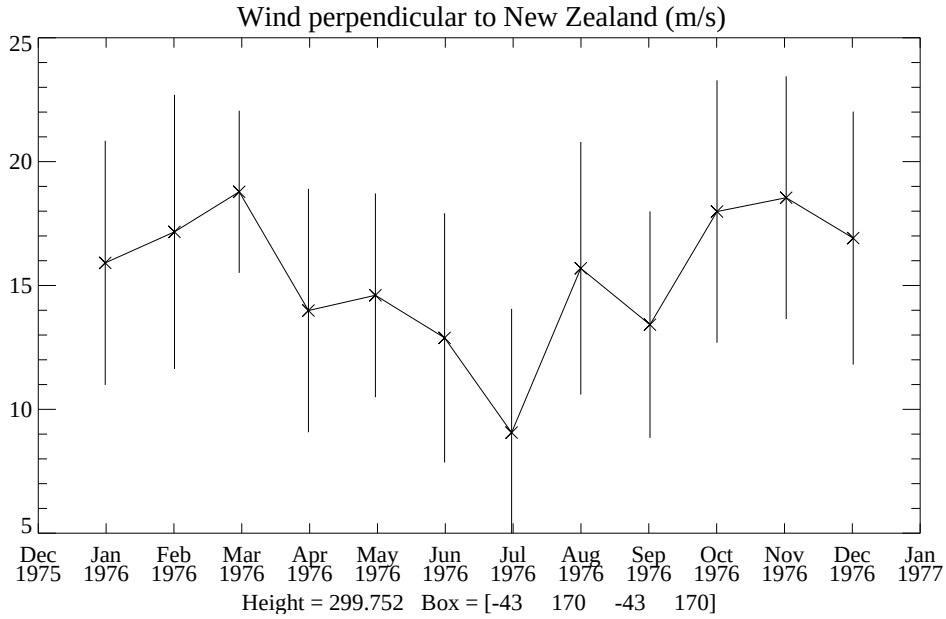

Figure 9.16: Mean of the PARAM component of the level eleven wind (ms^{-1}) perpendicular to the orientation of New Zealand's mountains. Vertical bars indicate one standard deviation, with respect to the 10 months, either side of the mean.

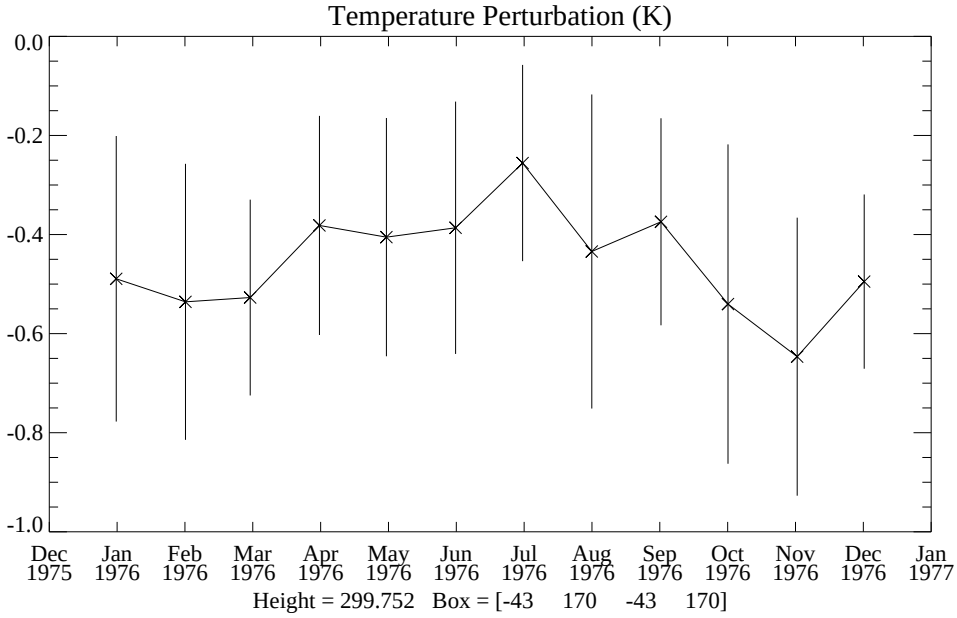

Figure 9.17: Mean temperature perturbation generated by the parameterised gravity waves over NZ in level eleven of the PARAM run. Vertical bars indicate one standard deviation, with respect to the 10 months, either side of the climatological monthly mean.

9.1.3 Cloud radiative forcing

Clearly the parameterisation has significantly changed the high cloud cover in some areas. Whether the model is sensitive to these changes in terms of the radiative balance can be considered by re-examining the cloud radiative forcing. Figure 9.18 is the difference in shortwave cloud radiative forcing between PARAM and CONTROL. There has been a significant increase in the cloud radiative cooling (i.e. blue means that PARAM has a more negative forcing and should be compared with figure 8.17) over a number of land based areas. Some of these areas, such as in Asia and South America, are the same ones in which a decrease in cirrus was seen in figure 9.1. This change in cirrus was identified as being a re-classification caused by an increase in the amount of low level cloud. Areas where there were large increases in high cloud, such as the bottom of South America show no changes in the cloud radiative forcing, suggesting the model is insensitive to changes at these heights.

The areas of weaker longwave forcing (blue, compare with figure 8.16) in figure 9.19 are also most likely caused by the decrease in low level cloud, which strongly absorbs longwave radiation. The stronger longwave forcing over the Himalayas (red) is caused by the increase in cloud generated by the parameterisation. Once again the model is insensitive to the changes in cloud seen at midlatitudes. It seems that the model is quite sensitive to the changes in cloud generated by the parameterisation in equatorial regions.

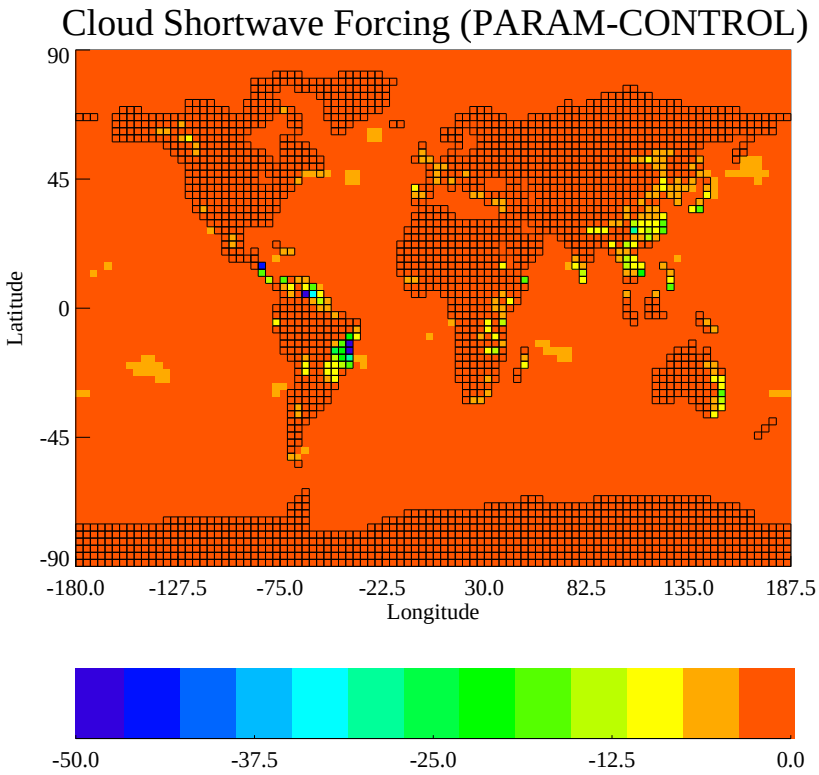

Figure 9.18: Difference in the shortwave cloud radiative forcing (Wm^{-2}) between CONTROL and PARAM.

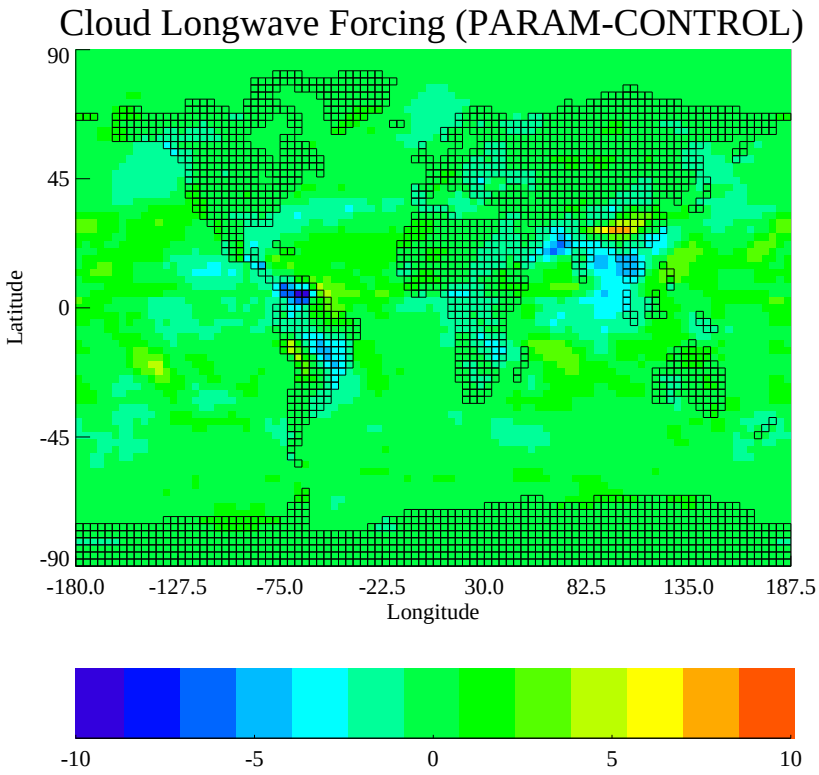

Figure 9.19: Difference in the shortwave cloud radiative forcing (Wm^{-2}) between CONTROL and PARAM.

9.2 Conclusions

The parameterisation succeeded in producing increases in the amount of high cloud over some of the Earth's major mountain ranges. However, the parameterisation was unable to significantly increase thin cirrus amounts. Over New Zealand small changes in cirrus were observed but on a global scale these changes were insignificant.

That the extra cloud created is optically thick is likely to be due to the fact that the parameterisation will cause coherent cooling over a number of model levels (whose spacing is of the order of 1 km in the upper troposphere). It is possible that because the humidity profiles in the UM are often very smooth (see figure 7.11) the model does not capture the strongly layered structure of the real atmosphere.

There was also no evidence of high cloud advection in the global figures, despite evidence of ice advection into the first grid box downwind of mountain ranges. Over New Zealand ice generation over the orography was large enough in some months for ice to be advected considerable distances downstream. However, this was one of the strongest areas of parameterisation activity. In general the lack of trailing lee clouds was further evidence (following chapter 8) that the microphysics parameterisation in the model has insufficient capacity to allow for ice hysteresis.

The changes in high cloud were clearly linked to strong temperature perturbations generated by the parameterisation. There were weak temperature perturbations over much of the world's orography but these did not generate statistically significant changes in high cloud. This widespread activity was reflected more in the large changes in low cloud amounts. This is may be a useful effect of the parameterisation, as low cloud amounts are increased over high orography by lifting that occurs directly adjacent to the surface, but would require further investigation. The changes in the global cloud radiative forcing were also predominantly associated with the large increases in low cloud generated by the parameterisation. Only over the Himalayas did the changes in high cloud have a significant effect. This does suggest that future work should examine more closely the parameterisations effect on low cloud and the relationship with observations of cloud radiative forcing such as that provided by the Earth Radiation Budget Experiment (ERBE).

The parameterisation was also found to be inherently limited in its ability to modify the seasonal trends in orographic cloud compared to observations by the ability of the model to correctly simulate the observed peaks in winds as seen in the ERA analysis (chapter 4).

Additional simulations that address the impact of the temperature perturbation in diagnosis of cloud amount and the tuning of the parameterisation can be found in appendix D.

Chapter 10

Summary

It is important to draw together the findings of this thesis and address the aims, as laid out in the introduction. These were to investigate the nature of orographic wave clouds as well as to consider their simulation in a global climate model. Because of the current horizontal resolution of climate models many of the gravity waves that generate orographic clouds are not resolved and so models cannot correctly simulate these clouds. Thus it was hoped to introduce a parameterisation of orographic cloud into the Unified Model. The key findings for each chapter will now be summarised. This allows fresh connections between the different parts to be identified. Suggestions for further work and development of the parameterisation are also made.

10.1 Observations

New Zealand was identified as an ideal location for studying orographic clouds. A frequent orographic cloud known as a Northwest Arch was analysed as a dramatic example of orographic cirrus generation. Satellite images identified that it is the orographic cirrus component of the Northwest Arch that is advected for hundreds of kilometres downstream of the mountains. Observations from glider pilots emphasised the smooth nature and dramatic lift velocities of the gravity wave that generates the orographic cirrus. Modelling studies showed that a stationary large amplitude gravity wave is most likely responsible for this, as opposed to a large, highly nonlinear, hydraulic jump mechanism.

The satellite cloud climatology of *Uddstrom et al.* (2001) showed that high level orographic cirrus exists over, and for a large area in the lee of the South Island, at all times of year. The mean frequency of occurrence is about 25%. This compares with the upstream cirrus frequencies of about 10%. Cirrus frequency was also found to be higher around the equinoxes, when the westerlies are strongest.

Fifteen years of ISCCP cloud observations were also used to study the global coverage. Over New Zealand there was a significant increase in cirrus at all times of year with absolute changes in the range of 4% to 12% cloud cover. However the seasonal cycle predominantly showed more cirrus in summer and less in winter. Globally the ISCCP analysis showed significant increases in cirrus over many land areas compared to the oceans in general.

Winds from the ECMWF ERA-15 Reanalyses were used in conjunction with a topographical dataset to identify areas of potentially strong gravity wave activity across the globe. The strongest of these areas show a good qualitative correlation with areas of high cirrus amounts over land seen in the ISCCP data. This gives confidence that these cirrus clouds are, at least partially, of orographic origin. Except for New Zealand, the seasonal cycle in wave activity was not correlated with changes in global cirrus amounts. This emphasised the importance of other factors such as seasonal changes in humidity and the possibility of convectively generated cirrus over orography.

10.2 Testbed

All of these observations suggested that the simulation of orographic cirrus in the Unified Model could be improved by implementing an orographic cirrus parameterisation which was based on linear hydrostatic gravity wave theory. Gravity waves have been parameterised in GCMs for a number of years but only in the way that they act as a drag on the winds in the atmosphere. The idea of the parameterisation in this thesis was to predict the temperature perturbations caused by gravity waves. These could then be used to generate orographic clouds in the existing cloud scheme.

In order to develop and validate the parameterisation an offline testbed was constructed. Studies using this testbed showed that a linear hydrostatic gravity wave scheme was capable of being used to generate orographic cloud directly over orography. A feature of the scheme is that the launch amplitude of the gravity waves is predicted by a directional variance function which accounts for anisotropy in the subgrid orography. This was shown to give a reasonable representaion of the true variance in the topography for different wind directions.

Idealised simulations using the testbed, with constant wind and stability, correctly simulated the vertical wavelength predicted by the analytical solution. When wind shear was introduced the parameterisation exhibited complex behaviour which was caused by competing effects. Positive shears in wind and stability act to dampen the wave growth due to decreasing density. The saturation mechanism was found to be more important in limiting wave growth in the stratosphere than the troposphere.

A realistic profile over New Zealand for a situation in which orographic cirrus is expected showed that the parameterisation is capable of significantly increasing the amount of orographic high cloud. In a situation that is ideal for the formation of orographic cirrus, cloud cover fraction over orography increased significantly from 0.05 to 0.4.

Within the testbed the parameterisation was also compared with a nonlinear two dimensional high resolution model forced by observations. The mesoscale model, which includes considerably more physical processes than the parameterisation, showed good

agreement, particularly in the amplitude. This gave confidence in the model's ability to reproduce the 'average' effect of gravity waves in producing orographic clouds.

10.3 Unified Model Simulations

Before considering the effect of the orographic cloud parameterisation in the UM it was necessary to examine control runs of the model. Climatological cloud amounts were compared to the ISCCP cloud amounts. The UM was found to be significantly lacking in optically thin cirrus, over both ocean and land when compared to ISCCP. The major deficiencies existed over high orography. It was found that the model did produce extra high cloud over orography, but not extra cirrus. Despite the extra optically thick cloud the model still showed a deficiency in the total high cloud compared to the observations.

There was also no evidence that any of the additional high cloud generated over New Zealand, or globally, was being advected downstream. While there was a considerable amount of ice advection into the first gridbox downstream of New Zealand it was evaporated by the microphysics. Thus large trailing orographic clouds were not observed in the control run.

A simulation that was identical except for the inclusion of the orographic cloud parameterisation was then analysed. The implementation included the temperature perturbation predicted by the gravity wave scheme being applied to the microphysics to generate extra ice over the orography. It was hoped that this extra ice would then be advected downstream by the model advection scheme to create trailing cirrus clouds.

The parameterisation succeeded in producing increases in the amount of high cloud over some of the world's major mountain ranges. However as with the control run experiment, there was no evidence of statistically significant high cloud advection in the global figures, despite evidence of ice advection into the first grid box downwind of mountain ranges. Over New Zealand ice generation over the orography was large enough in some months for ice to be advected considerable distances downstream. However, globally this was one of the strongest areas of parameterisation activity. In general the lack of trailing lee clouds was further evidence that the microphysics parameterisation in the model has insufficient capacity to allow for ice hysteresis.

The changes in high cloud were clearly linked to strong temperature perturbations generated by the model. The model showed weak temperature perturbations over much of the world's orography but these did not generate statistically significant changes in high cloud. This widespread activity was reflected more in the large changes in low cloud amounts. This is potentially a useful effect of the parameterisation as low cloud amounts are increased over high orography by lifting occuring directly adjacent to the surface.

The changes in the global cloud radiative forcing were predominantly associated with

the large increases in low cloud generated by the parameterisation. Only over the Himalayas did the changes in high cloud have a significant effect.

10.4 Future Work

There are a number of obvious areas of future work. The first would be to run simulations of the UM in a configuration that would provide higher resolution in the upper troposphere. A thirty one level version of the UM, which has the same top pressure level, has been successfully used elsewhere. The extra twelve levels are primarily distributed so as to give extra resolution about the tropopause. This would then require evaluating the impact on global cirrus from simply the increase in resolution, as well as effect on the resolution of the gravity wave and finally the effect on the parameterisation. Additionally, it will be necessary to investigate the humidity distributions simulated by the model and how well they compare with what is observed in reality.

The apparent lack of ice hysteresis in the mixed phase precipitation scheme represents a major hurdle to the simulation of large trailing orographic cirrus clouds. The ice transfer equations were probably not designed with these sort of clouds in mind; the simulation of anvil cirrus from cumulus convection is more of a priority. Thus a full investigation of how changing the formulation of the microphysics might help achieve better ice advection is necessary.

Even without adequate ice advection the parameterisation has demonstrated that a useful contribution to the cloud cover simulated over orography can be made . However a number of steps still need to be taken before the scheme could be given wider release in the UM. By also using the scheme to predict the drag on the atmosphere due to gravity waves, only one gravity wave scheme would be needed in the model. The drag predicted should be as good as that predicted by the existing scheme, although this would need verification. Alternatively the existing gravity wave drag scheme could be modified to include phase information and then the assumption that the wave amplitude is proportional to the stress could be made. This would still require the gravity wave scheme to be moved in the subroutine hierarchy to allow it to be called before the other physics subroutines, but there is no apparent reason why this would be an obstacle.

Further validation of the parameterisation using the testbed is required. The obvious first step would be to compare the cloud cover predicted by the model, with and without the parameterisation, to that predicted by a high resolution mesoscale model capable of resolving small scale gravity waves. The model would need to include moist physics and the ability to predict cloud cover. This could be done for both idealised topography profiles and realistic ones. This setup would allow for comparisons with the paramterisation similar to those done over the Andes in section 7.8.4, but this time with consideration of

the actual cloud amounts produced as well as the nature of the gravity waves.

A number of case studies should also be performed inside the UM to see whether orographic clouds are realistically simulated. To assist in this work a more refined version of the SRTex algorithm described in section 3.2 has been run on a year of AVHRR data from April 1998 to April 1999 by NIWA in New Zealand. This includes classification of the cloud cover on the 4^{th} October 1999, when a significant orographic cirrus cloud was observed over the South Island of New Zealand (see figure 3.13). A case study will be run for this date where the Unified Model is initialised by data from the ECMWF operational analyses for this time. These analyses give the best possible representation of the atmospheric winds and humidity upstream of New Zealand at this time. Importantly a short period case study will also enable timestep by timestep evaluation of the behaviour of the ice advection in the model.

Since this new SRTex data covers 13 months it will be analysed in detail for orographic cloud cover. It will also enable a more direct comparison between ISCCP and SRTex to see how well the global dataset identifies small scale orographic cirrus.

Appendix A

Images of the Northwest Arch

In this appendix photos of the Northwest Arch, referred to in the main body of the thesis, are presented. These are primarily shown to help in appreciation of the dramatic size and appearance of Northwest Arch clouds, as well as to observe their evolution in time.

Figure A.1: An early prefrontal arch beginning to form (11 March 1990). The cloud was observed to be thin and high. No low level clouds can be seen. From *Rankin* (1990).

Figure A.2: A more developed Arch cloud (12 March 1990). In the original photo low level rotor clouds can be identified. This is the Arch that *Rankin* (1990) flew a BAC Strikemaster jet through. From *Rankin* (1990).

Figure A.3: This photo is of stacked lenticular clouds which are different from the Northwest Arch in that they are associated with individual mountain ranges and thus do not form a continuous band of cloud (December 1989, day unknown). From *Rankin* (1990).

Figure A.4: An example of a contoured Arch in Rankin's description category. The photo is from the early morning of May 1990. From *Rankin* (1990).

Figure A.5: The Northwest Arch which *Hamilton* (1992) flew his glider through on July 19^{th} 1992. From *Hamilton* (1992).

Figure A.6: A photo of an intense Northwest Arch taken from the Port Hills in Christchurch looking back towards the mountains (October 1999, day unknown). Associated with this arch were very strong north west winds down to ground level.

Appendix B

WKBJ Solution for a Bell Shaped Ridge

In this thesis the WKBJ solution for the flow over a two dimensional bell shaped ridge is used. Since this solution has not been presented in the literature it is derived here. The derivation of the linear wave equation is in the body of the thesis and this derivation will follow the nomenclature used there. Thus the two dimensional Fourier transform of the vertical velocity perturbation can be defined as

$$\tilde{w}(k,z) = \frac{1}{\pi}\int_{-\infty}^{\infty} \hat{w}(x,z)\mathrm{e}^{-ikx}dx \tag{B.1}$$

where $\hat{w}$ is the scaled vertical velocity perturbation

$$\hat{w} = \left(\frac{\overline{\rho}(z)}{\overline{\rho}(0)}\right)^{\frac{1}{2}} w' \tag{B.2}$$

Then $\tilde{w}$ must then satisfy the Fourier transform of the wave equation (5.18),

$$\frac{\partial^2 \tilde{w}}{\partial z^2} + \left(l^2 - k^2\right)\tilde{w} = 0 \tag{B.3}$$

where,

$$l^2(z) = \frac{N^2}{\overline{u}^2} - \frac{1}{\overline{u}}\frac{\partial^2 \overline{u}}{\partial z^2} \tag{B.4}$$

To solve this equation upper and lower boundary conditions are needed. The upper condition is simply a 'radiation' condition that implies that there are no components of the flow that radiate energy downwards. The lower condition is that at the ground the flow must follow the topography. In Fourier terms this is

$$\tilde{w}(k,0) = \overline{u}(0)ik\tilde{h} \tag{B.5}$$

where $\tilde{h}(k)$ is the Fourier transform of the topography which in the case of a bell shaped ridge of maximum height h_m and half width a is

$$\tilde{h}(k) = h_m a\mathrm{e}^{-ka} \tag{B.6}$$

To solve B.3 using the WKBJ approximation we need to look for solutions of the form

$$\tilde{w} = A(z)\mathrm{e}^{i\Phi(z)} \tag{B.7}$$

where the radiation condition ensures the choice of the positive exponent. Substituting this into equation B.3 and equating complex and non-complex parts gives two equations,

$$\frac{\partial A}{\partial z}\frac{\partial \Phi}{\partial z} + A\frac{\partial^2 \Phi}{\partial z^2} + \frac{\partial A}{\partial z}\frac{\partial \Phi}{\partial z} = 0 \tag{B.8}$$

$$-A\left(\frac{\partial \Phi}{\partial z}\right)^2 + \frac{\partial^2 A}{\partial z^2} + \left(l^2 - k^2\right)A = 0 \tag{B.9}$$

The first order solution of B.9 involves ignoring the second derivative. Integrating then gives

$$\Phi = \int_0^z (l^2 - k^2)^{\frac{1}{2}}\, dz \tag{B.10}$$

Substituting equation B.9 into B.8 and integrating leads to the result,

$$A = \frac{A(0)}{(l^2 - k^2)^{\frac{1}{4}}} \tag{B.11}$$

Then substituting these two results back into B.6 gives

$$\tilde{w}(k, z) = \frac{A(0)}{(l^2 - k^2)^{\frac{1}{4}}}\mathrm{e}^{i\int_0^z (l^2-k^2)^{\frac{1}{2}}\, dz} \tag{B.12}$$

Using the bottom boundary condition,B.5

$$A(0) = \overline{u}(0)ikh_m a\mathrm{e}^{-ka}(l^2(0) - k^2)^{\frac{1}{4}} \tag{B.13}$$

which substituted back into B.12 leads to the solution for $\tilde{w}$. Taking the inverse Fourier transform of this solution gives the scaled velocity perturbation in real space.

$$\hat{w}(x, z) = Re\int_0^\infty \frac{\overline{u}(0)ikh_m a(l^2(0) - k^2)^{\frac{1}{4}}}{(l^2 - k^2)^{\frac{1}{4}}}\mathrm{e}^{-ka}\mathrm{e}^{i\int_0^z (l^2-k^2)^{\frac{1}{2}}dz}\mathrm{e}^{ikx}\, dk \tag{B.14}$$

The integration is made easier by solving for the vertical displacement, $\eta(x, z)$, defined as

$$w' = \overline{u}\frac{\partial \eta}{\partial x} \tag{B.15}$$

which using B.2 means that,

$$\eta(x,z) = \frac{1}{\overline{u}}\left(\frac{\overline{\rho}(0)}{\overline{\rho}}\right)^{\frac{1}{2}} \int \hat{w}\, dx \tag{B.16}$$

Using this result and making the hydrostatic approximation that $k \ll l$ leads to

$$\eta(x,z) = \left(\frac{\overline{\rho}(0)}{\overline{\rho}}\right)^{\frac{1}{2}} \frac{\overline{u}(0) h_m a l^{\frac{1}{2}}(0)}{\overline{u} l^{\frac{1}{2}}} Re\left(\mathrm{e}^{\int_0^z l\, dz} \int_0^\infty \mathrm{e}^{-k(a-ix)}\, dk\right) \tag{B.17}$$

Integrating and taking the real part,

$$\eta(x,z) = \left(\frac{\overline{\rho}(0)}{\overline{\rho}}\right)^{\frac{1}{2}} \frac{\overline{u}(0) h_m a l^{\frac{1}{2}}(0)}{\overline{u} l^{\frac{1}{2}}} \left(\frac{a\cos\left(\int_0^z l\, dz\right) - x\sin\left(\int_0^z l\, dz\right)}{a^2 + x^2}\right) \tag{B.18}$$

For any given z the WKBJ approximation allows the assumption that l, the Scorer parameter is changing so slowly that the second derivative term is negligible so that $l^2 = \frac{N^2(z)}{\overline{u}^2(z)}$ and thus

$$\eta(x,z) = h_m a \left(\frac{\overline{\rho}(0)\overline{u}(0)N(0)}{\overline{\rho}(z)\overline{u}(z)N(z)}\right)^{\frac{1}{2}} \left(\frac{a\cos\left(\int_0^z l\, dz\right) - x\sin\left(\int_0^z l\, dz\right)}{a^2 + x^2}\right) \tag{B.19}$$

It will also be useful to know the maximum and average displacement experienced by an air parcel as it moves along the trajectory predicted by B.19. This is not necessarily directly over the ridge. For the maximum this involves finding where

$$\frac{\partial \eta}{\partial z} = 0 \tag{B.20}$$

which is satisfied by,

$$x = a\left(\frac{\cos\left(\int_0^z l\, dz\right) \pm 1}{\sin\left(\int_0^z l\, dz\right)}\right) \tag{B.21}$$

Taking the second derivative of η and substituting the values of x from B.21 show that the choice of the negative sign gives the maximum displacement, $\eta_{\max}$, and the positive sign the minimum. Thus substituting B.21 into B.19 gives

$$\eta_{\max}(z) = h_m \left(\frac{\overline{\rho}(0)\overline{u}(0)N(0)}{\overline{\rho}(z)\overline{u}(z)N(z)}\right)^{\frac{1}{2}} \left(\frac{\sin^2\left(\int_0^z l\, dz\right)}{\sin^2\left(\int_0^z l\, dz\right) + \left[\cos\left(\int_0^z l\, dz\right) - 1\right]^2}\right) \tag{B.22}$$

Finding the average displacement, η_{mn}, involves solving the integral,

$$\eta_{\mathrm{mn}}(z) = \frac{h_m a}{2L}\left(\frac{\overline{\rho}(0)\overline{u}(0)N(0)}{\overline{\rho}(z)\overline{u}(z)N(z)}\right)^{\frac{1}{2}} \int_{-L}^{L}\left(\frac{a\cos\left(\int_0^z l\,dz\right) - x\sin\left(\int_0^z l\,dz\right)}{a^2+x^2}\right) dx \quad \text{(B.23)}$$

$$= h_m a\left(\frac{\overline{\rho}(0)\overline{u}(0)N(0)}{\overline{\rho}(z)\overline{u}(z)N(z)}\right)^{\frac{1}{2}} \frac{\cos\left(\int_0^z l\,dz\right)\tan\left(\frac{a}{L}\right)}{L} \quad \text{(B.24)}$$

where L is a distance from the ridge.

Appendix C

The Calculation of Cloud Variables

The exact equation for deriving cloud fraction using the triangular distribution function with standard deviation $\sigma_s = b_s/\sqrt{6}$ is:

$$C = \begin{cases} 0 & Q_N \leq -1 \\ \frac{1}{2}(1+Q_N)^2 & -1 < Q_N \leq 0 \\ 1-\frac{1}{2}(1-Q_N)^2 & 0 < Q_N < 1 \\ 1 & 1 \leq Q_N \end{cases} \tag{C.1}$$

where

$$Q_N = \frac{Q_c}{b_s} = \frac{a_L(q_t - q_s)}{b_s} \tag{C.2}$$

Similarly the normalised liquid water content is

$$q_N = \frac{q_c}{b_s} = \begin{cases} 0 & Q_N \leq -1 \\ \frac{1}{6}(1+Q_N)^3 & -1 < Q_N \leq 0 \\ Q_N - \frac{1}{6}(1-Q_N)^3 & 0 < Q_N < 1 \\ Q_N & 1 \leq Q_N \end{cases} \tag{C.3}$$

For the calculation of ice cloud fraction in the 2A and 2B schemes Q_N is found by inverting equation C.3 after assuming that $q_N = \frac{q_c}{b_s} = \frac{q_c^f}{b_s}$ so that

$$Q_N = \begin{cases} -1 & q_N = 0 \\ \sqrt[3]{6q_N} - 1 & 0 < q_N \leq \frac{1}{6} \\ 1 + 2\sqrt{2}cos\left(\frac{1}{3}cos^{-1}[\frac{3(1-q_N)}{2\sqrt{2}}] + \frac{4\pi}{3}\right) & \frac{1}{6} < q_N < 1 \\ q_N & 1 \leq q_N \end{cases} \tag{C.4}$$

Appendix D

Additional Unified Model Simulations

D.1 Microphysics

Chapter 9, in the main body of this thesis, raised the issue of the importance of temperature in the diagnosis of the ice cloud fraction. The suggestion was that perhaps it is the temperature perturbation in the cloud scheme that is creating all the extra cloud over orography, through the changing saturation point. It also implies the ice being created through the temperature perturbation in the microphysics has a lesser role. This would cause extra cloud to appear only directly over a mountain. It would also have implications for trailing lee wave clouds, in that even if ice is advected into adjacent gridboxes the absence of a temperature perturbation would lead to less cloud. To investigate this further a parameterisation run was performed in which the temperature perturbation calculated by the gravity wave scheme was only used in the cloud subroutine. This simulation was labelled PARAMNOICE.

Figure D.1 is the difference in high cloud between PARAM and PARAMNOICE for a longitude slice across New Zealand. Shown with the same range as figure 9.13, it is apparent that the temperature perturbation in the cloud scheme is responsible for about half the change in high cloud seen over the orography. Also the widespread change in high cloud seen in June in figure 9.13 is no longer present. The results confirm that downstream model temperatures will play a role in the diagnosis of the amount of ice cloud.

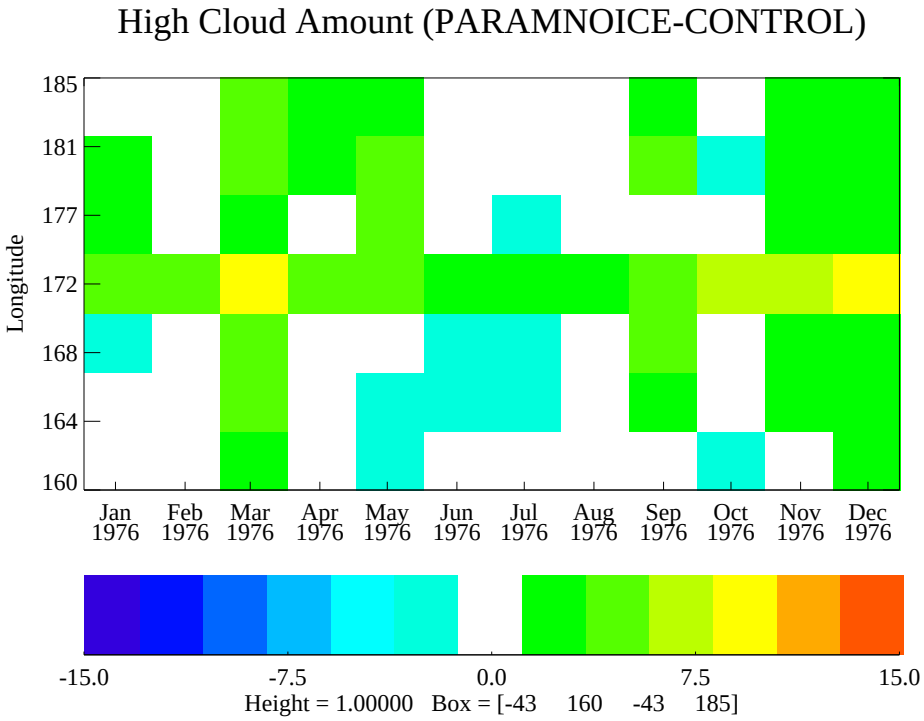

Figure D.1: NZ longitude slice of the difference in high cloud between PARAM and PARAMNOICE.

D.2 Coefficient Tuning

It is especially pleasing that the parameterisation has produced reasonable results with out the need to adjust tunable parameters. The only scalable parameter is the coefficient C, which has the value 6.3×10^8 and is used in the prediction of the launch amplitude. It is expected that the parameterisation should be fairly insensitive to changes in C as the atmosphere is usually saturated over large mountains and this will be the major constraint on wave amplitude. However, over small mountains the atmosphere will not be saturated so increasing C may result in larger amplitude waves being generated. To consider this two 10 year simulations were run, one with C increased to 1×10^9 (PARAM1E9) and another with C decreased to 5×10^8 (PARAM5E8). Changes of this order do significantly increase and decrease the launch amplitudes predicted by equation 7.21. From the earlier analysis it is the global high cloud that is a primary indicator in changes. As such figure D.2 is the difference in high cloud between PARAM and PARAM5E8 and similarly figure D.3 for PARAM and PARAM1E9. PARAM5E8, which included only a small decrease in C, shows virtually no significant changes over land compared to PARAM. There are considerable increases in high cloud in PARAM1E9 in association with the southern Andes but few changes elsewhere. Overall both simulations emphasise the relative insensitivity to small changes in C, which is probably related to waves over large mountains being immediately reduced in amplitute at launch by saturation.

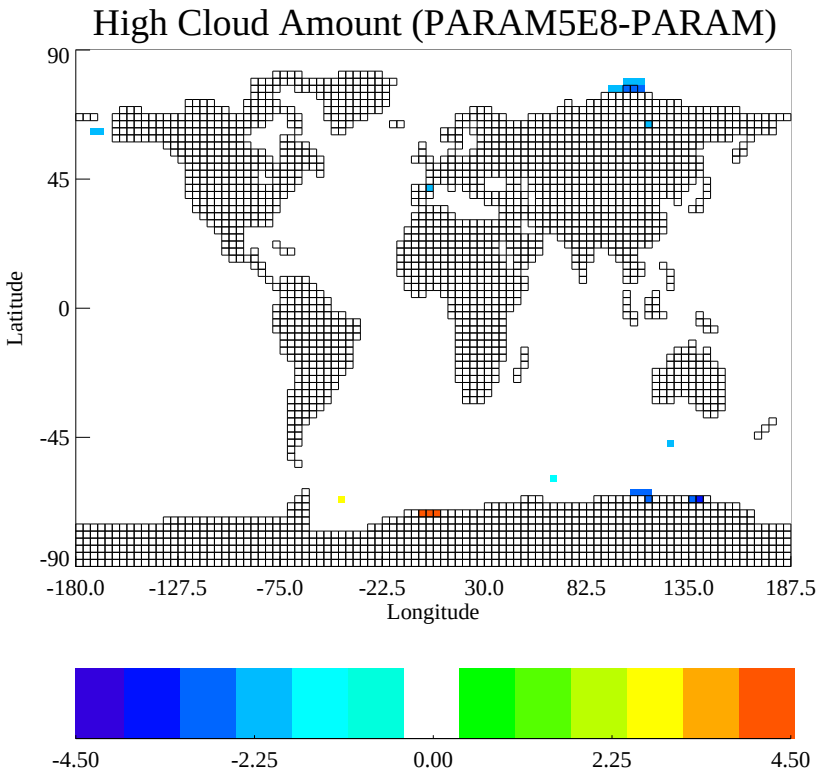

Figure D.2: Difference in global high cloud amount between PARAM and PARAM5E8.

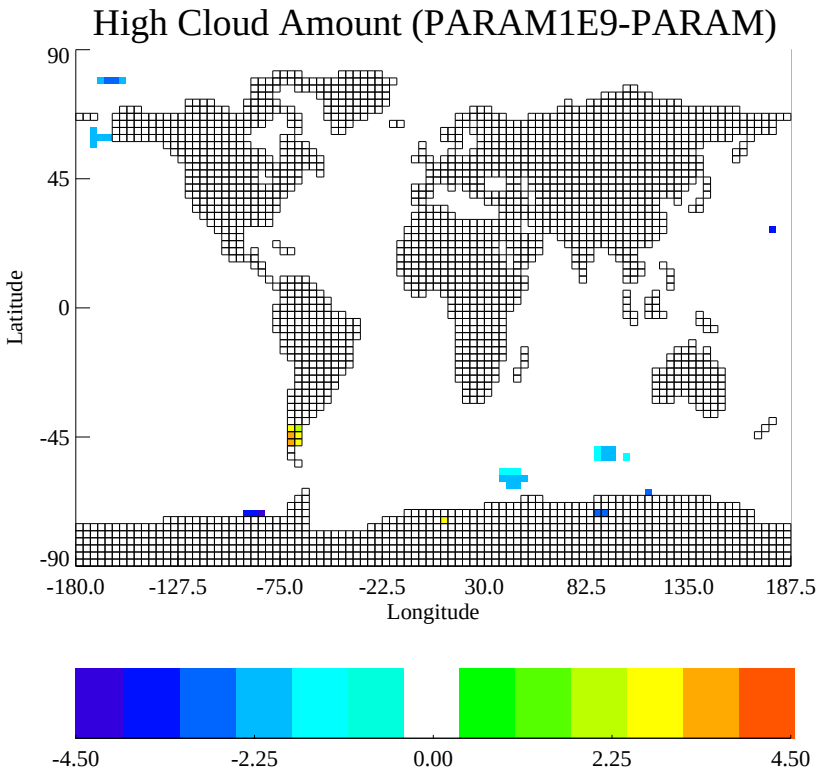

Figure D.3: Difference in global high cloud amount between PARAM and PARAM1E9.

References

Andrews, D. G., *An Introduction to Atmospheric Physics*. Cambridge University Press, 2000.

Auer, A. H., Wave cloud formations in the lee of southern New Zealand, *Weather*, *47*, 103–105, 1993.

Bachmeister, J. T., and R. T. Pierrehumbert, On high drag states of nonlinear stratified flow over an obstacle, *J. Atmos. Sci.*, *45*, 63–80, 1988.

Bacmeister, J. T., Mountain wave drag in the stratosphere and mesosphere inferred from observed winds and a simple mountain-wave parameterization scheme, *J. Atmos. Sci.*, *50*(3), 377–399, 1993.

Bacmeister, J. T., P. A. Newman, B. L. Gray, and K. R. Chan, An algorithm for forecasting mountain wave-related turbulence in the stratosphere, *Weather and Forecasting*, *9*, 241–253, 1994.

Bannon, P. R., and J. A. Yukas, On mountain drag over complex terrain, *Meteorol. Atmos. Phys.*, *43*, 155–162, 1990.

Banta, R. M., The role of mountains in making clouds, *Atmospheric Processes Over Complex Terrain*, pp. 229–283, William Blumen, Ed, 1990.

Bohren, C. F., and B. A. Albrecht, *Atmospheric Thermodynamics*. Oxford University Press, 1998.

Bretherton, F. P., Momentum transport by gravity waves, *Q. J. R. Meteorol. Soc.*, *95*, 213–243, 1969.

Brown, P. R. A., Aircraft measurements of mountain waves and their associated momentum flux over the British Isles, *Q. J. R. Meteorol. Soc.*, *109*, 849–865, 1983.

Butchart, N., and J. R. Knight, Estimates of sub-grid temperature perturbations from a gravity wave drag parameterization in a GCM, in *Mesoscale processes in the stratosphere—their effects on stratospheric chemistry and miscrophyysics*, edited by K. S. Carslaw, and G. T. Amanatidis, no. 69 in European Commission air pollution research report, pp. 31–34. 1999.

Carslaw, K. S., T. Peter, J. T. Bacmeister, and S. D. Eckermann, Widespread solid particle formation by mountain waves in the Arctic stratosphere, *J. Geophys. Res.*, *104*(D1), 1827–1836, 1999.

Champeney, D. C., *A Handbook of Fourier Theorems*. Cambridge University Press, 1987.

Cherry, N. J., A study of winds and waves, Ph.D. thesis, University of Canterbury, 1971.

Cherry, N. J., Winds and lee waves over Canterbury, New Zealand, *NZ J. Sci.*, *15*, 585–600, 1972.

Conover, J. H., The identification of orographically induced clouds observed by TIROS satellites, *J. Appl. Meteorol.*, *13*, 226–234, 1964.

Cooper, W. A., and G. Valli, The origin of ice in mountain cap clouds, *J. Atmos. Sci.*, *38*(6), 1244–1259, 1981.

Cotton, R. J., and P. R. Field, Ice nucleation characteristics in an isolated wave cloud, *Q. J. R. Meteorol. Soc.*, *128*(585), 2417–2437, 2002.

Cotton, W. R., and R. A. Anthes, *Storm and Cloud Dynamics*, vol. 44. Academic Press, 1989.

Cullen, M. J. P., T. Davies, and M. H. Mawson, *Conservative Finite Difference Schemes for a Unified Forecast/Climate Scheme*, Unified Model Documentation Paper 10, version 27, 1993.

Cusack, S., J. M. Edwards, and R. Kershaw, Estimating the subgrid variance of saturation and its parameterization for use in a GCM cloud scheme, *Q. J. R. Meteorol. Soc.*, *125*, 3057–3076, 1999.

Davies, L. A., and A. R. Brown, Assessment of which scales of orography can be credibly resolved in a numerical model, *Q. J. R. Meteorol. Soc.*, *127*, 1225–1237, 2001.

DelGenio, A. D., *Cirrus*, chap. GCM Simulations of Cirrus for Climate Studies, pp. 310–326. Oxford University Press, 2002.

Doyle, J. D., et al., An intercomparison of model-predicted wave breaking for the 11 January 1972 Boulder windstorm, *Mon. Wea. Rev.*, *128*, 901–915, 2000.

Durran, D. R., Another look at downslope winds. part I: The development of analogs to supercritical flow in an infinitely deep,continuously stratified fluid, *J. Atmos. Sci.*, *43*, 2527–2543, 1986a.

Durran, D. R., Mountain waves, *Mesoscale Meteorology and Forecasting*, pp. 472–492, Peter S. Ray, Ed, 1986b.

Durran, D. R., Mountain waves and downslope winds, *Atmospheric Processes Over Complex Terrain*, pp. 59–81, William Blumen, Ed, 1990.

Durran, D. R., and J. B. Klemp, Another look at downslope winds. part II: Nonlinear amplification beneath wave-overturning layers, *J. Atmos. Sci.*, *44*, 3402–3412, 1987.

Eckermann, S. D., and P. Preusse, Global measurements of stratospheric mountain waves from space, *Science*, *286*(5444), 1534–1537, 1999.

ECMWF, *User Guide to ECMWF Products 2.1*, European Centre for Medium-Range Weather Forecasting, 1995.

Edwards, J. M., and A. Slingo, Studies with a flexible new radiation code i: Choosing a configuration for a large scale model, *Q. J. R. Meteorol. Soc.*, *122*, 689–719, 1996.

Eliason, A., and E. Palm, On the transfer of energy in stationary mountain waves, *Geofys. Publ.*, *22*, 1–23, 1960.

Field, P. R., R. J. Cotton, K. Noone, P. Glantz, P. H. Kaye, and E. H. et al, Ice nucleation in orographic wave clouds: Measurements made durring INTACC, *Q. J. R. Meteorol. Soc.*, *127*(575), 1493–1512, 2001.

Fowler, L. D., and D. A. Randall, Simulation of upper tropospheric clouds with the Colorado State University general circulation model, *J. Geophys. Res.*, *104*(D6), 6101–6121, 1999.

Gibson, J., P. Kallberg, S. Uppala, A. Hermandez, A.Normura, and E. Serrano, ERA-15 description (version 2 -january 1999), Tech. rep., European Centre for Medium-Range Weather Forecasting, ERA ECMWF Re-Analysis Project Report Series, 1999.

Gill, A. E., *Atmosphere-Ocean Dynamics*, vol. 30. Academic Press, 1982.

Gregory, D., and P. Inness, *Convection Scheme*, Unified Model Documentation Paper 27, 1996.

Gregory, D., G. J. Shutts, and J. R. Mitchell, A new gravity-wave drag scheme incorporating anisotropic orography and low level wave breaking: Impact upon the climate of the UK Meteorological Office Unified Model, *Q. J. R. Meteorol. Soc.*, *124*, 463–493, 1998.

Hamilton, J., 30,000 feet and back before afternoon tea, *New Zealand Gliding Kiwi*, *21*(2), 16–18, 1992.

Harrison, E. F., P. Minnis, B. R. Barkstrom, V. Ramanathan, R. D. Cess, and G. G. Gibson, Seasonal variation of cloud radiative forcing derived from the earth radiation budget experiment, *J. Geophys. Res.*, *95*(D11), 18687–18703, 1990.

Harrison, T., 1000 km flight, *New Zealand Gliding Kiwi*, *24*(1), 3–5, 1997.

Hewson, T. D., Orographic cirrus generated by Iceland and the Faeroe Islands– 4-6 May 1993, *Meteorological Magazine*, *122*, 249–253, 1993.

Heymsfield, A. J., Microphysical structures of stratiform and cirrus clouds, *Aerosol-Cloud-Climate Interactions*, pp. 97–119, Peter V. Hobbs, Ed, 1993.

Heymsfield, A. J., and L. M. Miloshevich, Homogeneous ice nucleation and supercooled liquid water in orographic wave clouds, *J. Atmos. Sci.*, *50*(15), 2335–2353, 1993.

Heymsfield, A. J., and L. M. Miloshevich, Relative humidity and temperature influences on cirrus formation and evolution: observations from wave clouds and FIRE II, *J. Atmos. Sci.*, *52*(23), 4302–4326, 1995.

Heymsfield, A. J., L. M. Miloshevich, C. Twohy, G. Sachse, and S. Oltmans, Upper-tropospheric relative humidity observations and implications for cirrus ice nucleation, *Geophys. Res. Lett.*, *25*(9), 1343–1346, 1998.

Hobbs, P. V., Aerosol-cloud interactions, *Aerosol-Cloud-Climate Interactions*, pp. 33–69, Peter V. Hobbs, Ed, 1993.

Holmes, R. M., and K. D. Hage, Airborne observations of three Chinook-type situations in southern alberta, *J. Appl. Meteorol.*, *10*, 1138–1153, 1971.

Holton, J. R., *An Introduction to Dynamic Meteorology*, vol. 48. Academic Press, 3rd edn., 1992.

Houze, R. A., *Cloud Dynamics*, vol. 53. Academic Press, 1993.

Ingram, W. J., S. Woodward, and J. Edwards, *Radiation*, Unified Model Documentation Paper 23, 1997.

IPCC, *Climate Change 2001: The Scientific Basis*. Cambridge University Press, Contibution of Working Group 1 to the third Assesment Report of the Intergovernmental Panel on Climate Change, 2001.

Jacobowitz, H., AVHRR PATMOS datasets available online from NOAA, *Bull. Amer. Met. Soc.*, *80*, 967–968, 1999.

Jenson, E. J., O. B. Toon, S. A. Vay, J. Ovarlez, R. May, and T. P. B. et al, Prevalence of ice-supersaturated regions in the upper troposphere: implications for opitically thin ice cloud formation, *J. Geophys. Res.*, *106*(D15), 17253–17266, 2001.

Jin, Y., W. B. Rossow, and D. P. Wylie, Comparison of the climatologies of high-level clouds from HIRS and ISCCP, *J. Clim.*, *9*, 2850–2879, 1996.

Karcher, B., and U. Lohmann, A parameterization of cirrus cloud formation: Homogeneous freezing of supercooled areosols, *J. Geophys. Res.*, *107*(D2), ACL4–9,ACL4–10, 2002.

Katzfey, J. J., Simulation of extreme New Zealand precipitation events. part 1: Sensitivity to orography and resolution, *Mon. Wea. Rev.*, *123*, 737–754, 1995a.

Katzfey, J. J., Simulation of extreme New Zealand precipitation events. part 2: Mechanisms of precipitation development, *Mon. Wea. Rev.*, *123*, 755–775, 1995b.

Khvorostyanov, V. I., and K. Sassen, *Cirrus*, chap. Microphysical Process in Cirrus and their Impact on Radiation, pp. 397–432. Oxford University Press, 2002.

Klemp, J. B., and D. K. Lilly, The dynamics of wave-induced downslope windstorms, *J. Atmos. Sci.*, *32*, 320–339, 1975.

Klemp, J. B., and D. K. Lilly, Numerical simulations of hydrostatic gravity waves, *J. Atmos. Sci.*, *35*, 78–107, 1978.

Lane, T. P., M. J. Reeder, B. R. Morton, and T. L. Clark, Observations and numerical modelling of mountain waves over the Southern Alps of New Zealand, *Q. J. R. Meteorol. Soc.*, *126*, 2765–2788, 2000.

Laprise, J. P. R., An assessment of the WKBJ approximation to the vertical structure of linear mountain waves: Implications for gravity-wave drag parameterisation, *J. Atmos. Sci.*, *50*(11), 1469–1487, 1993.

Liao, X., W. B. Rossow, and D. Rind, Comparison between SAGE II and ISCCP high level clouds 1. Global and zonal mean cloud amounts, *J. Geophys. Res.*, *100*(D1), 1121–1135, 1995.

Lindzen, R. S., Turbulence and stress owing to gravity wave and tidal breakdown, *J. Geophys. Res.*, *86,NO.C10*, 9707–9714, 1981.

Lindzen, R. S., Supersaturation of vertically propagating internal gravity waves, *J. Atmos. Sci.*, *45*(4), 705–711, 1988.

Lohmann, U., J. Feichter, C. C. Chuang, and J. E. Penner, Prediction of the number of cloud droplets in the ECHAM GCM, *J. Geophys. Res.*, *104*(D8), 9169–9198, 1999.

Long, R. R., Some aspects of the flow of stratified fluids I. a theoretical investigation, *Tellus*, *5*, 42–58, 1953.

Long, R. R., Some aspects of the flow of stratified fluids III. continuous density gradients, *Tellus*, *7*, 341–357, 1955.

Ludlam, F. H., Orographic cirrus clouds, *Q. J. R. Meteorol. Soc.*, *78*(338), 552–562, 1952.

Lynch, D. K., *Cirrus*, chap. Cirrus:History and Definition, pp. 3–10. Oxford University Press, 2002.

Lyons, P., 1073.3 kms the easy way, *New Zealand Gliding Kiwi*, *23*(8), 28–30, 1996.

Maslowe, S. A., Critical layers in shear flows, *Annu. Rev. Fluid. Mech.*, *18*, 405–432, 1986.

McFarlane, N. A., The effect of orographically excited gravity wave drag on the general circulation of the lower stratosphere and troposphere, *J. Atmos. Sci.*, *44*(14), 1775–1800, 1987.

Nilson, E. D., L. Pirjola, and M. Kulmala, The effect of atmospheric waves on aerosol nucleation and size distribution, *J. Geophys. Res.*, *105*(D15), 19917–19926, 2000.

Norris, J. R., What can cloud observations tell us about climate variability, *Space Science Reviews*, *94*, 375–380, 2000.

Palmer, T. N., G. J. Shutts, and R. Swinbank, Alleviation of a systematic westerly bias in general circulation and numerical weather prediction models through an orographic gravity wave drag parameterisation, *Q. J. R. Meteorol. Soc.*, *112*, 1001–1039, 1986.

Peltier, W. R., and T. L. Clark, The evolution and stability of finite amplitude mountain waves. part II: Surface wave drag and severe downslope windstorms, *J. Atmos. Sci.*, *36*, 1498–1529, 1979.

Peltier, W. R., and T. L. Clark, Nonlinear mountain waves in two and three spatial dimensions, *Q. J. R. Meteorol. Soc.*, *109*, 527–548, 1983.

Pruppacher, H. R., and J. D. Klett, *Microphysics of Cloud and Precipitation*. Kluwer Academic Publishers, 2 edn., 1997.

Queney, P., The problem of airflow over mountains: A summary of theoretical studies, *Bull. Amer. Met. Soc.*, *29*, 16–26, 1948.

Queney, P., G. Corby, N. G. H. Koshmieder, and J. Zierep, The influence of mountains on the atmosphere, *WMO Tech. Note No.*, *34*, 1960.

Rankin, J. P., The structure of the northwest arch, Undergraduate Project Report, University of Canterbury, 1990.

Reid, S. J., Long-wave orographic clouds seen from satellites, *Weather*, *30*, 117–123, 1975.

Revell, C. G., High resolution satellite imagery of the New Zealand area; a view of lee waves, *Wea. and Climate*, *2*, 23–29, 1982.

Ridley, R. N., Observations and numerical modelling of air flows over New Zealand, Ph.D. thesis, Monash University, 1991.

Rogers, R. R., and M. K. Yau, *A Short Course in Cloud Physics*, vol. 113. Pergamon Press, 3 edn., 1989.

Rossow, W. B., and R. A. Schiffer, Advances in understanding clouds from ISCCP, *Bull. Amer. Met. Soc.*, *80*(11), 2261–2287, 1999.

Rossow, W. B., A. W. Walker, D. E. Beuschel, and M. D. Roiter, *International Satellite Cloud Climatology Project (ISCCP) Documentation of New Cloud Datasets*, World Climate Research Programme, 1996.

Rottman, J. W., and R. B. Smith, A laboratory model of severe downslope winds, *Tellus*, *41A*, 401–415, 1989.

Sassen, K., *Cirrus*, chap. Cirrus: A Modern Perspective, pp. 11–40. Oxford University Press, 2002.

Sawyer, J. S., Numerical calculation of the displacement of a stratified airstream crossing a ridge of small height, *Q. J. R. Meteorol. Soc.*, *unknown*(unknown), 326–345, 1960.

Scorer, R. S., Theory of waves in the lee of mountains, *Q. J. R. Meteorol. Soc.*, *76*, 41–56, 1949.

Senior, C. A., Comparison of mechanisms of cloud-climate feedbacks in GCMs, *J. Clim.*, *12*, 1480–1489, 1999.

Shaw, G. E., *Clouds and Climate Change*. University Science Books, 1996.

Shutts, G. J., *A New Gravity wave Drag Parameterization Scheme for the Unified Model*, U.K. Met. Office, 1990.

Shutts, G. J., Gravity-wave drag parameterization over complex terrain: The effect of critical-level absorption in directional wind shear, *Q. J. R. Meteorol. Soc.*, *121*, 1005–1021, 1995.

Slingo, A., Clouds and radiation in the Unified Model, U.K. Met. Office, Paper MOSAC 3-5, 1998.

Slingo, A., and D. W. Pearson, A comparison of the impact of an envelope orography and of a parameterization of orographic gravity-wave drag on model simulations, *Q. J. R. Meteorol. Soc.*, *113*, 847–870, 1987.

Smith, R. B., The influence of mountains on the atmosphere, *Advances in Geophysics*, *21*, 87–230, 1979.

Smith, R. B., On severe downslope winds, *J. Atmos. Sci.*, *42*, 2597–2603, 1985.

Smith, R. B., Hydrostatic airflow over mountains, *Advances in Geophysics*, *31*, 1–41, 1989.

Smith, R. B., A scheme for predicting layer clouds and their water content in a general circluation model, *Q. J. R. Meteorol. Soc.*, *116*, 435–460, 1990.

Smith, R. B., D. Gregory, C. Wilson, and A. C. Bushell, *Calculation of Saturated Specific Humidity and Large Scale Cloud*, Unified Model Documentation Paper 29, 1997.

Stephens, G. L., *Cirrus*, chap. Cirrus, Climate, and Global Change, pp. 433–448. Oxford University Press, 2002.

Stephens, G. L., S.-C. Tsay, P. W. Stackhouse, and P. J. Flatau, The relevance of microphysical and radiative properties of cirrus clouds to climate and climate feedback, *J. Atmos. Sci.*, *47*(14), 1742–1753, 1990.

Stowe, L. L., P. A. Davis, and E. P. McClain, Initial evaluation of the clavr-1 global clear/cloud classification algorithm for the advance very high resolution radiometer, *J. Atm. Ocean. Tech.*, *16*(6), 656–681, 1999.

Strom, J., and J. Heintzenberg, Water vapour, condensed water, and crystal concentration in orographically influenced cirrus clouds, *J. Atmos. Sci.*, *51*(14?), 2368–2383, 1994.

Sturman, A. P., A case study of lee waves in southwesterly airflow over Banks Peninsula, New Zealand, *Weather*, *35*, 32–39, 1980.

Sundqvist, H., Parameterization of clouds in large scale numerical models, *Aerosol-Cloud-Climate Interactions*, pp. 175–203, Peter V. Hobbs, Ed, 1993.

Sundqvist, H., *Cirrus*, chap. On Cirrus Modelling for General Circulation and Climate Models, pp. 297–309. Oxford University Press, 2002.

Tan, K., and S. D. Eckermann, Numerical simulations of mountain waves in the middle atmosphere over the southern Andes, *Geophysical Monograph*, *123*, 311–318, Atmospheric Science Across the Stratopause, 2000.

Uddstrom, M. J., J. A. McGregor, W. R. Gray, and J. W.Kidson, A high resolution analysis of cloud amount and type over complex orography, NIWA Document, 1999.

Uddstrom, M. J., J. A. McGregor, W. R. Gray, and J. W. Kidson, A high resolution analysis of cloud amount and type over complex orography, *J. Appl. Meteorol.*, *40*, 16–33, 2001.

U.K. Met Office, *Unified Model User Guide*, 1998.

Vergeiner, I., An operational linear lee wave model for arbitrary basic flow and two dimensional topography, *Q. J. R. Meteorol. Soc.*, *97*, 30–60, 1971.

Wallace, J. M., S. Tibaldi, and A. J. Simmons, Reduction of systematic forecast errors in the ECMWF model through the introduction of an envelope orography, *Q. J. R. Meteorol. Soc.*, *109*, 683–717, 1983.

Wang, P., P. Minnis, M. P. McCormick, G. S. Kent, and K. M. Skeens, A six year climatology of cloud occurence frequency from Stratospheric Aerosol and Gas Experiment II observations (1985-1990), *J. Geophys. Res.*, *101*, 29407–29429, 1996.

Weare, B. C., and I. I. Mokhov, Evaluation of total cloudiness and its variability in the atmospheric model intercomparison project, *J. Clim.*, *8*, 2224–2238, 1995.

Webb, M., C. Senior, S. Bony, and J.-J. Morcrette, Combining ERBE and ISCCP data to assess clouds in the Hadley Centre, ECMWF and LMD atmospheric climate models, *Clim. Dyn.*, *17*(12), 905–922, 2001.

Webster, S., *Gravity Wave Drag*, Unified Model Documentation Paper 22, 1997.

Wilson, D., and D. Gregory, The behavior of large-scale model cloud schemes under idealized forcing scenarios, *Q. J. R. Meteorol. Soc.*, *129*, 967–986, 2003.

Wilson, D. R., *3B and 3A Large scale Precipitation Schemes*, Unified Model Documentation Paper 26, version no. 4, 1999.

Wilson, D. R., and S. P. Ballard, A microphysically based precipitation scheme for the UK Meteorological Office Unified Model, *Q. J. R. Meteorol. Soc.*, *125*, 1607–1636, 1999.

Wurtele, M. G., R. D. Sharman, and A. Datta, Atmospheric lee waves, *Annu. Rev. Fluid. Mech.*, *28*, 429–476, 1996.

Wylie, D. P., and W. P. Menzel, Eight years of high cloud statistics using HIRS, *J. Clim.*, *12*, 170–184, 1999.

Wylie, D. P., and P. Wang, Comparison of cloud frequency data from HIRS and SAGE-II, *J. Geophys. Res.*, *102*, 29893–29900, 1997.

Xu, K.-M., and D. A. Randall, A semiempirical cloudiness parameterization for use in climate models, *J. Atmos. Sci.*, *53*(21), 3084–3102, 1996.

Young, G. S., and R. A. Pielke, Application of terrain height variance spectra to mesoscale modelling, *J. Atmos. Sci.*, *40*, 2555–2560, 1983.